Metallurgical development of high-performance biodegradable twinning-induced plasticity steels

Thèse en cotutelle
Doctorat en génie des matériaux et de la métallurgie
Doctoral programme in Mechanical Engineering (XXXII cycle)

Sergio Loffredo

Université Laval
Québec, Canada
Philosophiae Doctor (Ph. D.)

et

Politecnico di Milano
Milan, Italie
Philosophiae Doctor (Ph. D.)

Metallurgical development of high-performance biodegradable twinning-induced plasticity steels

Thèse en cotutelle
Doctorat en génie des matériaux et de la métallurgie
Doctoral programme in Mechanical Engineering (XXXII cycle)

Sergio Loffredo

Sous la direction de :

Diego Mantovani, directeur de recherche
Maurizio Vedani, directeur de cotutelle

Résumé

L'athérosclérose est une des maladies cardiovasculaires les plus récurrentes dans le monde, consistant dans l'obstruction d'une artère par des dépôts fibreux. Un des traitements les plus utilisés consiste dans l'implantation d'un stent, une mèche métallique tubulaire, afin de rouvrir l'artère et restaurer le flux sanguin. Un stent est normalement conçu pour rester dans le patient pour toute sa vie, mais des réactions inflammatoires peuvent se manifester à long terme. Pour cette raison, et pour pouvoir aussi traiter des jeunes patients, des stents biodégradables ont été pensés. Parmi eux, un dispositif à base de magnésium a reçu l'approbation à la commercialisation dans l'Union Européenne en 2016. Bien que ce dispositif se soit démontré sécuritaire dans des essais cliniques, sa taille est beaucoup plus grande que celle des stents permanents communément utilisés à cause des faibles propriétés mécaniques de la matrice. Une famille de matériaux avec des excellentes propriétés mécaniques et un bon potentiel de dégradation sont les aciers à plasticité induite par maclage, composés de fer, manganèse et carbone. En revanche, leur applicabilité clinique n'est pas actuellement possible car leur dégradation est entravée par la formation d'une couche de produits de dégradation pendant ce processus. Ce travail propose d'ajouter une petite quantité d'argent à un acier composé de fer, manganèse et carbone pour accélérer le processus de dégradation sans réduire ses propriétés mécaniques. Les travaux de cette thèse ont porté sur le développement de ces alliages, leur validation métallurgique et l'étude de leur dégradation. Ces études ont montré que l'ajout d'argent n'a pas affecté significativement les propriétés mécaniques de l'alliage de base. Au contraire, il a été observé que cet ajout a modifié la structure de l'alliage sous une déformation plastique et sa capacité de récupérer la structure initiale après une telle déformation. Au niveau de la dégradation, la présence d'argent n'a pas permis d'accélérer ce processus, étant efficace seulement dans les premiers jours. En opposition, l'évolution du mécanisme de dégradation jusqu'à six mois détecté dans cette thèse est très proche du comportement observé dans des tests sur des animaux conduits par d'autres chercheurs. En conclusion, bien que la stratégie retenue ne se soit pas révélée efficace pour atteindre l'objectif ciblé, les avancées dans la compréhension du mécanisme de dégradation et de la mise en forme des aciers à plasticité induite par maclage pour des stents vasculaires peuvent permettre le développement d'autres stratégies efficaces à long terme pour permettre à ces alliages de se dégrader dans le corps humain.

Abstract

Atherosclerosis is one of the most recurring diseases in the world, consisting in obstruction of an artery by fibrous deposits. One of the most used treatments consists in implanting a stent, a tubular metallic mesh, for reopening the artery and restoring blood flow. A stent is normally designed to remain in the patient for all his life, but inflammatory reactions may occur at long terms. Because of this, and also for treating young patients, biodegradable stents were designed. Among them, a magnesium-based device received approval for commercialization in the European Union in 2016. Although this device proved safe in clinical trials, its size is much larger than permanent stents. This is due to the low mechanical properties of the matrix. A family of materials with excellent mechanical properties and a good degradation potential are twinning-induced plasticity steels, made of iron, manganese and carbon. On the other hand, their clinical applicability is currently not possible since their degradation is hindered by formation of a stable product layer during this process. This work proposes to add a small quantity of silver to a steel made of iron, manganese and carbon to accelerate the degradation process without reducing its mechanical properties. The works in this thesis dealt with development of such alloys, their metallurgical validation and the study of their degradation. These studies showed that the addition of silver did not significantly affect mechanical properties of the base alloy. On the contrary, it was observed that this addition modified the alloy structure under plastic deformation and its capability to recover its initial structure after such a deformation. Concerning degradation, the presence of silver did not allow to accelerate this process, being effective only in the first days. In contrast, the evolution of degradation mechanism up to six months detected in this thesis is very close to the behavior observed in animal tests conducted by other researchers. In conclusion, although the retained strategy did not prove effective in attaining the targeted goal, the advances in the understanding of corrosion mechanism and processing of twinning-induced plasticity steels for vascular stents can foster the development of other strategies that are effective in the long term to allow these alloys to degrade in human patients.

Sommario

L'aterosclerosi è una delle malattie cardiovascolari più diffuse nel mondo, e consiste nell'ostruzione di un'arteria da parte di depositi fibrosi. Uno dei trattamenti più utilizzati consiste nell'impiantazione di uno stent, una struttura metallica tubolare, per riaprire l'arteria e restaurare il flusso sanguigno. Uno stent è normalmente concepito per restare nel paziente per tutta la sua vita, ma delle reazioni infiammatorie possono avere luogo a lungo termine. Per questo motivo, e per poter inoltre trattare pazienti giovani, degli stent biodegradabili sono stati pensati. Tra loro, un dispositivo a base di magnesio ha ricevuto l'approvazione per la commercializzazione nell'Unione Europea nel 2016. Sebbene questo dispositivo si sia dimostrato sicuro in test clinici, le sue dimensioni sono molto più grandi di quelle degli stent permanenti comunemente usati nella pratica clinica a cause delle scarse proprietà meccaniche della matrice. Una famiglia di materiali con eccellenti proprietà meccaniche e un buon potenziale di degradazione sono gli acciai a plasticità indotta da geminazione, composti da ferro, manganese e carbonio. Per contro, la loro applicabilità clinica non è attualmente possibile poiché la loro degradazione è ostacolata dalla formazione di uno strato stabile di prodotti durante questo processo. Questo lavoro propone di aggiungere una piccola quantità d'argento a un acciaio composto da ferro, manganese e carbonio per accelerare il processo di degradazione senza ridurre le sue proprietà meccaniche. I lavori di questa tesi si sono concentrati sullo sviluppo di queste leghe, sulla loro validazione metallurgica e lo studio della loro degradazione. Questi studi hanno mostrato che l'aggiunta di argento non ha influenzato significativamente le proprietà meccaniche dell'acciaio di base. Al contrario, è stato osservato che quest'aggiunta ha modificato la struttura della lega durante una deformazione plastica, oltre alla sua capacità di recuperare la struttura iniziale dopo una tale deformazione. Riguardo la degradazione, la presenza d'argento non ha permesso di accelerare questo processo, essendo efficace soltanto nei primi giorni. Al contrario, l'evoluzione del meccanismo di degradazione fino a sei mesi rilevato in questa tesi è molto vicino a quanto osservato da altri ricercatori in test animali. In conclusione, sebbene la strategia utilizzata non si sia rivelata efficace per raggiungere l'obiettivo prefissato, i progressi nella comprensione del meccanismo di degradazione e della produzione degli acciai a plasticità indotta da geminazione per gli stent vascolari possono permettere lo sviluppo di altre strategie efficaci a lungo termine per permettere la degradazione di queste leghe nel corpo umano.

Table of contents

List of figures

List of tables

List of abbreviations

α: ferrite
γ: austenite
ε: martensite with an HCP (s.) structure
AAS: atomic absorption spectroscopy
AM: additive manufacturing
BCC: body-centered cubic
BCT: body centered tetragonal
BMS: bare metal stents
CABG: coronary artery bypass grafting
CAD: coronary artery disease
CPE: constant phase element
CR: corrosion rate
CRA: cold rolled and annealed
CR10: cold rolled with a 10% thickness reduction
CR25: cold rolled with a 25% thickness reduction
CR50: cold rolled with a 50% thickness reduction
CVDs: cardiovascular diseases
DAPT: dual anti-platelet therapy
DED: direct energy deposition
DES: drug eluting stents
DPs: degradation products
DSA: dynamic strain aging
EBM: electron beam melting
EBSD: electron backscattered diffraction
ECs: endothelial cells
EDS: energy dispersion x-ray spectroscopy
EIS: electrochemical impedance spectroscopy
FBs: fibroblasts
FT-IR: Fourier transform infrared spectroscopy
HMSS: Hanks' modified salt solution
HCP: hexagonal close packed
IPF: inverse pole figures
ISR: in-stent restenosis
LST: late stent thrombosis
MMCs: metal matrix composites
MP-AES: microwave plasma atomic emission spectrometry
MRI: magnetic resonance imaging
MUD: mean uniform deviation
OCP: open circuit potential

ODF: orientation distribution functions
OIM: orientation image map
PDLLA: poly-d, l-lactic acid
PDP: potentiodynamic polarization
PLA: polylactic acid
PLGA: poly lactic-co-glycolic acid
PLLA: poly l-lactic acid
PM: powder metallurgy
PTCA: percutaneous transluminal coronary angioplasty
PTFE: polytetrafluoroethylene
Q.I.: quality index
REE: rare earth elements
SBF: simulated body fluid
SCE: saturated calomel electrode
SEM: scanning electron microscopy
SF: stacking fault
SFE: stacking fault energy
SHE: standard hydrogen electrode
SLM: selective laser melting
SMCs: smooth muscle cells
TEM: transmission electron microscopy
TWIP: twinning-induced plasticity
UTS: ultimate tensile strength
WDS: wavelength dispersion x-ray spectroscopy
WHO: world health organization
wt. %: weight percentage
XRD: x-ray diffraction
YS: yield strength

Acknowledgements

This work involved an international collaboration between three institutions in Europe and North America. The project would not have been possible without my two research supervisors, Profs. Diego Mantovani and Maurizio Vedani, that I thank deeply for their guidance, their trust in my work ethic and their willingness to challenge my thoughts and push me outside my comfort zone, which made this journey very exciting and definitely developed me as a better person.

Three more people were decisive for achieving the results presented in this thesis: Carlo Paternoster and Sofia Gambaro from LBB at Laval University, together with Nicolas Giguère at the Quebec Metallurgy Center. Their constant availability to answer my questions and scientific knowledge in a plethora of fields were fundamental for making these results come to reality. I am deeply grateful for your support.

I met loads of colleagues at all institutions involved in this work. All of them contributed to making me a better scientist and, most of all, a better person. I am definitely forgetting someone, and I apologize for that. At LBB, a special mention goes to Pascale for making the lab always functional and solving every possible problem arising. In addition, I would like to give a special thanks to Linda, Dimitria and Carolina, who were in the lab since day 1 and made this journey very enjoyable. I would also like to acknowledge my first peer mentor at LBB, Essowè, who introduced me to the particularities of biodegradable metals. A big thank you to all past and present members of the Biometal Team at LBB: Leticia, Samira, Vinicius, Malgo, Beatrice, William, Maxime and Souhila. Each of you taught me a lot, and I am grateful for that. I also acknowledge all other past and present members of LBB: Francesco, Sergio, Vane, Maxime, Gabriel, Alessandro, Lorenzo, Caroline, Sara, Gloria, Fede, Ludi and my Rouge et Or labmate Nele. I also have a special mention to those who made this journey less enjoyable at times. You made me understand how I do not want to be treated and how I do not want to behave, so thank you.

I would also like to thank the wonderful people I met at the Department of Mining, Metallurgy and Materials Engineering at Laval University. First of all, I would like to acknowledge the work of all lab technicians and administrative staff, Nathalie, Vicky, Daniel, Andrée, Geneviève et Anne. Secondly, I thank all students at the department who made this

journey a wonderful one, albeit with a relatively noisy office when we had one: Simon, Keven, Justin, Geoffroy, JF, Ramzi, Behzad, Denis, Cyril, Tohid, Maryam (times n), Pierre, Maude, Reza.

I am also very grateful to have had the opportunity to spend a significant part of my project at the Quebec Metallurgy Center in Trois-Rivières, which was an incredibly formative experience, and was pivotal in the success of this project. In addition to Nicolas, whom I thanked before, I would like to thank the general manager of CMQ, Gheorghe Marin, for greenlighting the project and having total trust in what we did. I would also like to thank all my former colleagues and collaborators, Bernard, David, Jean-Nicolas, NicolasD, Caroline, Patrick, Hugues, Tony, Line, Julie, Pierrette, Louise, Lise, Luc, Guy.

In addition, I would like to thank all the professors, technicians and fellow students at the Department of Mechanical Engineering at Politecnico di Milano: Riccardo, Silvia, Andrea, Andrea, Marco, Claire, Ruben, Filippo, Joao, Chiara, Zhiwei, Dario, Anna, Claudia, Cinzia, Maurizio, Silvia, Ludovica, Luca, Lorenzo, Lorenzo, Sergio, Filippo, Salvatore.

Moving outside the work environment, I would like to deeply thank the family that welcomed and supported me during these five years in Quebec, the Rouge et Or track and field team. My first thanks go to the first head coach and throws coach who allowed me to enter this wonderful world, Félix-Antoine et Simon. I also have a special mention to my fellow throwers who were there from day one and welcomed my strange accent in the group: Simon, Joey, Noémie, Isabelle, Philippe. I would also like to thank all the throwers whom I met during this journey: Nadine, Gab, Derek, Eve-Ma, Mauricio, Jeffson, Frank et Issa. I would like also to thank the freshmen who just entered the group and will make Laval the place to be in the near future: Mathieu, Felix-Antoine et Jordan. I would also like to thank all former team captains: Simon, Ben, Catherine, Nicolas, Rose, Roxanne, Jessy, Aurélie, Peter, Jean-Samuel. Having had you as role models was a real honor, and filling your shoes during my last year was an incredible privilege. I would like to deeply thank my current head coach Sylvain for trusting me with this responsibility, which was very challenging but at the same time the most rewarding experience in these five years. I also thank my three co-captains who accompanied me in this crazy adventure: Rose, Roxanne and Félix. I would also like to thank all my other past and present teammates who made this experience amazing and unforgettable. All the titles and medals we won in these four years together are just the beginning of the journey. As long as this family remains bound, great things await us.

At last, but definitely not for importance, I would like to thank my family who, even thousands of kilometers afar, always supported me in this journey. A big thank you to my grandmother who raised me when my mother was at work. I also have a special thanks to my other grandparents who are no longer in this world, but they will always have a place in my heart, either if they are seeing this achievement from somewhere else or they are no longer. Lastly, a very heartfelt thank you to my mother, who managed to grow me up not without difficulty and made me the man I am today. From the bottom of my heart, thank you. I love you.

Foreword

This thesis work was carried out as a double doctoral degree between *Université Laval* (Quebec City, Canada) and *Politecnico di Milano* (Milan, Italy). The work was also conducted in partnership with the *Centre de Métallurgie du Québec* (Trois-Rivières, Canada). The project revolved around the development and the validation of twinning-induced plasticity (TWIP) steels enriched with silver for high performance biodegradable implants. The work as a whole required technical and scientific expertise from several domains, which prompted the collaboration between the three aforementioned institutions.

The **Laboratory for Biomaterials and Bioengineering (LBB)** at *Université Laval*, directed by prof. Mantovani, has an established expertise in the development of Fe-based biodegradable metals for cardiovascular stents. In addition, it possesses a strong know-how in the characterization of the corrosion behavior and biological performances of biomaterials. More in detail, static immersion tests, electrochemical tests and part of the related surface characterization were conducted here, namely Fourier transform infrared spectroscopy (FT-IR). In addition, the candidate performed part of the work presented here at the laboratories of the **Department of Mining, Metallurgy and Materials Engineering** at the same institution. Metallographic preparation of specimens for the works presented in chapters 4 and 5 was partly performed here, together with all the microwave plasma atomic emission spectrometry (MP-AES) analyses presented in chapters 4 and 5 and the x-ray diffraction (XRD) analyses presented in chapters 2 and 4.

The **Advanced Materials and Smart Structures** section of the Department of Mechanical Engineering at *Politecnico di Milano*, where prof. Vedani operates as section head, has a proven know-how in processing and characterization of biodegradable metals of various types. All sheets of the developed alloys were rolled here. All tensile tests were carried out here, together with the XRD, scanning electron microscopy (SEM) and electron backscattered diffraction (EBSD) analyses presented in chapter 3.

The **Centre de Métallurgie du Québec** is a *Centre Collégial de Transfert Technologique* attached to the *CÉGEP de Trois-Rivières*, possessing a renowned expertise in the development of new metallurgical products and processes for various industries, together with their characterization. The developed alloys were cast and thermally treated here. All SEM and energy dispersion x-ray

spectroscopy (EDS) analyses presented in chapters 2, 4 and 5 were performed here, together with the EBSD and wavelength dispersion x-ray spectroscopy (WDS) analyses included in chapter 3.

This work is proposed as an article insertion thesis. It includes four research papers and a book chapter in which the candidate was the principal investigator. The thesis is divided in 8 chapters.

The **Introduction** presents the problem statement, the formulation of the hypothesis, the definition of the objectives and the chosen methodology for validating the hypothesis

Chapter 1 provides a comprehensive literature review on the state of the art of Fe-based biodegradable metals for cardiovascular stents

Chapter 2: *The addition of silver affects the deformation mechanism of a twinning-induced plasticity steel: Potential for thinner degradable stents*

Authors: S. Loffredo, C. Paternoster, N. Giguère, G. Barucca, M. Vedani, D. Mantovani

Publication history:

Journal: Acta Biomaterialia
Submitted on December 13, 2018
Submitted in revised form on March 11, 2019
Accepted on April 11, 2019

SL and CP designed the study. SL and NG designed and performed the foundry and thermal treatment processes. SL and MV designed and performed the rolling treatments. SL performed all mechanical characterization, together with SEM, WDS and EBSD analyses. GB designed and performed TEM analyses. SL wrote the manuscript. All authors commented and discussed the manuscript prior to submission.

Chapter 3: *Effect of silver in thermal treatments of Fe-Mn-C degradable metals: Implications for stent processing*

Authors: S. Loffredo, S. Gambaro, C. Paternoster, N. Giguère, M. Vedani, D. Mantovani

Publication history:

Journal: Bioactive Materials
Submitted on October 20, 2020

SL, CP and SG designed the study. SL, NG and MV prepared the material. SL performed all thermal and mechanical treatments. SL performed all microstructural and mechanical characterizations. SG provided critical discussion on the EBSD results and assisted with thermodynamic simulation. SL wrote the manuscript. All authors commented and discussed the manuscript prior to submission.

Chapter 4: *Effect of Silver on Corrosion Behavior of Plastically Deformed Twinning-Induced Plasticity Steel for Biodegradable Stents*

Authors: S. Loffredo, C. Paternoster, N. Giguère, M. Vedani, D. Mantovani

Publication history:

Journal: JOM
Submitted on November 29, 2019
Submitted in revised form on February 16, 2020
Accepted on February 25, 2020

SL and CP designed the study. SL, NG and MV produced the samples for the analyses. SL performed all corrosion studies and related characterizations. SL and CP critically analyzed the data. SL wrote the manuscript. All authors commented and discussed the manuscript prior to submission.

Chapter 5: *Six-months long in vitro degradation tests of biodegradable twinning-induced plasticity steels alloyed with Ag for stent applications*

Authors: S. Loffredo, S. Gambaro, L. Marin de Andrade, C. Paternoster, R. Casati, N. Giguère, M. Vedani, D. Mantovani

Publication history:

Journal: ACS Biomaterials Science & Engineering
Submitted on March 15, 2021

SL, CP and SG designed the study. SL, NG and MV produced the samples for the study. SL, LMA, SG and CP performed the static immersion tests. LMA performed and analyzed the FT-IR experiments. SL and SG performed and analyzed the MP-AES experiments. SL performed SEM, EDS and EIS analyses. SL wrote the manuscript. All authors contributed to the manuscript through discussion.

Chapter 6 elaborates on the results presented in chapters 2 to 5 and provides a general discussion of the results obtained in this work. Finally, a general **conclusion** to this thesis work is given, together with perspectives for future research.

The following book chapters and paper were also published by the candidate during the doctorate, but are not included in this thesis:

1. S. Loffredo, C. Paternoster, D. Mantovani. Iron-based degradable implants, *in: Encyclopedia of Biomedical Engineering,* vol. 2 (2019), ed. R. Narayan, Elsevier, 374-385.

2. S. Loffredo, H. Hermawan, M. Vedani, D. Mantovani. Absorbable metals for cardiovascular applications, *in: Metals for Biomedical Devices, 2nd Edition* (2019), ed. M. Niinomi, Elsevier, 523-543.

3. H.-S. Han, S. Loffredo, I. Jun, J. Edwards, Y.-C. Kim, H.-K. Seok, F. Witte, D. Mantovani, S. Glyn-Jones. Current status and outlook on the clinical translation of biodegradable metals, *Materials Today* **23** (2019), 57-71.

Introduction

Context and motivation

Cardiovascular diseases

Cardiovascular diseases (CVDs) are the leading cause of decease worldwide. According to the World Health Organization (WHO) [1], in 2016 CVDs accounted for 26.8% of all deaths recorded in the world, as visible from figure 0.1. The two most common types of CVDs are ischaemic heart disease (also known as coronary artery disease, CAD) and cerebrovascular disease. The risk factors for the insurgence of CVDs can be divided in two main categories: behavioral and congenital ones [1]. Behavioral risk factors include, for example, a sedentary lifestyle, poor alimentary habits, and tobacco consumption. These risk factors can be mitigated by a healthy lifestyle and regular physical activity, among others.

Both behavioral and congenital factors can lead to mild to severe CVDs, eventually provoking a heart attack (in the case of CAD) or a stroke (in the case of cerebrovascular diseases). In both cases, atherosclerosis is the predominant disease resulting in such severe complications [2].

Atherosclerosis

A healthy arterial wall is composed of 3 concentric layers: the *tunica intima*, the *tunica media* and the *tunica adventitia*, as visible in figure 0.2. Each layer is constituted of different cell types: the *tunica intima* by endothelial cells (ECs), the *tunica media* by smooth muscle cells (SMCs) and the *tunica adventitia* by fibroblasts (FBs) supported by connective tissue [2]. The free space inside the artery, where blood flows, is known as *lumen*.

The ECs in the *tunica intima* can suffer traumatic events, which can be due to many factors. In such cases, SMCs can proliferate inside the *intima*, creating a thickening of the vascular wall, known as neointimal formation. One of the factors causing such injury is the accumulation of lipoproteins on the vessel wall. In this case, the first response to injury consists in the activation of macrophages, which phagocytise the majority of lipoproteins, followed by the aforementioned migration of SMCs. However, an excess of lipids may be accumulated inside the *neointima* without being phagocytised by macrophages, causing a reduction in lumen cross

section, which alters blood flow. This disease is known as atherosclerosis, and the *neointima* comprising the excess lipids is called atheroma. Further expansion of the atheroma may lead to complete occlusion of the artery (stenosis), formation of a blood clot (thrombus) on the atheroma, or excess bulging of the artery itself (aneurysm). All these phenomena may ultimately result in myocardial infarction or stroke, ultimately leading to patient death.

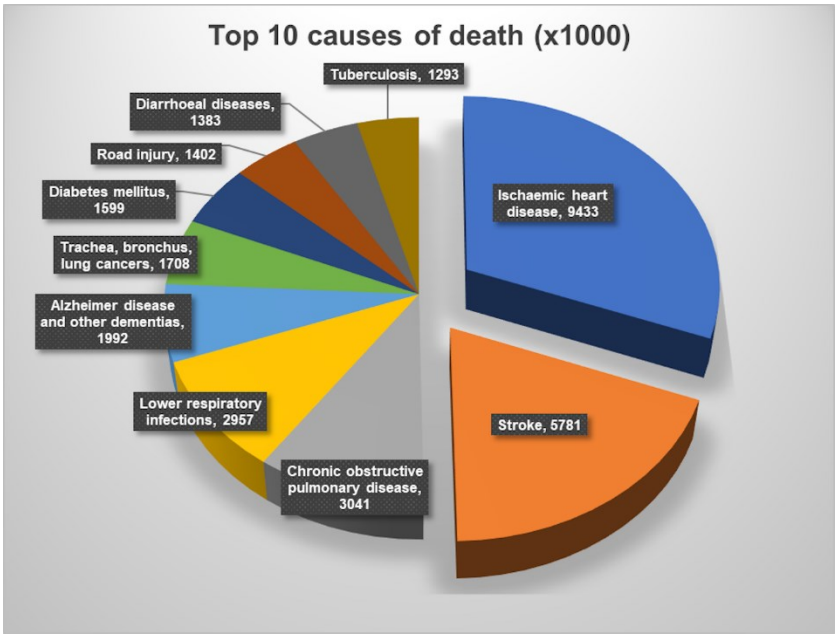

Figure 0.1 Overview of the top 10 causes of death in the world as of 2018 [1]

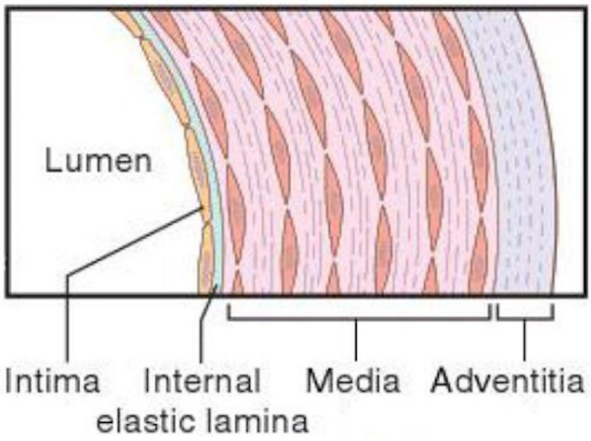

Figure 0.2 Structure of a vessel wall [2]

Treatments for atherosclerosis

Several options are available to clinicians when treating patients presenting atherosclerosis, depending on disease severity [19]. All strategies are aimed at restoring normal blood flow at the diseased site. In mild cases, the adoption of a healthy lifestyle is generally recommended, including modifying alimentary habits and eliminating tobacco smoke. For moderate cases, treatment with drugs such as statins can be sought. Finally, in more severe cases, one of the following surgical procedures must be employed to restore circulation:

- Balloon angioplasty [20]. This procedure consists in driving an inflatable balloon, mounted on a catheter, at the diseased site. The balloon is then inflated to crush the atheroma, thus re-opening the artery and restoring normal blood flow. This procedure is plagued by a high incidence of artery re-occlusion, known as restenosis.
- Percutaneous transluminal coronary angioplasty (PTCA) [21]. This procedure resembles closely the previously described balloon angioplasty. The difference lies in the introduction of a tiny tubular mesh inside the artery, known as **stent**. The stent is mounted on a catheter and placed at the diseased site, either by inflation by a balloon or by self-expansion, allowing permanent placement of the device to avoid re-occlusion of the artery.
- Atherectomy [22]. This procedure involves bulk removal of the atheroma by means of laser ablation or using a rotative device driven at the diseased site. On the other hand, clinical studies have not demonstrated a clear superiority of this technique with respect to PTCA.
- Coronary artery bypass grafting (CABG) [21]. In cases where the diseased artery is completely occluded by the atheroma, the only possible solution is to bypass the site by grafting a replacement artery at the two extremities of the occlusion. The replacement artery can be either autologous (taking a portion of a blood vessel from the patient and using it as replacement, most commonly the saphenous vein) or artificial (using polymeric tubes, commonly made from woven filaments of Dacron ® or bulk polytetrafluoroethylene (PTFE))

An overview of PTCA is presented in figure 0.3. PTCA can also be used for treatment of cerebrovascular diseases, including cerebral atherosclerosis and intracranial aneurysms [23].

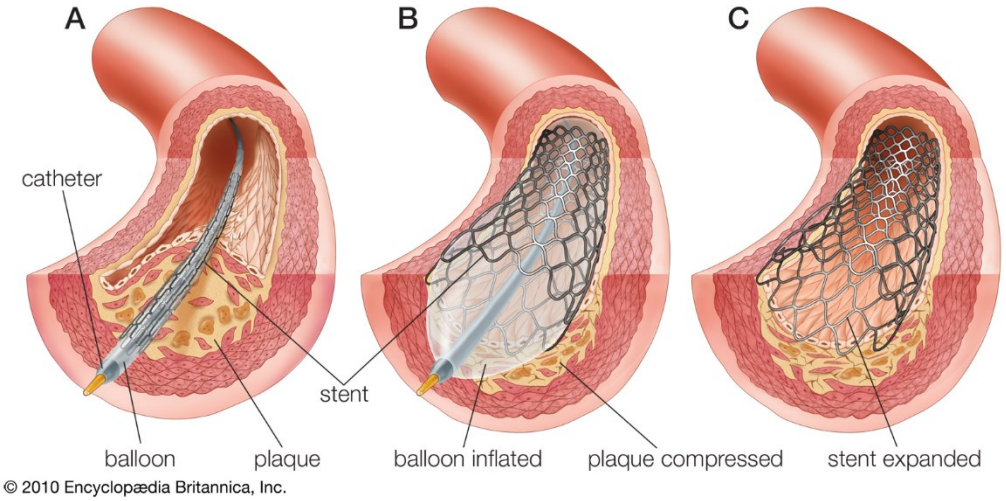

Figure 0.3 Schematic representation of PTCA: A) the catheter is guided at the atherosclerotic site; B) the balloon is inflated, placing the stent; C) the balloon is deflated, the catheter removed, leaving only the expanded stent in the artery [3]

Cardiovascular stents – an overview

Medical perspective

As described before, a cardiovascular stent is a small tubular mesh placed at a diseased site by means of a catheter. Stents can be divided in three families, depending on the position of the artery they are designed to treat in the body:

1. Coronary stents, when the artery is in close proximity to the heart.
2. Peripheral stents, when the artery is not close to the heart, but not in the brain.
3. Cerebrovascular stents, when the artery is inside the brain.

These three types of arteries differ in their distance from the heart, diameter, wall thickness, relative thickness of the three *tunica* layers and tortuosity of the path through which the catheter must be driven. Because of these differences, the catheter and the stent itself shall possess mechanical performances suited to the site where they will be deployed. Different arteries also have a different compliance to deformation, thus reducing or totally eliminating the amount of inflation that can be applied by a balloon for placing the stent [24].

Once the stent is placed at the diseased site, the spontaneous reaction of the cells in the vessel wall is to trigger a foreign body reaction, where macrophages are activated to remove the stent [25]. When the clinical outcome is positive, endothelialisation occurs, consisting in encapsulation of the stent by a new layer of ECs in the first 2 to 4 weeks following surgery. In order to guarantee proper endothelialisation, the patient must also receive dual anti-platelet

therapy (DAPT) to prevent platelet adhesion to the stent, which may stimulate the formation of a thrombus [2]. Furthermore, the stent must not trigger chronic inflammatory reactions, which can provoke severe long-term complications, such as in-stent restenosis (ISR) or thrombosis (figure 0.4). ISR consists in the re-occlusion of the artery due to excessive proliferation of SMCs in the *neointima* during the life of the patient.

Engineering perspective

Starting from the considerations made from a medical perspective, a stent must possess suitable properties from a mechanical, corrosion and biological point of view. An overview of these requirements can be found in table 0.1. When considering cerebrovascular stents, the flexibility of the stent is also of utmost importance, since the arteries in the brain are very small and the path to deliver the stent is very tortuous [23]. The shape of the stent and of the metallic struts composing it also determines the flexibility and compliance of the stent [5].

Historically, it was always assumed that stents must be corrosion resistant in order to guarantee proper support to the artery during the entire lifetime of the patient. On the other hand, clinical evidence suggested that a diseased artery is capable of supporting itself 12 months after device implantation [26]. After this period, the stent is no longer needed. From this observation, stents that guarantee mechanical support to the artery for 12 months, for then dissolving safely in the body by 18-24 months after implantation, can be envisaged [27]. In addition, more and more younger patients suffer from atherosclerosis, increasing the needed lifetime of a permanent device with respect to an elder patient [27].

Stents can thus be divided in two main categories, depending on the desired corrosion behavior: permanent stents and biodegradable stents. A comprehensive review of these two classes of devices is provided in the following sections.

Production of a stent

As discussed before, stents are metallic tubular meshes with varying dimension, depending on the material and device design. The design phase involves the choice of the material and the optimization of the mesh design, namely the strut size and shape (figure 0.5), together with cell design, which can either be open or closed (figure 0.6) [5].

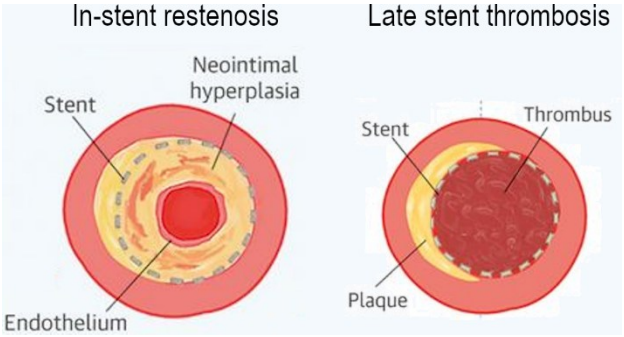

Figure 0.4 Schematic representations of in-stent restenosis and late stent thrombosis (adapted from [4]**)**

Table 0.1 Overview of required mechanical properties for cardiovascular stents [15]

Property	Value
0.2% yield strength	> 200 MPa. Too high may lead to acute recoil, below this value mechanical resistance is not sufficient
Elastic modulus	As high as possible to prevent recoil. Materials for inert stents have an elastic modulus around 200 GPa
Ultimate tensile strength	> 300 MPa, but as high as possible for giving maximal radial strength to the device
Elongation to failure	> 30% to withstand expansion
Fatigue life	> 10^7 cycles, since the required mechanical integrity is of 6 months
Yield strength to elastic modulus ratio	As low as possible to limit acute recoil after expansion

Device production involves several steps, as outlined in figure 0.7 [6]. First, the material should be cast into cylindrical billets with a suitable dimension. Second, a billet is extruded into cylindrical tubes, which are then cold drawn in several passes to obtain minitubes with the final diameter and wall thickness. A recrystallization annealing treatment is performed after each cold drawing pass in order to restore the initial microstructure, thus allowing to perform further plastic deformation. Successively, the final design of the device is obtained by laser cutting, removing the unwanted portions of the minitubes with the aid of acid pickling. Finally, an electropolishing step is performed to obtain the final surface roughness, which should be as low as possible. In the case of DES, the drug eluting coating is then applied. Sterilization of the device is then performed, making it ready to be implanted.

Permanent stents

Permanent stents are made from corrosion resistant metallic alloys, guaranteeing their integrity throughout the life of the patient. The most commonly used alloys are 316L stainless steel, L605 Co-Cr alloy, platinum alloys, and Nitinol [16]. A stent may have a drug-eluting coating (drug-eluting stent, DES) or not (bare metal stent, BMS). An overview of the mechanical properties of these alloys can be found in table 0.2. Among those materials, Nitinol is a shape

memory alloy composed of an equal amount of Ni and Ti, which is used for self-expanding stents. A device made from Nitinol can be trained prior to implantation to expand under the effect of heat when inserted in a body at 37°C, thus removing the need for balloon expansion, which is used for all other materials. This feature makes Nitinol the material of choice for peripheral [28] and cerebrovascular stents [23]. On the other hand, coronary stents are mostly made of 316L or L605 alloys.

316L was the first used material for cardiovascular stents, the first report dating to 1987 [29]. While it proved more efficient in the treatment of atherosclerosis with respect to plain angioplasty [30], a significant incidence of ISR was detected [31,32]. The release of nickel ions from the stent was observed to be one of the causes for ISR [33].

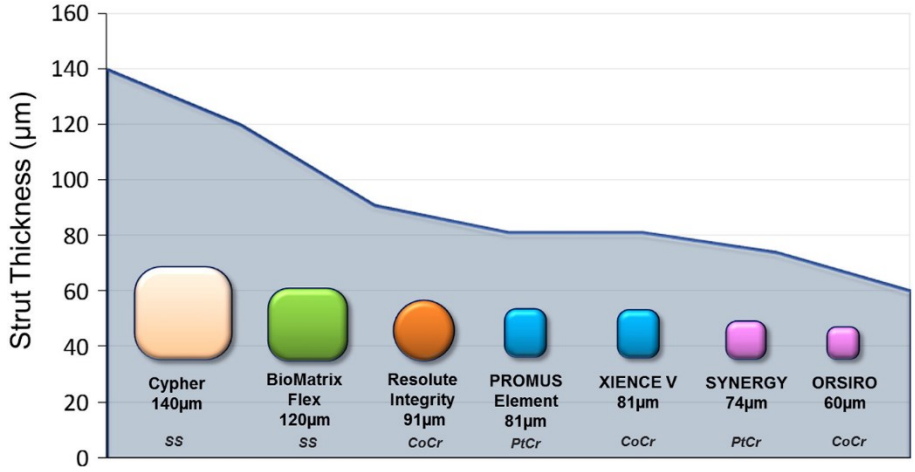

Figure 0.5 Overview of strut size of commercial permanent stents [5]

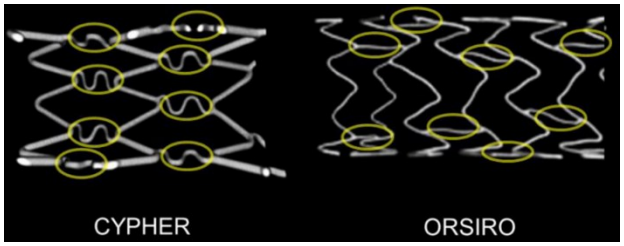

Figure 0.6 Difference between a closed cell stent design (CYPHER, left) and an open cell design (ORSIRO, right) (adapted from [5]**)**

Table 0.2 Overview of mechanical properties of the three most used materials for permanent stents [16,17]

Material	Density	Elastic modulus	Yield strength	Ultimate tensile strength	Elongation to failure
	g/cm³	GPa	MPa	MPa	%
Stainless steel 316L	7.95	193	340	670	48
Co-Cr alloy L605	9.10	243	380-780	820-1200	35-55
Nitinol	6.45	40	200-300	1200	25

Co-Cr alloys were successively developed to replace 316L as the material of choice for stents. The main advantage of Co-Cr alloys lies in their highly superior mechanical properties, which allow to manufacture stents with a smaller diameter and a thinner strut size. This guarantees two main advantages. First, it improves the flexibility and deliverability of the device, allowing to treat smaller arteries. Second, it allows to reduce ISR, as a direct correlation between the strut thickness and the incidence of ISR was discovered [5]. An overview of the strut sizes of commercially available stents is reported in figure 0.5. Nowadays, the smallest available stent has a strut thickness of 60 μm.

The third commercially used metallic materials for stents are platinum alloys. While they show inferior mechanical properties with respect to Co-Cr alloys, the higher density of the constituting elements grant higher radiopacity, in turn giving better visibility of the stent by imaging techniques such as magnetic resonance imaging (MRI), reducing the risk of stent misplacement and allowing a better post-implantation follow-up [16].

Unfortunately, it was observed that BMS still result in ISR in a significant number of cases. In order to limit this risk, DES were developed. In this family of stents, the metallic surface is covered with a polymeric coating, into which an antiproliferative drug is embedded [34]. The role of the drug is to limit the excessive proliferation of the SMCs on the stent surface, thus decreasing the incidence of ISR. While this strategy proved effective, a higher incidence of late stent thrombosis (LST) was observed in long-term follow-ups [35,36]. In order to solve this limitation, degradable coatings were developed [34], showing good outcomes.

Biodegradable stents

Biodegradable stents are devices meant to reopen an atherosclerotic artery with a similar implantation procedure to permanent stents, support it for at least 6 months, for then dissolving gradually without releasing any harmful products. A schematic view of this process can be observed in figure 0.8. Because of the temporary nature of the implant, it cannot be made from knowingly toxic materials used for permanent stents, such as Cr, Ni, Co [27]. In addition, other toxic materials should be avoided in the design of biodegradable stents, such as Al.

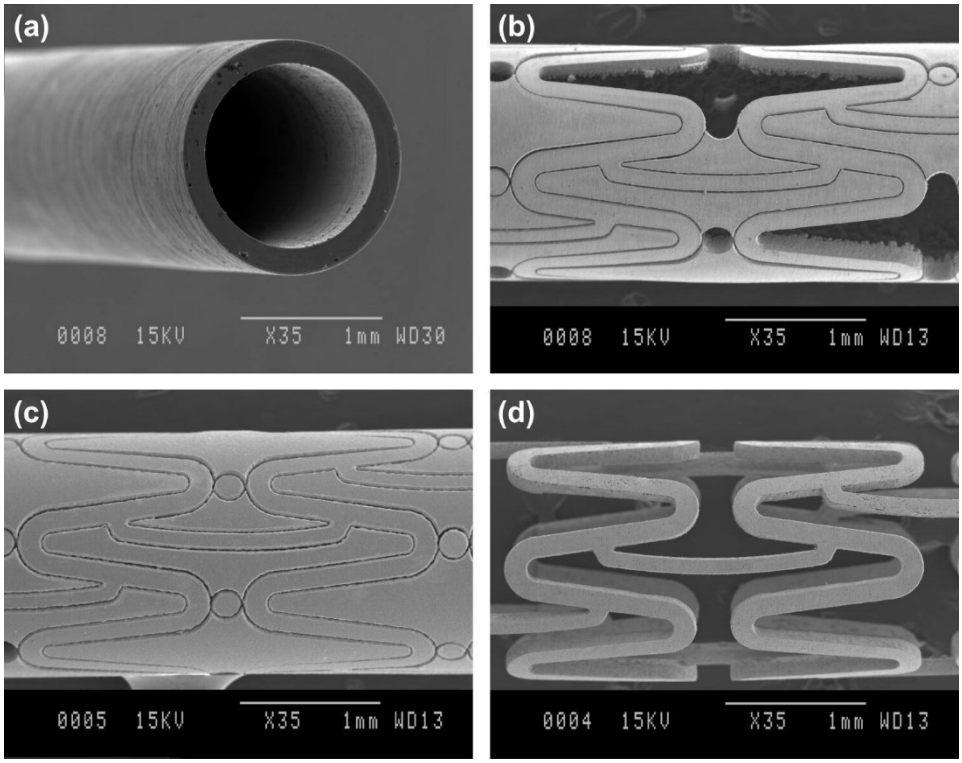

Figure 0.7 Overview of the production process of a stent: a) minitube production; b) laser cutting; c) descaling (or acid pickling); d) electropolishing and finished stent [6]

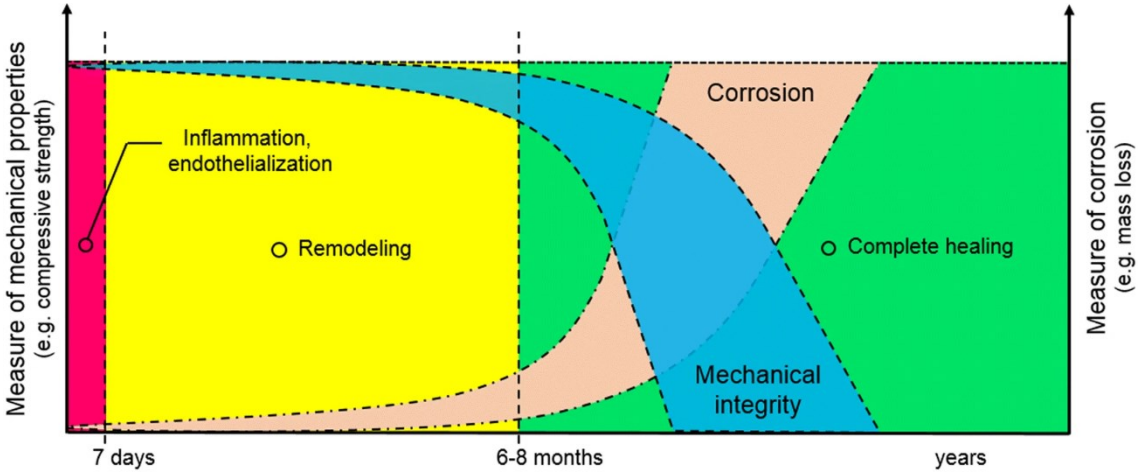

Figure 0.8 Overview of the life cycle of a biodegradable stent [7]

Biodegradable polymeric stents

The first type of biodegradable stents that was developed consists in polymeric stents, made from degradable polymers, mainly poly l-lactic acid (PLLA) [26]. This semicrystalline polymer undergoes degradation by hydrolysis, converting polymer chains to lactic acid, which is then decomposed in carbon dioxide and water [37]. Its mechanical properties are vastly inferior to those of corrosion resistant alloys outlined in table 0.2: its elastic modulus is in the order of 3

GPa, its tensile strength between 60 and 70 MPa, and its elongation to failure below 6% [37]. It should also be noted that, due to the viscoelastic nature of polymers, such mechanical properties are subjected to evolution during time under the action of mechanical stresses imposed by the cardiac cycle of human heartbeat.

Some PLLA-based stents were granted approval for clinical practice by the European Community, such as the Igaki-Tamai stent, the DESolve stent and the ABSORB stent, the latter one having also received FDA approval [38]. As a general rule, these devices are made of a PLLA scaffold, acting as structural component, coated with another polymer into which an antiproliferative drug is embedded. The function of this coating is identical to that of drug-eluting coating in permanent stents. It must be noted that long-term clinical trials showed contrasting results on the safety of such devices in comparison with DES. While the Igaki-Tamai stent was degraded without adverse reactions in a 10 years time frame [39], the ABSORB stent showed a significantly increased occurrence of LST, together with inferior overall performances in comparison with control DES [40–42], leading to its withdrawal from the market [43]. The failure of ABSORB was attributed to several factors, the majority of which can be reconducted to the very poor mechanical properties of PLLA in comparison with standard corrosion resistant alloys.

Biodegradable metallic stents

A different approach involves the use of metallic alloys that can be corroded thanks to electrochemical reactions stimulated by physiological fluids, releasing products that are not harmful to the body [44]. Three classes of materials are currently studied for biodegradable metallic stents: Mg-, Zn- and Fe-based alloys [45]. An overview of the mechanical properties of these metals in comparison to PLLA is presented in table 0.3.

Table 0.3 Mechanical properties of pure metals for biodegradable stents

Material	Metallurgy	Elastic modulus	Yield strength	Ultimate tensile strength	Elongation to failure	Ref
		GPa	MPa	MPa	%	
Pure Mg	As cast	41	20	86	13	[45]
Armco Fe	Annealed	200	150	200	40	[45]
Pure Zn	As cast	94	150	150	20.5	[46]
PLLA	n.a.	3.1	---	70	6	[37]

Mg-based alloys are by far the most studied system among the aforementioned three. They have superior mechanical properties in comparison with polymeric stents, while they are inferior to metallic alloys used for permanent stents. The most recent patented Mg alloys for cardiovascular stents, such as Synermag ® or the JBDM systems [47–49], satisfy the minimal requirements in terms of mechanical properties for cardiovascular stents [47,50]. The Magmaris ® stent (Biotronik), based on the Synermag alloy with a degradable drug-eluting coating, showed excellent clinical performance on human patients, not causing any acute or chronic inflammatory reaction while degrading fully in 12 months [51–53]. The major limitation of this device lies in its size when compared to permanent stents. In its smallest iteration, this device has an outer diameter of 3 mm and a strut thickness of 150 μm [54]. In comparison, a Co-Cr DES from the same company (known as Orsiro ®) has an outer diameter as low as 2.25 mm with a strut thickness as low as 60 μm [55]. This strongly limits the arteries into which Magmaris can be delivered, such as the aorta or large coronary arteries.

Zn-based alloys are metallurgically similar to Mg-based alloys, since they both have a hexagonal close packed (HCP) structure. Two elements distinguish it from Mg and its alloys:

- A higher electrochemical potential, implying that material degradation proceeds more slowly, as shown by long-term *in vivo* tests [56,57].
- Strain softening during plastic deformation [58].

Zn alloys have similar mechanical properties to Mg alloys [59], implying that they could show the same shortcomings in terms of applicability into arteries smaller than the coronary ones in adults.

The final option is constituted by Fe-based alloys. This system is based on a material that has a superior combination of strength and ductility with respect to Mg- and Zn-based alloys [16], making it a more viable option for high-strength and high ductility stents with comparable performances to those of Co-Cr alloys. On the other hand, as far as pure Fe is concerned, preclinical tests in animal models showed that full degradation of the device is hampered by formation of a stable layer of degradation products (DPs), mainly composed of phosphates [60,61]. Most strategies aimed at solving this limitation exploit alloying with Fe with a soluble element, most commonly Mn, in order to decrease the overall electrochemical potential of the alloy [62,63]. In order to sufficiently reduce the electrochemical potential, high amounts of Mn require to be added [11]. This is also necessary to stabilize only austenite (γ-Fe) at room

temperature, promoting higher ductility than with a low amount of Mn, up to levels similar to those of 316L stainless steel [62,64]. One of the drawbacks of adding high amounts of Mn consists in the long-term toxicity risks, since accumulation of excess Mn in the brain was reported to be related to neurodegenerative diseases, such as Parkinson's [65].

A particular class of Fe-Mn alloys with an outstanding combination of strength and ductility are twinning-induced plasticity (TWIP) steels, matching or even exceeding those of Co-Cr alloys [15]. These alloys contain Fe and Mn in variable proportion, together with either C or a combination of Al and Si [66]. Their name comes from the peculiar deformation mechanism they show, that is formation of mechanical twins upon plastic deformation [67]. For biomaterials applications, the use of Fe-Mn-Al-Si alloys should be excluded due to the fact that Al accumulation is a well known factor in the insurgence of Alzheimer's disease [68]. Laboratory tests, however, showed that these alloys are plagued by the same issues of Fe-Mn alloys in terms of corrosion, namely the formation of a stable layer of DPs on the surface [12,69]. The addition of further elements that can form small second phases was explored, with good results *in vitro* but poor outcomes *in vivo*, such as Pd [12,70]. An element that showed interesting outcomes *in vitro* is Ag, but the only reports available in literature discuss fabrication by either powder metallurgy [71,72] or additive manufacturing [73,74].

Current challenges in clinical treatment of cardiovascular diseases

At the time when this thesis was written, a single treatment option was available for biodegradable stents, namely Magmaris ®. The size of this device is much larger (2 to 3 times) when compared to that of permanent DES, such as those based on Co-Cr alloys. The smallest iteration of Magmaris ® has an outer diameter of 3 mm and a wall thickness of 150 μm [54], while a Co-Cr DES from the same company can have an outer diameter as small as 2.25 mm and a wall thickness of 60 μm [75], significantly improving deliverability.

Three other clinical challenges require the development of biodegradable stents with small dimensions from high-performance alloys. First, the median age of the population affected by CVDs is lowering in the last years [76], mainly because of increased incidence in behavioral risk factors [77], implying that the life expectancy of patients who have a stent implanted in their body could be longer. The long-term harmful effects of permanent stents are nowadays known, and can be partly related to the fact that permanent stents aren't actually inert inside the body [78]. Not having anymore a stent after 2 years from implantation could remove the risk of very

late ISR or thrombosis [4]. Second, congenital heart diseases are a rare but existing condition. The most common pediatric vascular diseases include aorta coarctation and pulmonary artery stenosis [79]. In the event that a child requires stent implantation and the complication is resolved, a permanent stent would remain in his body for the rest of his life. Furthermore, human growth also involves arteries: having a permanent stent may result in displacement and breakage of the neointima, thus causing severe conditions. Third, cerebral atherosclerosis currently presents a very limited range of treatment options. No biodegradable stents are used nowadays, since commercially available devices are too large to be delivered to arteries inside the brain.

Proposed strategy

Fe-based degradable alloys, although superior in mechanical properties with respect to Mg and Zn alloys, are limited by a slower degradation process. However, they represent the only realistic choice for treating CVDs occurring in small arteries, such as those present inside the human brain, or for young patients, for which temporary devices represent the only possibility for healing and conduct a life without the risk of long-term complications, which were observed in several cases [79]. Pure Fe and Fe-Mn show mechanical properties that only match those of 316L stainless steel [80], making them unsuitable for fabricating stents as small as those made from Co-Cr alloys, which can attain an outer diameter of 2.25 mm with a strut thickness of 60 μm [5]. TWIP steels, on the other hand, have mechanical properties that can match those of the L605 alloy used for fabricating the smallest stents available on the market, thus having the potential for a major breakthrough in biodegradable metallic stents. However, the issue consisting in the formation of a passive layer during corrosion must be addressed.

This project aims specifically at addressing the problem of long-term degradation by developing a Fe-Mn-C alloy composition which shows mechanical properties at least equal to those of the L605 alloy. A modification of this composition will also be explored by adding a fourth element, promoting formation of second phases inducing corrosion of the matrix by galvanic coupling. The next section details the strategic choices that were made with this goal in mind, followed by a summary of the general hypothesis and objectives of this project.

Alloy design

Metallurgy of TWIP steels: a primer

While the quasi totality of industrially produced steels deforms by means of dislocation gliding, TWIP steels, as the name itself says, form twins during plastic deformation. A twin is a surface defect, falling in the same category of grain boundaries. Contrarily to the latter ones, which are a disordered interface of few atomic lengths between two regions of uniformly oriented material better known as grains, twin boundaries act as mirror planes inside a material: the crystalline arrangement of atoms is mirrored on the two sides of a twin boundary, as visible in figure 0.9. A twin contains two twin boundaries, each acting as mirror plane. In metallic alloys, twins may form either during thermal treatments (in this case named thermal twins) or during plastic deformation (named mechanical twins). Twins found in TWIP steels fall in the latter category.

The preferential deformation mechanism of all metallic alloys is ruled by the stacking fault energy (SFE), which is the energy required by the material to form a surface defect known as stacking fault (SF). By definition, a stacking fault is a defect in the pile-up of atomic planes inside a material.

Most engineering materials deform by dislocation gliding since the formation of an SF requires a high amount of free energy or, in other words, is not energetically favorable. For some

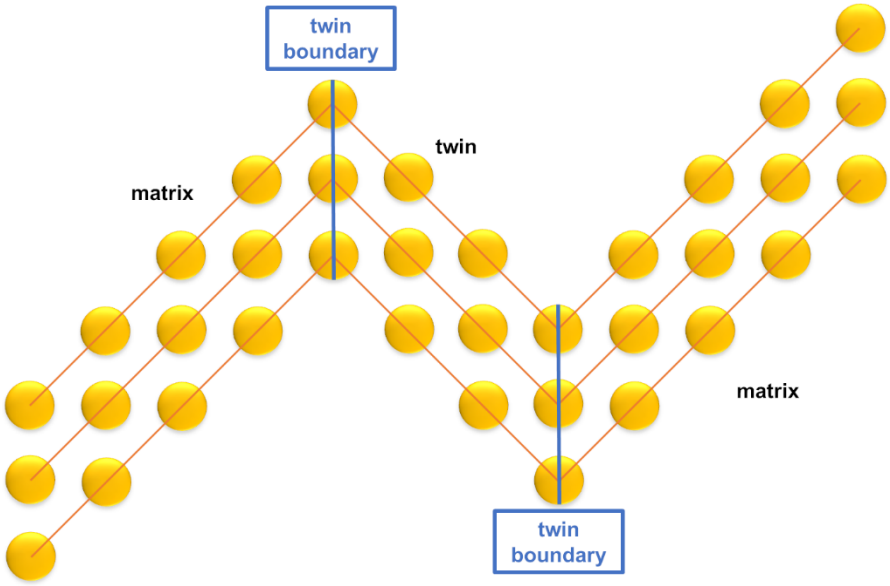

Figure 0.9 Schematic representation of a twin

materials, such as HCP metals (for example Mg and Zn), the SFE is particularly low, thus an SF will form. This is also true for TWIP steels: the SFE is a function of the composition of the alloy, following this equation [81]:

$$\Gamma = 2\rho_A \Delta G^{\gamma \to \varepsilon} + 2\sigma^{\gamma - \varepsilon}$$

where ρ_A is the planar packing density of a close-packed plane, $\Delta G^{\gamma \to \varepsilon}$ is the difference in Gibbs free energy between the γ (austenite) and ε (martensite) phases, and $\sigma^{\gamma - \varepsilon}$ is the interfacial energy between these two phases. It was shown that, for Fe-Mn-C steels, twinning is the predominant deformation mechanism when Γ is comprised between 12 and 35 mJ m^{-2}, while martensite is present when Γ is lower than 18 mJ m^{-2}. Above 35 mJ m^{-2} only dislocation gliding takes place [82]. It must be noted that the SFE of TWIP steels is a function of their composition: in addition to thermodynamic modelling, an estimation of the SFE can be obtained using iso-SFE maps, as reported in figure 0.10. Another tool to assess the phases that are present inside a Fe-Mn-C TWIP steel is the Schumann diagram [83], also shown in figure 0.10.

Mechanical properties of Fe-Mn-C TWIP steels depend strongly on SFE, which, as discussed before, depends on alloy composition. As a general rule, the higher SFE, the lower the material strength, but the higher the ductility [66]. Conversely, a lower SFE TWIP steel will have higher mechanical strength, but lower elongation to failure. An overview of stress-strain curves of different TWIP steels can be found in figure 0.11.

One of the most noticeable features of TWIP steels are the serrations in the plastic deformation region observed at room temperature, which disrupt plastic flow. This phenomenon is known as dynamic strain aging (DSA) and is present only for Fe-Mn-C TWIP steels without Al, which can suppress this behavior [67]. The most common classification of DSA is based on the shape and frequency of serrations in the stress-strain curves. Five different serration types were identified in the past, named type A, B, C, D and E, as outlined in figure 0.12 [9]. In the case of TWIP steels, types A and B were most commonly observed [67]. The mechanism behind DSA in Fe-Mn-C TWIP steels is often related to the interactions between C atoms in solution and moving partial dislocations: C atoms are believed to be disruptors in the normal movement of such dislocations, which in turn originate mechanical twins [66]. The general tendency in TWIP steels for automotive applications consists in suppressing DSA for

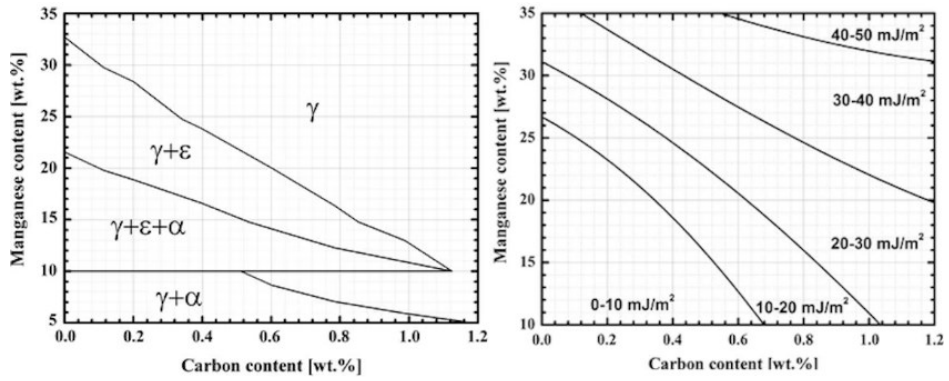

Figure 0.10 Two semi-empirical tools for evaluating the phases formed in TWIP steels: left, Schumann diagram; right, iso-SFE diagram (adapted from [8]**)**

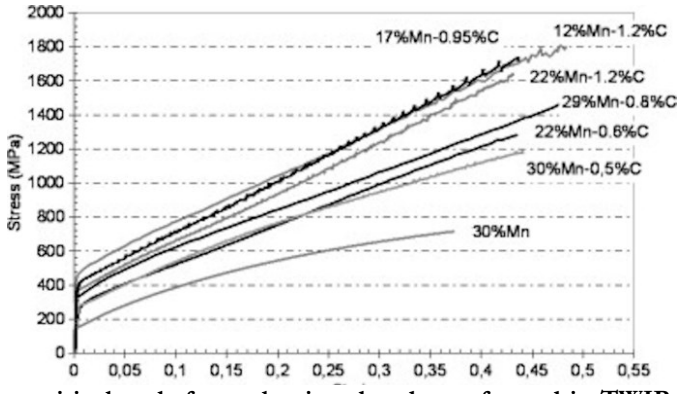

Figure 0.11 Two semi-empirical tools for evaluating the phases formed in TWIP steels: left, Schumann diagram; right, iso-SFE diagram (adapted from [8]**)**

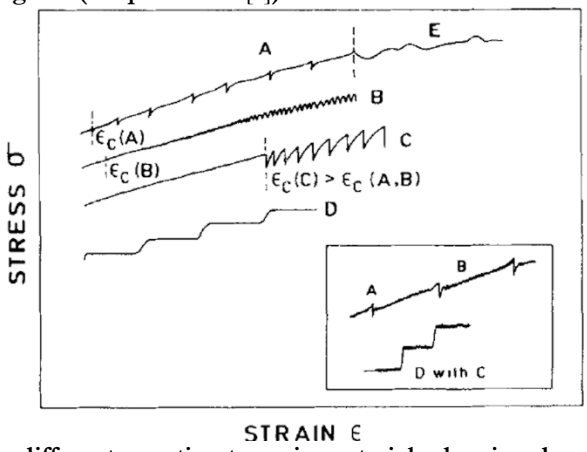

Figure 0.12 Overview of the different serration types in materials showing dynamic strain aging [9]

having a more uniform plastic behavior: this can be obtained by adding Al to the mixture, as mentioned above.

Another reason for eliminating DSA for automotive applications lies in processing steel sheets for structural components of cars and body panels. Such processes include deep drawing and involve high levels of plastic deformation. "Jerkiness" in plastic flow can cause unexpected cracking of the piece or excess local deformations, possibly leading to premature failure of the

finished component [67]. This phenomenon may also occur during balloon-expansion of a stent, since it is known that plastic deformations can attain up to 30% during this process, leading to localized stresses attaining up to 950 MPa [84]. At such levels of plastic deformation, a TWIP steel may have already initiated DSA depending on its composition, which should thus be controlled in order to avoid this occurrence.

TWIP steel design for biodegradable stents

The previous section outlined the general principles ruling the design of TWIP steels for a variety of applications. In the specific case of biodegradable stents with high strength and high ductility, those principles can be better detailed and expanded criteria, as outlined below:

- Mechanical properties. Performances of most TWIP steels are matching those of Co-Cr alloys commonly used for manufacturing permanent stents, showing a relatively low yield strength (around 400 MPa), an engineering tensile strength around 1000 MPa and an elongation to failure exceeding 50% [67]. The most important factor in deciding the composition of a TWIP steel for biodegradable stents from a mechanical point of view consists in ensuring to have only mechanical twinning as deformation mechanism.
- Deformation mechanism [82]. SFE determines the preferential deformation mechanism of TWIP steels, which varies as a function of the composition. As mentioned before, in order to have only mechanical twinning taking place, SFE must be comprised between 12 and 35 mJ mol^{-1}. With the aid of iso-SFE diagrams, like that outlined in figure 0.10, an alloy composition can be designed to ensure to have only mechanical twinning, which is the mechanism giving the best combination of strength and ductility, as observed before.
- Martensite structure. In addition to formation of mechanical martensite, its structure can vary as a function of the Mn and C content. The Schumann diagram (figure 0.10) reports the possible martensitic structures that form as a function of alloy composition. For higher contents of Mn and C (and thus, higher SFE), no martensite can be formed upon deformation. ε-martensite, with an HCP structure, can develop for lower contents of Mn and C. For the lowest amounts of Mn (and roughly for SFE values below 10 mJ m^{-1}), α' martensite can form, which has a body-centered tetragonal (BCT) structure. The BCT structure produces a lower ductility with respect to a fully austenitic structure or even with respect to ε martensite [66]. The presence of α' martensite should thus be avoided.

Furthermore, the formation of ε-martensite upon plastic deformation should also be avoided in order to enhance the ductility of the steel.

- Carbides. For high concentrations of C (above 0.8 wt. %), the formation of Fe and/or Mn carbides may be stimulated, as predicted by the Fe-Mn-C ternary phase diagrams [85]. In order to avoid the presence of hard and brittle phases, the content of C should be kept below this threshold.
- Mn toxicity. It should not be forgotten that having a too high content of Mn can have long-term toxicity concerns, since an excess of Mn was found to be a factor in the insurgence of Parkinson's disease [86]. Its tenor should be kept as low as possible while maximising strength and ductility.

These four considerations were taken into account to design an alloy composition optimized for the challenges of cardiovascular stents, aiming at surpassing the mechanical properties of Co-Cr alloys. This composition is **Fe-16Mn-0.7C** (wt. %), fulfilling all the criteria outlined above.

Improving degradation rate in TWIP steels

Generalities on of TWIP steels corrosion

TWIP steels were the subject of several studies concerning their corrosion behavior, aimed at understanding the underlying mechanisms. One of the most well-known features of TWIP steels in non-physiological environments consists in its sensitivity to chloride attack, which results in severe corrosion of high-Mn steel structures in seawater [87]. It must be considered that chloride attack can produce itself in physiological environments too, since chloride ions are among the most abundant ones in human blood plasma [18]. This indicates the potential of TWIP steels to corrode themselves in environments with high blood perfusion, such as arteries. Chloride containing solutions were also found to stimulate pitting corrosion in such steels [88]. Pitting is a localized form of corrosion where the material is attacked at preferential sites, promoting the formation of small holes (pits) that can propagate over time and cause catastrophic failures of the component [89], and shall thus be avoided. Another corrosion phenomenon commonly observed in TWIP steels resides in hydrogen embrittlement, where the presence of H in the atmosphere can promote premature failure of a component under stress [66].

Focussing on corrosion of TWIP steels in pseudo-physiological solutions, some studies reported development of pits due to localized release of Fe and Mn caused by the attack of aggressive media [12]. It was also observed that a compact corrosion layer can form during exposure for at least 14 days, preventing long-term corrosion of TWIP steels to occur [69,70,90].

Galvanic coupling as a strategic mechanism for increasing corrosion rate

The basic idea of galvanic corrosion is well-known since a long time. This type of corrosion occurs when two materials with a different electrochemical potential in a corrosive environment are coupled together by means of an electrical contact, allowing a current to circulate. The material with the lower electrochemical potential will corrode preferentially, guaranteeing that the material with the higher potential is not affected by corrosion [91]. The material with the higher potential will act as cathode, while that with the lower potential will act as an anode, thus dissolving. In industrial practice, this strategy can be exploited to protect some metallic components from corrosion by putting them in electrical contact with a sacrificial anode, which will dissolve on purpose.

In the case of biodegradable metals with a low degradation rate or affected by problems of premature passivation, low quantities of elements having a higher electrochemical potential can be added to form second phases, thus promoting local dissolution of the matrix around these impurities [63]. This strategy was exploited in the past 10 years by a very limited number of researchers with alternate fortunes. One of the first extensive studies explored the use of Pd as additional element, which is actually soluble in a Fe-Mn-C matrix. Appropriate thermal treatments stimulated the formation of Pd-rich second phases, which were found to effectively accelerate corrosion up to 28 days [12]. However, long-term studies in animals found that corrosion was halted since a stable layer of phosphates formed on top of the material [70].

An element which is completely insoluble in Fe and C but has partial solubility in Mn is Ag. With appropriate processing, it can thus be ensured that very electrochemically noble phases rich in Ag are formed. This would create strong local galvanic couples that could significantly accelerate corrosion rate by promoting preferential dissolution of the matrix with a much lower electrochemical potential. Design of a Fe-Mn-C-Ag alloy must also take into account the effect that a large amount of second phases could generate on mechanical performances and deformation mechanism, together with toxicity concerns. Ag is known to be a strong antibacterial agent, but the presence of excessive quantities may create adverse effects on

necessary biological functions [92]. For these reasons, this work explores lean alloying of the aforementioned Fe-16Mn-0.7C alloy with only 0.4 wt. % Ag, leading to a final alloy composition of **Fe-16Mn-0.7C-0.4Ag** (wt. %).

Processing

Alloy production

The first step in processing the retained compositions is to actually produce the alloys starting from raw materials. Three methods could be used: casting, powder metallurgy (PM) or additive manufacturing (AM). Each of these processes has its own advantages and limitations.

Casting constitutes the most commonly used process for producing metallic alloys in industrial practice. In this process, various types of starting materials can be melted in a furnace for obtaining the final alloy composition. Its main advantages lie in the relative inexpensiveness of starting materials when compared to powders, together with the possibility of producing large batches of materials in a single casting session. Moreover, a variety of materials shapes can be used, such as ingots, pellets, or others. Master alloys can be used as starting materials, together with pure elements. One of the main inconveniencies of casting lies in possible fire losses, i.e. evaporation of a portion of melted material under the effect of heat. In addition, making a biphasic alloy with an insoluble element is difficult.

Powder metallurgy, on the other hand, may not involve the passage of metals from the liquid state in order to produce an alloy. In this case, powders of the alloy are pressed at high pressure and, under the action of heat, sinter together to form a dense piece of the metal. One of the main advantages of this technique compared to casting lies in the ease of producing alloys of elements that have a limited solubility with each other, like in this case Ag with Fe and C. Mechanical alloying can also be made by milling powders at high energy, forcing the mixing of different elements under this action. Two well-known challenges in PM lie in powder production, which can reveal itself expensive, and the need for careful control of processing conditions to avoid defects such as non-densification of parts.

Additive manufacturing involves the layer-by-layer building of metallic components starting from metallic powders, which can be either put on a plate (creating a powder bed) or projected directly on a plate thanks to a nozzle. Powder particles are melted with the aid of a laser or electron beam only where the piece shall be formed [93]. The main advantage of AM with respect to the other two techniques lies in the near-net-shape nature of the process,

potentially allowing to produce a stent directly from a powder bed. However, powder geometry and size must be strictly controlled for such processes, increasing costs; furthermore, surface quality coming out from the process is typically poor, requiring further steps of post-processing.

For this project, in order to facilitate integration of the material with industrial practice outlined above, casting was chosen as production method for the Fe-16Mn-0.7C(-0.4Ag) alloys. In order to address both challenges in distribution of Ag and fire losses, which are a problem mostly concerning Mn, a specific production process was developed. The first step consisted in developing this process for the Ag-free alloy, for then adapting it for the Ag-containing one. The use of an induction furnace was retained in order to ensure better mixing of the starting materials. The protective atmosphere used to limit fire losses consisted in a custom liquid Ar protection system: droplets of liquid Ar were directed to the melt pool as soon as it formed. These droplets instantaneously evaporated, resulting in a homogeneous gaseous Ar atmosphere at the surface, effectively blocking evaporation of elements. The molten alloy was then cast in permanent cylindrical moulds.

This casting process was then adapted to the case of the Ag-containing alloy. In order to ensure proper dispersion of Ag, fine shots were introduced in the melt pool as last elements prior to pouring the melted alloy in the moulds. Sufficient time was guaranteed to have proper stirring but not long enough to produce gravity segregation of Ag at the bottom of the melting crucible. This strategy allowed a good compositional control.

Alloy processing

Once the alloy is cast, internal stresses coming from this process must be relieved. This can be done by means of solution heat treatments, in which the material is put in a furnace at high temperature for a sufficiently long time. It is also important to note that a controlled atmosphere is needed to prevent oxidation of the surface, together with the possibility of decarburation. For these reasons, solution heat treatment was carried out on slices cut from the billets using a vacuum furnace. In order to quench the slices after the treatment was completed, gaseous Ar was poured at high pressure to quickly reducing the temperature without risking to cause alterations in surface composition.

Normal processing of stents involves extrusion of billets into tubes, which are then precision cold drawn into minitubes, as explained previously. In this work, a simplified processing setup was chosen to carry out the exploratory work on the new alloying systems,

aimed at assessing hot and cold formability. A further aim consisted in evaluating if and how the presence of Ag provoked alterations in deformation mechanism. Another aspect of processing that should be evaluated consists in the recrystallization behavior and the influence of Ag in it. The importance of it lies in the fact that, when forming a minitube from which a stent is cut, several intermediate recrystallization steps must be carried out for restoring the initial microstructure [6]. It is indeed known that second phases can impact both deformation and recrystallization mechanisms in Fe-Mn-C steels [94].

Summary: hypothesis and objectives of the thesis

This thesis aimed at developing a new ternary Fe-Mn-C TWIP steel with a composition suited to be used for small vascular stents. This composition was then modified to include the addition of a small quantity of Ag to enhance material corrosion without resulting in performance reduction from a mechanical and biological point of view.

More in detail, the three main work packages that were developed in this project to validate the aforementioned hypothesis are the following:

1. Design two Fe-Mn-C(-Ag) alloys and showing the feasibility of producing them by casting.
2. Validate the effect of Ag on processing and of mechanical properties of such alloy, including both deformation and recrystallization mechanism.
3. Understand the effect of Ag and plastic deformation on corrosion mechanism of the developed Fe-Mn-C steel and assessing its evolution over time.

Chapter 1 will provide a thorough review of the current state and outlook of biodegradable metals for cardiovascular stents. Chapters 2 to 6 will discuss the experimental outcomes of this work. Chapter 2 will present and elaborate the findings concerning the production process of the Fe-Mn-C(-Ag) alloys, together with how Ag affects deformation mechanism. Chapter 3 will focus on understanding how Ag impacts the recrystallization behavior of the developed TWIP steel. Chapters 4 and 5 are dedicated to the understanding of corrosion properties and mechanisms of the developed alloys: while chapter 4 focusses on the electrochemical characteristics of the materials and on short-term corrosion, chapter 5 goes more in depth on the evolution of corrosion mechanism over time with *in vitro* tests up to 6 months. Chapter 6 will provide a general discussion of the results presented in the scientific papers reported in

chapters 2 to 5. Finally, the conclusions of this work are provided and future research directions for succeeding in clinical translation of high performance TWIP steels for small biodegradable stents are suggested.

1. Biodegradable metallic stents – State of the art

1.1 Mg-based biodegradable stents

Magnesium and its alloys were explored for use as biodegradable stents since the early 2000s [95]. The reasons for choosing Mg for temporary implants lie in two main aspects: its biological functions and its reduced resistance to corrosion [27]. Mg is an essential element for the body, actively participating in several functions such as enzymatic regulation, protein function and DNA stabilization [96,97]. Moreover, it is one of the least noble metals in the electrochemical series, showing a potential of – 2.372 V vs. the standard hydrogen electrode (SHE) [98]. Furthermore, it shows an active electrochemical character at physiological pH in aqueous solution, as evidenced by its Pourbaix diagram [99]. In aqueous environment, corrosion of Mg can be schematized by the following oxidation reaction:

$$Mg(s) \rightarrow Mg^{2+}(aq) + 2e^{-}$$

In the case of biodegradable Mg, it was observed that the reduction reaction is most commonly hydrogen evolution [96]:

$$2H_2O(l) + 2e^{-} \rightarrow H_2(g) + 2OH^{-}(aq)$$

Finally, magnesium hydroxide is formed at the surface [46]:

$$Mg^{2+}(aq) + 2OH^{-}(aq) \rightarrow Mg(OH)_2(s)$$

Hydrogen is formed as gas bubbles on the surface of Mg. Several researchers observed that such bubbles stimulate inflammation around the implant: hydrogen evolution shall thus be limited or eliminated.

Mechanical properties are another major inconvenient of Mg. This metal has a hexagonal close packed (HCP) structure at equilibrium, resulting in poor ductility, as also visible from table 0.3. In addition, its strength and elastic modulus are much lower with respect to 316L stainless steel or L605. This can increase recoil after expansion and possibly result in premature failure of the device.

In order to improve mechanical properties of Mg, the addition of elements that are soluble in Mg and capable of promoting smaller grain size was explored in several studies, such as Zr, Y and various rare earth elements (REE) [100]. The relationship between grain size and yield

strength (YS) of a material is described by the well-known Hall-Petch relation [101], saying that the YS is inversely proportional to the average grain size of the material. In addition to improving mechanical properties, these elements also contribute to reducing corrosion rate, since they are soluble in Mg and have a higher electrochemical potential with respect to it. The first example of such alloy is named WE43, containing 4% of Y and a total of 3% of various REE [95]. While a significant improvement in strength was reached, elongation to failure remained low. Moreover, early clinical trials showed that complete dissolution of the implant was achieved in four months, short of the at least 6 months required for artery remodelling [95]. Nowadays, several compositions of Mg alloys with a high number of alloying elements specifically formulated for biodegradable stents were patented [47–49]. Mechanical properties of such alloys, like Synermag ® (Magnesium Elektron, now Luxfer/MEL Technologies, UK) or the JBDM system, are compliant to the minimal requirements outlined in table 0.1, albeit with a low elastic modulus [47,50]. An overview of mechanical properties of such alloys, together with outcomes of animal tests, is visible in table 1.1.

Early pre-clinical trials of bare Mg stents (AMS, Biotronik) on newborns showed that implantation of the device can be successfully achieved, while corrosion is completed in only 3 to 4 months, insufficient to promote full artery remodelling [102–104]. Another important problem that was detected is the significant reduction of the lumen cross-section, clear indication of ISR, also confirmed by animal studies [105]. The modification of the alloy composition, together with the adoption of a degradable drug-eluting coating, allowed to obtain a good corrosion profile, with 95% of the stent degraded after 12 months in human patients, as visible in figure 1.1 [51,53], resulting in the approval of the device by the European Community, commercially known as Magmaris ® (Biotronik, Germany/Switzerland) [52]. The previously outlined JBDM alloy was also the subject of animal studies using stents in rabbits or minipigs, showing no reduction in lumen diameter after 12 months from implantation, together with an appropriate degradation [50,106].

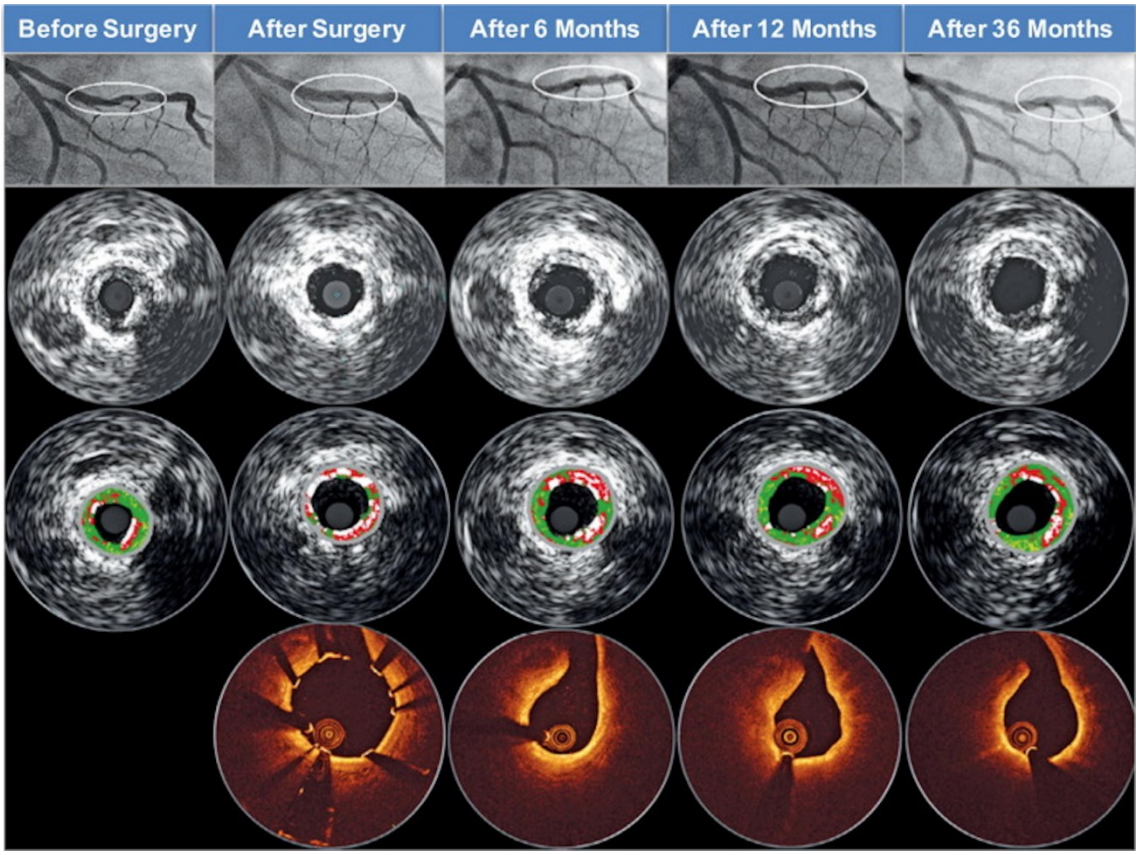

Figure 1.1 Degradation of the DREAMS-2G (Magmaris ®) stent. The stent struts are no longer visible after 12 months [10]

The main limitation of Magmaris with respect to permanent stents lies in its larger strut size. As mentioned before, the smallest strut size that has been achieved for Co-Cr stents is 60 μm, while the strut size of Magmaris is 150 μm [54], thus limiting its deliverability to smaller arteries. Although Mg-based alloys work very well for treating large arteries, intrinsic limitations in the improvement in mechanical properties make them unfeasible for replacing Co-Cr DES in treatment of most patients, especially for very small arteries, such as in the brain or in newborns.

Table 1.1 Mechanical properties of commercial Mg alloys for biodegradable stents

Material	Metallurgy	Elastic modulus	Yield strength	Ultimate tensile strength	Elongation to failure	Ref
		GPa	MPa	MPa	%	
WE43	Extruded	44	180	280	10	[7]
SynerMag	Extruded	Unknown	200	300	20	[47]
JBDM-1	Extruded	Unknown	188	238	30	[48]
JBDM-2	Extruded	Unknown	204	247	21	[50]

1.2 Zn-based biodegradable stents

The idea of using Zn and its alloys for manufacturing biodegradable stents is relatively recent compared to Mg-based systems. Zn, such as Mg, is known to be an essential nutrient for the body, being a cofactor for enzymatic regulation and protein function [107]. Its recommended daily intake oscillates between 6 and 10 mg, depending on the individual [46]. An excessive intake of Zn may lead to Cu deficiency and cause negative effects on lipid metabolism [46].

The main advantage of Zn with respect to Mg lies in its corrosion properties. From a merely electrochemical point of view, its corrosion potential lies at - 0.762 V vs. SHE [98], significantly higher with respect to Mg, while lower with respect to Fe (- 0.447 V vs. SHE). In addition, it can undergo corrosion at neutral pH in aqueous environments, as visible from its Pourbaix diagram [108]. The anodic half-reaction in aqueous solution is the following:

$$2Zn(s) \rightarrow 2Zn^{2+}(aq) + 4e^{-}$$

The cathodic half-reaction consists predominantly in formation of hydroxide ions:

$$O_2(g) + 2H_2O(aq) + 4e^{-} \rightarrow 4OH^{-}(aq)$$

Finally, product formation involves first Zn hydroxide, which recombines to form Zn oxide, releasing water:

$$2Zn^{2+}(aq) + 4OH^{-}(aq) \rightarrow 2Zn(OH)_2(aq) \rightarrow 2ZnO(s) + 2H_2O(l)$$

Most importantly, animal tests in rats showed that pure Zn does not significantly degrade in the first six months, for then dissolving steadily in the following year up to complete resorption [56]. Several other animal tests have been conducted since, confirming the safety of pure Zn into arteries, together with its steady corrosion [57,109–111].

The main limitation of Zn lies in its poor mechanical properties, similar to the case of Mg. Zn also possesses an HCP structure, limiting its strength and ductility, depending on previous processing [59]. Another important phenomenon specific to Zn is strain softening, meaning that the strength of the material is reduced when it is plastically deformed [58,112].

Several efforts have been conducted to improve the mechanical properties of Zn and limit strain softening, mainly by alloying with soluble elements. The first investigated element was Mg, which has a limited solubility in Zn (up to 0.1 wt. %), forming a eutectic phase at a concentration of 3 wt. %. Good cytocompatibility was observed [113], together with an improvement in

strength proportionally to the amount of Mg [114]. However, ductility remained limited, with a peak around 15% for a Zn-0.15Mg alloy [114]. Moreover, strain softening was not suppressed. Al resulted in a similar effect [114], also showing acceptable biocompatibility in vivo [115]. Other alloying elements were explored, such as Cu [116], Li [117], Ca, Sr [118], all showing good biocompatibility without affecting the degradation process. However, the inconvenient of strain softening still remained. At present, the most promising alloying element in for Zn is Ag, which was shown to suppress strain softening and improving the strength and ductility of Zn [112,119]. Recent works added further elements to the Zn-Ag system, resulting in further improved mechanical properties [112]. Moreover, the biosafety of this system was proven to be acceptable [120].

It must be noted, however, that the improvements in the mechanical properties of Zn are not yet matching the performances of the most used corrosion resistant metals, such as 316L and L605 alloys. This can also limit their application outside big coronary arteries, like in the case of Mg alloys.

1.3 Fe-based biodegradable stents – state of the art

Pure Fe was the first investigated material for biodegradable stents before Mg and Zn, the earliest animal study dating back to 2001 [60]. This work already identified the key advantages and inconveniences that are still characteristic of iron and its alloys: it possesses higher strength and ductility with respect to Mg- and Zn-based materials, but its corrosion proceeds too slowly in the long term. Iron and its alloys can be the best choice for developing biodegradable stents with reduced strut section, improving deliverability and broadening clinical applications. On the other hand, the limitation in corrosion still stands nowadays.

From a physiological point of view, Fe is involved in the regulation of enzymatic activity and is considered an essential element for humans, with a required daily uptake of 1 mg [107]. On the other hand, an excessive intake of Fe is associated with the development of gastrointestinal and liver cancer, and it may be a co-factor in the insurgence of Alzheimer's and Parkinson's diseases [121].

From an electrochemical point of view, Fe has a higher electrochemical potential with respect to Mg and Zn, namely – 0.447 V vs. SHE [98]. Its Pourbaix diagram indicates that Fe

can undergo corrosion in neutral pH in aqueous environments [99]. Corrosion of pure Fe in aqueous solution can be schematized by the following two half-reactions:

$$2Fe(s) \rightarrow 2Fe^{2+}(aq) + 4e^{-}$$

$$O_2(g) + 2H_2O(aq) + 4e^{-} \rightarrow 4OH^{-}(aq)$$

The global corrosion reaction can be thus written as follows:

$$2Fe^{2+}(aq) + 4OH^{-}(aq) \rightarrow 2Fe(OH)_2(s)$$

If Fe hydroxide recombines with water, iron oxide can be obtained, although this reaction is not normally observed.

Fe may also oxidize to the +3 state, giving the following anodic half-reaction:

$$4Fe(s) \rightarrow 4Fe^{3+}(aq) + 12e^{-}$$

To which the following cathodic half reaction corresponds:

$$3O_2(g) + 6H_2O(aq) + 12e^{-} \rightarrow 12OH^{-}(aq)$$

In this case the overall corrosion reaction can be written as follows:

$$4Fe^{3+}(aq) + 12OH^{-}(aq) \rightarrow 4Fe(OH)_3(s)$$

Eventually, iron hydroxide can recombine with water to form iron oxide (III), which was observed in some studies:

$$4Fe(OH)_3(s) \rightarrow 2Fe_2O_3(s) + 6H_2O(l)$$

Oxidation state of Fe is a very important factor in its long-term cytocompatibility. When Fe is oxidized to Fe^{3+} instead of Fe^{2+}, the degradation products (DPs) were seen to induce a higher acute cytotoxicity towards both fibroblasts [122,123], ECs and SMCs [124,125]. The products formed when pure Fe was implanted in animals have not been clearly identified yet. On the other hand, it was seen that the corrosion of Fe controls the proliferation of SMCs in the *neointima*, thus reducing the risks of ISR [126].

It must be noted that physiological fluids are not solely composed by water: as visible in table 1.2, whole blood includes several other metallic and non-metallic ions, together with proteins, which are seldom considered in electrochemical studies. Several species other than oxides or hydroxides can be formed because of the reactions of Fe with those ions, such as

phosphates ($FePO_4$), and carbonates ($FeCO_3$) [127]. Furthermore, Fe-free species can be adsorbed on the surface of the material, such as calcium carbonate ($CaCO_3$) or proteins [11].

Mechanical properties of pure Fe surpass those of pure Mg and Zn by a significant margin. As visible in table 0.3, both elastic modulus, YS, UTS and elongation of pure Fe are the best among biodegradable materials, coming close to the values observed for 316L stainless steel. From a metallurgical point of view, this superiority in mechanical properties comes from the body centered cubic (BCC) crystal structure of Fe, which has a much higher number of slip systems that can be activated to accommodate plastic deformation, contrarily to Mg and Zn, both HCP.

The main limitation in the clinical translation of Fe lies in its low corrosion rate. Animal trials found that a pure Fe stent remained mostly intact after 18 months from implantation, with undissolved degradation products surrounding the implant [60,61]. Another important concern to be considered is the ferromagnetism of pure Fe: such behavior can lead to misplacement of the stent during implantation because of poor visibility, in addition to limiting post-implantation follow-up by magnetic resonance imaging (MRI) [27].

Table 1.2 Comparison between the composition of blood plasma and that of the most commonly used pseudo-physiological solutions [18]

Ions (mg/L)	Blood plasma	NaCl 0.9M	HBSS	HMSS	PBS	PBS with albumin	SBF
Na^+	3000–3400	5425	3258	2795	3519	3519	3265
K^+	130–210	—	227	172	162	162	195
Cl^-	3400–3750	3518	5043	3542	4947	4947	5275
HCO_3^-	1100–2400	—	254	1654	—	—	256
HPO_4^{2-}	270–450	—	75	48	920	920	96
Ca^{2+}	84–110	—	—	35	—	—	100
Mg^{2+}	15–30	—	—	14	—	—	36
SO_4^{2-}	5–15	—	—	78	—	—	—
D-glucose	600–1100	—	1000	720	—	—	—
Albumin	35000–50000	—	—	—	—	1000	—

The above-mentioned findings led to three key strategies for improving the performances of Fe-based biodegradable stents, which are concurrently pursued nowadays:

- Alloying. The idea of adding other elements to Fe stems from the need of improving corrosion rate by either lowering the overall electrochemical potential of the material or by adding elements that induce formation of second phases, leading to galvanic corrosion. Furthermore, the choice of appropriate elements can eliminate the

ferromagnetic behavior, improve the biological performances and enhance the mechanical properties, up to levels similar to those of Co-Cr alloys [63].

- Processing. Another way to tailor the properties of Fe consists in applying different thermo-mechanical treatments in order to alter its structure, such as cold rolling or extrusion. Moreover, alternative routes to casting and plastic deformation were explored, such as electroforming or additive manufacturing.
- Surface modification. The principle consists, as the name says, in altering the surface of the material in order to change the chemical composition of its surface as well as its roughness. Surface modification procedures include the application of a coating (either bioinert or bioactive), the implantation of other elements in the first atomic layers, or a combined strategy. Such an approach can also be used alone or in combination with alloying or processing.

1.3.1 Alloying

1.3.1.1 Fe-Mn alloys

Mn is the most studied alloying element for biodegradable Fe stents for a multitude of reasons. From a metallurgical point of view, it is a powerful stabilizer of the austenitic (γ) phase of Fe, eliminating ferromagnetism [62,63]. Moreover, it improves mechanical properties by solid solution strengthening, increasing both ultimate tensile strength (UTS) and elongation to failure.

From an electrochemical perspective, Mn is less noble than iron in the electrochemical series, showing a corrosion potential of - 1.185 V vs. SHE [98]. Being fully soluble in Fe, it can decrease the overall potential of the alloy, as shown by numerous studies [62,128,129]. Similarly to the case of Fe, the anodic and cathodic half-reactions for Mn in aqueous solution are the following:

$$2Mn(s) \rightarrow 2Mn^{2+}(aq) + 4e^-$$

$$O_2(g) + 2H_2O(aq) + 4e^- \rightarrow 4OH^-(aq)$$

Thus leading to the overall reaction:

$$2Mn^{2+}(aq) + 4OH^-(aq) \rightarrow 2Mn(OH)_2(s)$$

Also in this case, it is common for Mn to interact with other species in the body, giving most frequently rise to carbonates ($MnCO_3$) [130]. The general corrosion mechanism for Fe-Mn alloys is schematized in figure 1.2.

Physiologically speaking, Mn is a regulating factor for enzymes inside the body [65], and its deficiency is correlated to osteoporosis, a common bone disease [131]. Its recommended daily uptake is of 4 mg [27]. On the other hand, an excess of Mn is a known factor in the development of Parkinson's disease [65], although the main transport mechanism of Mn to the brain is through the respiratory system, while blood transport plays a limited role [65].

The first studies on Fe-Mn alloys for biodegradable implants aimed at establishing the optimal content of Mn for improving the mechanical properties of Fe to a level comparable to 316L stainless steel [62,64]. As mentioned before, Mn stabilizes austenite at room temperature; however, this is true only when at least 28 wt. % of Mn is added. For lower amounts, if an annealed and quenched material is considered, martensite can form, either HCP ε or body centered tetragonal (BCT) α' [132,133], as predicted by Schumann's diagram (figure 0.10). The presence of martensite can increase the strength of Fe but can conversely reduce its ductility. Fe-xMn alloys (x = 20, 25, 30, 35 wt. %) processed by powder metallurgy showed this same trend: if Mn was lower than 30%, high strength and low elongation to failure were observed, while for a content of Mn of at least 30% wt., lower strength and high elongation to failure were detected [64]. Both YS and UTS of the Fe-35Mn alloy were comparable to those of 316L, although the elongation to failure was of 30%, significantly lower than that of 316L [62]. Another study showed that, for a Fe-10Mn alloy, very high strength was achieved (UTS above 1000 MPa), although at the expenses of elongation to failure (below 15%) [63].

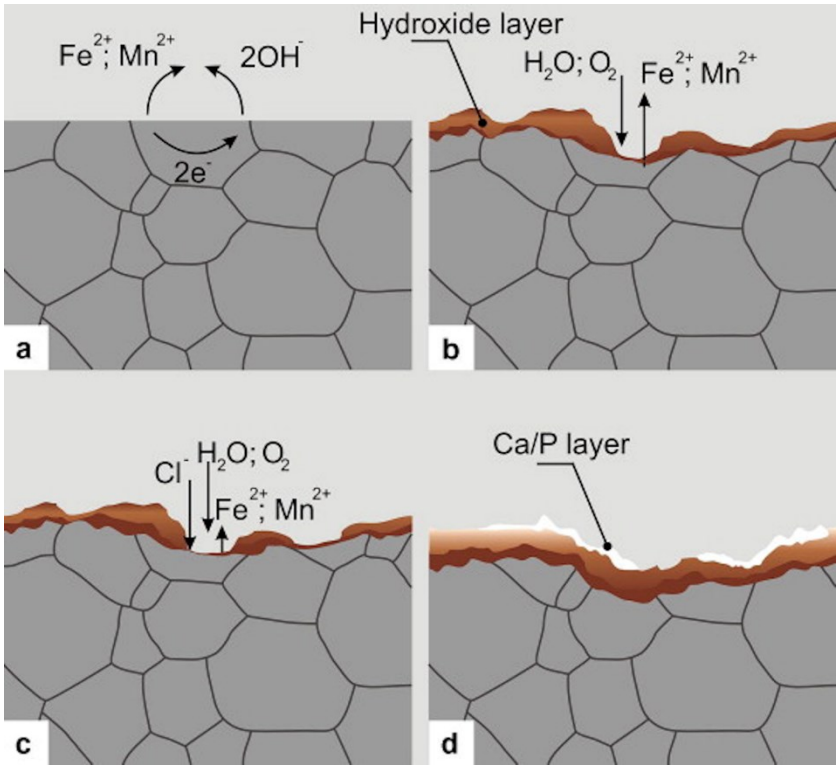

Figure 1.2 Schematic representation of the corrosion mechanism of Fe-Mn alloys in a pseudo-physiological solution: a) redox reaction at the interface material/solution; b) formation of a porous hydroxide layer; c) localized corrosion at the layer pores; d) formation of a compact layer with a composite Ca/P layer on top [11]

The effect of Mn on corrosion behavior of Fe was assessed by several studies, using both electrochemical, immersion and animal tests. Potentiodynamic polarization (PDP) tests conducted by different researchers showed that the corrosion potential of Fe-Mn alloys with at least 20% of Mn is a direct function of the Mn content, with the lowest corrosion potential obtained for the highest amounts of Mn [11,64,134]; however, no difference in corrosion rate was detected from dynamic immersion tests up to 84 days [11], while static immersion tests showed the same direct relationship observed in PDP tests for 30 days of immersion [134]. Other researchers showed that plastic strain applied to Fe-Mn alloys with at least 20% of Mn promotes a faster corrosion rate with respect to an undeformed state [135,136]. Similarly, tests on a deformed Fe-35Mn stent showed a lower corrosion potential and higher corrosion rate with respect to an annealed coupon [129]. It was also seen that even adding 10% of Mn can increase the corrosion rate up to 28 days with respect to pure Fe [63].

Several studies also assessed the cytocompatibility of Fe-Mn alloys using different cell lines. It was observed that Fe-xMn alloys (x = 20, 25, 30, 35) do not cause a reduction in cell viability with respect to 316L stainless steel when put in contact with fibroblasts [11]. Similar

results were obtained for Fe-xMn alloys (x = 20, 30, 35) in contact with osteoblasts [134]. Other authors found that a Fe-30Mn alloy shows cytotoxicity towards bone marrow stem cells if a significant amount of Mn is released in cell culture medium [137].

Although the addition of Mn generally promoted a faster corrosion rate after few days, a stable corrosion layer formed after some weeks since the start of the corrosion process, as detected both in laboratory setups [11,129,135,136] and in animal tests [138], preventing degradation of the material in the first 12 months. For this reason, researchers looked for adding one or more alloying elements to the Fe-Mn system without compromising mechanical properties and cytocompatibility. Such elements may increase the corrosion rate either by decreasing the overall electrochemical potential of the system or by creating galvanic couples [63].

Several elements have been explored, including C, Si, Pd, Ag, Mg and Ca. The addition of C will be treated in section 1.3.1.3, since its presence heavily modifies the metallurgy of the Fe-Mn system, giving rise to alloys known as twinning-induced plasticity (TWIP) steels.

Among those elements, Si is a stabilizer of the body-centered cubic (BCC) ferritic α phase of Fe and has a limited solubility in it. When Mn is also present, however, there is a wide solubility range of the three elements, granting a single-phase austenitic alloy for low amounts of Si. An interesting system explored in past years is the Fe-30Mn-6Si (wt. %) alloy. Such material showed vastly superior mechanical properties to pure Fe [139], together with a shape memory effect [140,141]. The presence of Si, on the other hand, was shown to decrease the cytocompatibility with ECs and SMCs, while decreasing the corrosion potential of the material with respect to pure Fe [139].

In comparison, Pd is a potent γ-stabilizer for Fe and is partially soluble in both Fe and Mn [63]. Its addition can increase the short-term corrosion rate of Fe-Mn alloys by precipitation of Pd-rich second phases during appropriate thermal treatments, promoting galvanic coupling with the matrix [63]. Aging treatments were also shown to improve significantly the strength of the material with respect to Fe-Mn alloys [142]. Pd was also added to Fe-Mn-Si alloys, reducing the corrosion potential, increasing the corrosion rate without altering cytocompatibility [143,144].

Contrarily to the previously discussed elements, Ag is completely insoluble in Fe [145], while showing a limited solubility in Mn [146]. Because of this, all reports available at present

produce such materials by powder-based techniques, either PM or AM (also known as 3D printing). This particular feature was shown to promote corrosion by galvanic coupling of Ag particles with a Fe-Mn matrix by several researchers [71,147]. In addition, Ag is a widely recognized antibacterial agent [92], which can be useful in minimizing the risk of surgery associated infections.

Mg and Ca are both alkaline earths, with properties completely different to those of Fe and Mn. Both elements have much lower melting and boiling points, making liquid-phase processing unfeasible and even dangerous. Both elements have a very low electrochemical potential, namely – 2.868 V vs SHE for Ca and 2.372 V vs SHE for Mg [98]. The only successful reports on the use of such material in a Fe-Mn alloy involve the use of solid AM techniques, indicating an increase in corrosion rate [148].

1.3.1.2 Mn-free alloys

As mentioned in the previous section, one of the main drawbacks of Mn is the possible long-term insurgence of severe diseases, such as Parkinson's. This is especially true since the amounts of Mn added to Fe to improve mechanical properties are of at least 20% wt. For this reason, Mn-free alloys can be sought.

Most reports discuss the addition of elements already used in the case of Fe-Mn alloys. For example, Pd was added to pure Fe using PM processes, showing no significant advantage in both corrosion and biological behavior over pure Fe [149–151]. Ag was also shown to increase the corrosion rate of pure Fe without compromising its biological performances [152].

Another studied element was Pt, among the most noble elements in the electrochemical series, with a potential of + 1.180 V vs SHE [98]. Moreover, its Pourbaix diagram in aqueous solution shows no active region [99], meaning that Pt may effectively act as cathode in a local galvanic couple with Fe. This was confirmed by researchers, finding a significant increase in corrosion rate because of the addition of Pt [151], while the cytocompatibility and hemocompatibility remained acceptable.

Similarly to Pt, Au is a very noble element, with an electrochemical potential of + 1.692 V vs SHE [98]. Analogously to the case of Ag, Au was shown to increase the short-term corrosion rate of pure Fe as a function of the content of Au [152], without compromising the biological performances either.

PM techniques also permitted to develop Fe-based MMCs with metallic or non-metallic reinforcements. This strategy was mainly pursued to fabricate porous scaffolds for orthopedic applications; however, MMCs aimed at cardiovascular stents were also reported.

An example is constituted by Fe-Mg_2Si composites, aiming at creating galvanic coupling with the Fe matrix by introduction of a less noble phase. Depending on the mixing of powders, such composites showed an increased strength and decreased ductility with respect to pure Fe [153]. In addition, the corrosion rate was increased with respect to pure Fe in the short term, while slowing down after 100 days of immersion [154,155]. It was observed that phosphates formed on the surface of the material after 50 days from immersion, similarly to animal tests [154].

1.3.1.3 Twinning-induced plasticity (TWIP) steels

Twinning-induced plasticity steels were originally developed in the 19th century by Sir Robert Hadfield [156]. They are composed of Fe and Mn with the addition of either C or a combination of Al and Si. The content of Mn and C (or Al and Si) must be sufficiently high to stabilize only austenite at room temperature. For Fe-Mn-C TWIP steels, Schumann established the relationship between the contents of Mn and C to obtain only austenite at room temperature [83]:

$$(wt.\%\, Mn) = -20(wt.\%\, C) + 32$$

showing that the higher the content of C, the lower the amount of Mn needed to stabilize austenite at room temperature.

In the last 20 years there has been a renewed interest in such alloys because of their excellent mechanical properties. On average, TWIP steels possess a YS around 400 MPa, an UTS around 1000 MPa and an elongation to failure of at least 40%, indicating that strain hardening takes place during plastic deformation [67]. Because of such properties, these alloys are sought for crash-resistant structural parts in car bodies [132], with patents deposited by major players in the automotive market such as Daimler and Hyundai [67]. Furthermore, these values match those of Co-Cr alloys (table 0.2), making TWIP steels viable for manufacturing cardiovascular stents with smaller dimensions in comparison with Mg- and Zn-based devices.

One of the main limitations of TWIP steels for automotive applications is their poor resistance to chloride corrosion [87]. On the other hand, since chloride ions are among the main

constituents of human plasma [18], they may be degraded by the action of physiological fluids, thus becoming high strength degradable stents, overcoming the limitations of Mg-based implants.

TWIP steels for biodegradable stents

In addition to the automotive market, in the last 10 years TWIP steels have attracted research in the field of biodegradable stents. As outlined above, the biggest advantage of TWIP steels over Mg-based, Zn-based and other Fe-based alloys lies in the outstanding mechanical properties, matching those of L605. In contrast with automotive applications, the alloying elements that can be used are limited by considerations on their effect on human body. Since, as already outlined before, Al is a known factor in the development of Alzheimer's disease, its use for biomedical applications involving biodegradable metals should be avoided. Thus, the only viable TWIP steel system for cardiovascular stents becomes the Fe-Mn-C one.

The overall corrosion mechanism of TWIP steels is comparable to that of Fe-Mn alloys, implying that the addition of C does not play a significant role in it. Tests in simple aggressive media, however, showed that TWIP steels are sensitive to chloride corrosion [87]. Since chloride ions are the most abundant ones in physiological fluids [18], TWIP steels may be corroded effectively under the action of such fluids. In addition, several works found that Fe-Mn-C steels in contact with non-physiological media were subject to hydrogen embrittlement [157,158].

In a similar fashion to Fe-Mn alloys, Fe-Mn-C steels suffer from the formation of a stable layer of degradation products on the material surface during the corrosion process. It was shown that this layer is mainly composed by carbonates and phosphates [130]. The nature of the degradation products varies according to the testing medium and atmosphere [69]: these factors should be taken carefully into account when designing tests, in order to replicate *in vivo* conditions as reliably as possible. On the other hand, it was shown that TWIP steels have a lower electrochemical potential with respect to pure Fe. Moreover, plastic deformation can affect corrosion, since twins may act as preferential corrosion sites [147]. This same study showed that proteins can reduce the corrosion rate of TWIP steels. Another study showed that both cytocompatibility towards human ECs and SMCs and hemocompatibility were acceptable [159].

Like in the case of Fe-Mn alloys, the most employed strategy to improve the corrosion rate relies in adding other elements in order to form galvanic couples [63]. Among others, Pd

was explored, showing an improvement in the short-term corrosion performances of a TWIP steel in a laboratory setup, although a compact corrosion layer was formed, as visible in figure 1.3 [12]. Moreover, it did not affect the mechanical properties nor the biological performances of the same steel [94,160]. However, when this steel was implanted into rat bones, no evident corrosion was observed 1 year after implantation [70]. It should however be noted that a bone is a much different environment with respect to a blood vessel, with a much lower blood perfusion.

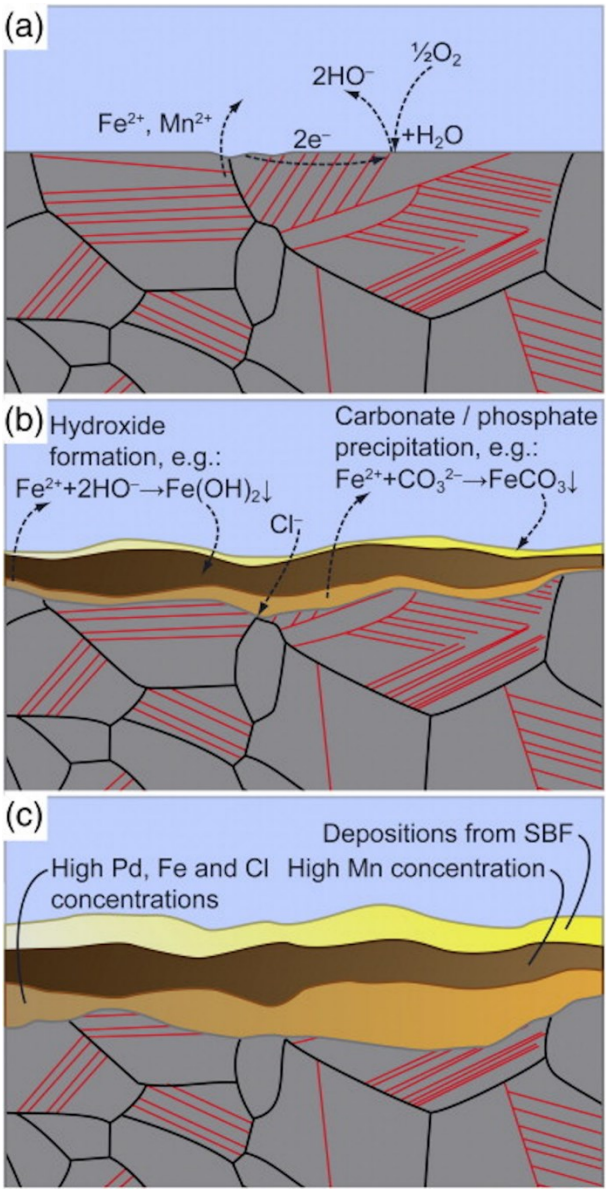

Figure 1.3 Schematic representation of the corrosion mechanism of Fe-Mn-C-Pd alloys in SBF [12]

Microalloying a Fe-30Mn-1C alloy with S was also studied. Small quantities of S could be fully dissolved in the matrix, allowing not to modify mechanical properties in the as cast state, while generating a small improvement in corrosion behavior [161,162]. In addition, cytocompatibility towards fibroblasts was similar to that of the S-free steel. In addition to S, B microalloying was also explored using the same base alloy. In contrast with S, B is insoluble in the matrix, resulting in the formation of boron carbides that could lead to premature failure of the material [162]. Corrosion and cytocompatibility were similar to the case of S.

Some studies reported the production of Fe-Mn-C steels alloyed with Ag aimed at biodegradable stents: contrarily to Pd and S, Ag is completely insoluble in the matrix [146]. In addition, its high density makes production of such alloys by casting non-trivial, leading to preparation of pieces from such alloys by additive manufacturing (AM). The presence of Ag resulted in a reduction of mechanical properties, while it increased the short-term corrosion rate of the alloy [73,74]. Another interesting feature of Ag lies in its well-known antibacterial behavior, which may have the side effect of minimizing the risk of surgery-associated infections, although no studies on the antibacterial properties of Fe-Mn-C-Ag steels are available at present.

Another antibacterial element that was explored for increasing the corrosion rate of TWIP steels is Cu. In more acidic environments (artificial urine) than that of blood vessels, the presence of 0.8% wt. of Cu in a Fe-30Mn-1C alloy was shown to double the corrosion rate, while showing a strong antibacterial activity.

At the time this thesis was written, no reports were available on *in vivo* studies of TWIP steels in arteries, leaving open questions on clinical translation of such a material.

1.3.2 Processing

Production of a biodegradable stent is carried out similarly to that of a permanent one, as outlined in the Introduction. In the case of Fe-based degradable alloys, the use of alternative processing routes was explored to enhance corrosion rate while possibly simplifying the production chain.

1.3.2.1 Electroforming

A near net shape technique reported for biodegradable Fe is electroforming, which involves deposition of metallic ions onto a substrate by means of an electrochemical reaction in a solution [163]. More in detail, a cathode and an anode are immersed in a conductive medium

and are electrically connected so that a current can circulate. An oxidation reaction occurs at the anode, releasing metallic ions that are deposited onto the cathode, acting as a substrate. After the process is completed, the final electroformed product can be removed from the substrate using a variety of techniques, such as mechanical removal, selective chemical dissolution of the substrate, or melting of the same if a low melting point metal was used (e.g. Sn). A schematic view of the process is shown in figure 1.4.

One of the main advantages of electroforming lies, as mentioned above, in its one-step nature, considerably reducing the time needed to produce a stent precursor. In addition, the thickness of an electroformed tube can be easily controlled by adjusting process parameters, which also govern the microstructure of the obtained product [164]. The microstructure of an electroformed device can also be controlled by applying post-process thermal treatments. This can also impact mechanical properties: in the case of pure Fe, it was shown that the as-electroformed material has a UTS above 400 MPa but an elongation to failure below 10%, while annealing resulted in a lower UTS but higher elongation to failure, which could exceed 30% [13]. It was also shown that electroformed and cast Fe have no difference in cytocompatibility towards fibroblasts, while electroformed Fe had a higher corrosion rate with respect to cast Fe in tests up to 2 weeks [165].

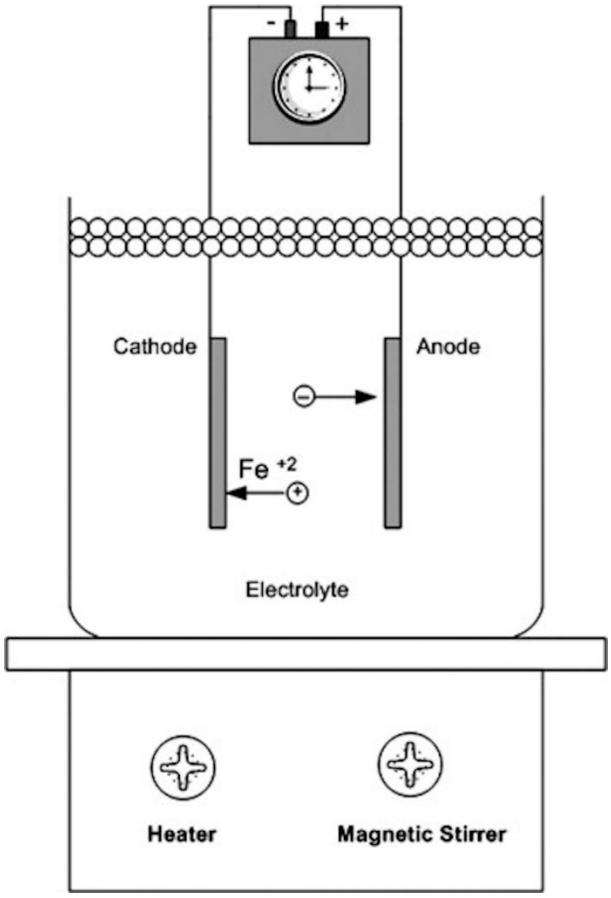

Figure 1.4 Overview of a planar electroforming apparatus [13]

In addition to pure Fe, also Fe-based alloys can be produced. A report showed the feasibility of electroforming Fe-P sheets on top of a Fe substrate, producing some increase in corrosion rate in electrochemical tests [166].

So far, the only literature reports on electroforming of Fe-based alloys discuss pure Fe or very simple systems. In addition, only one report discusses electroforming of stents made of pure Fe [167], and *in vivo* tests have not been performed yet.

1.3.2.2 Magnetron sputtering

Another bottom-up technique used to build Fe-based biodegradable metals is magnetron sputtering. In this technique, a target of a certain material is bombarded by ions generated in a plasma directed to it, allowing to remove atoms from the target and depositing them onto the surface of a substrate. Magnets help directing target atoms onto the substrate to increase deposition efficiency [168]. This process is used in a large variety of fields to deposit coatings having different properties [168].

In recent years, deposition of thin foils of Fe-based materials for biomedical applications was reported. The main advantage over conventional top-down approaches described in section 1.4.1 lies in the possibility of producing very thin structures with good thickness control [169]. Pure Fe foils were deposited by researchers, showing higher strength and lower ductility with respect to annealed pure Fe but similar corrosion rate from electrochemical tests [169]. Fe-Mn alloys were also produced by magnetron sputtering with varied compositions, ranging from 5% to 70% wt. Mn [170,171] or using a layer-by-layer (Fe-Mn)-Fe structure [172]. Similarly to bulk alloys, foils with low Mn content show very low elongation to failure and high tensile strength, while foils with high Mn content have opposite behavior [172]. Annealing treatments on Fe-32Mn foils resulted in overall improved ductility, with elongation to failure reaching 25% while keeping a tensile strength above 600 MPa [170]. Fe-Mn foils showed a decreased short-term CR with respect to magnetron sputtered pure Fe: while the CR of the latter was found to be in the order of 0.10 mm/year, Fe-Mn alloys ranged from 0.08 to 0.02 mm/year [172]. This is a function of Mn content: the more Mn is in the material, the lower the corrosion rate, as already observed for Fe-Mn alloys. Cell viability towards fibroblasts was independent from Mn content for magnetron sputtered films, and was similar to a negative control [171].

1.3.2.3 Additive manufacturing

Additive manufacturing (AM), also known as three-dimensional (or 3D) printing, collects a number of fabrication techniques involving the building of pieces by successive layers. In the case of metal AM, the starting material is commonly supplied in the form of powders with spherical particle shape. Powder particles are locally melted with either a laser or electron beam on each layer to form the final component in near net shape. As soon as the beam is moved from the melted region, this latter part solidifies very rapidly. Three big families of AM processes are available nowadays: selective laser melting (SLM), electron beam melting (EBM), and direct energy deposition (DED) [93].

SLM and EBM are both powder bed processes, where a powder bed is prepared on a movable plate within a chamber filled with a protective gas, such as N_2 or Ar. The beam locally melts the powder which will form a layer of the final piece. Right after the beam has passed, the part solidifies. Once a layer is solidified, the plate lowers, a layer of powder is added, and the successive layer is prepared with the same procedure. This scheme is repeated until all layers have been melted and solidified. The unmelted powder is recovered on a tray in the chamber for

reuse or discard. The only conceptual difference between SLM and EBM lies in the beam source: a laser for SLM, an electron beam for EBM [93].

DED differs from SLM and EBM in the fact that the material is deposited with a nozzle coaxial with the laser beam, requiring less material than in powder bed technologies. More than one feedstock can also be added, making alloy preparation or co-deposition directly in the nozzle possible [93]. The main advantage of AM techniques in comparison with subtractive technologies lies in the near net shape nature of the process. However, post-processing is commonly necessary since AM parts have generally high surface roughness. Piece geometry and thickness is limited by how focussed the beam can be, which in turn requires powders with a minimal size and spherical shape.

At present, no reports on additively manufactured stents or stent precursors from Fe-based alloys are available in the literature. Fe-based additively manufactured scaffolds were reported [173,174], with strut size as low as 200 μm and an increased corrosion rate up to 28 days. In addition, no cytotoxicity towards osteoblasts was reported.

The main challenge that AM technologies face is miniaturization, since the powder particle size to manufacture solid components is still too large to think towards a stent with 60 μm struts, such as obtainable from Co-Cr alloy using precision cold drawing.

1.3.3 Surface modification

An alternative and complementary strategy to adding alloying elements to bulk Fe is surface modification. This approach can either involve the application of a coating of varied nature, adding other elements to the alloy in the first atomic layers, modifying the surface roughness, or a combination of these strategies. Since corrosion of a given material starts from its surface, modifying it can alter the corrosion behavior, possibly hindering the formation of a passive layer; this could allow full degradation of a Fe-based stent.

1.3.3.1 Mechanical modification

Surface roughness can be modified using several treatments, either chemical or mechanical. When corrosion is considered, having a higher surface roughness results in a higher surface area available for attack by an aggressive medium. An example of mechanical surface treatment is sandblasting, where a gun projects sand particles with known characteristics on the

surface of a material in order to modify its roughness. In the case of pure Fe, it was shown that sandblasting can increase its corrosion rate for immersion in simulated body fluid (SBF) up to 28 days while promoting good cytocompatibility towards osteoblasts [175].

Surface treatment may also be used to locally change the alloy microstructure, thus provoking a different reaction to corrosive attack. Shot peening is a technique somewhat similar to sandblasting, but it was reported to induce dynamic recrystallization by local severe plastic deformation induced by particles hitting the material surface at high speed [176]. Dynamic recrystallization involves high levels of plastic deformation on a material, leading to nucleation and growth of new grains by releasing the excess internal energy stored by plastic deformation by applying further deformation [177]. This contrasts with static recrystallization, where nucleation of new grains is stimulated by heating the previously deformed material. Shot peening was applied to pure Fe to produce nanostructured grains on the material surface [178]. It was shown that shot peening induced a decrease in the electrical resistance of the surface of pure Fe in a simple 0.9% NaCl solution, implying that it may be more prone to corrosion. This was associated to a reduction in grain size caused by shot peening.

1.3.3.2 Ion implantation

Another process that can be used to modify the composition of the first tens of nanometers of Fe is ion implantation of other elements. This technology involves bombarding a material with ions of the element to implant which, travelling at very high speed, will impact the surface and penetrate the first atomic layers.

The element for which the most results were reported is Zn. It was seen that corrosion rate increased when the content of implanted Zn increased, although this was valid up to 10% wt. Zn, after which the corrosion rate decreased, based on electrochemical tests in SBF [179]. Implanting a lower amount of Zn (around 3% wt. in the first 60 nm from the surface) resulted in an increase in corrosion rate versus pure Fe in the first 15 days of immersion; however, the effect was nullified after 30 days immersion in Hanks' modified salt solution (HMSS) [180]. In both cases, cytotoxicity towards osteoblasts and fibroblasts was higher than in the case of pure Fe. When hemocompatibility is considered, hemolysis was kept at acceptable levels, while ion implantation caused a marked increase in adhered platelets, indicating possible thrombogenicity.

Another element for which ion implantation was studied into pure Fe is Ag [181]. It was seen that the presence of Ag did not alter corrosion current density from PDP tests in Hanks' solution, but it decreased its polarization resistance with respect to pure Fe. On the other hand, a similar behavior to Zn implantation was reported for hemocompatibility: while hemolysis remained at acceptable levels, platelets adhesion was strongly increased in the presence of Ag.

Finally, implantation of Ta into pure Fe was also explored [182]. Ta increased the corrosion potential and current density with respect to pure Fe and promoted cell attachment on the surface.

In synthesis, while ion implantation looks like a promising technique for increasing corrosion rate, care should be taken when considering platelet adhesion, since the implantation of different ions resulted in possible thrombogenicity. This may be due to intrinsic limitations in the technique.

1.3.3.3 Nitriding

Another surface modification technique consists in nitriding, where N atoms are introduced in the first atomic layers of a material, either by gaseous diffusion or by plasma bombardment. Nitriding of pure Fe stents was reported, showing the potential of the technique to be used for real devices. The first study reports *in vivo* results for relatively big stents (8 mm outer diameter, 120 μm strut thickness) in pigs up to 12 months [183]. Electrochemical tests showed a twofold increase in corrosion rate in comparison with pure Fe; on the other hand, dissolution of the stent in pigs was only partial after 12 months. In addition, lumen loss was observed at 12 months, which was absent at 3 and6 6 months timepoints. No chronic inflammation was observed.

A second version of this device had much smaller dimensions (3 mm outer diameter, 70 μm strut thickness). *In vivo* tests were carried out on rabbits (up to 12 months) and pigs (up to 53 months) [184]. While full degradation of the nitride stent was achieved in rabbits, this was not the case for implantation in pigs at 53 months. This also shades the validity of *in vivo* assessments in rabbits, since pigs are a more realistic model for the human cardiovascular system.

A newer nitride stent with even smaller dimensions (3 mm outer diameter, 53 μm strut thickness) was also tested in rabbit aortae for up to 13 months [14]. The design of the surface was also modified, including a drug releasing PDLLA coating and a Zn conversion coating. It

was found that 95% of the stent volume degraded in 13 months, but the validity of the approach should be validated with a more representative animal model, since adverse results were found in the aforementioned study after positive outcomes in rabbits. Degradation of such device *in vivo* is shown in figure 1.5.

1.3.3.4 Surface patterning

Patterning a surface with another material to modify its properties is another surface modification process that was explored for Fe-based alloys. Both a polymer and a metal were used for making a patterned coating on pure Fe. Pt was deposited in the form of discs on a flat pure Fe surface by photolithography with 2 different diameters, 4 and 20 μm [185]. Static immersion tests in Hanks' solution showed an increased corrosion rate with respect to pure Fe up to 42 days. In addition, both cell viability towards SMCs, hemolysis and platelet adhesion were improved with respect to pure Fe.

Another option consisted in applying a patterned polylactic acid (PLA) coating on a pure Fe sheet in order to favor corrosion by local acidification [186]. This approach appeared to have accelerated short-term corrosion of pure Fe. This same paper reported *in vivo* results of PLA-coated Fe stents in rabbits for up to 12 months. It is claimed that the struts disappeared after 1 year from implantation, but the degradation products are still present at the strut sites.

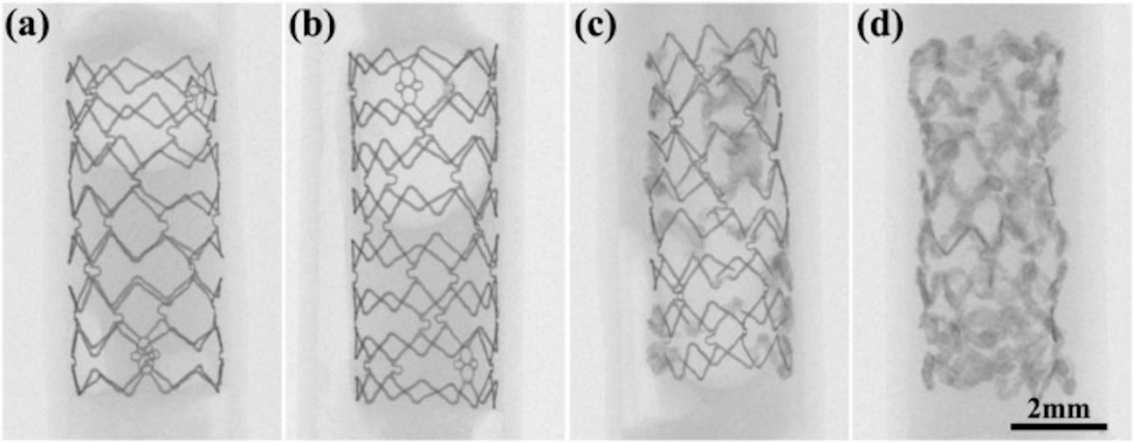

Figure 1.5 Degradation of a nitrided Fe stent in the abdominal aorta of rabbits by micro-computer tomography a) 1 month; b) 3 months; c) 6 months; d) 13 months [14]

2. The addition of silver affects the deformation mechanism of a twinning-induced plasticity steel: Potential for thinner degradable stents

Sergio Loffredo[a,b], Carlo Paternoster[a], Nicolas Giguère[c], Gianni Barucca[d], Maurizio Vedani[b], Diego Mantovani[a,*]

a: Laboratory for Biomaterials and Bioengineering, Canada Research Chair I in Biomaterials and Bioengineering for the Innovation in Surgery, Department of Min-Met-Materials Engineering, Research Center of CHU de Quebec, Division of Regenerative Medicine, Laval University, Quebec City, QC G1V 0A6, Canada

b: Department of Mechanical Engineering, Politecnico di Milano, Milan 20156, Italy

c: Quebec Metallurgy Center (CMQ), Trois-Rivières, QC G9A 5E1, Canada

d: Dipartimento di Scienze e Ingegneria della Materia, dell'Ambiente ed Urbanistica – SIMAU, Università Politecnica delle Marche, Ancona 60131, Italy

Keywords

Twinning-induced plasticity steel; Biodegradable metals; Silver; Deformation texture; Stents

Publication status

Published in Acta Biomaterialia **98** (2019), 103-113. DOI: 10.1016/j.actbio.2019.04.030

2.1 Résumé

Les alliages de fer ont des excellentes propriétés mécaniques pour les stents cardiovasculaires, mais leur taux de dégradation est insuffisant. Les aciers à plasticité induite par maclage (TWIP) possèdent des propriétés mécaniques excellentes pour envisager des stents cardiovasculaires dégradables plus minces. Pour accélérer la dégradation, l'ajout d'éléments nobles pour promouvoir la corrosion par couplage galvanique a été proposé, dont l'argent. En revanche, son impact sur le mécanisme de déformation des aciers TWIP est méconnu. L'ajout d'Ag réduit significativement la ductilité sans changer la résistance du matériau, quand il promeut une texture de déformation différente, stimulant ainsi la formation de martensite mécanique. La compréhension de la microstructure et de la texture résultantes de la déformation plastique peut aider à prédire les mécanismes de dégradation qui se produisent pendant l'implantation. En ajout, connaître la microstructure déformée permet de comprendre la formabilité des stents dégradables à section mince.

2.2 Abstract

While Fe-based alloys have already been reported to possess all mechanical properties required for vascular stenting, their relatively low degradation rate in vivo still constitutes their main bottleneck. The inflammatory reaction generated by a stent is inversely proportional to its mass. Therefore, the tendency in stenting is to lower the section so to reduce the inflammatory reaction. Twinning-induced plasticity steels (TWIP) possess excellent mechanical properties for envisaging the next generation of thinner degradable cardiovascular stents. To accelerate the degradation, the addition of noble elements was pro- posed, aimed at promoting corrosion by galvanic coupling. In this context, silver was reported to generally increase the degradation rate. However, its impact on the deformation mechanism of TWIP steels has not been reported yet. Results show that the use of Ag significantly reduces the ductility without altering the strength of the material. Furthermore, the presence of Ag was found to promote a different deformation texture, thus stimulating the formation of mechanical martensite. Since a stent works in the deformed state, understanding the microstructure and texture resulting from plastic deformation can effectively help to forecast the degradation mechanisms taking place during implantation and the expected degradation time. Moreover, knowing the deformed microstructure allows to understand the formability of very small tubes, as precursors of the next generation of thin section degradable stents.

2.3 Introduction

Biodegradable metallic stents have long been seen as the next revolution for treating cardiovascular diseases [16,26,27,96]. Since 2016, a Mg-based stent is available on the market [51,52,187]. However, its structure is much bigger with respect to current state-of-the-art drug-eluting or bare metal stents [10], possibly reducing deliverability and long-term safety [5]. This is also a competitive disadvantage, since the strut size of permanent stents has constantly decreased thanks to technological innovations [5,188]. Moreover, the volume of the implanted stents is inversely proportional to its expected clinical success, mainly due to the fact that the generated inflammatory reaction is expectedly lower [5].

Iron-based alloys are considered a viable material for producing smaller degradable vascular stents, since they possess better mechanical properties than Mg-based alloys [45,189]. Moreover, as explained before, a thinner degradable stent has a significant clinical advantage in reducing the risk of late adverse reactions such as thrombosis, which already provoked negative outcomes for an absorbable polymeric stent [40]. While pure Fe proved to be biologically safe in an animal model [60,61], it has a low degradation rate [27] and is ferromagnetic, making post-implantation follow-up more difficult [127]. Alloying with Mn was proposed to improve the mechanical properties while making the material non-ferromagnetic [11,62]. While the accumulation of high amounts of Mn in the brain is known to favor the appearance of Parkinson's disease, blood transport is a minor cause [190]. Recent *in vivo* tests also proved the biological safety of Fe-Mn alloys. [138].

Twinning-induced plasticity steels (TWIP), made of Fe, Mn and C, constitute an interesting compromise between degradable materials and high-resistance steels, showing mechanical properties far superior than those of Fe-Mn alloys [67]. Mechanical properties approach those of Co-Cr alloys commonly used for corrosion-resistant stents [10], and their structural section reaches now as low as 65 microns [5,188]. TWIP steels mainly deform by mechanical twinning instead of dislocation gliding, mostly because of their chemical composition [83]. From a degradation point of view, TWIP steels degrade faster than pure Fe [12,161]. However, a compact passive film is formed during degradation, preventing long-term corrosion to occur [69,130]. In order to accelerate corrosion, the addition of noble elements has been proposed by several authors, aiming at promoting galvanic coupling between the matrix and noble second phases [63,73,94,162].

The addition of Ag to TWIP steels has been proposed for promoting galvanic corrosion, showing promising results [73,74]. However, the influence of Ag on the microstructure and mechanical properties of the TWIP alloys has not been understood yet. In this work, the effect of Ag on the deformation mechanism was investigated, in an attempt to explain its influence on the microstructure and mechanical properties at various levels of deformation. A new Fe-16Mn-0.7C (wt. %) alloy served as the base material for adding Ag, which was produced by melting and casting. This composition was selected to limit the amount of Mn present in the alloy, while promoting pure mechanical twinning with the lowest amount of C possible. An insufficient quantity of C may promote the formation of mechanical martensite instead of twins, thus reducing the ductility [82]. Production by casting contrasts with the works on powder metallurgy done at present [73,191]. Studies on cast materials are more appropriate for technological transfer, since stents are commonly cut from minitubes extruded from cast billets [6,24].

2.4 Materials and Methods

2.4.1 Material preparation

Two alloys, with nominal composition Fe-16Mn-0.7C and Fe-16Mn-0.7C-0.4Ag (wt. %), were cast from pure elements (Fe > 99.9%, Allied Metals, USA; Mn > 99.7%, Hickman, Williams & Company, USA; C > 99.9%, Tianjin Dashi Carbon Co. Ltd, China; Ag > 99.95%, Pyromet, USA). The two alloys will be named 0Ag and 0.4Ag in the following. An induction melting furnace with a liquid argon protection system was used in order to minimize the evaporation of manganese during casting (VIP Inductotherm, USA). The obtained billets (12.5 mm x 25 mm x 130 mm) underwent solution heat treatment at 1100°C for 12h in a vacuum furnace to prevent excessive decarburization (Vac Aero VAH Series, Canada). Quenching was performed by injecting gaseous Ar in the chamber at a pressure of 2x105 Pa.

The billets were brought to a thickness of 2 mm by means of hot rolling at 800°C. The material was kept at 800°C for 15 minutes in a resistance furnace prior to each rolling pass (Lenton AWF 13/25, UK). After the final hot rolling pass, the sheets were annealed at 800°C for 15 minutes in air, followed by water quench. Cold rolling was then performed for inducing different degrees of plastic deformation inside the material: the billet thickness was reduced by 10% (CR10), 25% (CR25) and 50% (CR50) respectively. Some billets deformed at 25% were annealed at 800°C for 15 minutes in a resistance furnace and water quenched, in order to create a deformation-free state (CRA).

2.4.2 Mechanical properties

The mechanical properties of the developed alloys were studied by means of tensile tests at a static strain rate (0.5 mm/min) on a universal mechanical testing machine (MTS Alliance RT-100, USA), following the ASTM E8/E8m-15a standard (n = 3). Flat samples were cut from the obtained sheets along the rolling direction. The loading direction was parallel to the rolling direction. In addition to this, Vickers microhardness tests were performed to assess the effect of thermo-mechanical treatments on the mechanical properties, using a 500 g load with a dwell time of 15 s (Clemex JS-2000, Canada) (n=5). Prior to microhardness testing, the samples were mechanically polished with SiC abrasive papers of 180, 320 and 600 grit, followed by 3 μm and 1 μm diamond suspension on a polishing cloth. Final polishing was performed with a colloidal alumina suspension having an average particle size of 50 nm.

2.4.3 Microstructure

The amount of Fe, Mn and Ag in both alloys was determined by atomic absorption spectroscopy (AAS). On the other hand, the amount of C was analyzed by means of a pyrolytic carbon/sulphur detector (LECO CS200, USA).

X-Ray Diffraction (XRD, Siemens D5000, Germany) was performed to identify the crystalline phases present in both alloys, using a Bragg-Brentano geometry with a Cu Kα radiation (λ = 1.54 nm). Scans were performed for 2θ ranging from 20 to 100°. Peak identification was performed using CrystalDiffract software (CrystalMaker Software Limited, UK). Prior to XRD, samples were mechanically polished similarly to those used for Vickers microhardness tests up to 3 μm diamond suspension.

In order to study the microstructure of both alloys, scanning electron microscopy analyses (SEM) were performed on mechanically polished samples (Hitachi SU-3500, Japan). Prior to observation, the samples were polished similarly to what was done for Vickers microhardness tests. The samples were then etched with Picral reagent (4 g of picric acid dissolved in 100 mL of ethanol). For analyzing the chemical composition of the Ag-rich particles, wavelength dispersion X-Ray spectroscopy analyses (WDS) were performed on a polished sample using a WAVE detector coupled with the INCAEnergy+ software for data collection (Oxford Instruments, UK).

Electron backscattered diffraction analyses (EBSD) were performed for understanding the texture and preferential orientations of the observed phases of the studied alloys, using a NordlysMax detector (Oxford Instruments, UK) installed on the same SEM used for microstructural analyses. The analyzed area was of 200 x 150 μm in all conditions. Data were collected with AZtec HKL software (Oxford Instruments, UK). Post-processing of the obtained data was done by means of Channel5 software (Oxford Instruments, UK). Prior to EBSD, polished samples underwent Broad Ion Beam milling under an Ar+ beam at 4 kV in order to produce a polished, deformation-free surface (BIB, Hitachi IM-4000 Plus, Japan). The obtained quality index (Q.I.) was superior to 90% for the CRA and CR10 samples, while it dropped to 75% for the 0Ag CR25 sample. However, Q.I. decreased to 43% for the 0.4Ag CR25 sample because of the important residual stresses. EBSD analyses on the CR50 samples could not be conducted because of the excessive residual stresses stored in the samples, not allowing to obtain a Q.I. above 15%.

Transmission electron microscopy (TEM) analyses were carried out by a Philips CM200 microscope operating at 200 kV and equipped with a LaB6 filament. For TEM observations, samples were prepared using the conventional thinning procedure consisting of mechanical polishing by grinding papers, diamond pastes and a dimple grinder. Final thinning was performed by an ion beam system (Gatan PIPS) using Ar ions at 5 kV.

2.4.4 Statistical analyses

Errors are reported in terms of standard deviations. In Figure 2.2, the error bars were calculated as the uppermost and lowermost deviation from the calculated average. In order to determine whether tensile tests and microhardness tests generated significant differences, one-way ANOVA tests with Tukey's post-hoc comparison were performed using Minitab 18 software (Minitab Inc., USA). Differences were considered statistically significant when $p < 0.05$ at least.

2.5 Results

2.5.1 Chemistry

The chemistry for both cast alloys is reported in Table 2.1. It can be observed that the actual composition closely resembles the nominal one. The difference in manganese content between the 0Ag and the 0.4Ag alloys was not found to be statistically significant.

Table 2.1 Chemical composition of the 0Ag and 0.4Ag alloys. The amounts of Fe, Mn and Ag were quantified by AAS, while the amount of C was determined by C/S pyrolytic detector.

Material	Fe (wt. %)	Mn (wt. %)	C (wt. %)	Ag (wt. %)	
Fe-16Mn-0.7C	Balance	15.22 ± 0.20	0.72 ± 0.01		
Fe-16Mn-0.7C-0.4Ag	Balance	15.60 ± 0.20	0.73 ± 0.01	0.38	0.02

Table 2.2 Average values for yield strength (YS), ultimate tensile strength (UTS) and elongation to failure (εf) for both alloys (* p < 0.01).

Material	σ_y (MPa)	σ_u (MPa)	ε_f (%)*
Fe-16Mn-0.7C	376 ± 7	1946 ± 11	54.7 ± 2.1
Fe-16Mn-0.7C-0.4Ag	433 ± 7	1768 ± 84	41.7 ± 4.0

2.5.2 Mechanical properties

The true stress – true strain curves for the 0Ag and 0.4Ag alloys after annealing are reported in Figure 2.1. Detailed results for the yield strength, ultimate tensile strength and elongation to failure are visible in Table 2.2. On one hand, the addition of Ag does not generate any statistically significant difference in terms of both yield and ultimate tensile strengths. On the other hand, the difference in elongation to failure is statistically significant ($p < 0.01$). The strength and ductility values far exceed the recommended thresholds for cardiovascular stents [24,45]. As commonly reported for TWIP steels [67], serrations in the stress-strain curves associated to dynamic strain aging (DSA) are visible for both alloys. On the other hand, DSA starts at around $\varepsilon = 16\%$ in the case of the 0.4Ag alloy, as compared with the 0Ag alloy, where the first serrations appear at $\varepsilon = 25\%$.

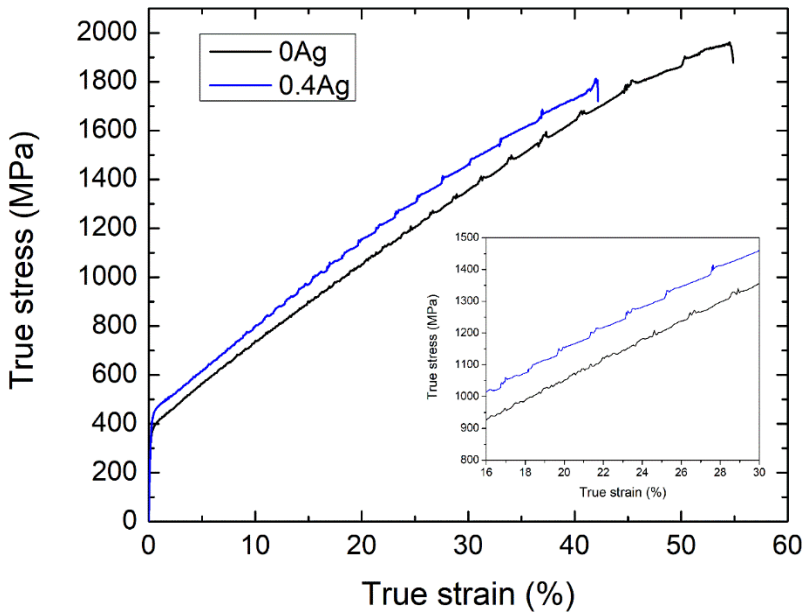

Figure 2.1 True stress – True strain curves for the 0Ag and 0.4Ag alloys in the annealed state. The inset shows the region with strain ranging between 15 and 30%, highlighting the beginning of DSA.

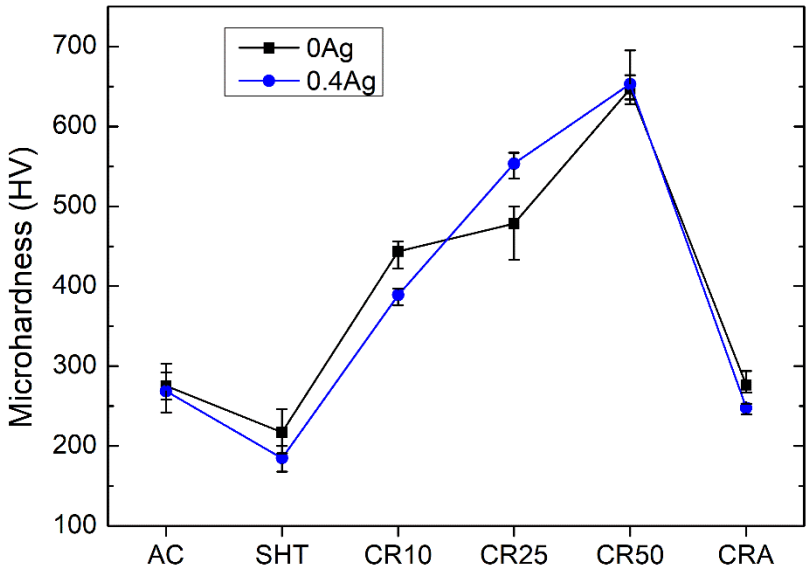

Figure 2.2 Vickers microhardness evolution for the 0Ag and 0.4Ag alloys after the different thermo-mechanical treatment steps (AC: As Cast; SHT: Solution Heat Treated; CR10: cold rolled at 10% reduction; CR25: cold rolled at 25% reduction; CR50: cold rolled at 50%

Vickers microhardness values for all the thermo-mechanical treatment conditions are found in Figure 2.2. It can be seen that microhardness varies with the same trend for both alloys: Solution heat treatment (SHT) is effective in relieving thermal stresses due to casting ($p < 0.01$). Moreover, microhardness increases by increasing the amount of plastic deformation imposed on the material (excluding the case of the 0Ag alloy, for which there is no difference between the CR10 and CR25 conditions).

Finally, annealing is effective in inducing recrystallization, since hardness is significantly decreased and brought back to the same value observed after casting (no statistically significant difference is present between the as cast and the annealed condition for both alloys).

2.5.3 X-ray diffraction

The XRD spectra for both alloys are reported in Figure 2.3. The 0Ag alloy (Figure 2.3a) shows only peaks that can be associated to different austenitic planes (γ-iron, FCC). When the 0.4Ag alloy is considered (Figure 2.3b), austenite is the only observed phase for the CRA and CR10 conditions. However, new peaks appeared in the CR25 condition: such peaks can be associated to ε-martensite (HCP) (Figure 2.3c). These additional peaks are also visible in the spectrum of the CR50 condition.

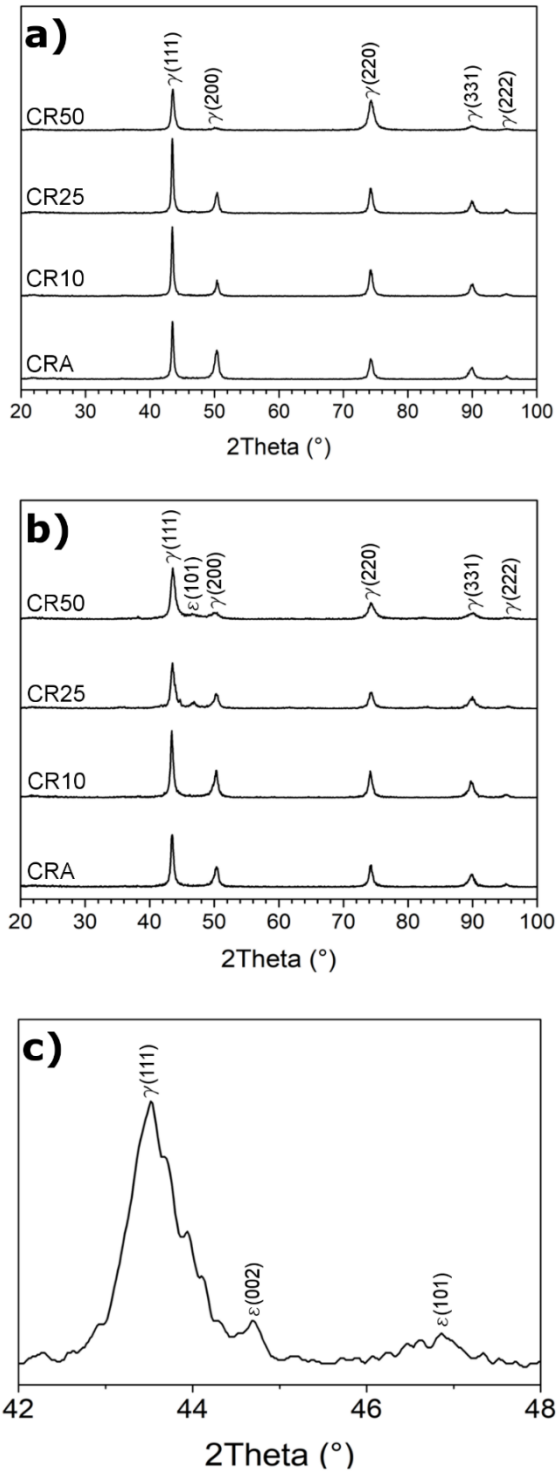

Figure 2.3 XRD spectra for the 0Ag and 0.4Ag alloys: a) 0Ag alloy, all deformation conditions; b) 0.4Ag alloy, all deformation conditions; c) 0.4Ag alloy after cold rolling thickness reduction of 25%, detail for 2θ between 42 and 48° showing the different ε-martensite peaks.

2.5.4 Scanning electron microscopy

The microstructural evolution of the 0Ag alloy is outlined in Figure 2.4 a-d. In the annealed condition (CRA, Fig. 2.4a), the grains are equiaxed, without any alignment along the deformation direction. The black particles that are visible inside some grains are pits caused by etching. In the CR10 condition (Fig. 2.4b), the grains are still equiaxed, and their size looks similar to the case of the annealed material. Mechanical twins are visible inside some grains. The white particles that are visible at some grain boundaries could be associated to carbide clusters. When the cold rolling reduction is increased to 25% (CR25, Fig. 2.4c), the amount of mechanical twins inside the grains increased. Twins are visible as straight needles going through an entire grain. The grain size and shape is comparable to that of the CR10 condition. Finally, after 50% cold rolling (CR50, Fig. 2.4d), grains started to elongate along the rolling direction, while a high amount of twins is formed. The grain size appears not to have been modified significantly.

When the 0.4Ag alloy is considered (Fig. 2.4e-h), the microstructure is different. In the CRA state (Fig. 2.4e), it can be seen that grains are much finer than in the case of the 0Ag alloy. Silver-rich second phase particles appear as bright spots, elongated along the rolling direction. Moreover, some grains contain a small fraction of mechanical twins, indicating that Ag influences the recrystallization of the alloy. When deformed to a small extent (CR10, Fig. 2.4f), as in the case of the 0Ag alloy, some twins are present inside the grains. The shape and size of the Ag-rich particles has not been modified. However, the grains are of comparable size with respect to the annealed state, which is similar to the case of the 0Ag alloy. Increasing the amount of thickness reduction up to 25% (CR25, Fig. 2.4g), a great number of twins is visible inside the grains. Moreover, some shorter plates are visible inside some grains. Such plates can be associated to the ε-martensite detected from XRD measurements. Finally, as in the case of 0Ag, grains start to elongate along the rolling direction in the CR50 condition.

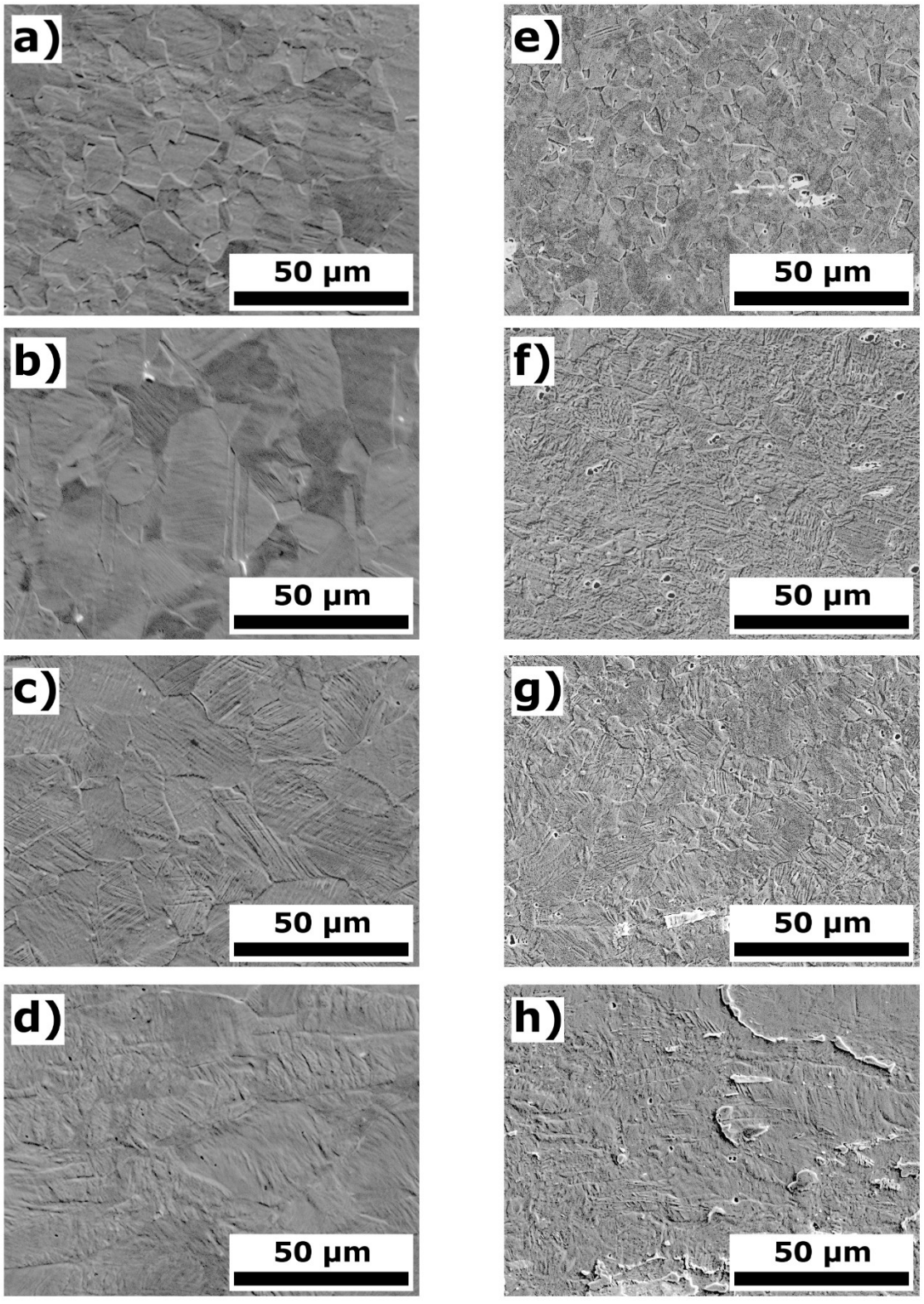

Figure 2.4 SEM micrographs from the 0Ag (a-d) and 0.4Ag (e-h) alloys after cold rolling: a) 0Ag, CRA; b) 0Ag, CR10; c) 0Ag, CR25; d) 0Ag, CR50; e) 0.4Ag, CRA; f) 0.4Ag, CR10; g) 0.4Ag, CR25; h) 0.4Ag, CR50.

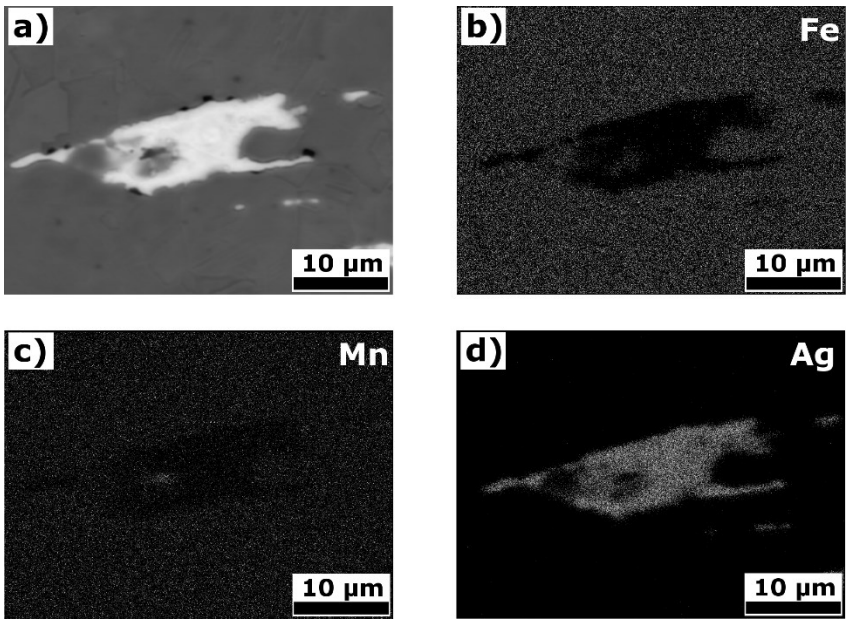

Figure 2.5 WDS elemental mapping of an Ag-rich particle: a) back-scattered electron image; b) Fe mapping; c) Mn mapping; d) Ag mapping.

The WDS elemental mapping of an Ag particle in the annealed state is visible in Figure 2.5. From the maps, it can be clearly seen that no Fe is present inside the particle. Moreover, no Ag appears to be dispersed inside the Fe-Mn-C matrix. While Ag is the predominant element, some Mn is also present. Looking at the Ag-Mn phase diagram [192], it can be seen that the solubility limit of Mn in Ag is of 28% wt., indicating that the secondary phase observed in the 0.4Ag alloy can be associated to the (Ag) FCC phase. No precise identification of the phase could be done by XRD measurements because the volume fraction was too low.

3.5.4.1 Electron backscattered diffraction (EBSD)

The orientation image maps (OIM) and inverse pole figures (IPF) along the normal direction obtained from EBSD analyses of the 0Ag alloy are visible in Figure 2.6, together with the section of the orientation distribution functions (ODF) at $\varphi_2 = 45°$. In the annealed state (Fig. 2.6a), the OIM shows that the grain shape is equiaxed, without twins being visible inside the grains. Moreover, different orientation components are present. Examining the inverse pole figure (Fig. 2.6d), the predominant orientations are (101), (212), (312), (211) and (311), while other orientations are present with a smaller incidence. If one looks at the orientation distribution function (Fig. 2.6g), the material shows a predominant Brass texture component (type {110}<112>). When the material is cold rolled at 10% (Fig. 2.6b), the grain shape and orientation components are modified. Looking at the IPF (Fig. 2.6e), the texture is clearly

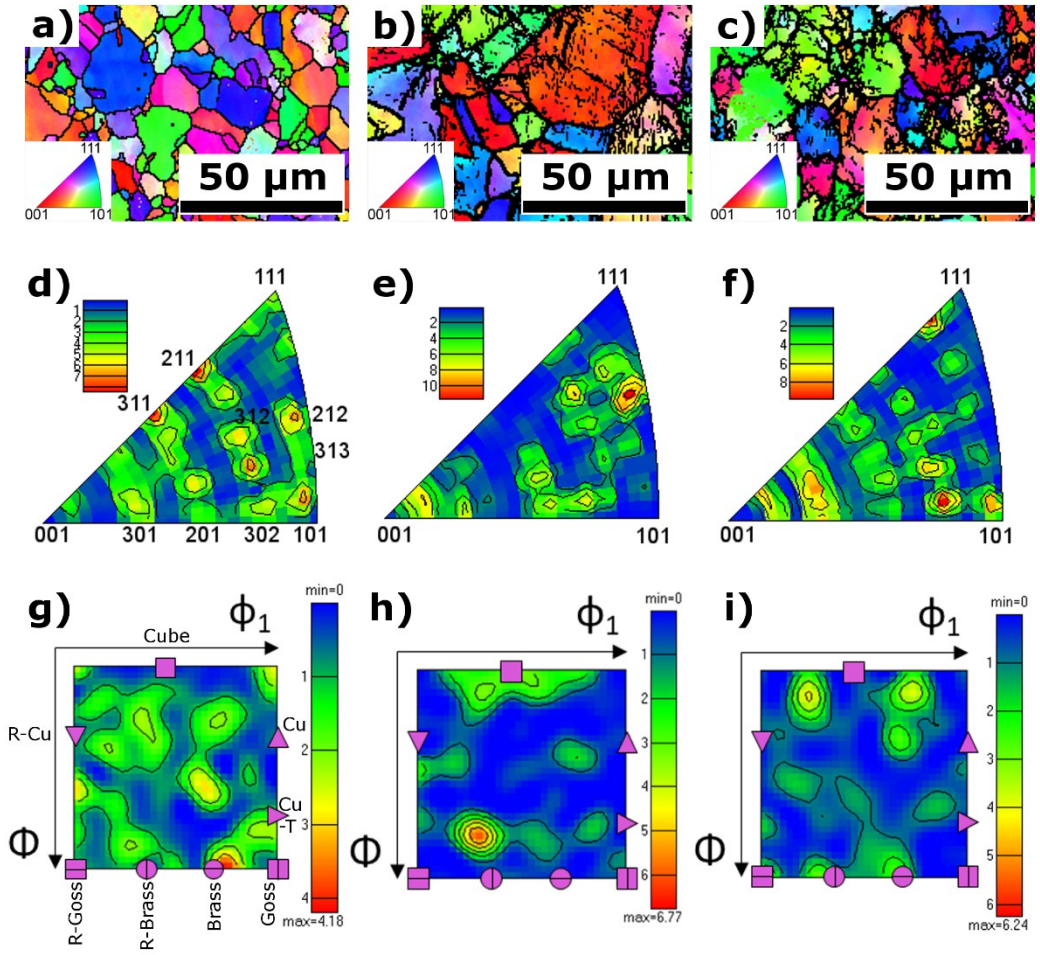

Figure 2.6 EBSD results for the 0Ag alloy after cold rolling. a) orientation image map along the normal direction (OIM-z), CRA; b) OIM-z, CR10; c) OIM-z, CR25; d) inverse pole figure along the normal direction (IPF-z), CRA; e) IPF-z, CR10; f) IPF-z, CR25; g) orientation distribution function (ODF) at ϕ_2 = 45°, CRA; h) ODF at ϕ_2 = 45°, CR10; i) ODF at ϕ_2 = 45°, CR25. The legend for the ideal orientations in the ODFs is defined in Figure 6g. Figure 6d shows the entirety of the orientations that can be observed by an IPF. The color scales in figures 6d-f) describe the relative intensity of each detected orientation. The color scales in figures 6g-i) defines the intensity of each ideal orientation. The maximum intensity for each ODF is reported.

different than in the annealed case. The predominant orientations are (212) and (312), while also the (001) orientation is present. The (111) component, which was observed in the annealed state, now appears to be absent. From the ODF (Fig. 2.6h), the predominant texture component is Rotated Brass (type {110}<111>), while a minor Cube component (type {001}<100>) is also present. The intensity of the R-Brass component is much higher than that of the Brass component observed after annealing. Increasing the deformation to 25% (CR25, Fig. 2.6c), the observed orientations change again. According to the IPF (Fig. 2.6f), the (111) and the (302) orientations are the predominant ones, while the (001) and (301) orientations are also present.

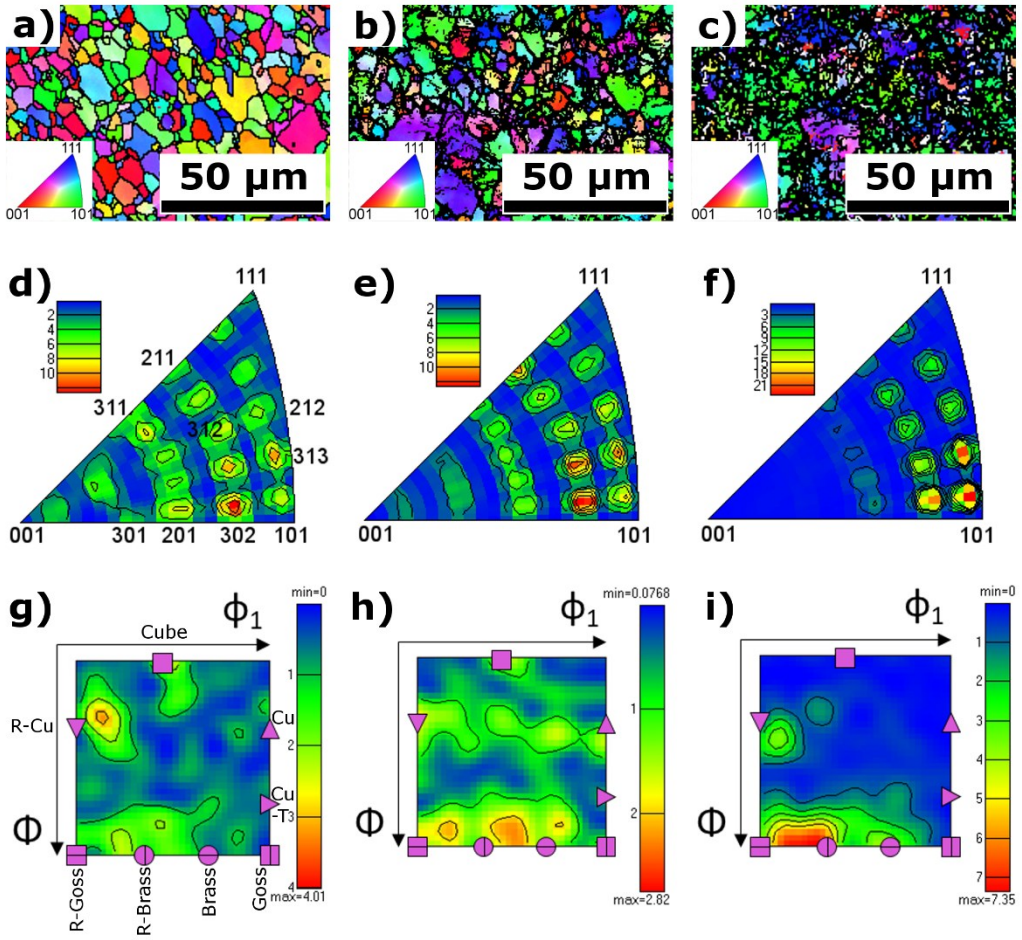

Figure 2.7 EBSD results for the 0.4Ag alloy after cold rolling. a) OIM-z, CRA; b) OIM-z, CR10; c) OIM-z, CR25; d) IPF-z, CRA; e) IPF-z, CR10; f) IPF-z, CR25; g) ODF at ϕ_2 = 45°, CRA; h) ODF at ϕ_2 = 45°, CR10; i) ODF at ϕ_2 = 45°, CR25. The legend for the ideal orientations in the ODFs is defined in Figure 7g. Figure 7d shows the entirety of the orientations that can be observed by an IPF. The color scales in figures 7d-f) describe the relative intensity of each detected orientation. The color scales in figures 7g-i) defines the intensity of each ideal orientation. The maximum intensity for each ODF is reported.

From the ODF (Fig. 2.6i), the texture is now predominantly Cube, while the Rotated Brass and Brass components are also present, albeit with a lower intensity. Overall, the component intensities for the CR25 are lower than in the case of the CR10 material, indicating that the material is less textured.

The EBSD results along the normal direction for the 0.4Ag alloy, together with the ODF section at φ_2 = 45°, are visible in Figure 2.7. In the annealed condition (Fig. 2.7a), grains have a smaller size if compared to the 0Ag CRA condition (Fig. 2.6a). From the IPF (Fig. 2.7d), several orientations are observed. The predominant orientations are (302) and (313). The (211) and (311)

components are much less intense than in the case of the 0Ag alloy. From the ODF (Fig. 2.7g), the Rotated Copper component (type {112}<110>) is the predominant one, while the Cube, Rotated Brass and Copper (type {111}<110>) components are also present. The relative intensity is however fairly low, indicating that the material has a weak texture after annealing. Imposing a thickness reduction of 10% (Fig. 2.7b), no increase in grain size is observed. From the IPF (Fig. 2.7e), the same texture components as in the case of the annealed material are observed. Furthermore, the (211) orientation also appears. From the ODF (Fig. 2.7h), the Brass and rotated Brass textures are observed with low intensity, while also the Rotated Copper, Copper and Cube components are also present. This implies that the material remains weakly textured after a limited plastic deformation. For the CR25 condition (Fig. 2.7c), no clear conclusions can be drawn on the grain size and shape due to the poor pattern indexing, as described in section 2.3. It appears that the (101) and (313) orientation are the predominant ones (Fig. 2.7f), giving rise to clear material texturing. From the ODF (Fig. 2.7i), the material appears strongly textured around the Rotated Brass component, while the Brass and Rotated Copper components were also observed with low intensity.

2.5.5 Transmission electron microscopy (TEM)

The effect of the Ag presence on the inner structure of the alloys was investigated by using TEM techniques. In particular, Figure 2.8 shows a typical bright field image of the 0.4Ag sample in CRA condition (Fig. 2.8a) and the corresponding selected area electron diffraction (SAED) pattern (Fig. 2.8b). Two large twins are clearly visible in the image and the study of the SAED pattern has allowed to determine that twins forms on the {111} planes of the face centred cubic (FCC) austenitic phase. Indeed, the most intense diffraction spots of Figure 2.8b can be associated to the austenitic γ phase in [110] zone axis (blue cell). Because of the twinning on (1-11) plane, the γ cell is rotated 180° about [1-11] direction giving rise to the green cell. Some other feeble diffraction spots are visible in the image and can be attributed to the presence of the orthorhombic $(Fe,Mn)_3C$ phase in [123] zone axis (red cell) [193]. Dark field TEM images obtained selecting these feeble diffraction spots (see inset Fig. 2.8a), have revealed that the $(Fe,Mn)_3C$ phase is present as nanometric precipitates distributed inside the austenitic γ phase. All the other extra diffraction spots are due to double diffraction phenomena. In order to investigate the effect of the deformation on the microstructure, TEM observations were also performed on the 0.4Ag sample in the CR25 condition. Analyses have revealed the presence of

only the FCC austenitic phase and an increase in the number of twins and nanotwins always formed on the {111} planes of the austenitic γ phase. Differently from X-ray measurements, TEM observations did not reveal the presence of the martensitic ε phase. Considering the local nature of the technique (only small portion of the sample can be analysed by TEM), this result suggests a probable non-homogeneous distribution of the ε phase.

TEM observations carried out on the 0Ag sample in CRA condition, have showed neither the presence of twins nor the presence of $(Fe,Mn)_3C$ precipitates, as shown in figures 2.9a and 2.9b. Only samples submitted to a large deformation have revealed features comparable with the 0.4Ag sample in CRA condition. In particular, a typical TEM bright field image of the sample 0Ag in CR25 condition and the corresponding SAED pattern are shown in Figure 2.9c and 2.9d, respectively. A large number of nanotwins formed on crossed $\{111\}_\gamma$ planes is clearly visible. The diffraction pattern shows spots revealing the presence of the face centred cubic austenitic phase in [110] zone axis (blue cell), of nanotwins on $(1\text{-}11)_\gamma$ plane (green cell) and of the orthorhombic $(Fe,Mn)_3C$ phase in [123] zone axis (red cell), in complete agreement with the diffraction pattern of Figure 2.8b concerning the 0.4Ag sample in CRA condition. The only difference is due to the presence of diffraction streaks in the $[1\text{-}11]_\gamma$ direction due to the nanometric thickness of the twins present in this sample with respect the larger ones in the other sample.

2.6 Discussion

2.6.1 The influence of silver on mechanical properties

2.6.1.1 Reduction of ductility

As it can be observed in Figure 2.1, the presence of Ag decreases the ductility of the material, while the increase in strength is statistically insignificant. Moreover, from TEM analyses (Figures 2.8 and 2.9), it was observed that the 0.4Ag alloy in the annealed state still has a number of twins. As commonly found for TWIP steels [194,195], these mechanical twins are formed on the austenitic γ{111} planes. The presence of twins from the annealed state acts as a barrier to dislocation motion during plastic deformation [196]. Moreover, the progressive increase in twin density creates a higher number of barriers to dislocation motion (Dynamic Hall-Petch effect) at lower strains.

In addition to this, a fine network of $(Fe,Mn)_3C$ carbides is present in the 0.4Ag CRA

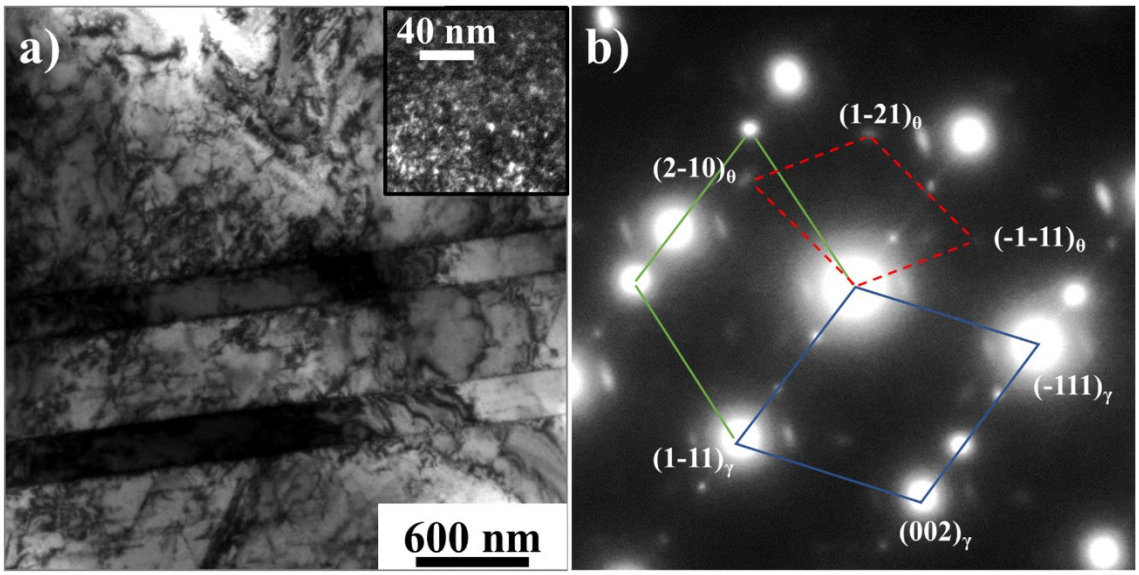

Figure 2.8 Sample 0.4Ag in CRA condition: a) TEM bright field image showing large twins; b) corresponding selected area diffraction pattern. The blue cell identifies the austenite γ phase in [110] zone axis; the twinning on (1-11)γ plane gives rise to the green cell; the red cell is due to the orthorhombic (Fe,Mn)3C phase in [123] zone axis. The inset is a magnified dark field image of the sample obtained selecting the (1-21)θ diffraction spot.

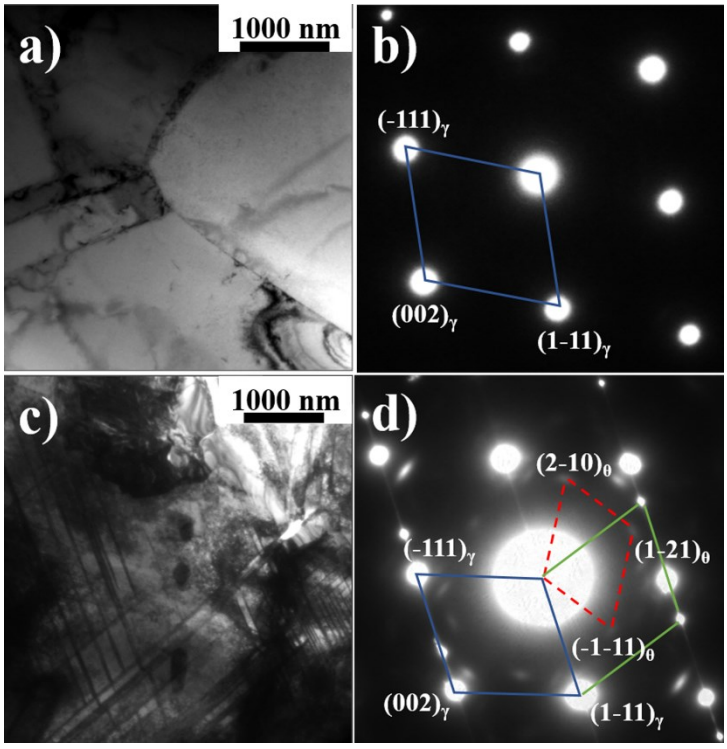

Figure 2.9 Sample 0Ag in CRA and CR25 conditions: a) TEM bright field image showing the austenitic grains; b) selected area diffraction pattern showing the presence of austenite; c) TEM bright field image showing nanotwins on crossed {111}γ planes; d) corresponding selected area diffraction pattern. The blue cell identifies the austenite γ phase in [110] zone axis; the green cell is due to twinning on (1-11)γ plane; the red cell can be associated to the orthorhombic (Fe,Mn)3C phase in [123] zone axis.

sample. The sample without silver (0Ag CRA) showed neither twins nor carbides. It can thus be inferred that the presence of Ag promotes the formation of carbides during annealing. Furthermore, carbon atoms are known to be the cause for the serrated plastic flow (or DSA) observed in TWIP steels [67]. The presence of carbides from the annealed state in the 0.4Ag alloy may indicate that the solid solution is saturated in C due to the Mn that migrated into solid solution with Ag (Fig. 2.8). This saturation in C can in turn lead to the presence of broader C atmospheres, causing earlier onset of DSA.

On the other hand, the earlier onset of the dynamic Hall-Petch effect can cause a faster increase in dislocation density. This provokes a progressive reduction in the mean free path of dislocations, thus possibly resulting in failure at lower strains [66,197]. In addition to this, it was observed that mechanical twins were thicker in the case of the 0.4Ag alloy than for the 0Ag one. Moreover, the presence of ε at high strain levels prevents more effectively planar slip, since this HCP phase has a lower number of slip systems with respect to the FCC matrix. The combination of these observations can explain why the alloy with Ag has a significantly lower elongation to failure than the 0Ag alloy.

2.6.1.2 Dynamic strain aging

Concerning the different DSA behavior, as stated in section 2.1, the onset of DSA is moved to lower strains for the 0.4Ag alloy. In addition to this, it can be observed from Figure 2.1 that DSA evolves in a different fashion for the two alloys. For the 0.4Ag alloy, pure type A serrations are the only observed DSA family, until the material fails. Looking at the stress-strain curve, type A serrations consist in a sudden increase in stress, followed by a sharp drop, for then resuming the regular stress-strain flow [9]. In the 0Ag alloy, type A serrations are visible up to ε = 45%. Above this threshold, type B serrations are present until failure. These serrations consist in quick and repeated oscillations around the average level of the stress-strain curve [9]. Type B serrations were already observed for a Fe-22Mn-0.6C steel tested at the same strain rate used in this work, although the onset for this behavior was at strains below 5 % [198]. Moreover, no type A serrations were observed in the Fe-22Mn-0.6C steel. The presence of type A serrations can be ascribed to the low SFE typical of TWIP steels, which limits the effectiveness of dislocation glide, as predicted by different models on SFE [8,199,200]. Because of the lower dislocation mean free path of the 0.4Ag alloy, together with the higher number of twins and the

formation of ε-martensite at high deformation, it can be supposed that type B serrations cannot be formed in the 0.4Ag alloy at high strain levels.

If compared with other alloying elements added to Fe-Mn-C TWIP steels, it can be seen that the addition of Ag does not suppress the phenomenon of dynamic strain aging, unlike in the case of Fe-Mn-C-Al alloys [66]. Moreover, the promotion of twinning at lower deformation levels is opposite to what has been reported in the case of addition with Cu [201] and N [202].

2.6.2 Deformation texture

EBSD results showed that the predominant texture components in the 0Ag alloy are as follows (CRA → CR10 → CR25): Brass → Rotated Brass → Cube. This texture variation in the alloy without Ag aligns with the typical behavior of TWIP steels, where the material shows a texture also in the recrystallized state [66]. The texture components are also those normally observed during deformation and recrystallization of TWIP steel [67].

Nonetheless, the predominant texture components in the 0.4Ag alloy are different (CRA → CR10 → CR25): Rotated Copper → Brass → Rotated Brass. The rotated Copper texture component is not among those normally observed in recrystallized Fe-Mn-C TWIP steels [67], but was already observed in a Fe-Mn-Al-Si-Ni steel [203]. The explanation for the recrystallized Rotated Copper texture may lie in the different recrystallization behavior induced by the presence of Ag. In fact, TEM analyses showed the presence of twins for the 0.4Ag in the annealed state inside the {111} grains. It is argued that the presence of twins prevents the occurrence of multiple planar slip in the early stages of deformation [66,204]. This causes the activation of the sole {111}<110> slip system, which is responsible for the presence of the Copper texture. This may also justify the persistence of the Copper and rotated Copper components upon deformation, although with reduced intensity. On the other hand, the absence of twins in the 0Ag alloy promotes multiple slip, which can explain the preferential development of the Brass texture upon deformation. Further works are needed to investigate in detail the role of Ag in the recrystallization behavior of TWIP steels.

2.6.3 Twin and ε-martensite formation

As observed from XRD results (Fig. 2.3), the only phase detectable in the 0Ag alloy is austenite. On the other hand, for the 0.4Ag alloy, ε-martensite appeared starting from the CR25 deformation condition.

SEM analyses showed the formation of mechanical twins in both alloys, although the onset for their formation is different. In the 0.4Ag alloy, twins are already present in the annealed state in a small fraction. In the 0Ag alloy, they start to form in the CR10 condition. TEM analyses showed that twins are formed on {111} planes of both alloys. In the case of the 0Ag alloy in the CR25 condition (Fig. 2.9), TEM analyses showed only nanometric twins in the form of intersected lamellae. Instead, for the 0Ag alloy in the annealed condition (Fig. 2.8), also thick twins were observed.

ε-martensite, on the other hand, was formed only in the 0.4Ag alloy with a thickness reduction by cold rolling of at least 25%. If one looks at the texture evolution during deformation, this can be ascribed to the different components observed for the two alloys. It is known that the Copper and S texture components are favorable for developing ε-martensite, while the Brass and Goss components promote mechanical twinning [205]. Moreover, mechanical ε-martensite generates from mechanical twins on {111} planes [195]. Since the 0.4Ag alloy shows twins after annealing, they may serve as preferential nucleation sites during deformation. In addition to this, the 0.4Ag alloy has a Rotated Copper texture component present during the whole deformation process, together with a weak Copper component, which can explain why mechanical martensite is present only when Ag is added to the alloy. The absence of ε-martensite can indeed be ascribed to the predominant Brass texture observed after annealing and during deformation, together with the absence of the Rotated Copper and Copper texture components.

Although no ε martensite was observed by TEM analyses, it may be hypothesized that ε-martensite developed at high levels of deformation on preferential {111} planes embedding macroscopic Ag-rich particles. This can be ascribed to the important difference in lattice parameter between the Fe-Mn-C matrix and the Ag-rich second phases, which can give rise to stress concentration phenomena around the Ag-rich particles, thus locally favoring the appearance of ε-martensite at high deformation levels. This can be justified by literature data, showing that the lattice parameter for a Fe-22Mn-0.6C was estimated at 3.61 Å, while it was estimated at 3.60 Å for a Fe-13Mn-0.6C [206]. On the other hand, the lattice parameter of Ag-Mn intermetallic compounds ranges from 4.086 Å for pure Ag to 4.040 Å for a $Ag_{60}Mn_{40}$ compound [207,208].

2.6.4 Biodegradation behavior assessment

This work did not assess the effect of Ag on the degradation behavior of the studied TWIP steel nor its influence on biological performances. However, it is recognized that the addition of Ag increases the degradation rate of Fe-based alloys [74,152]. Moreover, the biological safety of pure Fe and Fe-Mn alloys for cardiovascular applications was already reported in animal studies [60,138,184]. Furthermore, twinning-induced plasticity steels were shown not to be toxic against vascular cells *in vitro* [209], thus supporting the potential of such materials for use in degradable vascular implants.

2.7 Conclusions

This study investigated the effect that the addition of Ag has on the deformation mechanism of a TWIP steel. It was shown that the presence of silver decreases the ductility of the alloy, which can be attributed to the presence of twins from the annealed state, reducing the dislocation mean free path. A further reason for the decreased ductility is the development of mechanical ε-martensite during deformation, which was not observed in the 0Ag alloy. ε-martensite developed starting from a thickness reduction of 25%. In addition to this, the modified DSA behavior observed for the 0.4Ag alloy can be ascribed to the presence of nano-sized carbides from the annealed state.

It can be supposed that martensite developed from specific twinning sites on γ{111} planes containing Ag-rich second phases, which are already present in the 0.4Ag alloy after annealing. A further reason for the development of martensite lies in the different deformation texture of the two alloys. The 0.4Ag alloy showed Copper-type texture components after annealing and during deformation, which are known to be favorable for the development of martensite versus mechanical twins.

In view of applying this Fe-Mn-C-Ag alloy for cardiovascular stents, the mechanical properties far exceed the minimum recommended thresholds for strength and ductility. The understanding of the evolution of mechanical properties is fundamental to develop and optimize the extrusion and drawing processes necessary for manufacturing advanced stents. Furthermore, the knowledge about the phases that form during plastic deformation improves the ability to tune the corrosion behavior during service life.

2.8 Acknowledgements

The authors would like to thank Nathalie Moisan from Laval University for assistance with metallographic analyses, together with Bernard Tougas and Jean-Nicolas Rousseau from CMQ for assistance with EBSD and WDS analyses. This work was funded by the Natural Science and Engineering Research Council of Canada under the CU-I2I program. Financial and technical support from AMEC Usinage, Plasmionique Inc., Umano Medical Inc. and Metalliage Inc. is also recognized. S. L. acknowledges funding from a Vanier Canada Graduate Scholarship. D. M. was supported by NSERC-Canada and holds a Canada Research Chair Tier I.

3. Effect of silver in thermal treatments of Fe-Mn-C degradable metals: Implications for stent processing

Sergio Loffredo[a,b], Sofia Gambaro[a,c], Carlo Paternoster[a], Nicolas Giguère[d], Maurizio Vedani[b], Diego Mantovani[a,*]

a: Laboratory for Biomaterials and Bioengineering, Canada Research Chair I in Biomaterials and Bioengineering for the Innovation in Surgery, Department of Min-Met-Materials Engineering, Research Center of CHU de Quebec, Division of Regenerative Medicine, Laval University, Quebec City, QC G1V 0A6, Canada

b: Department of Mechanical Engineering, Politecnico di Milano, Milan 20156, Italy

c: National Research Council, Institute of Condensed Matter Chemistry and Technologies for Energy (CNR-ICMATE), Genoa 16149, Italy

d: Quebec Metallurgy Center (CMQ), Trois-Rivières, QC G9A 5E1, Canada

Keywords

Twinning; Recrystallization; Biomaterials; Silver; Steels

Publication status

Submitted to Bioactive Materials, October 2020

3.1 Résumé

Les aciers à plasticité induite par maclage (TWIP) ont des propriétés mécaniques excellentes pour des stents dégradables. L'ajout d'Ag peut donner une dégradation appropriée. Afin de développer un procédé de production optimisé il faut élucider l'effet de l'Ag sur le mécanisme de recristallisation des aciers TWIP. Dans ce travail, le mécanisme de recristallisation de deux aciers Fe-Mn-C avec et sans argent a été investigué. L'Ag a promu une microstructure plus fine avec une différente évolution de la texture, quand la cinétique de recristallisation a été inaffectée. De plus, la présence d'Ag a réduit l'efficacité du traitement de recristallisation, ce qui a été attribué à la présence de phases secondaires riches en Ag et à la formation préférentielle de grains {111} après traitement thermique. Cela peut donner lieu à un maclage prématurée, ce qui explique le rôle de l'Ag dans la réduction de ductilité des aciers TWIP.

3.2 Abstract

Twinning-induced plasticity (TWIP) steels are considered excellent materials for manufacturing products requiring extremely high mechanical properties for various applications including thin medical devices, such as biodegradable intravascular stents. It is also proven that the addition of Ag, a known antibacterial element, can guarantee an appropriate degradation while implanted in human body without affecting its bioactive properties. In order to develop an optimized manufacturing process for thin stents, the effect of Ag on the recrystallization behavior of TWIP steels needs to be elucidated. This is of major importance, since manufacturing stents involves several intermediate recrystallization annealing treatments. In this work, the recrystallization mechanism of two Fe-Mn-C steels with and without Ag was thoroughly investigated by microstructural and mechanical analyses. It was observed that Ag promoted a finer microstructure with a different texture evolution, while the recrystallization kinetics resulted unaffected. The presence of Ag also reduced the effectiveness of the recrystallization treatment. This behavior was attributed to the presence of Ag-rich second phase particles and to the preferential development of grains possessing a {111} orientation upon thermal treatment. The prominence of {111} grains can also give rise to premature twinning, explaining the role of Ag in reducing the ductility of TWIP steels already observed in other works. These findings will allow the design of efficient treatments for supporting the transformation of Fe-Mn-C steels alloyed with Ag into commercial products.

3.3 Introduction

Biomaterials for medical devices have saved or improved the life and its quality for millions of patients around the globe in the last decades. Biodegradable metals are a new class of metallic biomaterials that open new horizons for revolutionising advanced surgical treatments. For example, metallic biodegradable stents, temporary devices used to restore blood flow in obstructed vessels [1], are expected to dissolve into the body after 1 to 2 years from their implantation [2]. The first commercial vascular device was based on a Mg – rare earth element alloy, and was approved by the European regulatory agency in 2016 [3]. While this stent meets the requirements in terms of resorption in the human body and biological performances [4–6], its low mechanical properties limit device miniaturization and, as a consequence, its deliverability in smaller vessels [7,8]. To fill this gap and satisfy cerebral and pediatrics needs, the development of biodegradable alloys suitable to produce reduced strut thickness devices is urgently required.

Twinning-induced plasticity (TWIP) steels, mainly composed of Fe, Mn and C, represent candidates of choice to manufacture small stents. This alloy family possesses equivalent mechanical properties to Co-Cr alloys [9,10] and their high amount of Mn stabilizes austenite at room temperature [11], whose paramagnetic behavior favors post-implantation imaging [2]. At the same time, the degradation behavior of such steels is inappropriate in the long-term: several in vitro and in vivo studies found that a stable corrosion layer is formed during the first weeks of implantation, reducing corrosion rate [12–14]. The addition of Ag to TWIP steels showed the ability to accelerate the short-term corrosion of these alloys [15–17]. In addition, the choice of Ag is of great interest because of its antibacterial properties [18]; furthermore, it was proven that Ag does not reduce the mechanical properties of TWIP steels below acceptable values [19,20].

In order for TWIP steels to be used as biodegradable stents, the material must be processed in the final shape through high plastic deformation processes, most commonly hot extrusion followed by cold drawing [21]. A recrystallization annealing treatment is normally performed after each drawing pass to restore the mechanical properties of the material. Successively, laser cutting and acid pickling are performed to obtain a stent from the drawn tubes and, after most of these steps, a further recrystallization annealing is again conducted. Finally, electropolishing is carried out to give the stent the final surface roughness, adequate for implantation.

It can thus be seen that recrystallization annealing treatments represent a critical step in manufacturing biodegradable stents. In fact, recrystallization of TWIP steels is in general a fast process, leading to nucleation of twin-free grains that grow over time [11,22]. When elements capable of forming second phases are added to TWIP steels, they impact significantly their recrystallization mechanism, as demonstrated in the case of V or Pd [23,24]. Ag is also known to form second phases in TWIP steels [19,20], potentially affecting their recrystallization behavior. This can have strong consequences for processing of small products like stents, including the need to adjust thermal treatments to ensure that the final product can be manufactured with the appropriate dimensional, microstructural and mechanical specifications. This work aims at understanding the impact of Ag on the recrystallization mechanism of a Fe-Mn-C TWIP steel, and to assess its implications on plastic deformation processes. The recrystallization behavior of two biodegradable steels (one with and one without Ag) as a function of treatment temperature and time was assessed in terms of microhardness, microstructure and texture evolution. The steels produced during the work were cast and cold rolled in order to simulate the production process of a stent with a simplified laboratory setup.

3.4 Materials and Methods

3.4.1 Material preparation and processing

Two alloys, with nominal composition Fe-16Mn-0.7C (wt. %) and Fe-16Mn-0.7C-0.4Ag (wt. %) and named 0Ag and 0.4Ag, respectively, were produced and processed as described elsewhere [210]. After hot rolling the cast billets at 800°C from a size of 12.5 mm down to plates of thickness 1.33 mm, thin sheets of both alloys were cold rolled imposing a 25% thickness reduction. This condition constituted the starting point for recrystallization annealing treatments.

Coupons of 10 mm x 10 mm x 1 mm were cut from cold rolled sheets in order to understand the recrystallization behavior as a function of the annealing temperature. Each coupon underwent a thermal treatment of 10 minutes in a resistance furnace operating in air (Lenton AWF 13/25, UK) and a subsequent water quenching to freeze the microstructure and precisely stop the treatment time. The selected temperatures varied from 500°C to 950°C with a step of 50°C.

In order to evaluate the effect of the annealing time on the recrystallization behavior, other coupons of both alloys underwent thermal treatments at 700, 800 and 900°C for 2, 5, 10, 15, 20, 30, 60 minutes, and subsequently water quenched.

3.4.2 Characterization

Before performing any analysis, all samples were mechanically polished with SiC abrasive papers up to 600 grit. Successively, fine polishing was performed with diamond paste of 3 μm and 1 μm. Final polishing was carried out with a 0.05 μm colloidal alumina suspension.

The recrystallization curve was built by means of Vickers microhardness tests, using a load of 500 gf and a dwell time of 15 s on each sample (FM-810, Future-Tech Corp., Japan). The phases present in each alloy as a function of the recrystallization treatment were evaluated by X-ray diffraction (XRD, SmartLab, Rigaku, Japan). XRD analyses were performed at a scanning rate of 3°/min in the range of 20 – 100° (stepsize 0.020°), using Cu K_α radiation (λ = 1.5406 Å) at 40 kV and 40 mA with a Bragg-Brentano geometry. Peak identification was performed using the SmartLab Studio II software (Rigaku, Japan).

The microstructure of both alloys as a function of the thermal treatment was evaluated by scanning electron microscopy (SEM), using a field emission gun SEM (FEG-SEM, Sigma 500, Zeiss, Germany). Prior to observation, samples were chemically etched with the Picral reagent (4 g picric acid in 100 mL ethanol). The composition of second phases was evaluated by energy dispersion x-ray spectroscopy (EDS, Ultim Max, Oxford Instruments, UK). Electron backscattered diffraction (EBSD, C-Nano, Oxford Instruments, UK) was performed to assess the grain orientations and the evolution of texture components present inside the materials, before and after annealing at 800°C for 10 minutes. For EBSD analyses, in addition to the previously described polishing procedure, samples were polished with colloidal silica (0.05 μm) for 20 minutes and rinsed with deionized water for 10 minutes in order to avoid any surface contamination. The obtained data were analyzed with the Channel5 software (Oxford Instruments, UK). The indexing rate for the analyzed conditions was of at least 82% for the deformed samples and of at least 97% for the annealed samples.

Finally, in order to validate the phases that precipitated during the various thermal treatments, a thermodynamic simulation of the amount of phases present at equilibrium as a function of temperature was carried out using the Thermocalc software using the TCFE9

database. However, since Ag is not available in the database, the calculation was carried out only for the 0Ag alloy.

3.4.3 Statistical analyses

All data are reported with standard deviation errors, with the exception of the recrystallized fraction components in figures 3.8 and 3.10. In figure 3.1, the error bars represent the uppermost and lowermost deviations from the average of each point. In order to estimate the statistical significance of differences in Vickers microhardness values, one-way ANOVA tests with Tukey's post-hoc analysis was carried out using the Minitab18 software (Minitab Inc., USA). The differences were considered statistically significant if $p < 0.05$ at least.

3.5 Results

3.5.1 Vickers microhardness

The results obtained from Vickers microhardness tests are reported in figure 3.1. The microhardness curve as a function of temperature for thermal treatments of 10 minutes (fig. 1a) showed that no sharp drop of hardness occurred for temperatures below 600°C, suggesting that no recrystallization takes place in this temperature range. Partial recrystallization occurred at 600°C, as inferable from the drop in hardness, while full recrystallization appeared to be achieved for temperatures exceeding 650°C, as visible from the lower hardness plateau. Fig. 3.1a also suggests that the two investigated alloys feature a substantially similar recrystallization behaviour. The only difference lies in the lower plateau for the 0.4Ag alloy which is at higher microhardness values than the 0Ag alloy for almost all temperatures.

Looking at the evolution of microhardness as a function of time for the 0Ag alloy (fig. 3.1b), it could be seen that the treatment time had no effect in changing the alloy microhardness. This was attributed to the very fast recrystallization kinetics of TWIP steels, as already observed by other authors [132,211]. After 2 minutes of treatment, the microhardness values were comparable to those obtained after 10 minutes at all temperatures. A similar effect was detected for the 0.4Ag alloy (fig. 3.1c). Furthermore, a marked increase in microhardness was detected when keeping the sample at 900°C for at least 30 minutes.

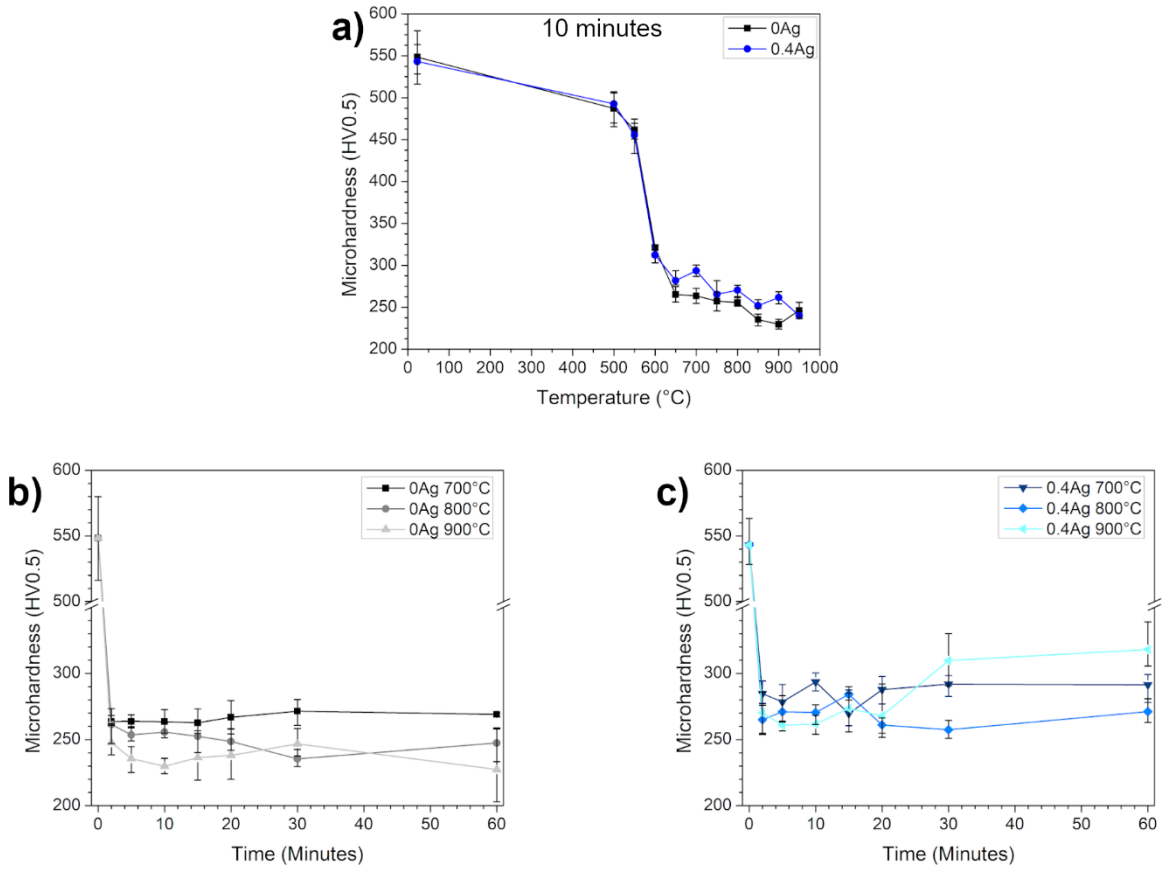

Figure 3.1 Evolution of Vickers microhardness as a function of the thermal treatment parameters for the 0Ag and 0.4Ag alloys: a) 0Ag and 0.4Ag after 10 minutes as a function of temperature; b) 0Ag at 700°C, 800°C and 900°C as a function of time; c) 0.4Ag at 700°C, 800°C and 900°C as a function of time.

3.5.2 Scanning electron microscopy

The microstructure of the 0Ag alloy after the 10 minutes thermal treatments can be observed in figure 3.2. After cold rolling (fig. 3.2a), all grains presented significant twinning; moreover, their size and shape was relatively homogeneous. After a thermal treatment at 500°C (fig. 3.2b), it could be seen that the grains still presented significant twinning, indicating that no recrystallization had taken place. In addition, some bright second phases appeared at grain boundary; they were also visible when the alloy was treated at 600°C (fig. 3.2c). Even if the material was still largely composed of unrecrystallized grains showing significant twinning, some recrystallized grains started to appear as small nuclei. After the treatment at 700°C, almost all grains underwent recrystallization, as a very limited number of twins was still visible (fig. 3.2d), and the second phases, segregated at grain boundaries after the treatment at 600°C, had almost disappeared. Their full disappearance occurred after the treatment at 800°C (fig. 3.2e). In this case, the grains also showed no mechanical twins coming from the unrecrystallized state. Finally,

after a treatment at 900°C (fig. 3.2f), it could be seen that regions subjected to local plastic deformation were present inside the grains, possibly because of the severity of the quenching process.

The microstructural evolution of the 0.4Ag alloy as a function of the treatment temperature is detailed in figure 3.3. After cold rolling, and prior to any thermal treatment, all grains showed twinning (fig. 3.3a) and Ag-rich particles (whose composition was assessed elsewhere [210]) were aligned along the rolling direction. After the thermal treatment at 500°C for 10 min, it could be seen that the grain structure was relatively unchanged, with twins still present inside the material (fig. 3.3b). As in the case of the 0Ag alloy, second phase particles precipitated along grain boundaries in a flake-like structure, composed by small needles radiating from the center of the particle, as visible in the higher magnification inset of figure 3.3b. After the treatment at 600°C, recrystallized grains started to appear (fig. 3.3c), as it happened for 0Ag alloy. Contrarily, unrecrystallized grains were still present, embedding twins at their interior, and the amount of second phase particles was reduced with respect to the case of the treatment at 500°C. Moreover, the big Ag-rich particles retained the same shape and distribution from the unrecrystallized state. Increasing the treatment temperature up to 700°C, the second phase particles visible at 500°C (fig. 3.3b) almost disappeared (fig. 3.3d). However, it could be seen that the grain size was inhomogeneous inside the material, with some grains still presenting mechanical twins. The reduced grains dimension of 0.4Ag compared to that of 0Ag alloy, both treated at the same temperature, could explain the higher hardness value measured for the 0.4Ag alloy. After the treatment at 800°C, no precipitates were observed and twins were still present inside some grains (fig. 3.3e), indicating that recrystallization was not completely achieved, contrarily to the case of the 0Ag alloy. Finally, after the treatment at 900°C, the microstructure resembled closely the one observed in the case of the 0Ag alloy (fig. 3.3f).

The nature of the second phase particles of the 0.4Ag alloy in both the as deformed state (CR25) and after a 500°C treatment (10 minutes) was studied by EDS element mapping (fig. 3.4). In the CR25 state (fig. 3.4a-e) just one type of second phase was detected: Ag-rich particles containing traces of Fe and Mn.

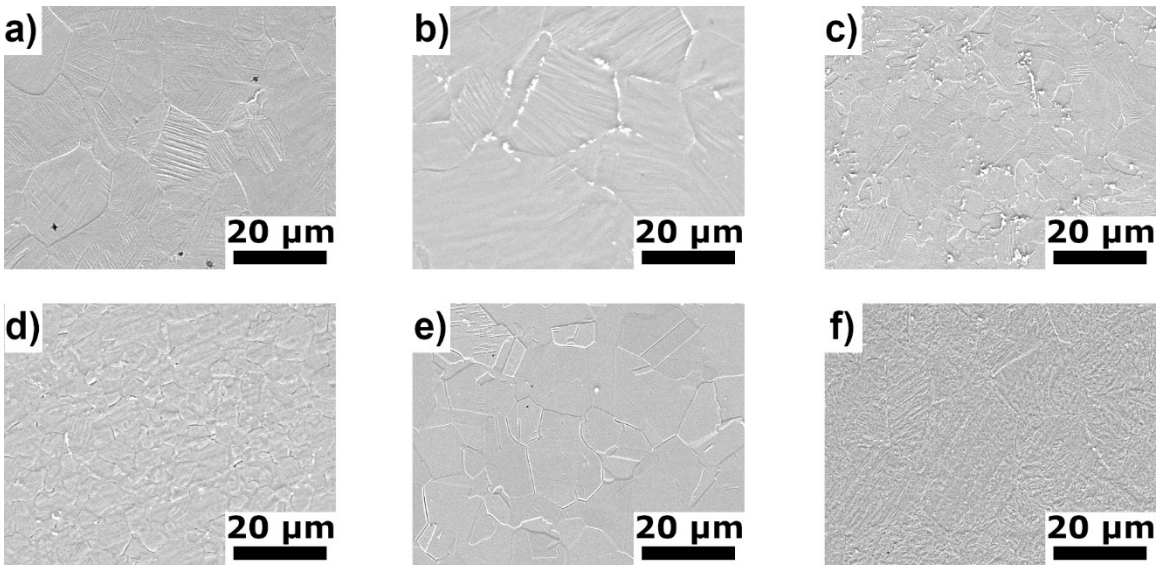

Figure 3.2 SEM micrographs detailing the microstructural evolution of the 0Ag alloy as a function of the recrystallization temperature after a 10-minute treatment: a) deformed; b) 500°C; c) 600°C; d) 700°C; e) 800°C; f) 900°C.

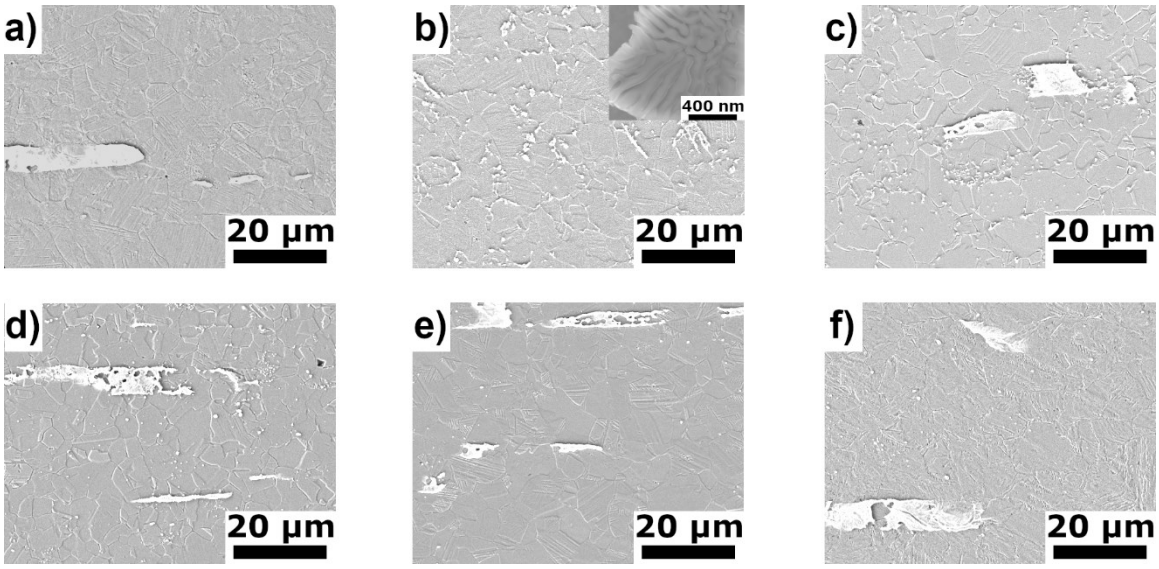

Figure 3.3 SEM micrographs detailing the microstructural evolution of the 0.4Ag alloy as a function of the recrystallization temperature after a 10 minute treatment: a) deformed; b) 500°C; c) 600°C; d) 700°C; e) 800°C; f) 900°C.

After the 0.4Ag alloy underwent the thermal treatment at 500°C (fig. 3.4f-j), two families of second phase particles were observed, also visible in the microstructure of figure 3.3b, where Ag-rich particles and precipitates appeared segregated at grain boundaries. The Ag-rich particles had a similar composition to that observed prior to thermal treatments (fig. 3.4a-e). The precipitates at grain boundaries appeared to be depleted in Mn and Ag, while they were rich in

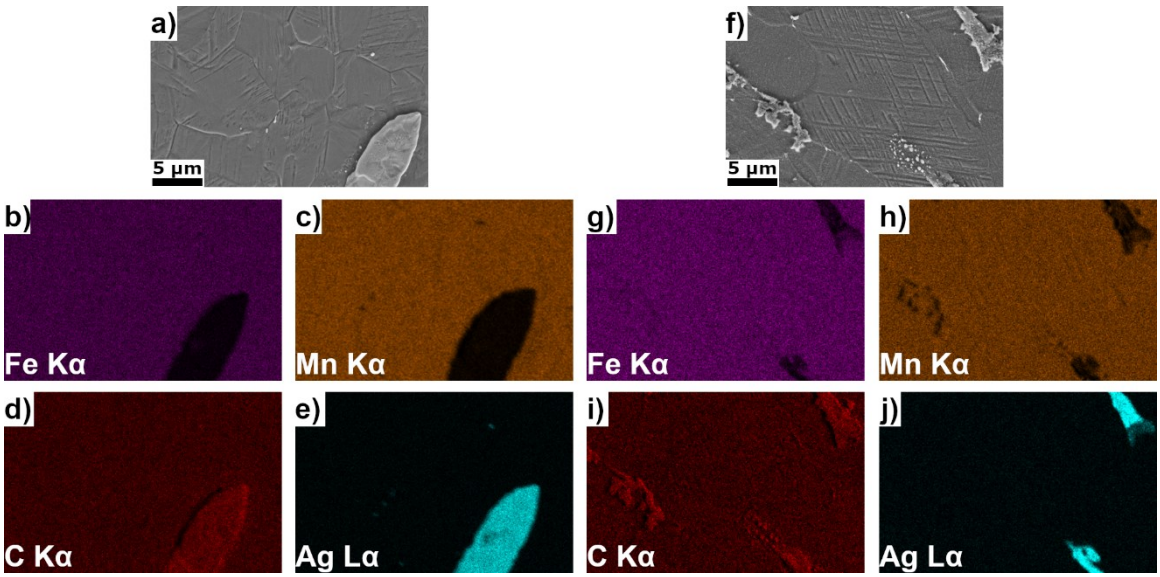

Figure 3.4 EDS elemental mapping of 0.4Ag alloy in the unrecrystallized state, when a-e) cold rolled (CR25) and f-j) treated at 500°C (500).

Fe and C: this could indicate the precipitation of iron carbides at low temperatures, which was not observed for treatments above 700°C.

3.5.3 X-Ray Diffraction

The measured spectra from XRD analyses as a function of the treatment temperature for both alloys can be found in figure 3.5. It could be seen that the only detected phase for the 0Ag alloys was austenite (γ), independently from the applied thermal treatment (fig. 3.5a). In addition, when the alloy containing Ag was considered (fig. 3.5b), a weak peak associated with the (111) plane of the face-centered cubic Ag phase also appeared in some conditions, depending on the local quantity of the phase. The Ag phase could be associated to the Ag-rich particles visible in figs. 3.2-4. No peaks associated to ε-martensite were detected, contrarily to a previous work [210], where ε-martensite was detected in the cold rolled condition. This could be due to a locally low amount of ε-martensite in the analyzed material, lower than the detection limit of the diffractometer.

3.5.4 Thermodynamic modelling

The phases formed in the 0Ag alloy as a function of temperature at equilibrium are plotted in figure 3.6. It can be observed that already starting from 745°C, Fe_3C-type carbides (cementite) that then evolve into $M_{23}C_6$ at lower temperature are formed. Under strict equilibrium

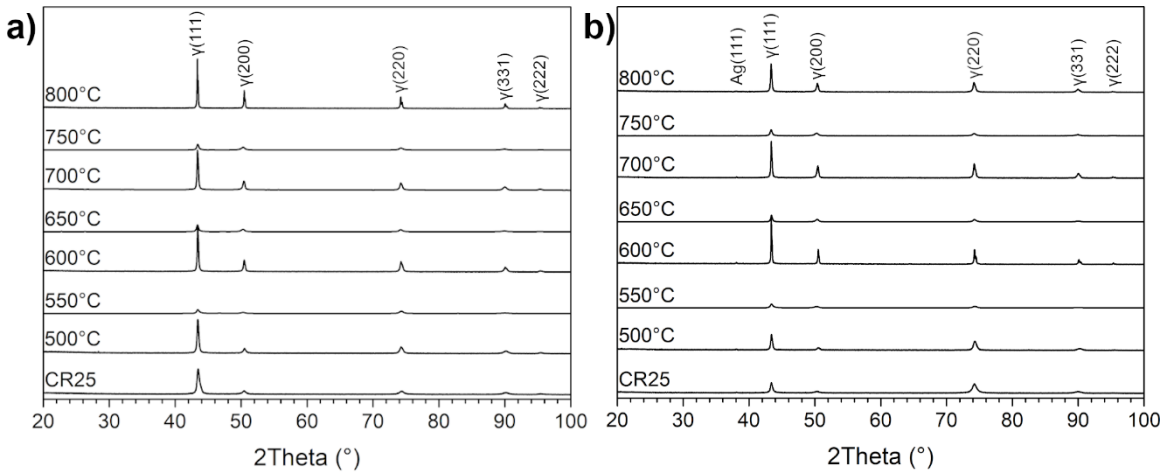

Figure 3.5 XRD spectra of a) 0Ag and b) 0.4Ag alloys after different recrystallization treatments for 10 minutes.

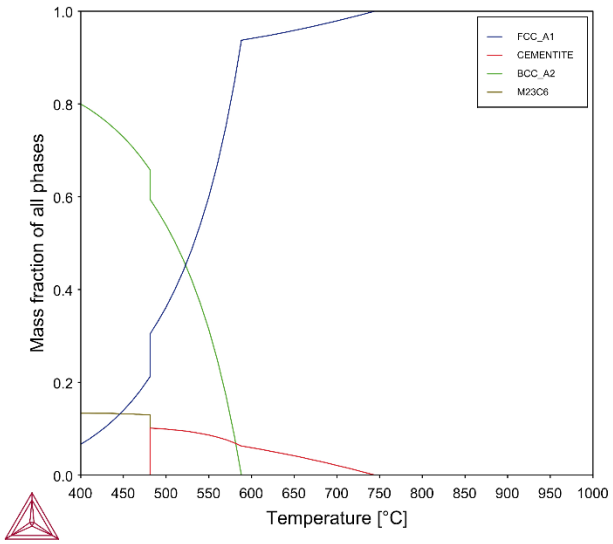

Figure 3.6 Thermodynamic simulation of the phases present in the 0Ag alloy as a function of temperature.

conditions, γ-Fe would progressively transform almost completely into α-Fe. This is apparently inconsistent with XRD and microstructural analyses indicating γ-austenite as the main matrix constituent. However, it can be considered that the investigated samples were analyzed after annealing at a fixed temperature and quenching. The rapid cooling tends to suppress the low-temperature transformation, preserving larger amounts of the structure created during the annealing holding period. Furthermore, the γ-Fe to α-Fe transformation in high Mn steels is believed to be quite sluggish due to the action of Mn and C as γ-stabilizers [67]. The Thermo-Calc simulation additionally allows to confirm that the tiny precipitates found at austenite grain boundaries can supposedly be carbides, either Fe_3C or more generally of $M_{23}C_6$ type.

3.5.5 Electron backscattered diffraction

3.5.5.1 Ag-free alloy

Figure 3.7 reports the orientation image maps (OIM) in the normal direction, inverse pole figure (IPF) in the normal direction and orientation distribution function (ODF) at $\varphi_2 = 45°$ for the 0Ag alloy before and after the treatment at 800°C for 10 minutes. After cold rolling, it could be seen that both deformation bands and mechanical twins were present inside the grains (fig. 3.7a), whose size was not uniformly distributed. The observed orientations were evenly spread, as visible from figure 3.7b, where no clear texturing of the material is observed, as the maximum mean uniform deviation (MUD) of the strongest orientation component {101} was equal to 1.75. On the contrary, when looking at the ODF (fig. 3.7c), it could be seen that the Rotated Goss {110}<110> texture component was the most present one. The Brass {110}<112> component was also present with a reduced intensity. The development of the Brass and Goss texture components upon deformation was commonly observed for TWIP steels [66,67], and it was an indication of twinning during plastic deformation.

After annealing at 800°C for 10 minutes (figure 3.7d), no mechanical twins nor deformation bands were detected within the grains. The annealing at 800°C did not change the orientations distribution, as confirmed by the inverse pole figure (fig. 3.7e), showing no prevalent orientation and a maximum MUD of 1.94 along directions other than the normal one. Contrarily to the case of the deformed alloy, the most predominant texture component after annealing was the F component {111}<112> along the γ fiber at $\Phi = 55°$. The Rotated Goss component was also very present, as in the case of the deformed material.

The evolution of the recrystallized fraction and of the Schmid factor distribution in the 0Ag alloy before and after the annealing treatment at 800°C for 10 minutes is visible in figure 3.8. The Channel5 software recognized a grain as deformed when the internal average misorientation angle θ within the grain exceeded 15° (value defined by default). A grain was classed as substructured if $\theta < 15°$ but the misorientation between detected subgrains was above 15°. All remaining grains were classified as recrystallized. From figures 3.8a-c, it could be seen that the material was almost entirely composed of unrecrystallized grains after cold rolling (either deformed or substructured), as one would expect. Similarly, the annealing treatment proved effective in recrystallizing the grains, with a recrystallized fraction above 93%. Moreover, it appeared from figures 3.8d-f) that the distribution of the Schmid factors in the analyzed regions

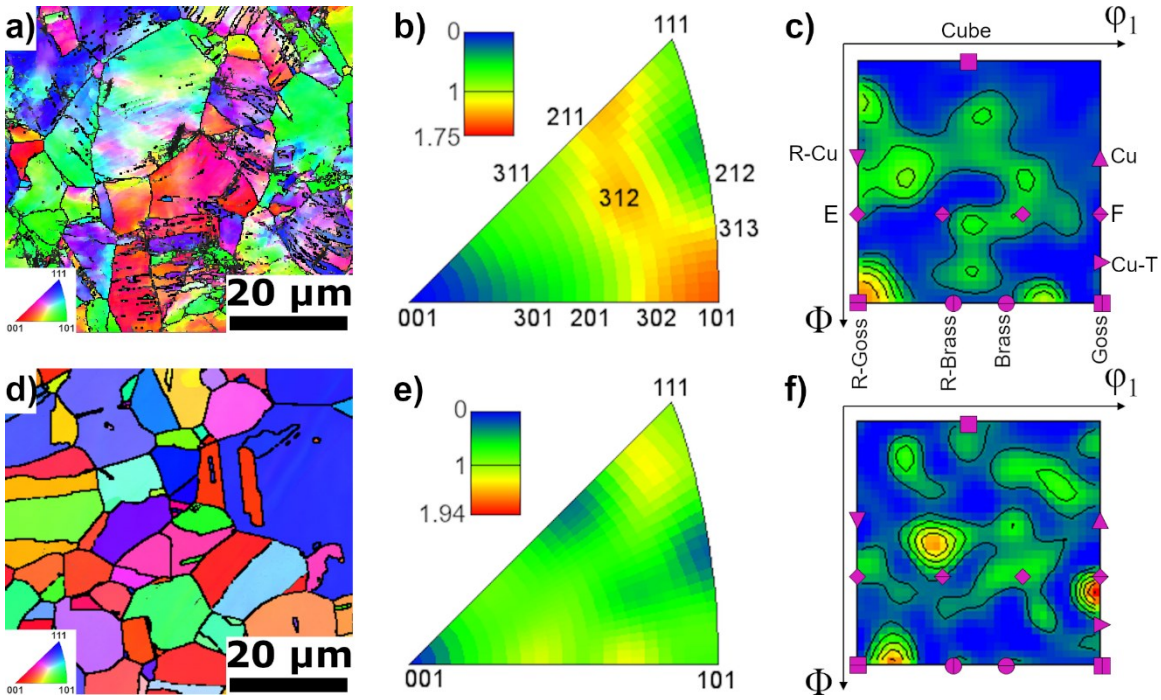

Figure 3.7 EBSD maps (along the normal direction) of the 0Ag alloy in both cold rolled (CR25) and treated (800°C;10 min) (800) states. Orientation image map (CR25: a); 800:d)); inverse pole figure (IPF) (CR25:b); 800:e)); orientation distribution function (ODF) at φ_2 = 45° (CR25:c); 800:f). The map of orientations in the IPFs is described in figure 6b. The relative intensity of each orientation is represented by the color scale, detailed in the histogram in figures b,e) . The map of the ideal texture components for ODFs is detailed in figure 6c).

was not significantly affected by the recrystallization process. In addition to this, the vast majority of grains showed a Schmid factor above 0.4, indicating that no premature twinning occurred upon deformation of the recrystallized material [212].

3.5.5.2 Ag containing alloy

Figure 3.9 shows the OIM, IPF and ODF at φ_2 = 45° along the normal direction for the 0.4Ag, before and after an annealing treatment at 800°C for 10 minutes. Before thermal treatment, several orientations were present inside the material (fig. 3.9a). Moreover, the grains appeared slightly elongated towards the rolling direction. The absence of a preferential crystalline orientation was confirmed by the IPF (fig. 3.9b), where the most present component, the {111} planes, had a MUD below 2. On the other hand, the ODF showed that several texture components were present inside the material: the most evident was the Brass {110}<112> one, together with an intermediate texture position between the Copper components and the γ fiber.

After the annealing treatment, it could be seen that, also in this case, several orientations were present inside the material. Moreover, the grains appeared to be more equiaxed than in the

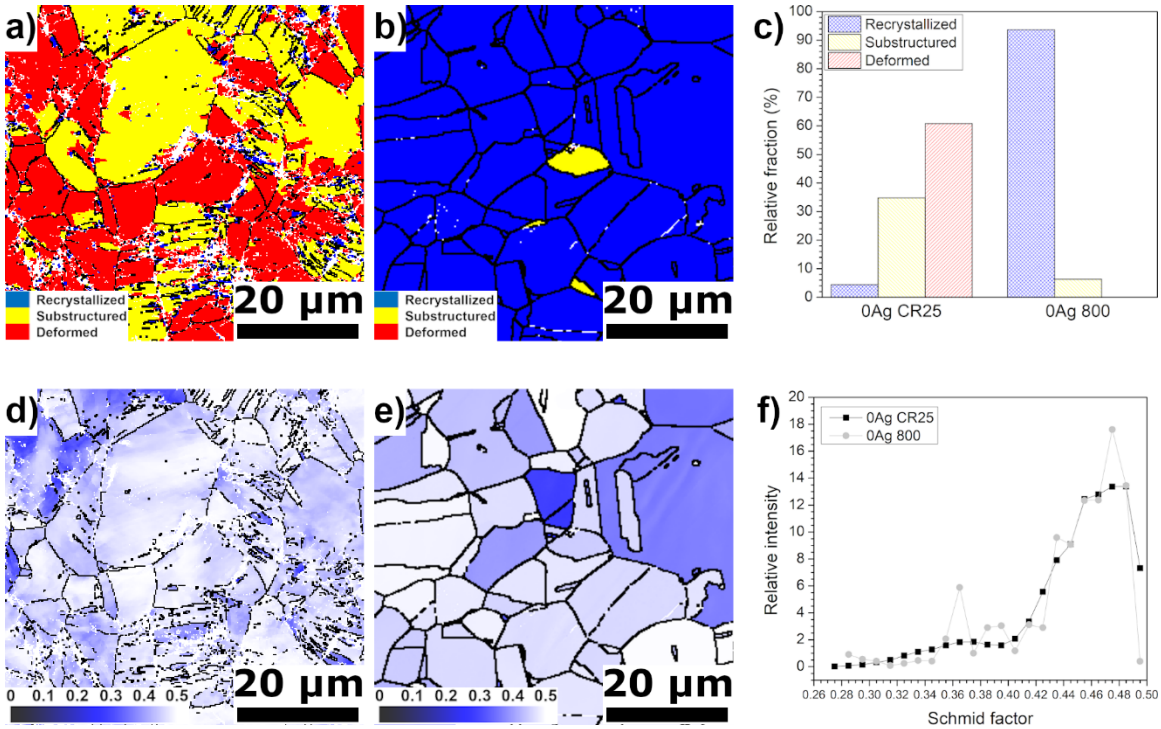

Figure 3.8 EBSD data of 0Ag alloy in both cold rolled (CR25) and treated (800°C; 10 min) (800) states along the normal direction. Recrystallized fraction map (CR25:a); 800:b)) comparison of the recrystallized fractions in CR25 and 800 states c); Schmid factor map (CR25:d); 800:e); comparison of Schmid factors intensities in CR25 and 800 states.

deformed state (fig. 3.9d). The absence of a preferential orientation was once again confirmed by the IPF (fig. 3.9e), where the MUD for the most present {111} orientation was of 1.53. The ODF (fig. 3.9f) highlights that several texture components developed during annealing, replacing the Brass component observed after cold rolling. The two main texture components were the Cube {001}<110> and the F {111}<112> ones associated to the γ fiber, together with the Copper {112}<111> and Rotated Copper {112}<110> ones. It can thus be inferred that the recrystallization mechanism was affected by the presence of Ag.

The evolution of the recrystallized fraction and of the Schmid factor distribution in the 0.4Ag alloy before and after the annealing treatment at 800°C for 10 minutes is visible in figure 3.10. Before the thermal treatment, it could be seen that around 70% of the indexed grains $\theta > 15°$ (fig. 3.10a, c), while the rest were indexed as substructured and, to a smaller extent, recrystallized. After the annealing treatment, contrarily to the case of the 0Ag alloy, less than 20% of the grains was classed as recrystallized. Over 80% of the grains were indexed as substructured grains, indicating that most of the material had not undergone full recrystallization. Looking at the Schmid factor maps and distribution (fig. 3.10d-f), it could be seen that the

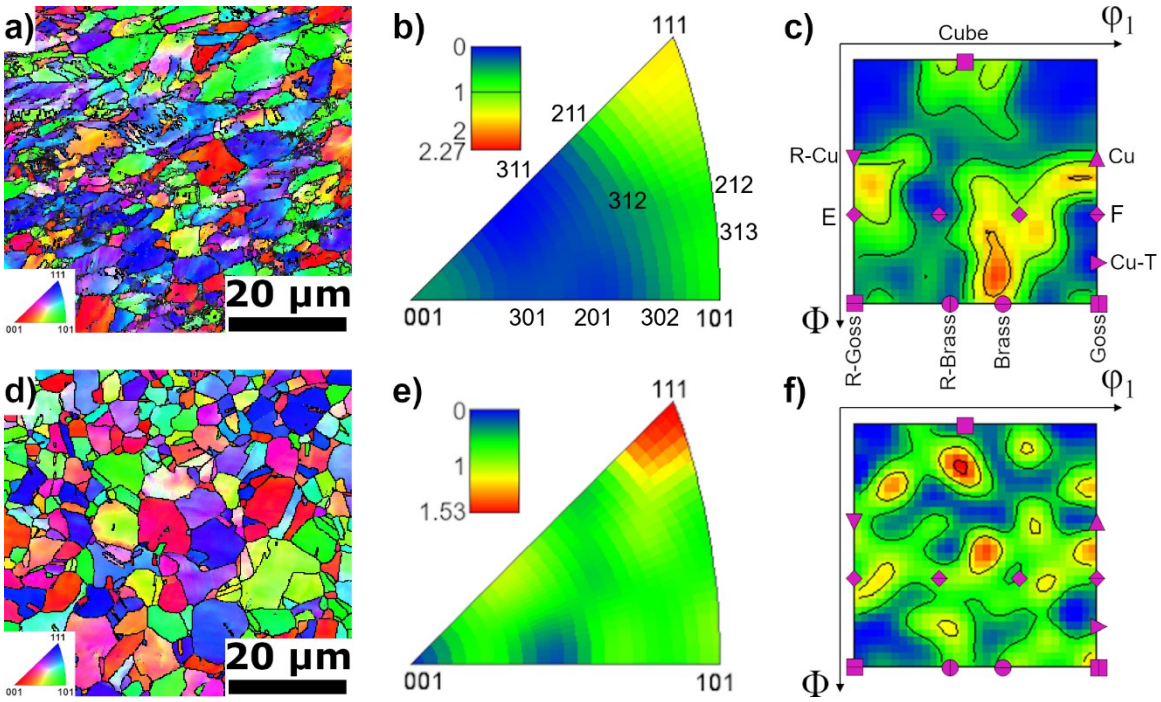

Figure 3.9 EBSD maps of 0.4Ag in both cold rolled (CR25) and treated (800°C; 10 min) (800) states along the normal direction. OIM (CR25:a); 800:d)); IPF (CR25:b); 800: e)); ODF at φ_2 = 45° (CR25: c); 800: f)).

annealing treatment reduced the amount of grains having a Schmid factor lower than 0.4, while providing more grains with a Schmid factor higher than 0.4. Contrarily, the distribution of Schmid factor in the grains was broader than in the 0Ag alloy.

3.6 Discussion

It was observed that the addition of 0.4 wt. %. of Ag influenced the microstructure of a Fe-16Mn-0.7C TWIP steel after recrystallization annealing. The microstructural evolution of the two alloys was found significantly different. Nevertheless, the overall recrystallization kinetics was globally unaffected, since the microhardness evolution was very similar for both the alloys.

3.6.1 Recrystallization kinetics

The Vickers microhardness evolution (fig. 3.1) showed that the overall recrystallization kinetics was not affected by the presence of Ag. On the other hand, the recrystallized plateau was at higher values for the 0.4Ag alloy, demonstrating that Ag-rich particles did not play a role on the kinetics, as also shown by the evolution over time. This finding contrasts with other works, which showed that the addition of soluble elements to a Fe-Mn-C matrix altered the recrystallization kinetics [94,213].

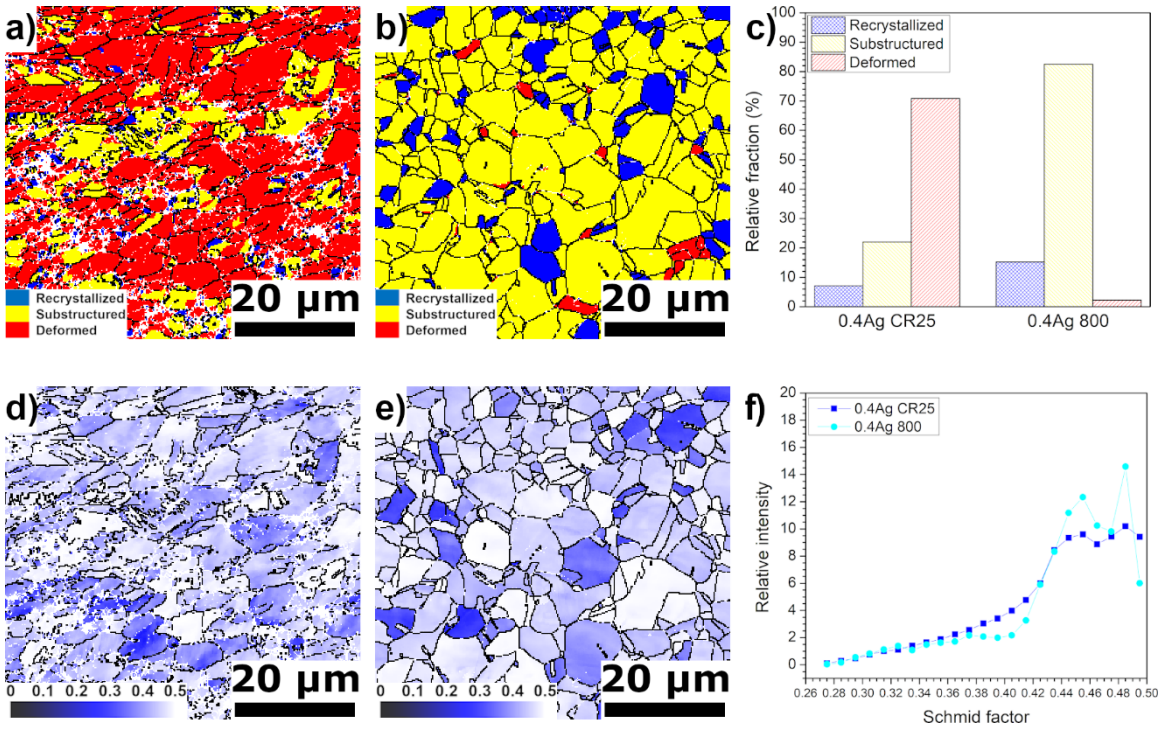

Figure 3.10 EBSD data of 0.4Ag alloy in both cold rolled (CR25) and treated (800°C; 10 min) (800) states along the normal direction. Recrystallized fraction map (CR25: a); 800: b)); comparison of the recrystallized fractions in the CR25 and 800 states c); Schmid factor map (CR25: d); 800: e)) comparison of the Schmid factors intensities in CR25 and 800 states f).

Another important phenomenon to be considered and analyzed was the evolution of grain size and twinning as a function of the applied thermal treatments. It could be observed that the 0Ag alloy had a bigger grain size before and after annealing with respect to the Ag-containing alloy, as one could also notice from figures 4.7 and 4.9. This phenomenon could be reconducted to the presence of the Ag-rich particles in transgranular positions, since they could hamper grain formation during thermal treatments. Such behavior was already observed by other authors in a Fe-Mn-C-Pd system [94], where Pd-rich particles precipitated inside grain boundaries and limited new grain nucleation and growth during annealing. This may also explain why the recrystallized fraction for the 0.4Ag alloy (fig. 3.10c) was significantly lower after annealing than the one observed for the 0Ag alloy considering the same condition (fig. 3.8c).

An additional factor that played a role in reducing grain size of the 0.4Ag alloy after annealing was the precipitation of second phase particles, observed at low temperatures (fig. 3.2-4). These precipitates appeared rich in Fe and C, and their stoichiometry can be reconducted to carbides (either Fe_3C or $M_{23}C_6$), as determined by thermodynamic simulation (fig. 3.6). It is known that segregation of second phases at grain boundaries could obstacle the recrystallization

process. Such precipitates appeared in higher amount for the 0.4Ag alloy heated between 500 and 700°C. The precipitation of second phase particles was already observed by other authors in the case of prolonged thermal treatments on Fe-Mn-C alloys above 700°C [26, 29], limiting grain growth. On the contrary, the reason why such precipitates were preponderantly present when Ag was added is still unknown and requires further thermodynamic investigations, to understand their formation kinetics and the role of Ag in favoring this phenomenon.

3.6.2 Texture evolution

It is clearly visible from figures 3.7 and 3.9 that the two alloys show some differences in preferential orientations and texture evolutions during annealing. The texture components in the 0Ag alloy changed during annealing at 800°C according to the following evolution (CR25 → 800): (Rotated Goss + Brass) → (Rotated Goss + F). On the other hand, the 0.4Ag alloy showed the following texture evolution (CR25 → 800): (Brass + mixed Copper/γ fiber) → (Cube + Copper + γ fiber). In both cases, the Brass fiber was present in the deformed condition, which was typical of TWIP steels [66,67]. Moreover, as already observed by other authors, the texture evolution was relatively stable during the annealing process [211,214]. The presence of the Goss-type components is also typical of TWIP steels [214,215].

A noteworthy feature was the development of the γ-fiber during recrystallization in both alloys, which was already observed in an annealed state for a Fe-Mn-Al-Si TWIP steel [216]. On the contrary, the γ-fiber was also observed for heavily deformed TWIP steels by other authors [212,215,217]. In those cases, the development of the γ-fiber was related with the formation of shear bands at high levels of deformation, and they were considered preferential sites for recrystallization. In this work, no shear banding was detected in the cold rolled state (fig. 3.2a and 3.3a), while only mechanical twinning was observed. At the same time, a preferential {111} orientation was developed after recrystallization (fig. 7 and 9), which could explain the development of the γ-fiber during the recrystallization process.

Another phenomenon that could be related with the development of the γ-fiber during recrystallization was the retainment of grains possessing a Schmid factor below 0.4 (fig. 3.8 and 3.10). This occurrence was preponderant in the 0.4Ag alloy: comparing figure 3.9a,d and figure 3.10d,e, it is clear that the grains with a lower Schmid factor were those possessing a {111} orientation, while the grains with a higher Schmid factor were those presenting a {101} orientation. The presence of grains with a low Schmid factor was associated with an earlier onset

of twinning during deformation by other authors [212]: this fact could definitively explain the role that Ag played in the ductility reduction of TWIP steels, as detected in previous works [73,210].

3.6.3 Impact of recrystallization annealing on processing

This work investigated the impact of Ag on recrystallization of a TWIP steel after cold rolling, which is a simplification of cold drawing, commonly used when manufacturing tubular precursors for stents [6]. Although the two processes differ in the distribution of applied forces generating plastic deformation [24], the impact of the second phases on recrystallization mechanism and microstructure are likely to affect the drawing processes required to thin the stent structure. It has been already reported that the presence of Ag impact the deformation mechanism of TWIP steels [210], and this has also be taken into account when designing thermal treatments. It was already demonstrated that tailoring recrystallization annealing treatments in TWIP steels can allow to finely tune grain size together with second phase size and shape, which in turn can alter processability and mechanical properties of final products [215,218,219]. Thermal treatments can also strongly impact texture evolution, which also affects the final microstructure and processability of TWIP steels into semi-finished products [215,220].

3.7 Conclusions

This work investigated the influence that Ag addition has on the recrystallization behavior of a Fe-16Mn-0.7C TWIP steel. The presence of Ag resulted in a harder material after recrystallization, due to a less effective recrystallization mechanism. Ag-rich second phase particles were identified as the cause for the lower efficacy of the annealing treatment, since they limited the growth of twin-free grains. In addition to this, the presence of Ag stimulated the development of more {111} grains upon recrystallization, which presented a lower Schmid factor and were more prone to twinning upon plastic deformation. This observation could also explain why the addition of Ag provided a reduction in ductility to TWIP steels, which could be detrimental to the deployment of a stent in a diseased artery. Post-process thermal treatments and the amount of Ag to be added to a Fe-Mn-C alloy for degradable stents should be carefully assessed in order to retain optimal processability characteristics, coupled with good corrosion behavior. Furthermore, in view of applying Fe-Mn-C-Ag steels for biodegradable stents, cytocompatibility and hemocompatibility should be thoroughly assessed. These findings will

contribute to the design of efficient treatments for supporting the transformation of TWIP steels alloyed with Ag into commercial products.

3.8 Acknowledgements

The authors would like to thank Marawan Abdelwahed, Ruben Beltrami, Maurizio Pardi and Ludovica Rovatti from Politecnico di Milano for assistance with XRD, SEM and EBSD analyses. The support of Jean-Nicolas Rousseau from Quebec Metallurgy Center for EBSD data analysis is also acknowledged. S. L. acknowledges funding from a Vanier Canada Graduate Scholarship (2017-2020). This work was partially supported by the Natural Science and Engineering Research Council of Canada (Discovery, Strategic, Collaborative Research and Development, and College-University-Industry Programs), the Quebec Ministry of Economy and Innovation, the Canadian Foundation for Innovation, and the FRQ-Santé through the support of the Research Center of the University Quebec Hospital, Regenerative Medicine Division.

4. Effect of silver on corrosion behavior of plastically deformed twinning-induced plasticity steel for biodegradable stents

Sergio Loffredo[a,b], Carlo Paternoster[a], Nicolas Giguère[c], Maurizio Vedani[b], Diego Mantovani[a,*]

a: Laboratory for Biomaterials and Bioengineering, Canada Research Chair I in Biomaterials and Bioengineering for the Innovation in Surgery, Department of Min-Met-Materials Engineering, Research Center of CHU de Quebec, Division of Regenerative Medicine, Laval University, Quebec City, QC G1V 0A6, Canada

b: Department of Mechanical Engineering, Politecnico di Milano, Milan 20156, Italy

c: Quebec Metallurgy Center (CMQ), Trois-Rivières, QC G9A 5E1, Canada

Publication status

Published in JOM **72**:5 (2020), 1892-1901. DOI: 10.1007/s11837-020-04111-w

4.1 Résumé

Les alliages de magnésium ont des propriétés mécaniques insuffisantes pour produire des stents aussi petits que ceux permanents. Les aciers à plasticité induite par maclage (TWIP), faits de Fe, Mn et C, ont un grand potentiel en termes de propriétés mécaniques, mais leur taux de corrosion est trop bas. L'ajout d'argent est très prometteur; cependant, l'effet de l'argent sur le mécanisme de corrosion, inclus à l'état déformé, reste méconnu. L'influence de l'argent sur le comportement à dégradation d'un acier TWIP a été étudié. L'argent n'a pas accéléré le taux de dégradation. En revanche, son ajout a promu une dégradation plus uniforme, ainsi indiquant le potentiel des aciers TWIP pour applications comme stents dégradables très minces.

4.2 Abstract

Magnesium-based alloys have insufficient mechanical properties to make stents as thin as permanent ones. Twinning-induced plasticity steels, made of Fe, Mn, and C, show significant potential in terms of mechanical properties, but their corrosion rate is too slow. Addition of silver shows promise in this sense; However, the corrosion mechanism promoted by addition of Ag remains unclear. Moreover, the effect of plastic deformation on the corrosion mechanism is still unknown for this system. The effect of silver on the degradation behavior of a deformed twinning-induced plasticity steel has been studied. It was observed that Ag did not accelerate the corrosion rate. On the other hand, its addition promoted more uniform degradation, thus indicating the potential of twinning-induced plasticity steels for application in very thin biodegradable stents.

4.3 Introduction

After the introduction of stenting in the late 1980s, followed by the use of drug-eluting stents, biodegradable metals have recently been considered the next revolution in the treatment of cardiovascular diseases [27]. Since 2016, a magnesium-based stent (Magmaris®, Biotronik) has been available on the European market [52] and has been shown to fully degrade in 12 months after implantation [51]. Moreover, it is biologically safe in human patients [53,221,222]. On the other hand, compared with state-of-the-art Co- Cr-based devices, Magmaris has a structure with significantly larger dimensions. The smallest available strut thickness for Magmaris is 150 μm, while a comparable product based on Co-Cr alloys possesses a strut thickness as low as 60 μm [5]. This large strut size and diameter limits the number of clinical indications and has the potential to induce long- term dysfunctions [5].

Twinning-induced plasticity (TWIP) steels, composed of Fe, Mn, and C, possess mechanical properties similar to those of Co-Cr alloys [10,94], making them ideal candidates for the manufacture of small stents. Several studies have already proven the in vitro and in vivo biological safety of TWIP steels [70,159,160]. Regarding the corrosion behavior of such alloys, it is known that they are sensitive to chloride corrosion [87]. Since chloride ions are abundant in human plasma [18], this implies that TWIP steels could undergo corrosion inside the human body. In the overall arterial environment, chloride ions are one of several factors contributing to the corrosion of TWIP steels; others include cyclic loading due to the systolic–diastolic cycle, other metallic ions, and adsorption of organic species, including proteins [25]. On the other hand, the formation of a stable layer of degradation products after some weeks of corrosion has been reported by several authors [12,90], preventing full degradation of the device in animal tests [70].

A strategy that can be employed to enhance the degradation rate of TWIP steels is addition of further alloying elements. These elements may have higher or lower electrochemical potential with respect to the matrix, thus forming a galvanic couple. The most common approach is to add an element that is more noble than the matrix and soluble in it, such as Pd [12]. Such an element was successful in increasing the short-term corrosion [12], but did not prevent stabilization of the corrosion layer of the material in the long term [70]. Other elements, such as Cu, showed promise in preventing the formation of stable passive films in the long term [223].

On the other hand, the efficiency of the galvanic couple for increasing the corrosion rate can be improved by adding insoluble elements to the alloy. Silver possesses a higher electrochemical potential with respect to both Fe and Mn, viz. + 0.800 V versus standard hydrogen electrode (SHE), compared with - 0.447 V versus SHE for pure Fe and - 1.185 V versus SHE for pure Mn [98]. Moreover, it is insoluble in both Fe and C, while it possesses limited solubility in Mn [145,192]. Several authors have found that addition of silver can enhance the in vitro degradation rate of pure iron [181], Fe-Mn alloys [191], and TWIP steels [74]. One of the main points missing from such evaluations of the corrosion behavior of TWIP steels is the effect of plastic deformation. It has already been observed that the degradation rate of Fe-Mn alloys is significantly higher when plastically deformed in comparison with the annealed state [135]. The aim of the work presented herein is to clarify the combined effect of silver and plastic deformation on the degradation behavior of a twinning-induced plasticity steel that shows excellent mechanical properties [210].

4.4 Materials and Methods

Two alloys, viz. Fe-16Mn-0.7C (FeMnC) and Fe-16Mn-0.7C-0.4Ag (FeMnCAg), were produced and processed as described elsewhere [210], being denoted 0Ag and 0.4Ag hereinafter. Four deformation states were produced after cold rolling and annealing: annealed (CRA), cold rolled with 10% thickness reduction (CR10), cold rolled with 25% thickness reduction (CR25), and cold rolled with 50% thick- ness reduction (CR50). In all cases, a final sheet thickness of 1 mm was obtained.

4.4.1 Static Immersion Tests

Coupons with dimensions of 20 mm x 10 mm x 1 mm were cut from the rolled sheets. A 2-mm- diameter hole was drilled in each sample to allow vertical positioning in static immersion tests. Prior to testing, the samples were mechanically ground with SiC papers up to 600 grit, followed by polishing with 3-μm and 1-μm diamond suspension. Final polishing was carried out using 0.05-μm alumina suspension. The samples were then immersed in anhydrous ethanol and cleaned ultrasonically for 10 min. Before testing, the samples were stored in a vacuum chamber to avoid any corrosion initiation. Five samples per each group were used, for a total of 40 samples.

Static immersion tests were carried out following the ASTM G31/12a standard [224]. Hanks' modified salt solution (HMSS) was chosen as the degradation medium, since it properly simulates the ionic composition of human plasma [18]. To prepare the solution, 9.5 g Hanks' balanced salts (H1387, Sigma- Aldrich, Canada) was dissolved in 1400 mL Nanopure water. Successively, 14.16g 4-(2-hydroxyethyl)-1-piperazineethanesulfonic acid (HEPES, H3375; Sigma-Aldrich, Canada), 16.65g of HEPES sodium salt (H7006, Sigma-Aldrich, Canada), and 3.30 g sodium bicarbonate (S8875, Sigma-Aldrich, Canada) were added to the mixture. The pH of the solution was then stabilized at 7.40 ± 0.05 by adding 1 M HCl solution.

All glassware was sterilized in an autoclave prior to the start of the test. Moreover, the samples were sterilized by immersion in 70% vol ethanol solution for 5 min, as described elsewhere [225]. The samples were then hung from the bottle cap by means of a polyamide fishing line and immersed in 92 mL HMSS poured into a 100-mL bottle. The bottles containing the samples were placed in an incubator at 37 ± 1°C with CO_2 partial pressure of 5% and relative humidity of 85%, to better reproduce the conditions found inside a human artery [90].

After 14 days of immersion, the samples were removed and cleaned ultrasonically with 70% vol ethanol at 80 Hz to remove loose degradation products from the surface of the samples, as suggested by the ASTM G31/12a standard. The mass of the samples after immersion was then measured. This cleaning procedure was repeated three times, after which the weight reached an asymptotic value. The corrosion rate (CR, in mm/year) was calculated from mass loss measurements using Eq. 4.1:

$$CR = \frac{kW}{Atd} \qquad (4.1)$$

where k is a constant equal to 87,600 mm h/ (cm year), W is the mass loss in g (rounded to the nearest 1 mg), A is the exposed area in cm^2 (rounded to the nearest 0.01 cm^2), t is the exposure time in hours (rounded to the nearest 0.01 h), and d is the density of the alloy in g/cm^3. The samples were then kept in a vacuum chamber for further analyses. The 92 mL solution, including the suspended degradation products, was collected in 50-mL tubes and stored before other analyses. All suspended degradation products were collected in one 50-mL tube with the solution after immersion. The other tube contained solution without degradation products in suspension.

Scanning electron microscopy (SEM, SU-3500; Hitachi, Japan) was performed to observe the corroded surface and the degradation products (DPs) that remained attached to the surface. Furthermore, energy-dispersive x-ray spectroscopy (EDS) was carried out using a silicon drift detector (X-Max^n; Oxford Instruments, UK) mounted on the SEM. Elemental maps were obtained to determine the distribution of elements on the surface. All EDS data were processed using AztecHKL software (Oxford Instruments, UK). Finally, x-ray diffraction (XRD) analysis (D5000; Siemens, Germany) was performed to identify the degradation products attached to both alloys, using a Bragg–Brentano geometry with Cu Ka radiation (k = 1.5406 Å). Scans were performed for 2 h in the range from 20° to 100° with a step size of 0.02° and step time of 1.2 s. Peak identification was performed using CrystalDiffract software (CrystalMaker Software, UK).

Elements released into solution were quantified by microwave plasma atomic emission spectrometry (MP-AES, 4200 MP-AES; Agilent, USA). The tubes were shaken for 2 min prior to collecting aliquots for MP-AES analyses, in order to collect a homogeneous suspension of degradation products in solution. Before analysis, 3 mL of complete degradation medium for each sample (HMSS after degradation, including solid degradation products in suspension) was digested on a heated plate at 115°C with 3 mL HNO_3 until 3 mL of solution remained, followed by digestion with 600 µL Nanopure H_2O and 900 µL H_2O_2 30 vol.% When 3 mL of solution was obtained after the second step of digestion, this solution was diluted with 2 mL 1 vol.% HNO_3 to obtain 5 mL of solution for analysis.

4.4.2 Electrochemical tests

Potentiodynamic polarization (PDP) and electrochemical impedance spectroscopy (EIS) tests were carried out to assess the electrochemical characteristics of the studied materials. For both tests, coupons with dimensions of 10 mm x 10 mm x 1 mm were cut from the rolled sheets. The samples were polished using the same procedure as applied for the static immersion tests. The electrochemical tests were carried out using a potentiostat/galvanostat (VersaStat 3; Princeton Applied Research, USA) in a three-electrode configuration with the sample as working electrode, saturated calomel electrode (SCE) reference electrode, and two graphite rods as counterelectrodes. HMSS was used as degradation medium, prepared in the same way as the electrolyte for the static immersion tests. The solution was kept at 37°C in ambient atmosphere using a thermostatic bath and a warm water recirculation system.

First, the open-circuit potential (OCP) was allowed to stabilize for 3600 s. After having determined the OCP, for PDP tests, a potential sweep was performed from - 0.35 V versus OCP to + 1 V versus the reference potential, with step height of 1 mV and step time of 6 s. The Tafel slopes for the anodic and cathodic parts of the polarization plot were calculated according to the ASTM G102-89 (2015) standard, in the region of 20 mV to 50 mV around the corrosion potential. On the other hand, for EIS tests, a frequency scan from 10^5 Hz to 10^{-2} Hz was performed using a potential amplitude of 10 mV around the OCP, recording 10 points per decade. Separate samples were used for PDP and EIS tests (n = 5 for each condition).

4.4.3 Statistical analyses

All errors are reported calculated standard deviations. On corrosion rate and elemental concentration plots, error bars represent the uppermost and lowermost deviation from the calculated aver- age. To test the statistical significance of observed differences, one-way analysis of variance (ANOVA) tests were performed, followed by post hoc Tukey tests (Minitab 18; Minitab Inc., USA). Differences were considered statistically significant for $p < 0.05$.

4.5 Results

4.5.1 Static immersion

The evolution of the corrosion rate for both alloys as a function of the imposed plastic deformation is reported in Fig. 4.1. For FeMnC alloy, the corrosion rate is known to be a function of the amount of deformation imposed. When the deformation level is low (CR10, CR25), the corrosion rate was the lowest, but the corrosion rate increased when the imposed deformation was the highest (CR50). On the other hand, the corrosion rate was highest in the annealed condition (CRA). Considering the microstructure prior to corrosion (Fig. 4.2), the alloy presented more grain boundaries in the annealed case (Fig. 4.2a), which may act as preferential corrosion sites, thus increasing the corrosion rate. On the other hand, in the deformed condition, the grain size was larger (due to the prior hot-rolling treatment). Moreover, mechanical twinning was present when the alloy is deformed, the number of twins present inside the grains being proportional to the level of deformation imposed (Fig. 4.2b, c, and d). It can thus be inferred that grain boundaries are more sensitive to corrosion with respect to twins in the case of the 0Ag alloy.

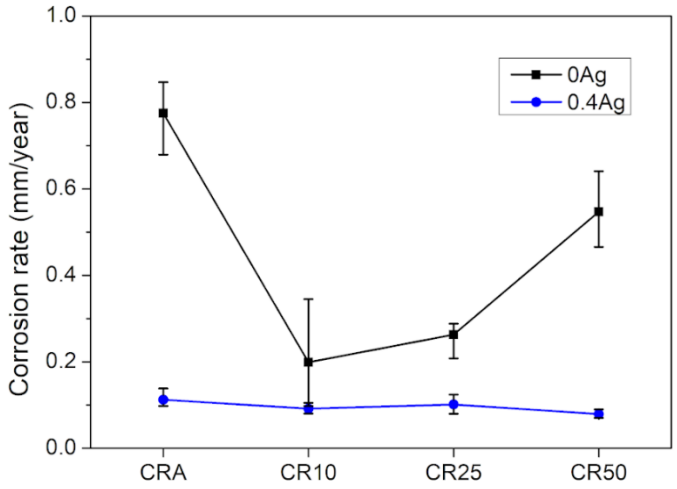

Figure 4.1 Corrosion rate as function of imposed plastic deformation for 0Ag and 0.4Ag alloys, calculated from static immersion data.

Considering the alloy with added Ag, it was observed that the corrosion rate after immersion for 14 days was lower in almost all the deformation conditions. In addition, the amount of deformation imposed on the material had no effect on the corrosion rate. Considering the microstructure before corrosion (Fig. 4.2e, f, g, and h), it can be seen that the silver-containing alloy had a significantly smaller grain size with respect to the silver-free one. The distribution of Ag-rich particles in all conditions can be seen in Fig. 4.3.

Examining the surface of both alloys after corrosion (Fig. 4.4), it is observed that a discontinuous layer of degradation products formed for both alloys at all deformation levels. The degradation products showed cuboid shape and tended to cluster locally. Intergranular corrosion was observed in all cases, while dark holes could be seen across the surface of the 0Ag alloy in all the deformation conditions, especially in Fig. 4.4a, b, and c. This may be associated with localized pitting. Considering the alloy with added Ag (Fig. 4.4e, f, g, and h), the degradation products were still predominantly cuboids. On the other hand, small flakes were also present on top of the cuboids, which were not observed in the case of the silver-free alloy. No severe pits were detected, in contrast to the case of the 0Ag alloy.

The nature of the degradation products can be understood from the EDS elemental maps shown in Fig. 4.5. Considering the alloy without silver (Fig. 4.5a, b, c, d, e, and f), it was observed that the degradation products were rich in oxygen, while they were depleted of iron with respect to the underlying material. Moreover, the distribution of carbon and manganese was homogeneous between the degradation products and the matrix. Finally, some calcium was

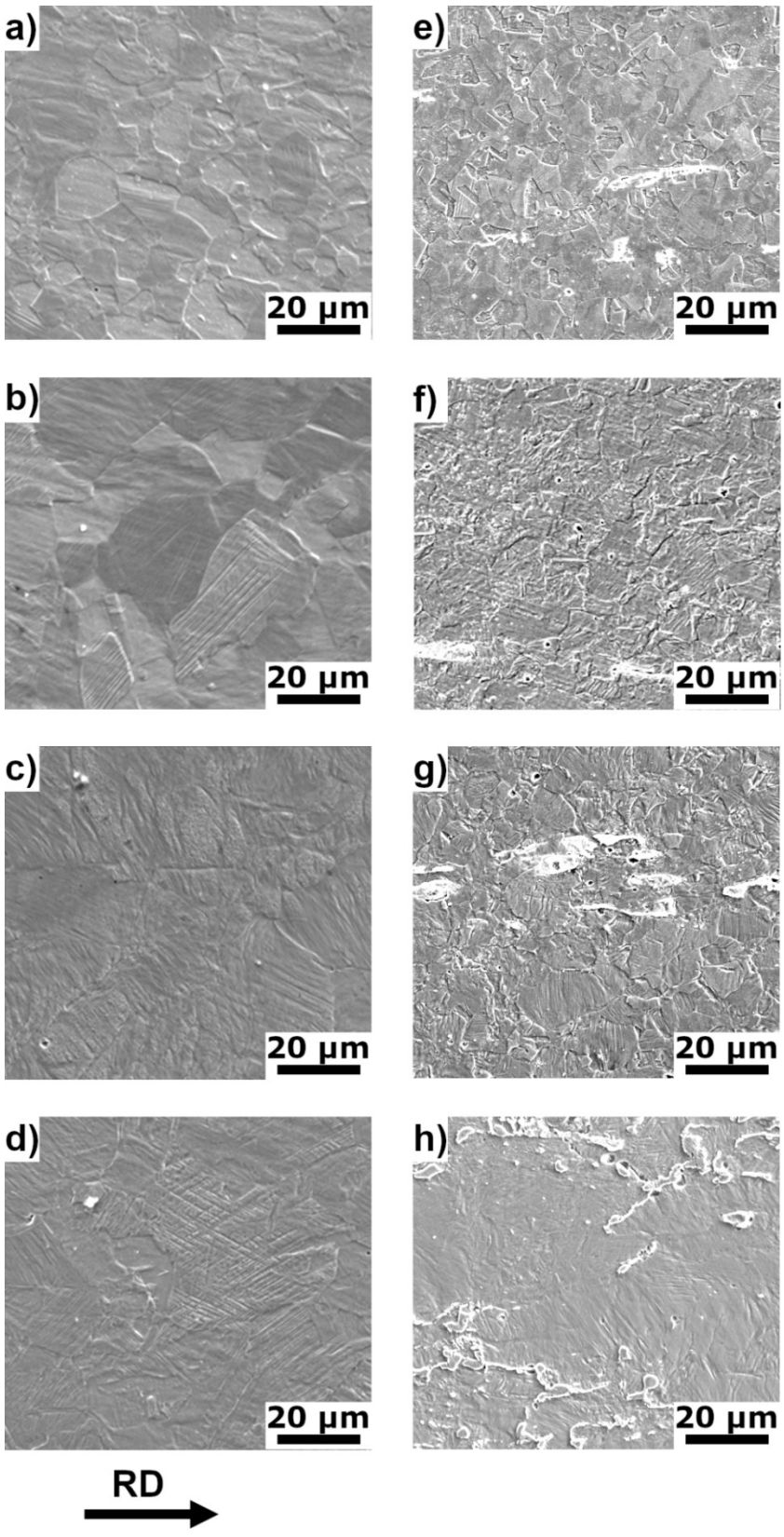

Figure 4.2 SEM micrographs of studied alloys before corrosion: (a) 0Ag CRA, (b) 0Ag CR10, (c) 0Ag CR25, (d) 0Ag CR50, (e) 0.4Ag CRA, (f) 0.4Ag CR10, (g) 0.4Ag CR25, and (h) 0.4Ag CR50.

present in the degradation products, indicating adsorption of ions from Hanks' modified

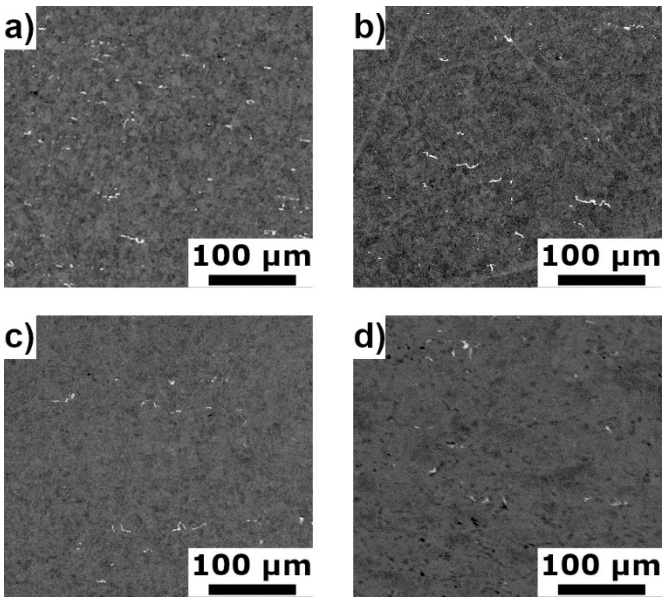

Figure 4.3 Backscattered electron SEM images of 0.4Ag alloy in various deformation conditions, highlighting the distribution of Ag-rich particles (bright spots): (a) CRA, (b) CR10, (c) CR25, and (d) CR50.

solution. When silver was added to the alloy (Fig. 4.5- g, h, i, j, k, l, and m), it was seen that the cuboids had a similar composition. On the other hand, close inspection of the flakes found on top of the cuboids revealed that they contained iron. XRD results clarified the crystalline structure of the attached degradation products. Considering the alloy without Ag (Fig. 4.6a), two phases were detected: austenite, coming from the underlying matrix, and rhodochrosite ($MnCO_3$). This is coherent with the EDS mapping results. By contrast, analysis of the alloy with added Ag (Fig. 4.6b) revealed the formation of a third phase, namely goethite (FeO·OH), which may be associated with the small flakes formed on top of the corroded material.

The amount of elements released into the complete medium is shown in Fig. 4.7, which reveals that the amount of Fe and Mn released into the complete medium was independent of the level of deformation imposed for both alloys. The release of Ag was below the detection limit (0.01 ppm) of the MP-AES device. Considering the differences between the alloys, it can be seen that no difference is present in the release of either Fe or Mn in the annealed condition. On the other hand, a significant difference in the release of Fe is observed between the CR25 and CR50 conditions, while the release of Mn was significantly different in the CR10 condition.

4.5.2 Electrochemical tests

The Tafel plots obtained from the PDP tests on both alloys are shown in Fig. 4.8, while the electro- chemical parameters are presented in Table 4.1. Considering the 0Ag alloy (Fig. 4.8a),

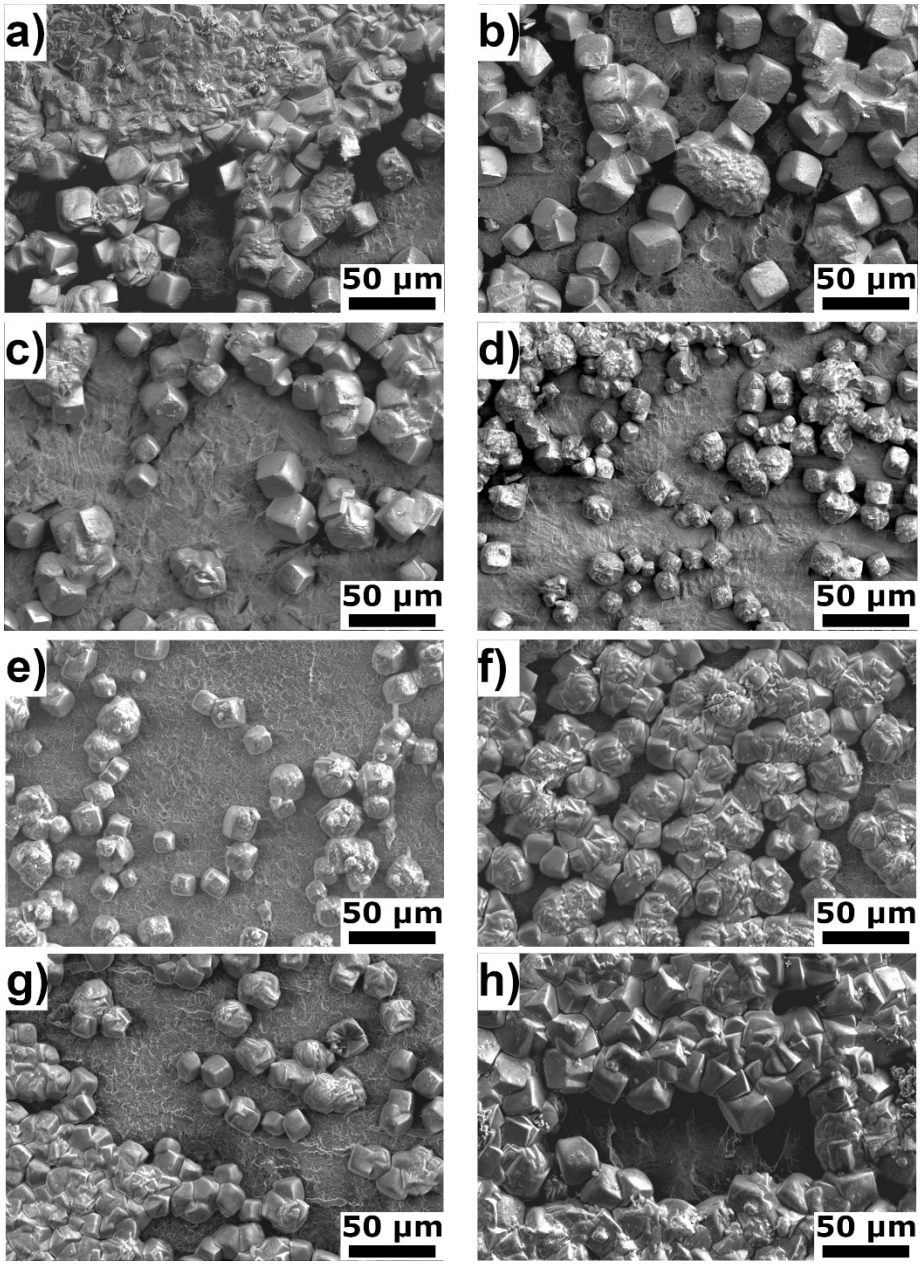

Figure 4.4 SEM micrographs of degraded surfaces after ultrasonic cleaning: (a) 0Ag CRA, (b) 0Ag CR10, (c) 0Ag CR25, d) 0Ag CR50, (e) 0.4Ag CRA, (f) 0.4Ag CR10, (g) 0.4Ag CR25, and (h) 0.4Ag CR50.

it can be seen that the Tafel plots at all the deformation levels showed a comparable shape, indicating an active material over the entire cathodic curve during the test. The calculated electrochemical parameters (Table 4.1) reveal that the corrosion potential was independent of the deformation level. On the other hand, the corrosion current density was influenced by the imposed deformation, causing the corrosion to be slowest in the annealed condition but faster when the alloy was deformed, independent of the deformation state. Considering the alloy with added Ag (Fig. 4.8b), the shape of the cathodic part of the curve varied as a function of the

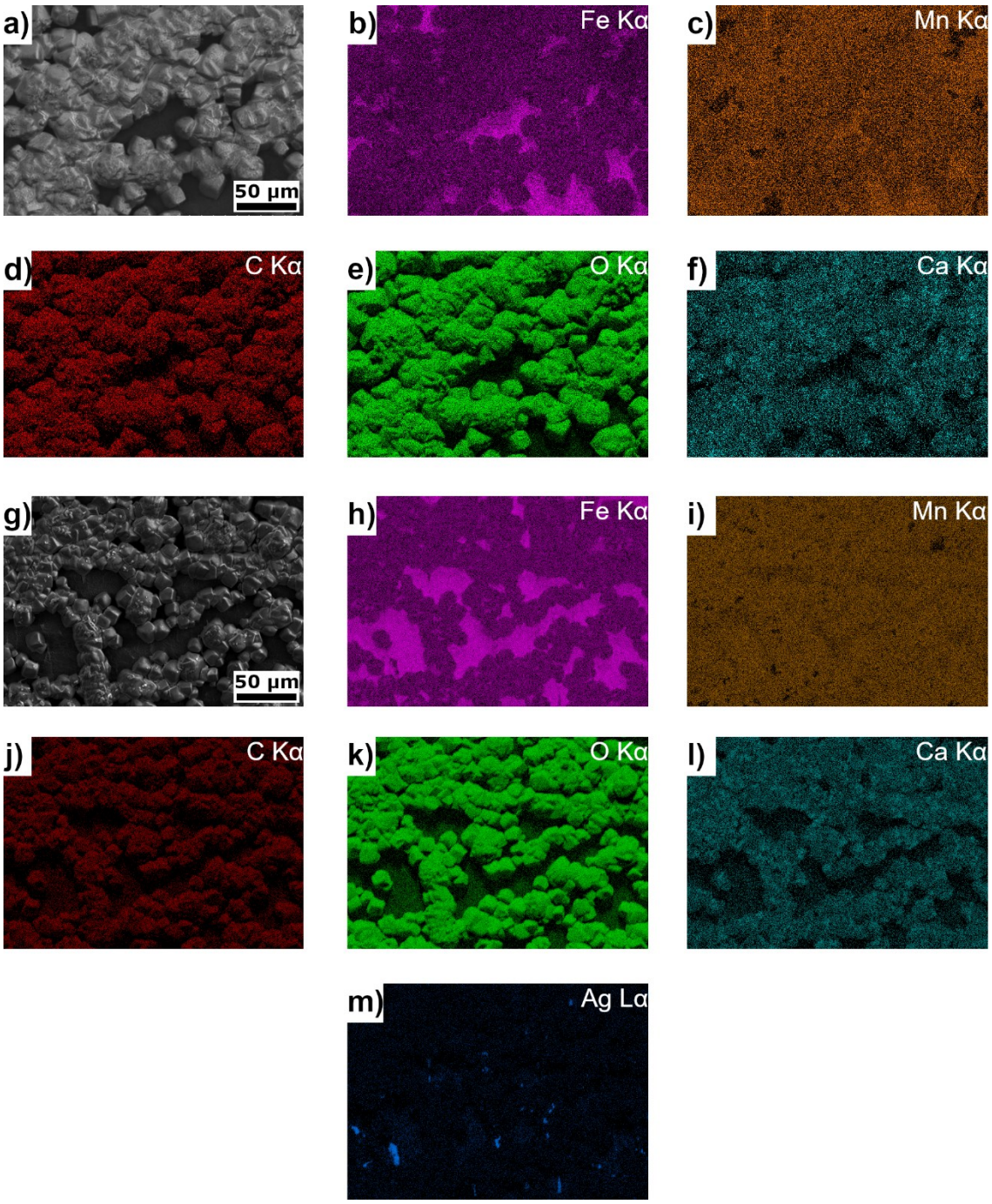

Figure 4.5 EDS elemental mapping of degraded surfaces of 0Ag CRA and 0.4Ag CRA: (a) 0Ag CRA, SEM micrograph, (b) 0Ag CRA, Fe Ka, (c) 0Ag CRA, Mn Ka, (d) 0Ag CRA, C Ka, (e) 0Ag CRA, O Ka, (f) 0Ag CRA, Ca Ka, (g) 0.4Ag CRA, SEM micrograph, (h) 0.4Ag CRA, Fe Ka, (i) 0.4Ag CRA, Mn Ka, (j) 0.4Ag CRA, C Ka, (k) 0.4Ag CRA, O Ka, (l) 0.4Ag CRA, Ca Ka, and (m) 0.4Ag CRA, Ag La.

deformation: When the alloy was in the annealed state, the curve was that of a fully active material. On the other hand, the deformed states showed a more or less pronounced reduction in the corrosion current at around - 0.4 V versus SCE. The corrosion current density increased again at higher potential values. Based on the electrochemical parameters (Table 4.1), it can be

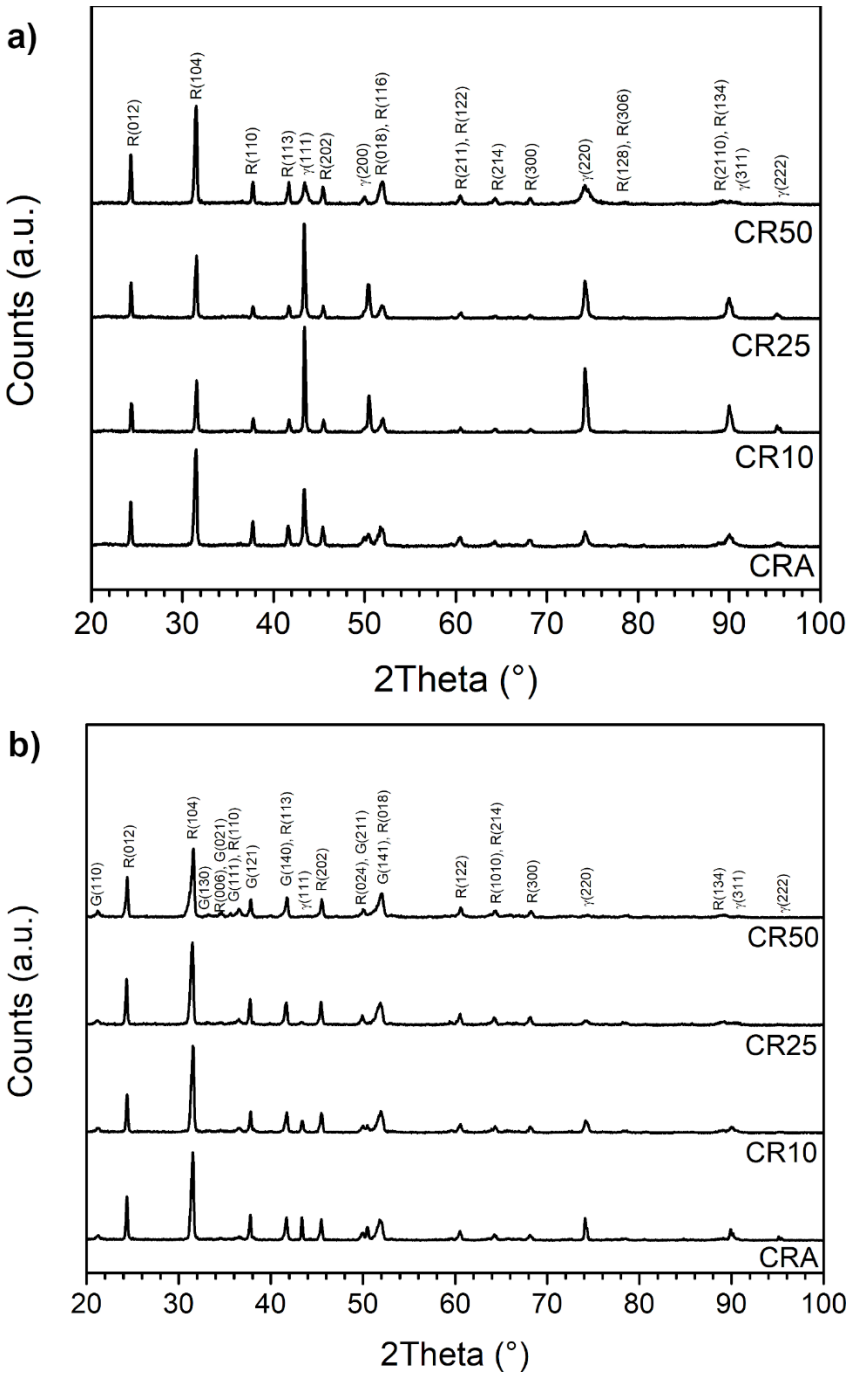

Figure 4.6 Indexed XRD spectra for (a) 0Ag and (b) 0.4Ag alloys in all deformation conditions.

seen that the alloy with added Ag in the annealed state showed a comparable corrosion current density to the annealed alloy without Ag. This implies that their corrosion rates were similar. Moreover, plastic deformation did not affect the degradation rate.

The results obtained from the EIS tests are reported in Fig. 4.8 and Table 4.1. For both alloys, the Nyquist plots show the formation of a porous passive layer, represented

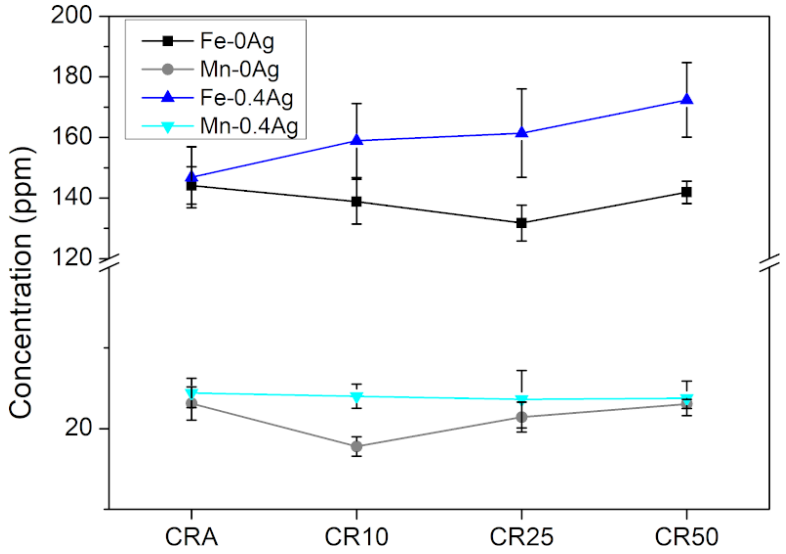

Figure 4.7 Concentration profile of Fe and Mn released in Hanks' modified salt solution after immersion, from MP-AES data.

electrochemically by a constant-phase element (CPE). In the low frequency region, an inductive loop is present in all conditions, indicating the adsorption of species from the solution onto the sample surface. This tendency in the electrochemical behavior may explain the formation of the porous layer at the longer times considered in the static immersion tests. More detailed inspection of the electrochemical circuit parameters (Table 4.1) reveals that no significant difference was observed for all the alloys. Moreover, the polarization resistance (R_p) of the alloy with added Ag showed a higher deviation with respect to that of the alloy without Ag, possibly due to the inhomogeneous distribution of Ag-rich particles in the studied alloy.

4.6 Discussion

This work assessed the effect of Ag and of plastic deformation on the corrosion behavior of a TWIP steel. It was observed that, overall, the presence of Ag did not accelerate the corrosion of the material in the short term, contrary to observations by other authors [71,74]. The reasons for this behavior may be ascribed to multiple factors. First, the methodologies used in this work differ from those applied previously, as other works focused only on electro- chemical analysis (PDP and/or EIS) over the very short term. This work also presented static immersion data, which were conducted only in one other study [72], which found outcomes similar those presented herein. In addition, different aggressive media were used in each study, which may significantly alter the degradation of Fe-based alloys and TWIP steels, as already observed elsewhere [18,69]. Second, all previous works studied alloys produced by powder metallurgy or

additive manufacturing techniques. This work differs in focusing on cast and plastically deformed alloys.

From the collected data, it appears that the microstructural characteristics of both alloys dominate their corrosion behavior in the short and medium term, in comparison with the presence of second phases. Moreover, there is a significant difference in the corrosion rate between the deformed and annealed states, at least for the alloy without Ag.

4.6.1 Overall Corrosion Mechanism

Examining the microstructural characteristics, it can be observed that, prior to corrosion, the alloy without Ag presented a larger grain size compared with the alloy with added Ag, independent of the amount of deformation imposed. After 14 days of immersion (Fig. 4.4), it was observed that pitting corrosion occurred at both transgranular and inter- granular sites. All deformation conditions showed severe pitting. On the other hand, for the alloy with added Ag, transgranular corrosion was the main mechanism observed, together with mild intergranular corrosion and intertwin corrosion.

MP-AES analyses showed that both Fe and Mn were present in solution after corrosion. Moreover, the degradation products observed on the surface of the samples consisted of $MnCO_3$ for both alloys, while FeO·OH was detected only for the Ag-rich alloy. The anodic half-reactions, leading to the dissolution of both Fe and Mn, can be described by Eqs. 4.2a and 4.2b:

$$Fe \rightarrow Fe^{2+} + 2e^{-} \qquad (4.2a)$$

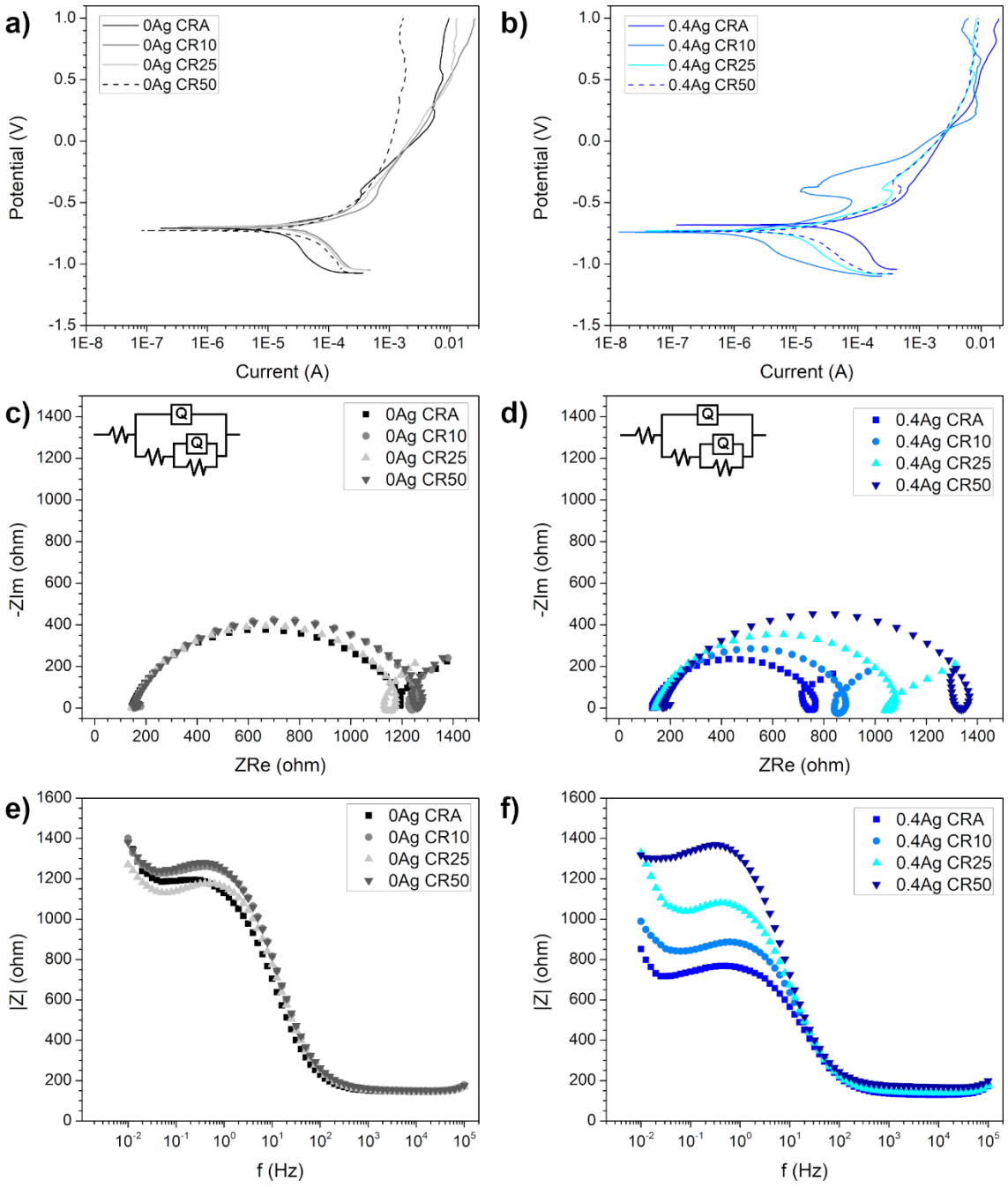

Figure 4.8 Plots obtained from PDP and EIS tests for both alloys in all deformation conditions: (a) 0Ag, Tafel plots, (b) 0.4Ag, Tafel plots, (c) 0Ag, Nyquist plots, (d) 0.4Ag, Nyquist plots, (e) 0Ag, Bode frequency plots, and (f) 0.4Ag, Bode frequency plots.

$$Mn \rightarrow Mn^{2+} + 2e^{-} \qquad (4.2b)$$

On the other hand, the presence of CO_2 leads to the formation of carbonic acid in the aqueous medium, as described by Eq. 4.3:

$$CO_2\ (g) + H_2O\ (l) \rightarrow H_2CO_3(aq) \qquad (4.3)$$

Table 4.1 Electrochemical data from PDP and EIS tests on 0Ag and 0.4Ag alloys for all deformation conditions

		PDP			EIS		
Alloy	**Condition**	**E_{corr} (V)**	**i_{corr} (μA/cm²)**	**CR (mm/year)**	**R_s (Ω)**	**R_p (Ω)**	**C_{dl} (μF)**
0Ag	CRA	-0.71±0.01	17.65±1.62	0.20±0.02	155.15±8.24	961.85±112.00	19.87±5.30
	CR10	-0.71±0.02	33.75±6.46	0.38±0.07	148.81±3.96	970.60±88.13	17.38±2.20
	CR25	-0.70±0.02	28.69±8.11	0.32±0.09	151.36±7.34	1120.97±115.48	15.67±0.73
	CR50	-0.72±0.01	28.19±4.05	0.32±0.05	156.91±9.49	1175.38±143.40	19.06±2.94
0.4Ag	CRA	-0.69±0.03	14.15±3.82	0.16±0.04	146.43±14.76	877.70±241.79	17.28±2.08
	CR10	-0.71±0.02	7.17±3.57	0.08±0.04	146.68±6.29	1041.88±362.17	19.82±3.89
	CR25	-0.73±0.01	6.06±2.30	0.07±0.03	150.24±10.51	1135.63±262.71	19.21±3.08
	CR50	-0.72±0.02	12.14±2.07	0.14±0.02	158.77±11.76	1031.93±220.01	18.36±2.75

Carbonate ions can be reduced from carbonic acid according to the two following cathodic half- reactions:

$$2H_2CO_3\ (aq) + 2e^- \rightarrow H_2\ (g) + 2HCO_3^-\ (aq) \qquad (4.4a)$$

$$2HCO_3^-\ (aq) + 2e^- \rightarrow H_2\ (g) + 2CO_3^{2-} \qquad (4.4b)$$

Finally, the formation of $MnCO_3$ is the result of the following overall reaction:

$$Mn^{2+}\ (s) + CO_3^{2-} \rightarrow MnCO_3\ (s) \qquad (4.5)$$

On the other hand, the formation of goethite in the case of the Ag-rich alloy is governed by the cathodic half-reaction of oxygen dissolution (Eq. 4.6):

$$O_2 + 2H_2O + 4e^- \rightarrow 4OH^- \qquad (4.6)$$

Two successive product formations can occur, leading to the formation of iron oxyhydroxide according to Eqs. 5.7a and 5.7b.

$$2Fe^{2+} + 4OH^- \rightarrow 2FeO \cdot 2H_2O \qquad (4.7a)$$

$$2FeO \cdot 2H_2O \rightarrow H_2 + 2FeO \cdot OH \qquad (4.7b)$$

In addition, the formation of corrosion pits in the 0Ag alloy can be governed by the chloride ions attacking the surface, as described by other authors in the case of Fe-Mn alloys with a porous corrosion layer [11] (Eqs. 4.8a and 4.8b):

$$Fe^{2+} + 2Cl^- \rightarrow FeCl_2 \quad (4.8a)$$

$$FeCl_2 + H_2O \rightarrow Fe(OH)_2 + HCl \qquad (4.8b)$$

4.6.2 Influence of Deformation on the Corrosion Rate

As mentioned above, both the static immersion and PDP tests showed that plastic deformation affected the corrosion rate of the silver-free alloy in the short term. Static immersion tests showed that the annealed material exhibited a higher corrosion rate than the deformed one. On the other hand, the PDP tests showed the opposite. Considering the alloy with added Ag, no influence of the deformation on the degradation rate was detected. This may be due to the different sites that are activated in the two tests, in addition to the intrinsic differences between the two techniques.

The origin of the difference in degradation rate as a function of the deformation can be elucidated from the microstructural differences induced by cold rolling. The annealed 0Ag alloy showed a significantly smaller grain size with respect to the deformed case, because of the previously applied hot-rolling treatment. The deformed 0Ag alloy, on the other hand, showed a number of twins present inside the grains, being directly proportional to the amount of deformation imposed. It can be supposed that transgranular and intertwin corrosion were the first mechanisms to be activated in the short term, thus explaining the lower corrosion rate of the annealed alloy observed in the PDP tests. Going to longer times, relative to the static immersion tests, localized intergranular corrosion may be activated by the chloride attack described above. The severity of the attack then leads to the formation of pits at grain boundaries, as already observed by other authors [11,12].

This reasoning does not explain the corrosion behavior observed for the 0.4Ag alloy. The lack of influence of the deformation level on the corrosion rate may be explained by the uniform grain size in all conditions. On the other hand, the lower corrosion rate may be explained by an earlier development of the degradation layer. Since the surface forms a porous film afterwards, it can be supposed that this corrosion layer is unstable but prevents the onset of intergranular corrosion up to 14 days of immersion, thus preventing pitting corrosion. On the other hand, further tests are needed to fully elucidate the short-term influence of Ag on preventing pitting corrosion in the studied TWIP steel.

4.7 Conclusion

The aim of this work is to understand how silver and plastic deformation affect the degradation behavior of a twinning-induced plasticity steel for biodegradable stents. The results show that addition of Ag slows down the degradation rate of the TWIP steel after 14 days. Moreover, it suppresses the effect of plastic deformation on the corrosion. This difference may be ascribed to an earlier formation of a layer of degradation products. On the other hand, the formation of a porous corrosion layer was absent after 14 days of immersion and prevented the formation of pits at grain boundaries. This indicates that addition of Ag contributes to a more uniform corrosion mechanism, which is desired in the case of high-strength materials for degradable stents. To further validate the conclusions drawn in this manuscript, degradation in more complex solutions including proteins should be assessed, together with long-term animal tests.

4.8 Acknowledgements

The authors would like to thank Leticia Marin de Andrade from Laval University and Ruben Beltrami from Politecnico di Milano for professional support with the interpretation of the electrochemical results, together with Vicky Dodier from Laval University for invaluable assistance with MP-AES analyses. This work was funded by the Natural Science and Engineering Research Council of Ca- nada under the CU-I2I and Discovery program. Financial support and technical collaboration from AMEC Usinage, Plasmionique Inc., Umano Medical Inc. and Metalliage Inc. is also acknowledged and much appreciated. S.L. acknowledges funding from a Vanier Canada Graduate Scholarship. D.M. was supported by NSERC-Canada and holds a Canada Research Chair Tier I.

5. Six-months long in vitro degradation tests of biodegradable twinning-induced plasticity steels alloyed with Ag for stent applications

Sergio Loffredo[a,b], Sofia Gambaro[a,c], Leticia Marin de Andrade[a], Carlo Paternoster[a], Riccardo Casati[b], Nicolas Giguère[d], Maurizio Vedani[b], Diego Mantovani[a,*]

a: Laboratory for Biomaterials and Bioengineering, Canada Research Chair I in Biomaterials and Bioengineering for the Innovation in Surgery, Department of Min-Met-Materials Engineering, Research Center of CHU de Quebec, Division of Regenerative Medicine, Laval University, Quebec City, QC G1V 0A6, Canada

b: Department of Mechanical Engineering, Politecnico di Milano, Milan 20156, Italy

c: National Research Council, Institute of Condensed Matter Chemistry and Technologies for Energy (CNR-ICMATE), Genoa 16149, Italy

d: Quebec Metallurgy Center (CMQ), Trois-Rivières, QC G9A 5E1, Canada

Publication status

Submitted to ACS Biomaterials Science and Engineering, March 2021

5.1 Résumé

Les aciers TWIP offrent les meilleures propriétés mécaniques de de tous les matériaux biodégradables, ce qui permettrait de produire des stents beaucoup plus minces. Ces aciers forment en revanche une couche passive de phosphates pendant leur dégradation dans les animaux. L'ajout d'Ag est prometteur pour améliorer la dégradation à court terme, mais l'évolution du mécanisme de corrosion avec le temps est inconnue. La présence d'Ag a promu un couplage galvanique dans la première semaine d'immersion, mais cet effet a été supprimé par la formation d'une couche mixte carbonate/hydroxyde. Cette couche s'est partiellement détachée après deux mois et a été remplacée par une couche stable de phosphates, sur laquelle une nouvelle couche mixte s'est formée après 4 mois, en bloquant la dégradation. Cela démontre que les tests d'immersion peuvent être corrélés aux tests animaux uniquement s'ils ont une durée suffisamment longue.

5.2 Abstract

Twinning-induced plasticity (TWIP) Fe-Mn-C steels are biodegradable metals with far superior mechanical properties to any biodegradable metal, including Mg alloys, used in commercially available devices. For this reason, the employ of Fe-Mn-C alloys to produce thinner and thinner implants can be exploited allowing to overcome the device size limitations that biodegradable stents still present. However, Fe-Mn steels are known to form a phosphates layer on their surface over long implantation times in animals, preventing device degradation in the required timeframe. The introduction of second phases in such alloys to promote galvanic coupling showed short-term promise, and particularly the use of Ag looked especially effective. Nonetheless, the evolution in corrosion mechanism of quaternary Fe-Mn-C-Ag alloys over time is unknown. This study aims at understanding how corrosion changes over time for a TWIP steel alloyed with Ag using a simple static immersion setup. The presence of Ag promoted some galvanic coupling just in the first week of immersion; this effect was then suppressed by formation of a mixed carbonate/hydroxide layer. This layer partly detached after 2 months, was replaced by a stable phosphate layer, over which a new carbonate/hydroxide formed after 4 months, effectively hindering sample degradation. Attachment of phosphates to the surface matches 1-year outcomes from animal tests reported by other authors, but this phenomenon cannot be predicted using immersion up to 28 days. These results demonstrate that immersion tests of Fe-based degradable alloys relate to animal tests only when carried out for sufficiently long time, and that galvanic coupling with Ag is not a viable strategy at long term. Future works should focus more on surface modifications to modify the interfacial behavior rather than alloying in the bulk.

5.3 Introduction

Biodegradable metals are seen as a pivotal innovation for treating cardiovascular diseases in young patients, with the earliest report dating from 2001 [60]. Such devices aim at total resorption inside the human body in 12-24 months [27]. Despite the efforts devoted to research in this field, only a Mg-based stent demonstrated to safely fulfill this requirement [51,53,187,222], receiving approval for commercialization from regulatory agencies in 2016 [52]. On the other hand, Mg alloys exhibit relatively poor mechanical properties respect to Co-Cr alloys used nowadays for most DES platforms [10], resulting in a device with a size 2 to 3 times larger than the latter.

Pure Fe demonstrated superior mechanical properties in comparison with Mg-based alloys [15], but *in vivo* tests in animal models revealed that the resorption process is hindered by the formation of a stable layer of corrosion products [60,61]. Several Fe-based alloys were developed, mainly including Mn as alloying element to decrease the overall potential of the material, thus hypothetically resulting in a higher tendency to corrode [62,63]. Among these materials, Fe-Mn-C twinning-induced plasticity (TWIP) steels show mechanical properties superior to those of Co-Cr alloys [10], thus having the potential of solving the size limitation of Mg-based stents and, consequently, enlarge their versatility in terms of applications. Other elements can also be included to favor galvanic coupling, having showed faster material dissolution *in vitro* [12,162]. Micro-alloying of a noble element as Ag to Fe-Mn-C alloy can result in better corrosion [74] without modifying mechanical properties of the material. However, the beneficial effect of Ag on corrosion behaviour of these alloys remains disputed [226].

Most studies on Fe-based alloys showed an increased corrosion and reduced electrochemical potential *in vitro* [127,189]. This should translate to faster material dissolution in animal models. However, when *in vivo* tests on such alloys were performed, device degradation did not show any difference with respect to the case of pure Fe [70,138]. For both pure Fe and Fe-Mn based alloys, it was found that a corrosion layer rich in phosphates is formed on top of materials surface after 1 year from implantation [61,138], which was rarely observed in *in vitro* tests, with some exceptions depending on the testing atmosphere [90,154]. Such laboratory tests in simplified setups most often involve either simple electrochemical tests including potentiodynamic polarization (PDP), static immersion tests on short durations (up to 28 days), or a combination of these two techniques. The use of long-term immersion tests is seldomly

reported: for a Fe-Mg_2Si composite, the formation of phosphates was observed only after 50 days of immersion, a much longer time span with respect to the 14-28 days normally considered [154]. In addition, a fundamental assumption of static immersion tests is the linearity of the corrosion process [224], which often does not correspond to the reality of a medical device degradation in a human body.

Immersion tests longer than 28 days were never reported for biodegradable TWIP steels. This work aimed at fulfilling this knowledge gap by statically immersing such alloys up to 180 days in a pseudo-physiological solution. In addition, the long-term effect of microalloying a TWIP steel with Ag was evaluated to validate whether this strategy is effectively advantageous for promoting device degradation.

5.4 Materials and Methods

5.4.1 Material preparation

Two alloys, with nominal composition Fe-16Mn-0.7C (wt. %) and Fe-16Mn-0.7C-0.4Ag (wt. %), were produced and processed as described elsewhere [210]. In the present work, Fe-16Mn-0.7C is shortened as 0Ag, and Fe-16Mn-0.7C-0.4Ag as 0.4Ag. Sheets of both materials were cold rolled with a thickness reduction of 25% (referred as CR25) to a final thickness of 1 mm. Part of these sheets were annealed for 15 minutes at 800°C in a resistance furnace operating in air (Lenton AWF 13/25, UK), producing annealed plates (referred as CRA) after water quenching. Small coupons, with nominal dimensions 20 x 10 x 1 mm, were cut from the previously obtained sheets. Moreover, a 2 mm diameter hole was drilled at a distance of 2 mm from the short edges of the samples prior to testing. All samples were ground with SiC abrasive paper up to 600 grit, followed by mechanical polishing with diamond paste suspensions, having a particle size of 3 and 1 μm, respectively. Final polishing was performed with a colloidal alumina suspension of 0.05 μm. Prior to testing, samples were rinsed in an ultrasonic bath with anhydrous ethanol for 10 minutes and stored in a vacuum chamber before further use.

5.4.2 Static immersion tests

Static immersion tests were conducted on 4 polished samples per alloy (0Ag, 0.4Ag) and condition (CRA, CR25) at different time points (3, 7, 14, 28, 60, 120 and 180 days). The chosen degradation medium was Hanks' modified salt solution (HMSS), since it properly simulates the ionic composition of human plasma [18]. Furthermore, the tests were carried out in an incubator

(37 °C, CO_2 partial pressure at 5%, relative humidity of 70%) in order to better reproduce physiological conditions [130]. The medium was prepared by dissolving 9.5 g of Hanks' balanced salts (H1387, Sigma-Aldrich, Canada) in 1.4 L of nanopure water. 14.16 g of HEPES acid (BP-310-1, Fisher Scientific, USA), 16.65 g of HEPES sodium salt (BP-410-1, Fisher Scientific, USA) and 3.30 g of sodium bicarbonate (S8875, Sigma-Aldrich, Canada) were added as buffering agents and allowed to mix for 20 minutes with a magnetic stirring plate. The pH was buffered at 7.40±0.05 by adding a solution of HCl 0.1 M. The solution was then sterilized by filtering, under a biological hood, with a vacuum-driven filter in sterile bottles (pore size 0.22 μm; Sarstedt, Germany).

Before starting the tests, 100 mL bottles were sterilized in an autoclave at 115 °C for 30 minutes and allowed to dry in an oven at 37 °C. Nylon fishing wire was used to hang the samples inside the bottles; the wire was sterilized by immersion in anhydrous ethanol for 30 minutes. Moreover, the samples were sterilized by immersion in ethanol 70% vol. for 5 minutes [225]. 92 mL of the prepared HMSS solution were used for each sample, according to the ASTM G31-12a standard [224].

At each timepoint the samples were extracted from the solution and immediately immersed in sterile scintillation vials filled with anhydrous ethanol to stop the degradation process. The vials containing the samples were ultrasonicated for 5 minutes, after which the degradation products that detached from the surface (labelled DP-II) were collected in a Petri dish and stored under vacuum until further characterizations. The samples were then dried with compressed air and weighed with a precision balance. This procedure was repeated 2 more times or until the measured mass became asymptotic. After immersion tests, 15 mL of the supernatant degradation medium were picked up from the solution and collected for further analyses. The remaining medium solution, including also solid degradation products, was collected in 50 mL conical tubes and centrifuged at 3000 rpm for 10 minutes. The obtained supernatant degradation medium was discarded while 10 mL of ethanol 70% were added to the degradation products (generally referred as DPs). The tube was vortexed for 30 s and then centrifuged again at 3000

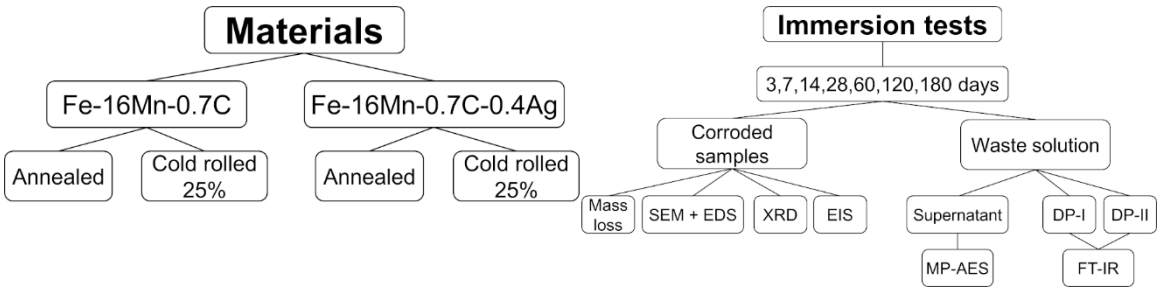

Figure 5.1 Overview of the experimental design for this study

rpm for 10 minutes. The obtained supernatant ethanol was discarded. 5 mL of fresh ethanol 70% were added before vortex the tube again for 30 s. Finally, the obtained degradation products (specifically referred as DP-I) were stored in a Petri dish for further analyses.

5.4.3 Characterization

Figure 5.1 reports an overview of the experimental design and summarizes the carried-out characterization techniques to analyse the samples after immersion test.

5.4.3.1 Corroded samples

Scanning electron microscopy (SEM, Hitachi SU-3500, Japan) was carried out on the surface of annealed samples after immersion at all timepoints. The samples were cut in half with a diamond blade in order to analyze the cross-section, together with the top surface. EDS elemental mapping (X-Max^n, Oxford Instruments, UK) was also performed in order to assess the elemental distribution in the degradation products that formed at the surface. For cross-sectional analysis, the corroded samples were mounted vertically in epoxy resin and mechanically polished following the same procedure used for preparing samples prior to static immersion tests. All samples were metallized with an Au-Pd sputter prior to SEM (FEI Quanta 250, USA) and EDS line analyses with a 1 μm step size (EDAX Octane, AMETEK, USA).

The structure of crystalline surface-attached degradation products was determined by x-ray diffraction (XRD, Rigaku Smartlab, Japan). XRD analyses were performed at a scanning rate of 3°/min in the range of 10 – 100° (stepsize 0.020°), using Cu K_α radiation (λ = 1.5406 Å) at 40 kV and 40 mA with a Bragg-Brentano geometry. Peak identification and indexation were carried out with the QualX software [227].

After static immersion tests, the electrochemical characteristics of corroded samples immersed on HMSS solution at different time points were evaluated by electrochemical impedance spectroscopy (EIS) using a potentiostat with a three-electrode cell setup (VersaSTAT

3, Princeton Applied Research, USA). HMSS was used as degradation medium, and it was prepared following the same procedure adopted for static immersion tests. The sample acted as working electrode, a saturated calomel electrode (SCE) was used as reference electrode, and two parallel graphite rods were used as counter electrodes. The open circuit potential (OCP) was recorded after 60 minutes of immersion in HMSS; successively, a frequency scan from 10^5 to 10^{-2} Hz was performed, using an amplitude of 10 mV around the OCP and recording 10 points per decade.

5.4.3.2 Waste solution

The concentration of elements released in solution was assessed by microwave plasma atomic emission spectroscopy (MP-AES, Agilent 4200 MP-AES, USA). 3 mL of the collected supernatant for each sample were put in scintillation vials and heated with an oil bath up to 90 °C, after which 3 mL of HNO_3 (trace metal grade) were added to each vial. The bath was heated at 115 °C and the mixture allowed to evaporate until 3 mL remained. Successively, 600 μL of nanopure water and 900 μL of H_2O_2 30% vol. were added to each vial; the mixture was then allowed again to evaporate until 3 mL of solution remained. The obtained solution was finally diluted with HNO_3 1% vol. to reach 10 mL to analyze.

Degradation products (both DP-I and DP-II) were analyzed by attenuated total reflectance Fourier transform infrared spectroscopy (ATR-FTIR, Agilent Cary 660 FTIR, Agilent Technologies, MN, USA). Detection was assessed by a deutered L-alanine doped triglycine sulfate (DLa-TGS) detector and a Ge coated KBr beam slitter. Spectra were obtained in the range of 4000–400 cm^{-1} at room temperature. IR signals were collected in 64 scans at a resolution of 4 cm^{-1} and compared to a background spectrum recorded from an empty cell. Analyses of spectral data were carried out using Thermo Scientific GRAMS Suite (ThermoFisher Scientific) and Origin Pro 2020 to appropriate fit the spectra with linear combination of Gaussian lineshapes and the centroids determined from a second-derivate analysis.

5.4.4 Statistical analyses

All error bars in the figures represent the uppermost and lowermost deviation from the average. Statistical significance of the differences between groups was assessed by one-way ANOVA followed by post-hoc Tukey tests (Minitab 18, Minitab Inc., USA). Differences were considered statistically significant when $p \leq 0.05$ at least.

5.5 Results

5.5.1 Corrosion rate and elemental release

The evolution of corrosion rate (CR) as a function of immersion time for both 0Ag and 0.4Ag alloys is reported in figure 5.2; both CR of the annealed (CRA) and deformed conditions (CR25) are shown. All states showed a similar trend in the corrosion rate. Up to 14 days, no significant differences in corrosion rate were observed with the lone exception of the 0Ag CR25 condition: at 7 days its corrosion rate was significantly higher than that of the 0Ag CRA alloy ($p < 0.01$). This corrosion rate ranged between 0.120 and 0.200 mm/year. However, corrosion rate then decreased at 28 days, showing values of 0.080±0.005 mm/year without any statistically significant difference between all conditions. Corrosion rate finally decreased to near nil values at 60 days, remaining stable at 120 and 180 days. Contrarily to all other timepoints, a large error bar was visible at 60 days. This was possibly due to inhomogeneities in the layer of corrosion products formed on top of the surface, leading to a large oscillation in corrosion rate. This phenomenon was observed by SEM analyses, (figure 5.4) which will be detailed further on.

Figure 5.3 shows the release of Fe and Mn from the material at different timepoints. Only the supernatant solution without solid degradation products (DPs) was used for MP-AES analyses. As a general observation, in both cases the amount of freely available Mn in solution was higher than the Fe one. Mn availability increased from 3 to 14 days of immersion to a maximum of 21±4 ppm for 0Ag and 17±1 ppm for 0.4Ag. It then decreased constantly from 28 to 60 days, finally stabilizing at around 4 ppm after 120 and 180 days. Fe availability, on the contrary, was almost nil at all timepoints, with the exception of 7 and 60 days, when it reached a maximum of 2 ppm. The release of Ag was found to be below the detection limits of the machine at all times (< 1 ppb). This trend could be associated to a preferential release of Mn from the surface rather than Fe, which then recombined at the surface at 28 days and 60 days, forming a compact corrosion layer which prevented further release to occur. In addition, the

formation of a compact corrosion layer could be the reason why no further free Mn recombines at the surface.

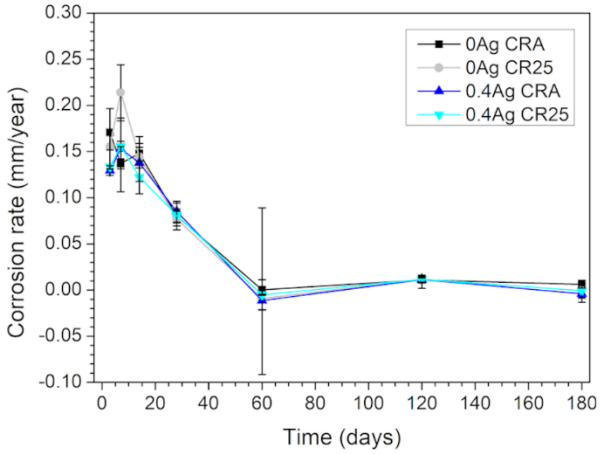

Figure 5.2 Evolution of corrosion rate over time for the 0Ag and 0.4Ag alloy in the annealed (CRA) and cold rolled with a 25% thickness reduction (CR25) states.

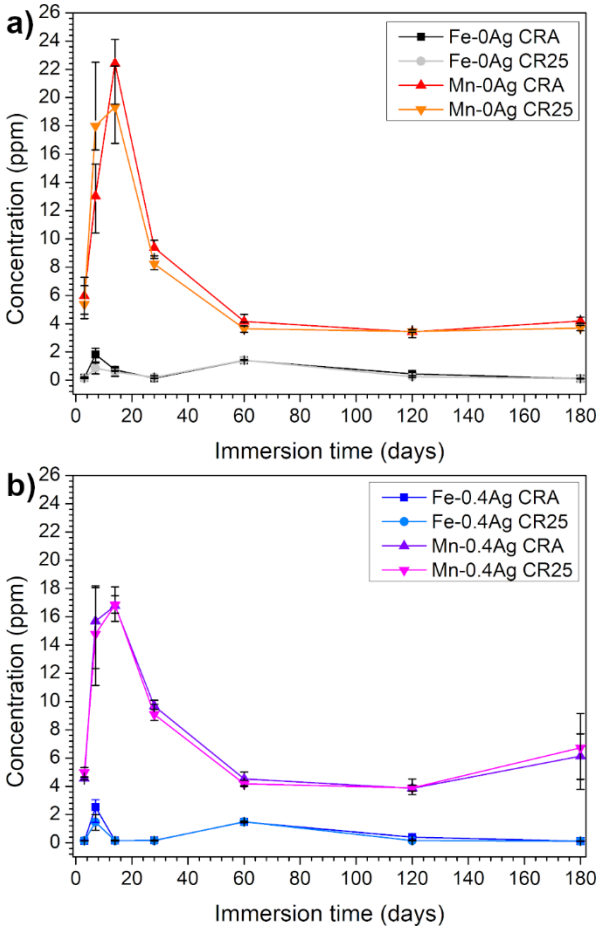

Figure 5.3 Evolution of release of Fe and Mn over time from MP-AES analyses: a) 0Ag, b) 0.4Ag.

5.5.2 Scanning electron microscopy

5.5.2.1 Corroded surfaces

Figure 5.4 shows CRA 0Ag and 0.4Ag surfaces using the BSE mode at different timepoints. 0Ag microstructure was generally composed by equiaxed grains, with residual twins present in some of them. After 3 days of immersion, some minor corrosion at grain boundaries could be seen without any DP buildup s. At 7 days, some DPs started to form at grain boundaries in the form of flakes, visible as dark spots in 0Ag 7 days micrograph of Figure 5.4. Moreover, some general corrosion phenomena started to take place inside most grains. At 14 days, such dark flakes grew in size, while corrosion inside grains became more important. Interestingly, at 28 days, most of the surface became covered with a porous corrosion layer, coming from clustering of the flakes that formed at 7 days and coarsened at 14 days. In addition, new spongy-like DPs were visible on top of the previously build corrosion layer. However, some areas of the pristine surface were still exposed. This was no longer the case at 60 days, where a fully compact corrosion layer was visible. The same compact layer that formed in the earlier stages appeared to still be present, while a new layer of spheroidal DPs formed on top of it at some places. The same situation was found at 120 and 180 days, where filament-like clusters were formed on top of the spheroidal DPs.

The DP layer overall evolution of 0.4Ag CRA appeared very similar the one already described. 0.4Ag CRA microstructure was mainly composed of equiaxed grains, albeit their average size was smaller than the CRA 0Ag one. In addition, bright particles corresponding to Ag-rich second phase were observed with a random distribution in the material. After 3 days, some corrosion started at grain boundaries. Moreover, black zones were observed around Ag-rich particles, possibly signifying galvanic corrosion between the Fe-Mn-C matrix and the Ag-rich second phases. At 7 days, formation of corrosion products started, in the form of irregular dark spots. The number of particles appeared to be higher than in the case of the 0Ag alloy. In fact, at 14 days, the small particles developed in larger cuboids that clustered together. It is interesting to note that Ag particles did not appear to be a preferential nucleation site for such cuboids, as DP-free areas were preferentially found around Ag inclusions. The situation at 28 days was once again similar to 0Ag, with a relevant formation of DPs in shape of cuboids. These particles clustered together in a porous corrosion layer while a new flake-like DP layer formed on top of the previous one. The cuboid-formed layer covered completely the base surface after

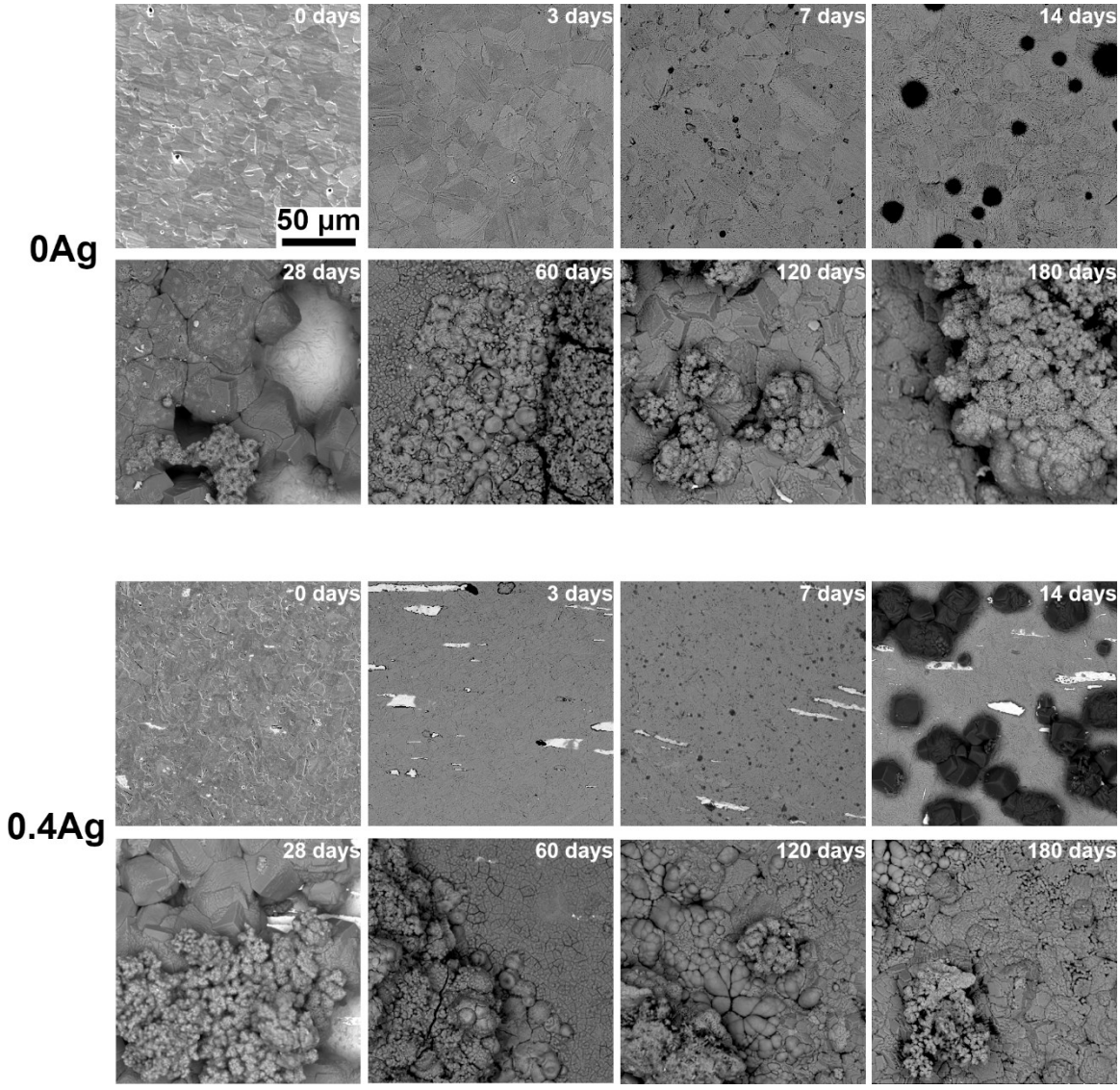

Figure 5.4 BSE-SEM micrographs of the surface of the 0Ag (top) and 0.4Ag alloys (bottom) as a function of immersion time.

60 days, while a spheroidal DPs layer appeared on the top of the previous one. The situation remained identical at 120 and 180 days, indicating an interruption of the corrosion process.

Figure 5.5 reports EDS elemental maps of the surface of the 0Ag alloy after 14 and 60 days of immersion. After 14 days, the formed cuboids were rich in Mn, C and O, while they were depleted in Fe. In addition, Ca appeared to be adsorbed on the surface in modest but not negligible quantity. After 60 days of immersion, the spheroidal DP layer appeared to be richer in Fe than the underlying one showing a higher content of P than at 28 days.

When EDS maps of 0.4Ag were considered (Figure 5.6), once again, no major differences were noticed in comparison to 0Ag. The cuboids observed at 14 days were rich in O, C and Mn,

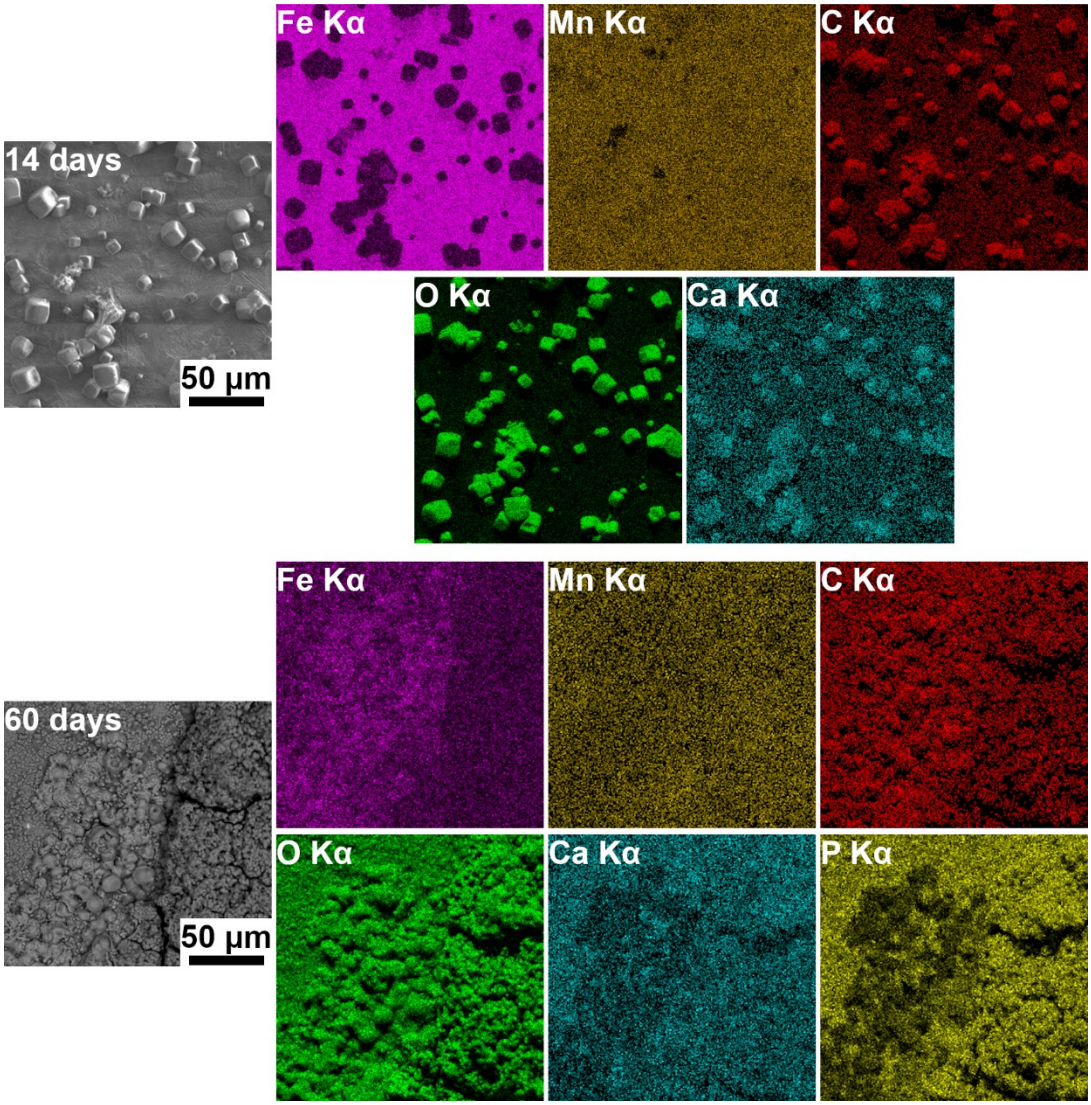

Figure 5.5 EDS element mapping of 0Ag in the annealed state after 14 (top) and 60 days (bottom) of immersion.

but not in Fe. Ag was not present in the cuboids. At 60 days, the spheroidal DPs showed a higher amount of Fe than the rest of the cuboid compact layer. Also in this case, P was present in the compact layer but not in the spheroids.

5.5.2.2 Cross-sectional analysis

Figure 5.7 reports cross-sectional images obtained by SEM for both alloys in the annealed condition at different time points. It must be noted that the cracks present on the surface came from the process of mounting the samples in thermosetting resin. Considering the 0Ag alloy first, it could be seen that at 3 and 7 days no DPs formed at the surface, in conformity with what was observed from surface images. A porous layer of corrosion products formed at 14 days,

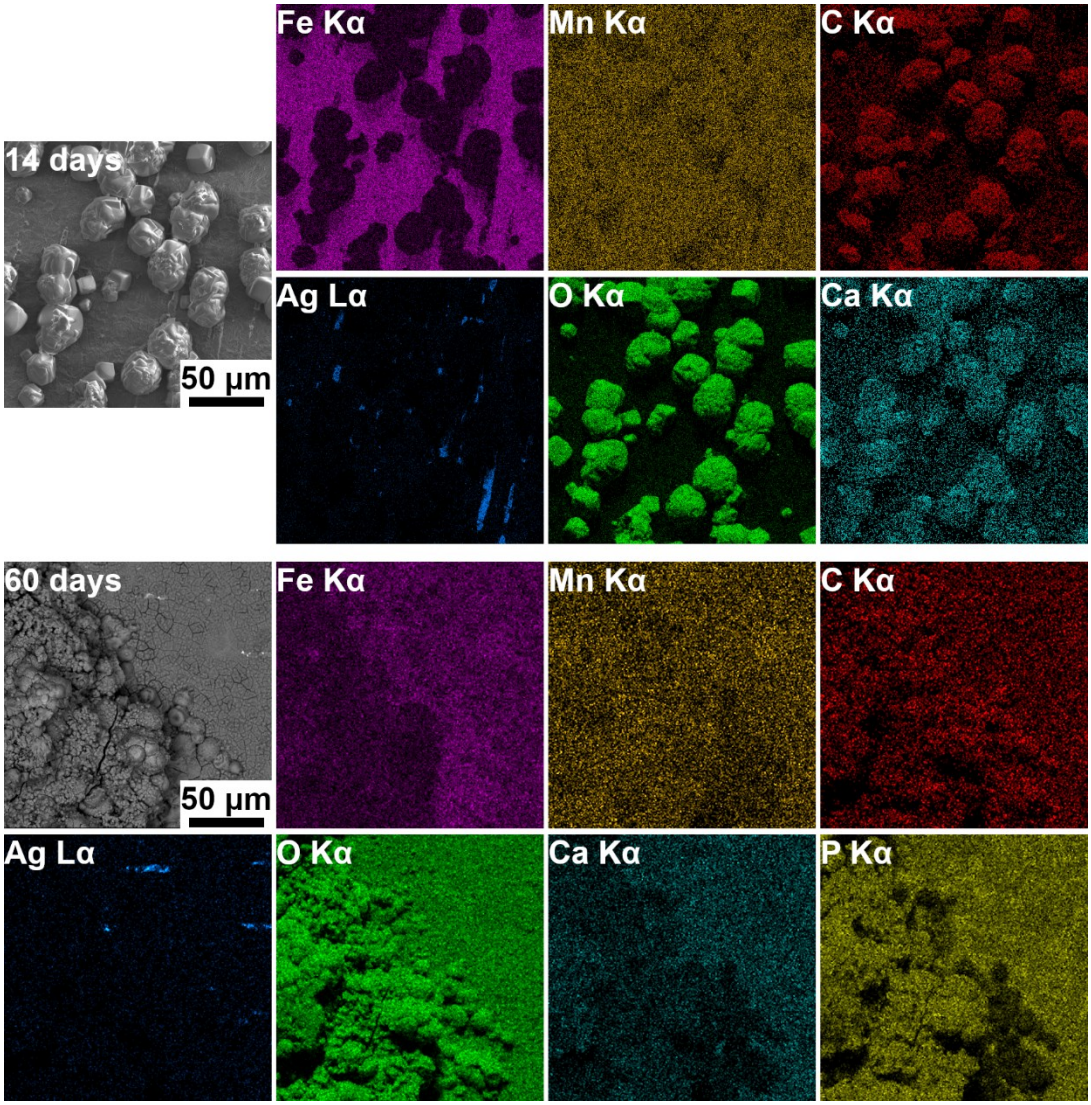

Figure 5.6 EDS element mapping of the 0.4Ag alloy in the annealed state after 14 (top) and 60 days (bottom) of immersion.

with DPs in the shape of a cuboids deposit on the surface, with a thickness of around 10 µm. In addition, corrosion appeared less uniform than at 3 and 7 days, with pits starting to form. The situation was similar after 28 days, where DPs further occupied the surface and they thickened to around 30 µm. Moreover, surface features caused by corrosion appeared in a less and less uniform way. At 60 days, the DP layer superposition became significantly different. No DPs in shape of cuboids were observed. Instead, a compact layer with a lower thickness appeared, which could be associated to the phosphate-rich layer that was observed by SEM and EDS on the top surface. The substrate underneath appeared relatively uniform, possibly relating to the detachment of a first layer of material comprising the cuboid DPs. Finally, after 120 and 180 days, the corrosion layer grew up to a thickness of around 50 µm. The base material showed an

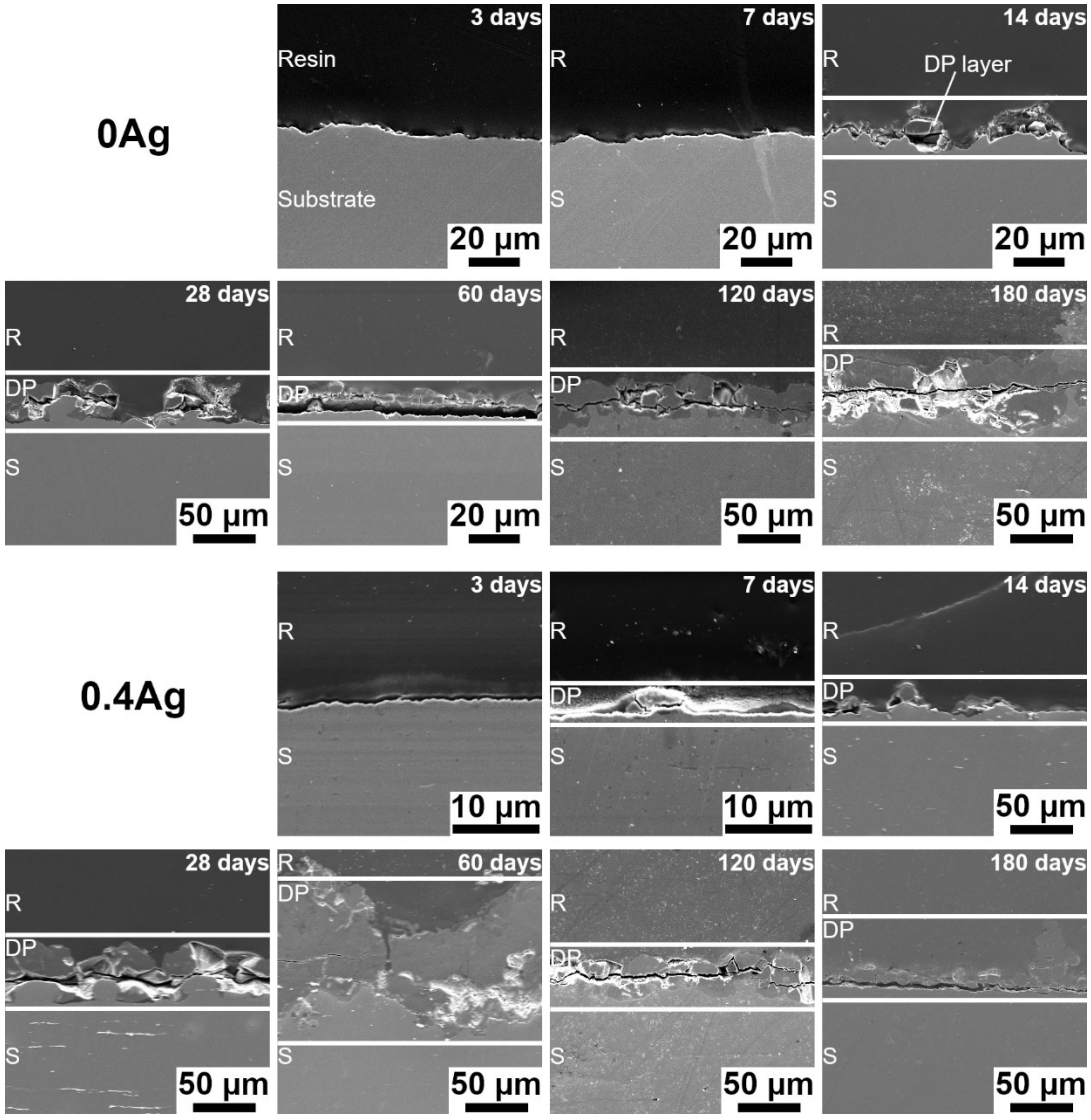

Figure 5.7 Cross-sectional SEM micrographs of the 0Ag (top) and 0.4Ag alloys (bottom) as a function of immersion time.

increase of roughness due to severe localized corrosion phenomena. The DP layer, strongly attached to the substrate, reproduced the morphology of the substrate, despite its more or less uniform thickness. The 0.4Ag alloy presented in general a similar behavior; however, significant inhomogeneities in layer thickness were observed at 60 days as reported in figure 5.7, which could explain the large deviation in corrosion rate reported in figure 5.2.

In order to analyze the compositional variations in the corrosion layer, EDS linear scans were taken for both alloys cross-sections at all timepoints, and the results are reported in figure 5.8. For both 0Ag and 0.4Ag, trends of the corrosion layer evolution were found to be comparable. At 3 days, just Fe, Mn and C were detected in the matrix, while no evident corrosion

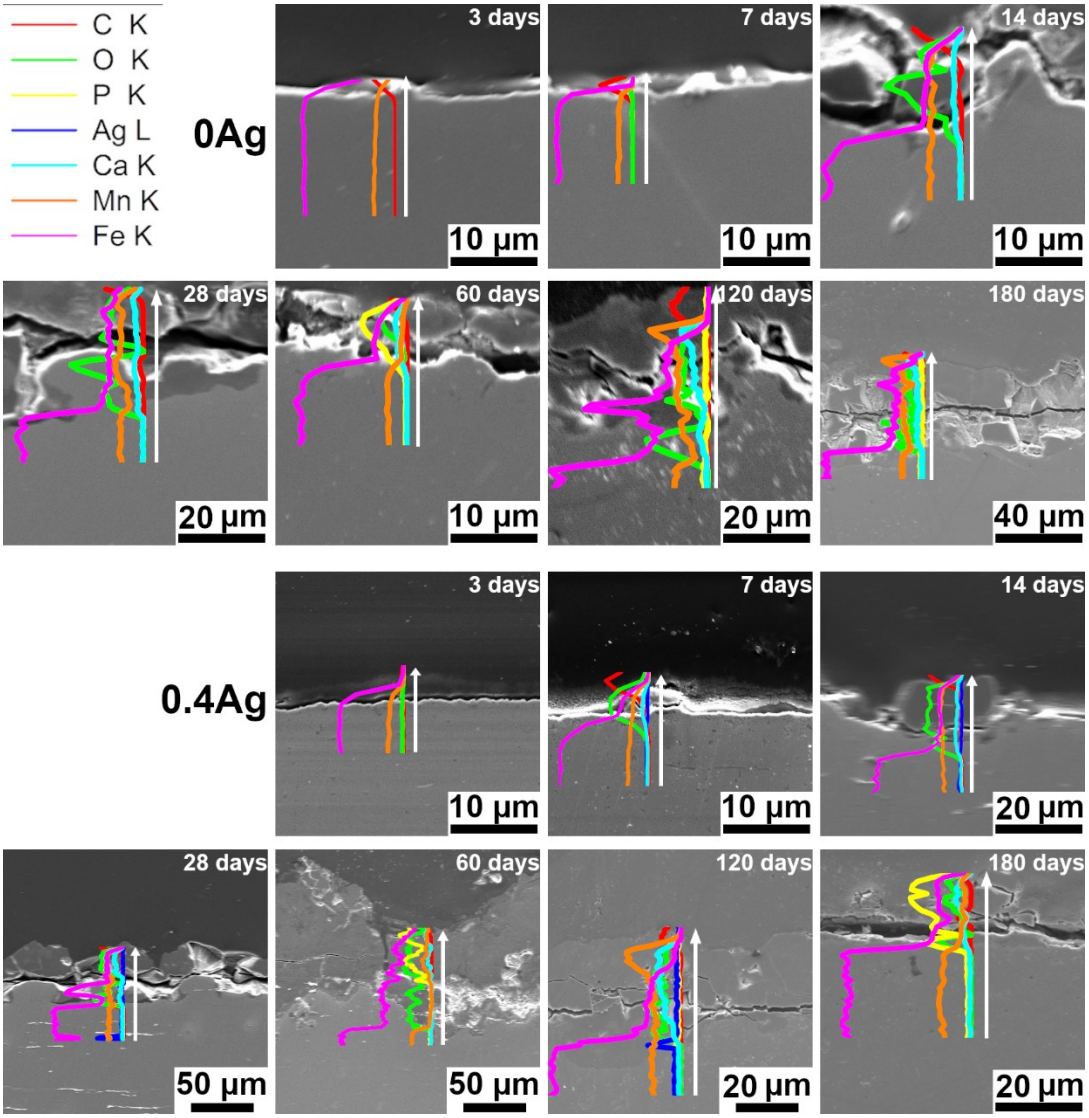

Figure 5.8 EDS line-scans on the cross-section of corroded samples of 0Ag (top) and 0.4Ag alloys (bottom) as a function of immersion time. The white arrows in each part of the figure represent the line-scan position and direction. The color legend for all figures is at the top left: if a colour is absent, this indicates that the corresponding element was not detected.

layers were visible in correspondence of the material surface. At 7 days, while no corrosion layer was present in the 0Ag alloy, some precipitates were found on top of 0.4Ag sample surface. These particles were mainly composed by O and C with some Mn and a lower Fe amount than the matrix. This analysis was in accordance with outcomes of the top EDS maps, showing clusters rich in O and C but poor in Fe. At 14 days, the cuboid DPs showed to be very rich in O, with some Fe, Mn and C present. In addition, a small quantity of Ca was detected. A similar overall elemental distribution was found at 28 days. At 60 days, the most striking difference consisted in the detection of large quantities of P in the degradation layer, together with Fe, O

and Ca, while Mn appeared to be in lower proportion with respect to previous timepoints. At 120 days the overall content of P appeared lower than at 60 days, while a higher concentration of Mn was detected. Finally, after 180 days, phosphates were again present, especially for the 0.4Ag alloy.

5.5.3 X-ray diffraction

X-ray diffraction results are reported in figure 5.9. For the 0Ag alloy (fig. 5.9a), both at 3 and 7 days the only observed phase was austenite. At 14 days, in addition to austenite, also peaks of rhodochrosite ($MnCO_3$) were detected. At 28 days, in addition to the already detected phases, also goethite (γ-FeO·OH) was found. Surprisingly, at 60 days, only austenite was detected, although SEM analyses showed the presence of a corrosion layer rich in phosphates. This could be attributed to the amorphous nature of those phases [228] which do not allow their detection, in addition to partial breakage of the previously formed film, which could have reduced the content of rhodochrosite and goethite below the detection limit. At 120 days, rhodochrosite and goethite were present and, in addition, a small peak at 29° was found, possibly associated to lepidocrocite (α-FeO·OH). No austenite was detected due to the thickness and compactness of the corrosion layer on top. At 180 days, only rhodochrosite and goethite were present. The 0.4Ag alloy presented a mostly similar behavior (fig. 5.9b). The only differences were observed at 120 and 180 days: in this case, no lepidocrocite was detected at 120 days. Moreover, at 180 days, peaks associated to both lepidocrocite and hematite (Fe_2O_3) were observed.

5.5.4 Fourier transform infrared spectroscopy

Figure 5.10 reports the FT-IR spectra that were acquired for DPs collected from the exhausted solution for both CRA alloys (DP-I), and for DPs that detached from the material surface during ultrasonic cleaning (DP-II). DP-II for both alloys could not be analyzed at 3 and 7 days because an insufficient amount of powders detached from the surface. This may indicate that the only products that formed at 3 and 7 days were weakly bound to the surface, which thus remained electrochemically active.

If DP-I are considered for both alloys, peaks associated to the carbonate (CO_3^{2-}), phosphate (PO_4^{3-}) and hydroxide (OH^-) functional groups were detected for each immersion duration. Phosphate peaks were the most intense at 3, 7 and 60 days, while carbonate and hydroxide peaks were in general weak for all the considered test durations. The situation for DP-

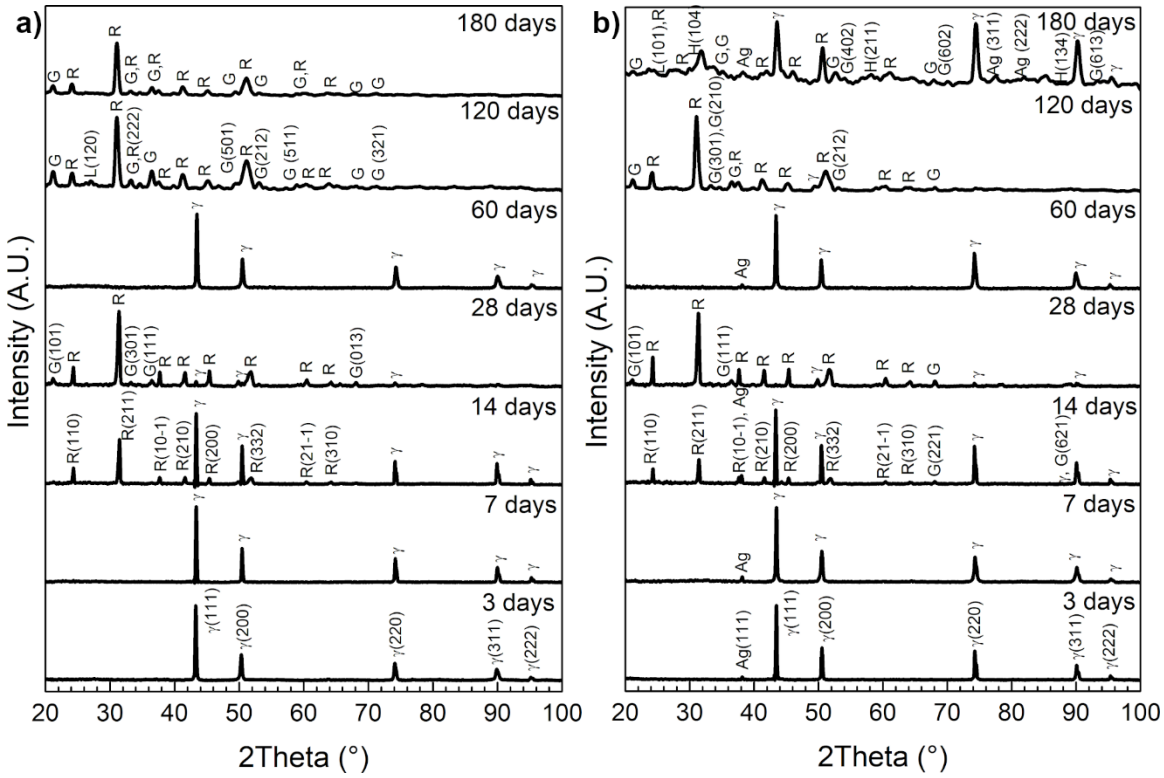

Figure 5.9 Indexed XRD spectra of the a) 0Ag and b) 0.4Ag alloys surfaces as a function of immersion time (legend of detected phases: γ: austenite; R: rhodochrosite; G: goethite; L: lepidocrocite; Ag: silver; H: hematite).

II was relatively similar, although the intensity of all peaks was weaker than that of DP-I peaks, possibly due to the limited amount of DP-II powders available for the FT-IR analysis. The only difference was detected for the 0.4Ag alloy at 14 days, where a peak associated to the stretching of the C=O bond was observed, which could be associated to ongoing carbonate formation from carbonic acid formed as an intermediate compound. The presence of phosphate group in both DP typologies indicated that these compounds were characterized by low binding strength with the samples surface especially at short times (up to 28 days), as discussed in the following section.

5.5.5 Electrochemical impedance spectroscopy

Figure 5.11 reports the results obtained for EIS tests on corroded surfaces of both alloys in the annealed state at different timepoints. Firstly, after 3, 7, 14 and 60 days of immersion, the alloys showed a behavior that could be reconducted to the formation of a porous film on the sample surface, signifying incomplete passivation. Secondly, at 28, 120 and 180 days, both materials had a behavior that could be associated to a completely passivated material, which was completely different from the behavior of the material for shorter exposition times to the

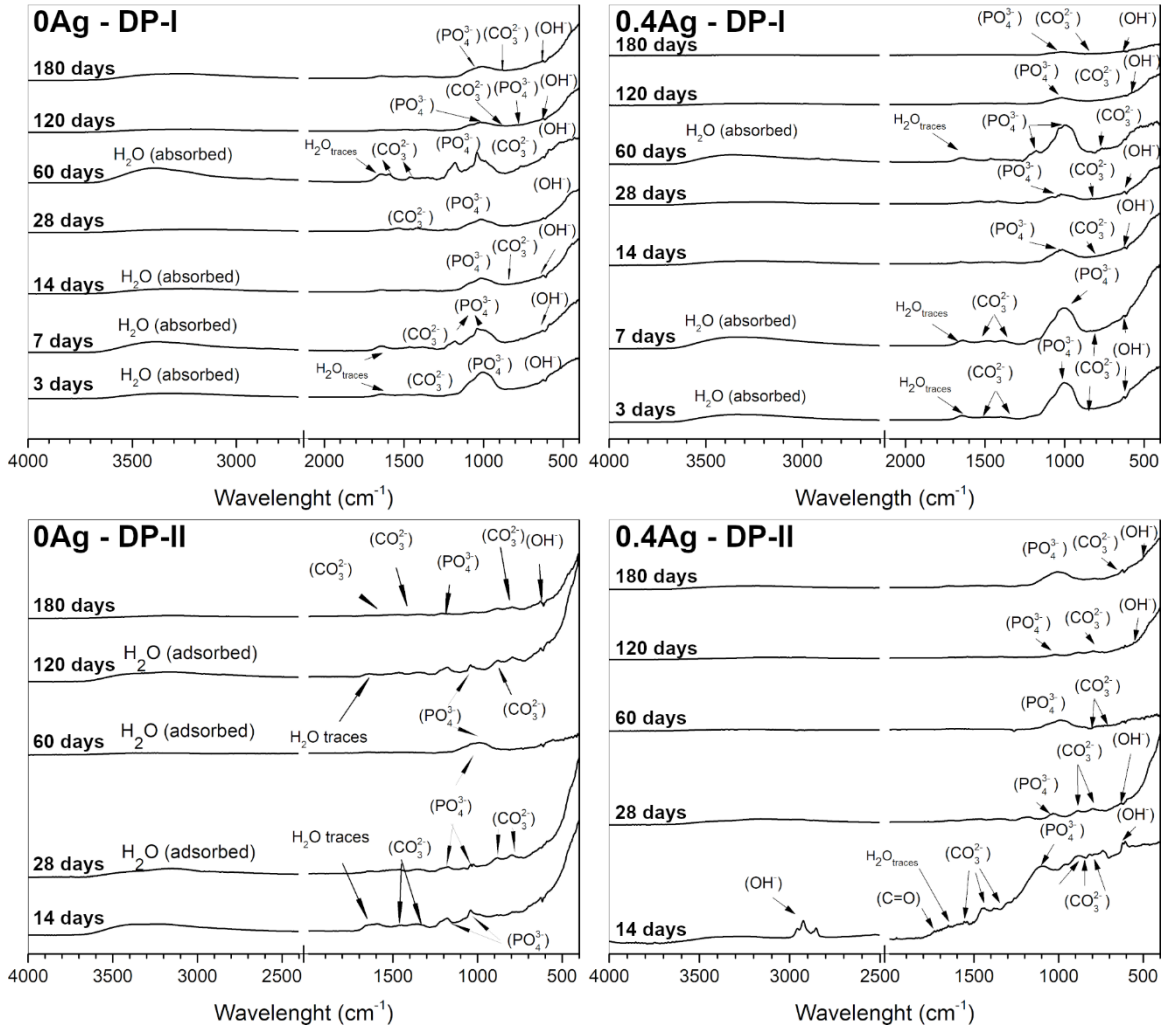

Figure 5.10 Indexed FT-IR spectra for both 0Ag and 0.4Ag alloys for degradation products collected from the exhausted solutions (DP-I) and that detached from sample surface during ultrasonic cleaning (DP-II).

medium. The particular characteristics after 60 days of immersion could be explained by the removal of the first corrosion layer observed at 14 and 28 days, replaced by a new growing layer showing an inhomogeneous thickness.

Nyquist plots for both 0Ag and 0.4Ag alloys (fig. 5.11 a,b) showed that, after 3, 7, 14 and 60 days of immersion, the surface had the characteristics of a constant phase element (CPE), representing formation of a porous layer. In addition, some samples showed an induction loop at frequency values below 1 Hz, which could represent adsorption of $CaCO_3$ from the solution, as detected from SEM images. These latter products were not detected by XRD, possibly because of the very low amount present on the surface. Looking at the Nyquist plots after 28 days, the shape of the curve suggested the presence of a pure capacitor, representing a compact

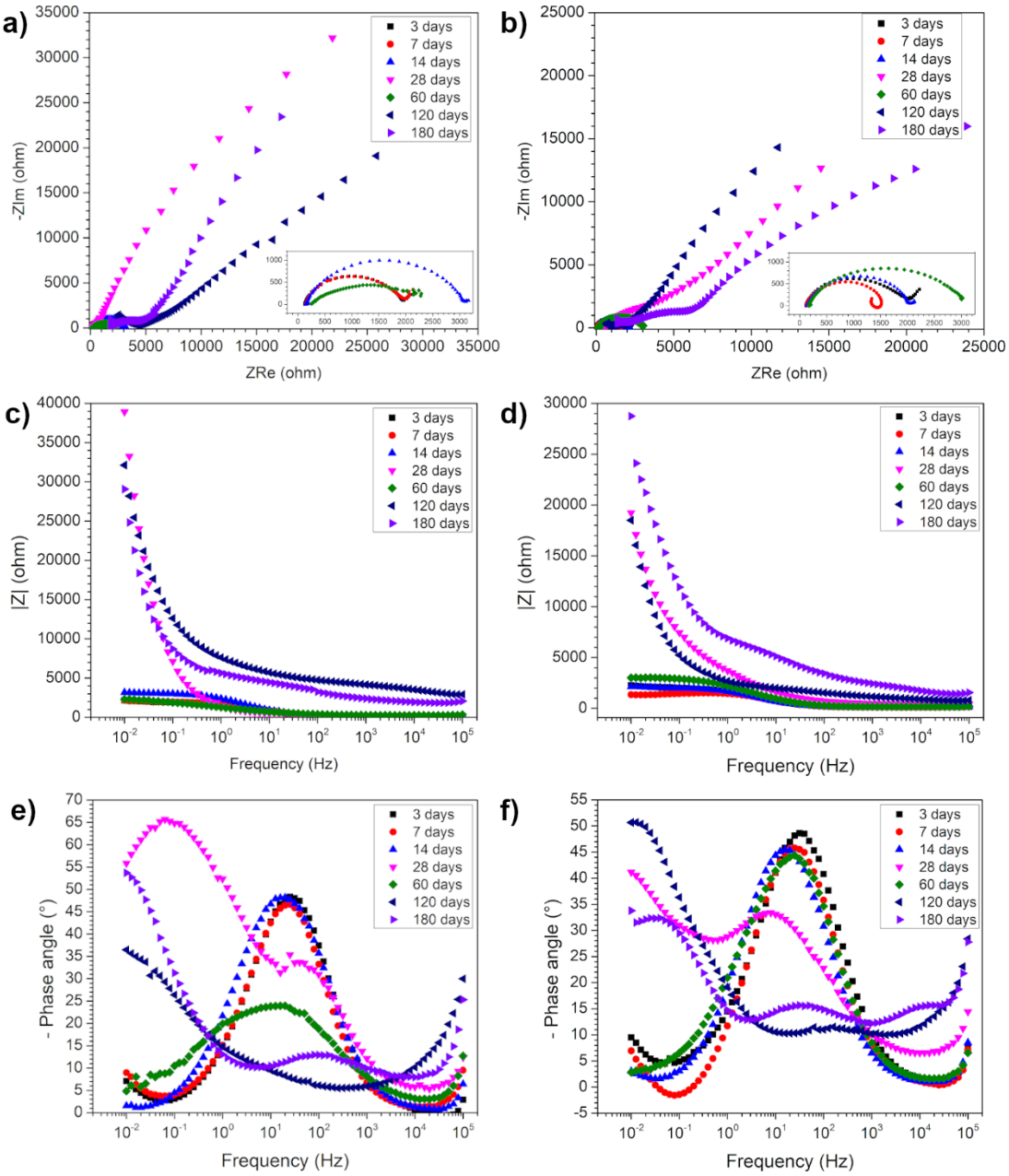

Figure 5.11 Results from EIS analyses on 0Ag and 0.4Ag alloys after different immersion times: Nyquist plot, a) 0Ag, b) 0.4Ag; Bode plot as a function of the impedance module, c) 0Ag, d) 0.4Ag; Bode plot as a function of the phase angle, e) 0Ag, f) 0.4Ag.

corrosion layer at the surface. Impedance reached much higher values than those obtained at short times. At 120 and 180 days of immersion, however, two different electrochemical characteristics were observed: At high frequency, a CPE was detected, while at lower frequency the Nyquist curves looked more like perfect capacitors, implying that two corrosion layers formed one on top of the other. First a porous corrosion layer, as detected after 60 day, reconducted to the thin phosphate-rich layer observed in figure 7; second, a compact corrosion

layer formed, associated with the thick rhodochrosite and goethite layer observed by SEM and XRD.

Bode plots, both as a function of absolute impedance (fig. 5.11 c-d) and of phase angle (fig. 11 e-f) supported the findings observed from Nyquist plots. Looking at the plots as a function of absolute impedance (fig. 5.11 c-d), the peak in absolute impedance is one order of magnitude lower at 3, 7, 14, 60 days with respect to 28, 120 and 180 days. This signified that polarization resistance of the former group was much lower than for the latter, implying that corrosion could proceed effectively at short term, while it was hampered at long term. It must always be noted that at 60 days, because of the breakdown of the previously formed film with formation of a new film that was very inhomogeneous, electrochemical characteristics resembled those at short term. These features were further confirmed by Bode phase angle plots (fig. 5.11 e-f), showing a maximum phase shift at low frequencies for 28, 120 and 180 days, indicating that the stability of the corrosion layer on the surface was high. This implied that further corrosion of the substrate was unlikely to take place unless the layer suddenly broke. On the contrary, for 3, 7, 14 and 60 days, the phase angle was maximum at medium frequencies and minimum at low frequencies, indicating that the surface was active and could undergo further corrosion. In the case of 60 days, this could be explained with the fact that the formed film was not stable enough to hinder substrate corrosion.

5.6 Discussion

Results showed that the addition of a small quantity of Ag did not provoke any relevant effect on corrosion behavior, As neither the corrosion rate or the formation pattern of degradation products were affected. On the contrary, corrosion behavior changed over the analyzed timescale, moving from an active surface at short term to passive characteristics with negligible corrosion rate at longer terms.

5.6.1 Interfacial electrochemical reactions

Corrosion mechanism of Fe-Mn alloys at short term (up to 28 days) is well known and reported by several authors [11,12,226]. The oxidation reactions for both Fe and Mn can be written as follows:

$$M \rightarrow M^{2+} + 2e^{-} \quad (5.1)$$

where M can be either Fe or Mn. In the case of Fe, oxidation to Fe^{3+} was also reported[122,165,229]:

$$Fe^{2+} + e^- \rightarrow Fe^{3+} + 3e^- \quad (5.2)$$

The reduction reaction for Fe and Mn oxidation in aqueous CO_2 rich environments consists in carbon dioxide evolution into carbonic acid, leading to formation of carbonate ions combining to form carbonates at the material's interface:

$$CO_2(g) + H_2O\ (l) \rightarrow H_2CO_3(aq) \quad (5.3)$$

$$2H_2CO_3\ (aq) + 2e^- \rightarrow H_2\ (g) + 2HCO_3^-\ (aq) \quad (5.4)$$

$$2HCO_3^-\ (aq) + 2e^- \rightarrow H_2\ (g) + 2CO_3^{2-}(aq) \quad (5.5)$$

$$M^{2+}\ (s) + CO_3^{2-}(aq) \rightarrow MCO_3\ (s) \quad (5.6)$$

In this specific case, it was observed that only $MnCO_3$ is formed and not $FeCO_3$. This can be justified by the preferential release of Mn in solution with respect to Fe, as highlighted in figure 2. The preferential release of Mn could be ascribed by its lower electrochemical potential with respect to that of Fe (-1.185 V and -0.447 V respectively versus the standard hydrogen electrode (SHE) [98]). Moreover, the preferential compound formation for Mn at physiological pH (7.4) could be drawn from its Pourbaix diagram in aqueous solution, where passivation is predicted for pH values above 7.0 [99]. Another study also showed that $FeCO_3$ has poor stability in CO_2-rich environments [230].

At 28 days formation of goethite was detected on top of the rhodochrosite layer, both by EDS (figures 5.4 and 5.5) and XRD analyses (figure 5.9). The electrochemical reactions occurring at the surface can be described as follows. First, the oxidation reaction can still be described by equation 1. In this case, however, the reduction reaction consists in the formation of hydroxide ions from the reaction between water and gaseous oxygen:

$$O_2\ (g) + 2H_2O\ (l) + 4e^- \rightarrow 4OH^-(aq) \quad (5.7)$$

Fe then combines with hydroxide ions to form goethite:

$$2Fe^{2+}(aq) + 4OH^-(aq) \rightarrow 2FeO\ (s) \cdot 2H_2O\ (l) \rightarrow H_2(g) + 2FeO \cdot OH(s) \quad (5.8)$$

Although FT-IR analyses (figure 5.10) revealed the presence of PO_4^{3-} groups in both degradation products (DP-I, DP-II) after 3 days of immersion, however, phosphates were not

detected on corroded surfaces underlying the weaknesses (or low stability) of their binding with the samples surface. Phosphor comes from the solution, as it is present in the Hanks' balanced salts as hydrogen phosphates ($H_2PO_4^-/HPO_4^{2-}$) [18]. Formation of phosphate ions from hydrogen phosphates can be described by the following 2 equations:

$$2H_2PO_4^-(aq) + O_2(g) + 2e^- \rightarrow 2PO_4^{3-}(aq) + 2H_2O\ (l)\ (5.9a)$$

$$4HPO_4^-(aq) + O_2(g) + 4e^- \rightarrow 4PO_4^{3-}(aq) + 2H_2O(l)\ (5.9b)$$

Depending on the oxidation state of metallic ions, especially in the case of Fe, two reactions can describe formation of metallic phosphates:

$$3Fe^{2+}(aq) + 2PO_4^{3-}(aq) \rightarrow Fe_3(PO_4)_2\ (s)\ (5.10a)$$

$$Fe^{3+}(aq) + PO_4^{3-}(aq) \rightarrow FePO_4\ (s)\ (10b)$$

Binding strength of such phosphates on the surface is low in the first stages of corrosion (up to 28 days) while it becomes higher at longer durations (from 60 to 180 days of immersion), as witnessed by attachment of phosphates detected by SEM analyses with EDS, both from top (figures 5.4, 5) and cross-sectional analyses (figure 5.8). This could be due to a change in local pH at the surface which favors stabilization of phosphates.

At 120 and 180 days, especially in the case of the 0Ag alloy, XRD analyses detected formation of lepidocrocite (α-FeO·OH, figure 5.9). In addition, hematite (Fe_2O_3) was detected in the 0.4Ag alloy at 180 days. Since the availability of free Fe remained constant throughout the corrosion process, it can be supposed that both lepidocrocite and hematite formed from recombination of previously formed goethite, as already described elsewhere [18].

One of the most peculiar features concerning the evolution in corrosion mechanism concerns the partial breakage of the stable layer detected at 28 days. This layer was first replaced by a thin phosphate layer on top of which a new layer grew, composed by rhodochrosite and goethite, together with lepidocrocite and, at 180 days, hematite. It was previously reported that dissolution of passive layers in chloride-rich solutions can be promoted by chloride attack, which locally destabilize the film by pitting, finally causing its detachment [231]. Since HMSS is also a chloride-rich solution closely mimicking the ionic composition of human plasma [18], it can be deducted that this mechanism can have taken place.

5.6.2 Overall corrosion mechanism from interfacial observations

The overall corrosion mechanism can be synthesized as reported in figure 5.12 and described as follows. First, a standard redox reaction occurs at the surface, where oxidation of Fe and Mn is promoted by oxygen reduction. Fe and Mn will start to form unstable phosphates with the corresponding ions present in solution, as detected by FT-IR analyses. Secondly, starting from 7 days of immersion and up to 14 days, Mn ions reacted with surface carbonate ions, preferentially stimulating formation of rhodochrosite which attaches to the surface, forming a porous layer with low polarization resistance. This layer showed the electrochemical characteristics of a constant phase element, indicating that the material is partially active. This layer will grow until 28 days of immersion, leading to formation of a single electrochemically stable layer, modelled as a capacitor accordingly to EIS tests. Due to chloride attack from ions present in solution, this layer was partially broken and locally replaced by a thin layer of phosphates which gives rise to a CPE-like behavior because of its low thickness, although attached phosphates are known to be stable at longer test durations on Fe-based alloys [11,154]. A new layer of rhodochrosite, goethite and lepidocrocite developed on top of this newly formed phosphate layer at 120 days, which was found after 180 days. This layer was described by the lower frequency part of the curve in Nyquist plots, where, after a high frequency CPE-like curve modelling the phosphate layer, a fully capacitive behavior was observed.

5.6.3 Role of Ag in corrosion

All analyses carried out in this work showed that micro-alloying of a TWIP steel with Ag does not produce any appreciable effect on corrosion rate, as already anticipated. A previous study focussing on the electrochemical behavior of Fe-Mn-C-Ag alloys already showed that such lean alloying does not produce any effect on the electrochemistry of these steels, leading even to a reduced corrosion current density [226]. A similar trend in mass loss was already observed in the literature for tests up to 28 days in a similar solution [232], while other researchers saw that the presence of Ag reduced the corrosion resistance of TWIP steels from electrochemical tests [72,74]. After 3 days, SEM analyses (figure 5.4) showed that some voids appeared around Ag particles, indicating that galvanic coupling could effectively take place, as the difference in electrochemical potential between Ag and TWIP steels could suggest. Galvanic coupling effect could explain why more nuclei of DPs were observed at the surface at 7 days with respect to the 0Ag alloy. However, the effect of galvanic coupling seemed to vanish after 14 days, where growth

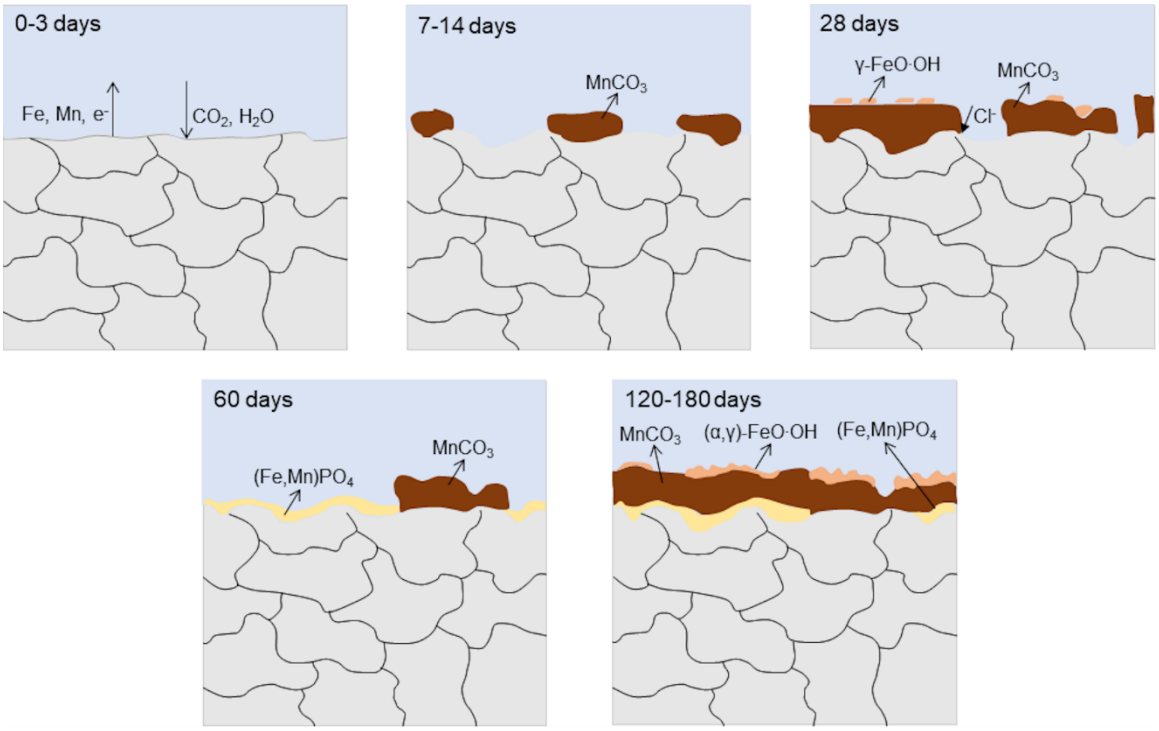

Figure 5.12 Schematics of the evolution of corrosion mechanism for the studied TWIP steels.

of rhodochrosite nuclei was observed, leading to XRD detection of such phase (figure 5.9). It could be supposed that interfacial reaction between free Mn and carbonate ions dominated over galvanic corrosion, promoting a faster product formation with respect to matrix dissolution. Once the corrosion layer became stable, this provided a protective effect preventing dissolution of the matrix, effectively hindering galvanic coupling promoted by the addition of Ag.

5.6.4 Correlation with *in vivo* studies

One of the most current issues in testing of Fe-based biodegradable alloys consists in poor data correlation between *in vitro* and *in vivo* studies. Several factors take part in this inconvenient, such as necessary setup simplifications [233,234], solutions that do not fully reproduce whole blood [18,235,236], and reduced test duration [237]. Most studies that limited immersion times below 28 days did not report phosphate formation [12,69,74,147], while other studies did but only after at least 28 days of immersion [154,175,191]. In this study phosphate formation on the sample surface was detected only after 60 days of immersion by EDS analyses in addition to partial breakage of the previously formed carbonate/hydroxide film. *In vivo* tests similarly detected formation of phosphates when implants were removed from animals after 12 months or more from implantation [60,61,70,138], which was deducted to be the cause for non-degradation of implants. One of the main conclusions that can be derived from this work is that

simple immersion tests can be good predictors for long-term *in vivo* corrosion behavior, at the following conditions. First, appropriate solutions must be used, mimicking as much as possible the composition of blood. Second, test duration must be of at least 2 months in order to ensure to analyze the temporal window were phosphates form, ensuring that newly developed materials can counter this phenomenon.

5.7 Conclusion

This work investigated the effect of a small Ag amount on the long-term *in vitro* corrosion of a biodegradable TWIP steel. It was found that corrosion rate was steady at 0.15 mm/year for the first 14 days of immersion, for then being reduced below 0.10 mm/year at 28 days, leading finally to negligible rates after 60 days. No DPs were observed after 3 days, while rhodochrosite started to nucleate at 7 days, growing into a porous layer made of cuboids at 14 days which became nearly compact after 28 days, where also goethite precipitated. Stoppage of corrosion was attributed to formation of a stable phosphate layer, which partly replaced the first porous layer that formed, composed by rhodochrosite and goethite. After 120 days, a fully stable and passive two-layer structure was observed, with a phosphate layer underneath a carbonate/hydroxide layer. Ag promoted galvanic coupling at early stages of corrosion, while its effect was suppressed after only 14 days of immersion because of product formation reactions at the solution/material interface. Lean alloying with Ag to promote galvanic coupling should be avoided as strategy to favor corrosion, since it showed limited efficacy over longer times. Even with a thoroughly simplified setup, formation of phosphates was successfully monitored, showing correlation with phenomena observed in existing *in vivo* studies preventing full degradation of Fe-based implants. Further research should focus in developing strategies which modify the surface electrochemistry on the alloys, preventing formation of stable carbonates and phosphates at long term, thus potentially promoting sustained device degradation over the required lifespan.

5.8 Acknowledgements

The authors would like to thank Vicky Dodier and Pascale Chevallier from Laval University for assistance with MP-AES and FT-IR analyses, respectively. S. L. acknowledges funding from a Vanier Canada Graduate Scholarship (2017-2020). This work was supported by the Natural Science and Engineering Research Council of Canada (Discovery, Strategic,

Collaborative Research and Development, and College-University-Industry Programs), the Quebec Ministry of Economy and Innovation, the Canadian Foundation for Innovation, and the FRQ-Santé through the support of the Research Center of the University Quebec Hospital, Regenerative Medicine Division.

5.9 Author contributions

SL, SG and CP designed the study. SL, NG and MV cast and processed the alloys. SL, SG, LMA and CP carried out sample preparation and immersion tests. SL prepared the solutions for MP-AES analyses, performed all SEM and EIS tests and analyzed such data. LMA performed and analyzed FT-IR analyses. RC performed XRD studies and critically assisted SL with spectra indexation. MV and DM supervised the research; DM provided the base idea and secured funding for this work. SL wrote the first manuscript draft; all authors critically contributed to revision of the manuscript and have given approval to its final version.

6. General discussion

This thesis was designed and developed with the aim of improving the corrosion behavior of TWIP steels by adding a small amount of Ag to the composition, with the hypothesis that galvanic coupling could be created between Ag-rich second phases and the Fe-Mn-C matrix. Thinking towards applying these alloys in an industrial scale production, casting and plastic deformation were retained for material production. This chapter first summarizes the experimental findings from this work in terms of microstructural, mechanical and corrosion properties. Successively, a critical discussion of such findings is provided in order to validate whether the Fe-Mn-C-Ag system is viable for thin biodegradable stents, also providing an outlook towards production of actual stents. Finally, the limitations of this work and of TWIP steels more in general are discussed.

6.1 Summary and significance of the findings of this work

The first challenge that was tackled in chapter 1 consisted in reviewing the state of the art in Fe-based degradable metals in order to assess current findings for identifying the shortcomings in previous works. The main limitation for biodegradable metals for stents lies in the vastly inferior mechanical properties with respect to Co-Cr alloys, preventing device miniaturization and limiting applicability. TWIP steels possess mechanical properties comparable to those of Co-Cr alloys. In order to improve corrosion, the strategy of promoting galvanic coupling by adding Ag was retained.

The first question that was answered in this project lied in how the presence of Ag affected the deformation mechanism of the studied TWIP steel. This is one of the most important aspects for materials for stents, since they are plastically deformed when implanted [24]. While some authors studied Fe-Mn-C-Ag alloys and performed basic studies on their tensile properties, no studies were carried out for thoroughly understanding if and how Ag modifies the microstructure as a function of the amount of plastic deformation imposed. First of all, a successful production process for Fe-Mn-C-Ag alloys was developed, involving casting, thermal treatments, and a combination of hot and cold rolling to obtain thin sheets from cast billets. All previous works involved production of the material via powder-based techniques (either PM or AM) which do not reflect industrial practice. After recrystallization annealing, tensile properties of a specific Fe-16Mn-0.7C alloy were found to be superior to those of L605 Co-Cr alloy. The addition of Ag

did not result in any improvement in yield and tensile strength, while it produced a lower elongation to failure, albeit still far superior to the requirements outlined in the introduction. Microstructural characterizations revealed that Ag actually impacts deformation mechanism in such a TWIP steel, moving from pure mechanical twinning to a combination of mechanical twinning and formation of mechanical martensite using a cold rolling thickness reduction of at least 25%. In addition, it was seen that texture evolution was modified by the presence of Ag.

The second question that was tackled in this project consisted in understanding how the presence of Ag impacts the recrystallization kinetics and mechanism of the TWIP steel presented in this work, directly correlating with the processing aspects outlined in chapter 2. The pertinence of this question lies directly within processing of stents, as they are typically processed by a succession of cold drawing steps followed by recrystallization annealing. Microhardness showed that the presence of Ag did not impact the recrystallization curve; however, the full recrystallization plateau was at higher values than in the case of the Ag-free alloy. EBSD analyses also revealed that, although it looked like both alloys underwent full recrystallization at temperatures above 650°C, only the 0Ag alloy underwent full recrystallization at 800°C, while the 0.4Ag alloy mostly underwent recovery. Moreover, it was found that the distribution of Schmid factors is broader in the Ag-containing alloys. Lower Schmid factors, indicating that activation of slip systems occurs with more difficulty, were directly associated to {111} grains. Together with formation of martensite at high levels of plastic deformation, this observation can explain why the presence of Ag reduced the ductility in the alloy after recrystallization annealing, as found in chapter 2. Such findings can help design better processes once these alloys are transferred to industrial practice.

After mechanical properties and processability, the most important property to assess for biodegradable metals is to validate that they effectively degrade. To do so, the first question to answer consists in assessing the electrochemical characteristics and the short-term degradation *in vitro*. Another important aspect in corrosion of biodegradable metals lies in the effect of plastic deformation since, as mentioned before, a stent works in a deformed state in the arteries. Electrochemical tests did not find any effect of plastic deformation on the electrochemical characteristics of the alloy, independently from the presence of Ag. The short-term corrosion mechanism consisted in the standard redox reactions leading to product formation, in this case rhodochrosite. In addition, adsorption of Ca on the surface was also observed. Moreover,

contrarily to what was expected and found in other works, the presence of Ag did not reduce corrosion resistance of the studied TWIP steel.

An oft neglected aspect for biodegradable metals is that corrosion evolves over time. The large majority of *in vitro* studies limit themselves to at most 28 days of immersion, while the normal life span of a stent is between 1 and 2 years, as described in the introduction. This often leads to misjudging the suitability of some materials for use as biodegradable metals, potentially leading to poor investments in costly animal studies. To bridge this gap, long-term immersion tests, with times ranging from 3 days to 6 months, were performed. First, it was observed that no difference in corrosion rate was present between the Ag-free and Ag-containing alloys, further validating that Ag has no impact over the corrosion rate of TWIP steels. Secondly, while corrosion of such TWIP steels went on between 3 and 14 days of immersion, it slowed down after 28 days for finally stopping after 60 days of immersion. This was attributed to formation of a stable phosphate layer after 60 days of immersion, which was not present up to 28 days. Contrarily to most *in vitro* studies on Fe-based biodegradable alloys, this correlates rather well with findings coming from *in vivo* tests, where formation of phosphates was found to be the cause for incomplete device degradation. These findings suggest that strategies aimed at sustained corrosion of Fe-based biodegradable metals should focus on modifying the surface electrochemistry in order to prevent phosphate formation.

6.2 Are Ag-alloyed TWIP steels viable candidates for thin cardiovascular degradable stents?

6.2.1 Validation of the metallurgical platform

From a metallurgical point of view, biodegradable metals should respect some minimal requirements in terms of tensile properties. Such requirements were outlined in section 1, and consist in having a YS above 200 MPa, an UTS above 300 MPa, an elongation to failure of at least 25% and an elastic modulus as high as possible. Validation of mechanical properties is rather straightforward, involving simple tensile tests that nonetheless must be performed. Most works found in literature showed the superiority of TWIP steels with respect to other candidate biodegradable metals [73,94], and this work further validates those findings. The inclusion of second phase particles mostly composed by Ag, as found in chapter 2, contributed to the

decrease in elongation to failure of the studied alloy. Similar results were found in another work [73].

This decrease in ductility can be explained by the findings contained in chapters 2 and 3. First, the presence of fine carbides was detected in both works for the 0.4Ag alloy as a function of the annealing treatment. The presence of Ag resulted in preferential formation and increased stability of such carbides, which were found to have either a M_3C or $M_{23}C_6$ structure from EDS analyses and thermodynamic simulations outlined in chapter 3. The effect of carbides on the reduction in elongation to failure was discussed in chapter 2, where their role in earlier onset of DSA was underlined. This earlier onset contributed to premature saturation of dislocation mobility, hence resulting in a reduced ductility. The second factor contributing to reduction in ductility was discovered in chapter 3, and directly correlates to the reduction in dislocation mobility just mentioned. Together with the reduced recrystallization effectiveness, it was discovered that the presence of Ag promoted formation of a higher ratio of grains with {111} orientation, which are the most favorable grains for developing mechanical twinning, as explained in chapter 1. In addition, those grains had the lower Schmid factor in the 0.4Ag alloy, which implies that dislocation gliding occurs with more difficulty. Combined with preferential formation of carbides, this can explain why the presence of Ag significantly reduced the elongation to failure of the here developed TWIP steel.

The use of other alloying elements, including Pd and S, produced somewhat contrasting results, indicating that the presence of second phases did not reduce ductility of a TWIP steel [94,161,162]. This difference in behavior can be ascribed to multiple factors. First, most alloys developed by other groups have a much higher content of Mn, which improves stability of the γ phase versus ε martensite. Secondly, such elements are soluble in the Fe-Mn-C matrix, contrarily to Ag. This implies that the second phases that are formed come from thermal treatments that promote such a trend. Moreover, such second phases are much smaller than what was found in this work: this could create less stress concentration around them, preventing earlier onset of DSA and allowing dislocations to glide more freely.

A more critical aspect in metallurgical validation lies in the assessment of processability of alloys through plastic deformation and recrystallization annealing, which also translates to the behavior in service of the device. In both chapters 2 and 3 the annealed material showed a variety of texture components, namely the γ fiber, Brass and Goss. In addition, no clearly predominant

grain orientations were detected, indicating that texturing of the material is weak. Such findings allow to conclude that, independently from the presence of Ag, the studied TWIP steel has good isotropy of mechanical properties, which is useful both for processing and stent deployment. After cold rolling, however, the presence of Ag promoted stronger texturing than in its absence. Moreover, the Copper texture component was more present, which directly correlates with the higher intensity of {111} grains detected in chapter 3, which in turn promoted stronger mechanical twinning. This resulted ultimately in the ductility reduction discussed above. Furthermore, the reduced recrystallization effectiveness observed in chapter 3 also suggests that additional care should be taken when processing the alloy containing Ag.

6.2.2 The importance of long-term corrosion tests

When it comes to biodegradable metals, one of the biggest challenges, if not the biggest one, lies in predicting their corrosion behavior and its evolution over time. The typical evaluation of this aspect is performed in three ways:

1. Electrochemical behavior assessment
2. Short-term immersion tests up to 28 days
3. *In vivo* tests up to 1 year.

Animal tests always constitute the last step in evaluation of corrosion behavior because of the time and resources required.

One of the most important aspects in corrosion tests for biodegradable metals lies in the choice of corrosive medium. Four mediums are most commonly used, namely NaCl 0.9 M, phosphate buffered saline solution (PBS), Hanks' balanced salt solution (either modified or not), and simulated body fluid (SBF). Such solutions reproduce more or less accurately the ionic composition of human plasma, as reported in table 0.2. As it can be seen, the solution that mimics the most closely our plasma is Hanks' modified salt solution, which was retained for this work.

Electrochemical analyses are often used because of testing rapidity with respect to static immersion or *in vivo* tests and can give good indications about the general corrosion rate of degradable metals and the reactions occurring at the surface, PDP and EIS tests being most commonly employed for these goals. These tests however use heavily simplified environments and do not consider the evolution of the same. Immersion tests, on the contrary, can better

elucidate the evolution in corrosion mechanism and the evolving environment, but care shall be taken concerning test times. This is especially important since corrosion of Fe-based biodegradable metals is not linear over time, thus making the use of multiple timepoints fundamental, as outlined in the ASTM F3268 standard. The more general ASTM G31 standard also outlines that static immersion tests at a single timepoint intrinsically assume linearity of the corrosion process. However, most papers limited testing time to 28 to 30 days at most [11,12,162,232] and/or using a single timepoint [69,90], which do not reflect the expected life cycle of a degradable stent.

From the results discussed in chapters 4 and 5, it was clearly observed that the presence of Ag did not induce any benefit on the degradation of the studied TWIP steel. In chapter 5, it was shown that Ag did not modify the corrosion potential nor the current density of the alloy independently from the deformation state, while promoting the same surface reactions (porous film formation and adsorption of ions from the solution). The only detected difference between the two alloys was formation of goethite after 14 days of immersion for the 0.4Ag alloy, together with a different effect of deformation on static immersion degradation rate, which is in turn based on mass loss. This was associated to the smaller grain size of the Ag-containing alloy already observed in chapters 2 and 3, which could have led to predominance of intergranular corrosion in this case with respect to the Ag-free alloy, which was supposed to be weaker than localized corrosion on twins, observed to be predominant on the latter material.

The findings discussed in chapter 5 appear however to tell a different story. At the same test duration (14 days), the corrosion rate for the 0Ag alloy is much lower than that reported in chapter 5, while that of the 0.4Ag alloy was comparable in both considered conditions. In addition, the reported standard deviations in corrosion rate for the 0Ag alloy are much larger in the works presented in chapter 4 in comparison to chapter 5. Two main factors can explain this difference. First, the solution used the works presented in chapter 4 was not sterilized, while that in chapter 5 was. It may be possible that some unwanted impurities present in the solution caused a faster corrosion. Second, the ultrasonic cleaning procedure adopted in chapter 4 slightly differed from that presented in chapter 5. In the former, the samples were left exposed to air for few minutes between extraction and ultrasonic cleaning, which may have destabilized some degradation products that attached to the surface, leading to a higher removal rate during ultrasonic cleaning, resulting in a higher corrosion rate. However, the differences between the

two works are limited to this point. The lack of effect of Ag on corrosion was clarified in chapter 5, where no difference in corrosion rate was evidenced at all timepoints (3-180 days). In addition, plastic deformation did not show any effect on corrosion, as seen by the electrochemical tests in chapter 5 and static immersion tests in both chapters 4 and 5.

One of the most interesting findings on corrosion mechanism can come from the analysis of exhausted solutions by MP-AES in both chapters 4 and 5. Such tests were carried out on the complete medium (including DPs) in chapter 4 while only the supernatant was analyzed in chapter 5. It can be seen that the concentration of Mn in solution after 14 days of immersion is very similar for both media, which can indicate that Mn released in solution is mainly unbound to other elements. On the contrary, the concentration of Fe is two orders of magnitude higher in the complete medium with respect to the supernatant. This could indicate the preference of Fe to bind to other elements in solution or atmosphere to form compounds that do not attach on the surface. Correlating these findings with FT-IR results shown in chapter 5, it could be deducted that DP-I are mostly Fe-based compounds that do not attach to the surface, such as $FeCO_3$ and $FePO_4$. Preferential stability of Mn compounds over Fe compounds can be justified by the Pourbaix diagrams of the two metals in aqueous solution [99], which predict passivation of Mn for a pH above 7, while passivation of Fe occurs only above pH 7.5. More stable compounds such as goethite attached only after 28 days of immersion for the Ag-free alloy, while they attached at 14 days for the Ag-containing alloy, as observed by XRD in both chapters 4 and 5. This can indicate that the presence of Ag can produce local chemical changes in the corrosion layer which promote earlier attachment of Fe-based compounds, while not affecting the overall evolution of corrosion mechanism.

6.2.3 The case for (not) adding Ag

It was seen in chapters 2 and 3 that, although Ag produces a reduction in ductility of the studied TWIP steel, as also reported by other authors [73], mechanical properties are still superior to those of Co-Cr alloys, implying that stents as small as those can be produced. It was however seen that the presence of Ag reduces recrystallization effectiveness, which is a cause of concern for streamlining processing of stents. Chapters 4 and 5 showed that the long-standing problem of formation of phosphates over long degradation times was not resolved by the addition of Ag as hypothesized at the beginning of the thesis. Although Ag promoted galvanic coupling at the early stages of corrosion (3-7 days of immersion), it was seen that product

formation after 14 days inhibited this mechanism, leading to formation and attachment of phosphates on the surface of the material from 60 days of immersion. On top of phosphates a new layer of carbonates and hydroxides formed at longer times, as shown in chapter 5. Overall, although mechanical performances are still excellent, the use of Ag cannot be recommended for enhancing degradation of TWIP steels because its effect is limited over time and does not hinder surface passivation.

6.3 From flat specimens to real stents

The previous section outlined the limitations of Ag as additional element for improving corrosion of TWIP steels. This section discusses the passage from flat surfaces to three-dimensional stents.

6.3.1 The choice of a production process

One of the biggest challenges of this work consisted in producing Fe-Mn-C-Ag alloys using casting, contrarily to literature reports using either PM or AM processes [71,73]. The choice of powders as starting material has the big advantage of ensuring easier and better mixing of Ag around the Fe-Mn-C matrix, since Ag is completely insoluble in it. In addition, Ag particle size could be tuned to have more micro-galvanic sites around the material, with the lower limit given by particle flowability in the case of AM processes. As explained in chapter 1, if the particle size is too low, it may not be melted by the scanning laser, leading to imperfections in the final piece. Results in chapters 2 and 3 showed that, by using a limited quantity of Ag (0.4% wt.), it is possible to achieve good particle distribution around the material by induction melting, which is most commonly used for production of industrial alloys.

The use of powder-based processes can have the undeniable advantage of creating near-net-shape products, especially in the case of AM. One of the biggest limitations of AM for producing stents lies in the size of the final device. At the current state of technology, a demonstrator made from 33 μm F75 powder (a Co-Cr alloy similar to L605) achieved a strut thickness of 230 μm [238], four times larger than the smallest commercial stent made from extrusion, drawing and laser cutting. The reason for such a large strut thickness was attributed to limitations in process resolution, where the minimal layer thickness is 20 μm with commercial AM machines. Another limitation of powder-based processes is porosity of the built parts, which

often requires post-process densification. Seen the very small size of the device, the presence of any porosity is unacceptable for ensuring proper reliability.

Other alternative technologies have emerged, including electroforming. However, electrodeposition of Fe-Mn-C steels is still an open question in research even for flat surfaces, which makes the choice inappropriate. Finally, reports on stents produced from photo-chemically etched flat sheets that were spot welded are present in the literature for Zn [239]. Such technology appears promising for reducing device cost. However, weldability should be validated for TWIP steels, and resistance of the welded spots should be verified.

6.3.2 Production of minitube prototypes

Beyond the works reported in chapters 2-5, this work also explored machinability of the Ag-free TWIP steel and the possibility of producing minitubes from such a process. These minitubes can be considered stent precursors, onto which laser cutting can be applied to obtain a final device. These results were achieved through a partnership with AMEC Usinage Inc. and proved the feasibility of machining small tubes. Starting from billets with a diameter of 5 cm and a length of 18 cm obtained from the larger cast billets described in the introduction and chapter 2, minitubes were machined by drilling a 5 mm hole in the center of such billets, for then turning the exterior of the billet up to a 100 μm wall thickness. After preliminary tests on billets with a length of 5 cm, a lot of 23 10 cm long minitubes with very small deviation from the nominal dimensions were obtained. A further test allowed to obtain a precursor with a wall thickness as small as 50 μm, even smaller than commercially produced stents. An example of such minitubes is reported in figure 6.1.

6.4 Limitations

6.4.1 Limitations of this work

This work focussed on the development of a metallurgical platform based on TWIP steels for biodegradable stents, investigating in depth the metallurgical and corrosion behavior and processability of an Ag-alloyed TWIP steel. However, several aspects on validation of such a platform were not examined in this thesis.

The first and most evident aspect lies in the lack of biological data. It is evident that, before performing any animal test, validation on both cytocompatibility and hemocompatibility of the

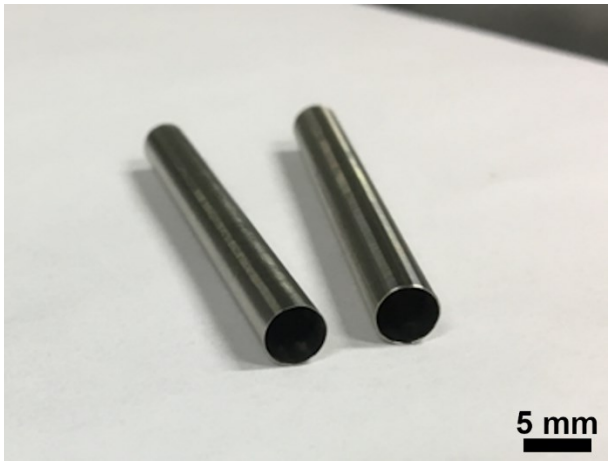

Figure 6.1 Minitube prototypes produced in this work.

studied TWIP steel shall be carried out. In order to do so, cell lines relevant to the considered application must be used, in this case human ECs and SMCs. Hemocompatibility assessment tests should validate that human blood does not tend to form thrombi on the material nor activates the release of free hemoglobin. Preliminary tests on the developed alloys (not shown here) highlighted that the presence of Ag does not cause any adverse effect on both cytocompatibility and hemocompatibility of the studied TWIP steel. Hemocompatibility was comparable to that of 316L, while acute cytotoxicity was reported towards ECs. This is a known effect due to the accumulation of insoluble DPs during cytotoxicity tests which cause a bias on the results [122,123].

Successively, no dynamic corrosion tests were performed. Such tests are more relevant because they remove loose DPs from the surface thanks to fluid flow [233]. However, the results obtained in chapter 5 correlated pretty well to *in vivo* tests in terms of formation of passive layers over time, indicating that the use of static immersion tests can suffice at the condition of using the appropriate timepoints and going beyond the first month of immersion.

A final aspect that was not treated in this thesis consists in the post-processing steps for moving from flat samples to cut and polished stents. As presented in the introduction, once minitubes are produced, laser cutting and electropolishing are performed to obtain the final device. Laser cutting tests performed in other works are encouraging towards obtention of a stent made from TWIP steels [6,240]. The development of an electropolishing procedure is however an unsolved challenge for TWIP steel stents and shall be addressed in future works. Some reports are currently available concerning electropolishing of flat specimens [195],

implying that transfer of such technique could be obtained, but care should be used for obtaining reproducible results on a complex geometry such as that of a stent.

6.4.2 Limitations of TWIP steels for cardiovascular stents

This work highlighted and validated the potential of TWIP steels for cardiovascular stents in terms of mechanical properties and processability. It however demonstrated that the modification of corrosion mechanism is still an unsolved challenge. The use of Ag, although promoting galvanic coupling at early stages of corrosion, did not prevent passivation of the material after at least 60 days of immersion, similarly to what was observed by *in vivo* tests on Fe-Mn alloys and Fe-Mn-C steels [70,138]. Similar conclusions could be drawn when other noble elements were added to a Fe-Mn-C matrix, especially in the case of Pd. The corrosion behavior of Fe-Mn-C-Pd steels was good after 28 days *in vitro* tests [12], but animal studies showed that an implant made from such a material did not degrade after 12 months due to the presence of phosphates on the surface [70]. Other works also showed very recently that the addition of Ag does not affect corrosion at 28 days or longer [232], including a report on animal tests [241]. One of the biggest causes for concern observed in this latter report comes from the detection of H_2 bubbles on the surface of a Fe-35Mn-1Ag implant, which was attributed to inflammatory responses locally lowering the pH. The released amount of H_2 was however much lower than what was detected for a Mg-based implant, suggesting that chronic cytotoxicity should not be a major cause for concern.

Other *in vitro* works on acute cytocompatibility showed that the presence of Fe-based insoluble DPs causes oxidative stress in ECs, which in turn leads to acute cytotoxicity [123,124]. This was especially detected for hydroxide species that bind with Fe^{3+} ions released from the surface [124,125], which was also hypothesized to occur for the alloys studied in this work. Accurate biological characterizations are necessary to assess whether the possible cytotoxic effect of Fe-based alloys is limited to the acute inflammation period, in which case it should not be a major cause for concern. However, if it was discovered that Fe-based alloys produce chronic cytotoxicity in cardiovascular environments, major reflections shall be undertaken to reassess whether Fe-based alloys can be used for degradable stents.

Conclusions and perspectives

This work successfully developed two TWIP steels, one with and one without Ag, with mechanical properties superior to those of Co-Cr alloys, indicating the potential for manufacturing small stents for pediatric and cerebrovascular applications. The presence of Ag led to modified deformation and recrystallization mechanisms, which should be considered when designing production processes for very thin stents. The addition of Ag was however found neither to modify the electrochemistry of the studied TWIP steel nor to prevent formation of a stable passive layer over immersion times beyond 1 month. The works on long-term corrosion carried out in this thesis showed very similar outcomes to animal tests, which is a unique occurrence. This proved the potential of simple immersion tests to properly predict *in vivo* outcomes, at the condition that the right timeframe and design of experiments is considered.

In view of clinical translation of TWIP steels for temporary vascular stents, the mechanical properties of the bulk alloy shall not be modified since they are already optimal. The focus should be put towards modifying the surface with the goal of altering the electrochemical behavior of the material. To do so, some strategies outlined in chapter 1 may be applied to the here studied TWIP steel. One of those strategies consists in nitriding the very first atomic layers, which proved effective in guaranteeing corrosion of pure Fe stents. Another strategy that should be explored is the application of a thin polymeric coating, which is normally employed to embed antiproliferative drugs in DES. In the case of TWIP steels, this could lower the local pH at the surface, expanding the electrochemically active region for both Fe and Mn where stable passive films are not formed by corrosion of the material.

Finally, three more steps should be undertaken towards clinical translation once the corrosion problematic will be solved. The first step should consist in thorough *in vitro* biological validation of the alloy and the eventual coating by means of appropriately designed cytocompatibility and hemocompatibility tests. Second, starting from the preliminary works outlined in the general discussion of this thesis, production of full stent prototypes should be carried out, aiming at outer tube diameters below 3 mm and strut thicknesses below 60 μm to at least match the dimensions of commercial Co-Cr DES. At last, once these two challenges are solved, animal tests will be the final validation step towards clinical trials in humans, by ensuring to use appropriate animal models which will not bias the transferability.

Bibliography

[1] World Health Organization, WHO - The top 10 causes of death, 24 Maggio. (2018) 1–7. http://www.who.int/mediacentre/factsheets/fs310/en/ (accessed May 20, 2020).

[2] R.N. Mitchell, F.J. Schoen, Blood Vessels, in: V. Kumar, A.K. Abbas, N. Fausto, J.C. Aster (Eds.), Robbins Cotran Pathol. Basis Dis., 8th ed., Saunders, Philadelphia, 2010: pp. 487–528.

[3] T.A. of the E. Britannica, Coronary Stent, (2010). https://www.britannica.com/science/coronary-stent (accessed September 8, 2020).

[4] J. Torrado, L. Buckley, A. Durán, P. Trujillo, S. Toldo, J. Valle Raleigh, A. Abbate, G. Biondi-Zoccai, L.A. Guzmán, Restenosis, Stent Thrombosis, and Bleeding Complications: Navigating Between Scylla and Charybdis, J. Am. Coll. Cardiol. 71 (2018) 1676–1695. https://doi.org/10.1016/j.jacc.2018.02.023.

[5] N. Foin, R.D. Lee, R. Torii, J.L. Guitierrez-Chico, A. Mattesini, S. Nijjer, S. Sen, R. Petraco, J.E. Davies, C. Di Mario, M. Joner, R. Virmani, P. Wong, Impact of stent strut design in metallic stents and biodegradable scaffolds, Int. J. Cardiol. 177 (2014) 800–808. https://doi.org/10.1016/j.ijcard.2014.09.143.

[6] H. Hermawan, D. Mantovani, Process of prototyping coronary stents from biodegradable Fe–Mn alloys, Acta Biomater. 9 (2013) 8585–8592. https://doi.org/10.1016/j.actbio.2013.04.027.

[7] H. Hermawan, Updates on the research and development of absorbable metals for biomedical applications, Prog. Biomater. 7 (2018) 93–110. https://doi.org/10.1007/s40204-018-0091-4.

[8] A. Saeed-Akbari, J. Imlau, U. Prahl, W. Bleck, Derivation and Variation in Composition-Dependent Stacking Fault Energy Maps Based on Subregular Solution Model in High-Manganese Steels, Metall. Mater. Trans. A. 40 (2009) 3076–3090. https://doi.org/10.1007/s11661-009-0050-8.

[9] P. Rodriguez, Serrated plastic flow, Bull. Mater. Sci. 6 (1984) 653–663. https://doi.org/10.1007/BF02743993.

[10] H.-S. Han, S. Loffredo, I. Jun, J. Edwards, Y.-C. Kim, H.-K. Seok, F. Witte, D. Mantovani, S. Glyn-Jones, Current status and outlook on the clinical translation of biodegradable metals, Mater. Today. 23 (2019) 57–71. https://doi.org/10.1016/j.mattod.2018.05.018.

[11] H. Hermawan, A. Purnama, D. Dube, J. Couet, D. Mantovani, Fe–Mn alloys for metallic biodegradable stents: Degradation and cell viability studies☆, Acta Biomater. 6 (2010) 1852–1860. https://doi.org/10.1016/j.actbio.2009.11.025.

[12] M. Schinhammer, P. Steiger, F. Moszner, J.F. Loffler, P.J. Uggowitzer, Degradation performance of biodegradable FeMnC(Pd) alloys, Mater. Sci. Eng. C. 33 (2013) 1882–1893. https://doi.org/http://dx.doi.org/10.1016/j.msec.2012.10.013.

[13] M. Moravej, F. Prima, M. Fiset, D. Mantovani, Electroformed iron as new biomaterial for degradable stents: Development process and structure-properties relationship, Acta Biomater. 6 (2010) 1726–1735. https://doi.org/10.1016/j.actbio.2010.01.010.

[14] W.-J. Lin, D.-Y. Zhang, G. Zhang, H.-T. Sun, H.-P. Qi, L.-P. Chen, Z.-Q. Liu, R.-L. Gao, W. Zheng, Design and characterization of a novel biocorrodible iron-based drug-eluting coronary scaffold, Mater. Des. 91 (2016) 72–79. https://doi.org/10.1016/j.matdes.2015.11.045.

[15] S. Loffredo, H. Hermawan, M. Vedani, D. Mantovani, Absorbable metals for cardiovascular applications, in: M. Niinomi (Ed.), Met. Biomed. Devices, 2nd ed., Elsevier, 2019: pp. 523–543. https://doi.org/10.1016/B978-0-08-102666-3.00020-1.

[16] G. Mani, M.D. Feldman, D. Patel, C.M. Agrawal, Coronary stents: A materials perspective, Biomaterials. 28 (2007) 1689–1710. https://doi.org/10.1016/j.biomaterials.2006.11.042.

[17] J. Poncin, P; Proft, Stent Tubing: Understanding the Desired Attributes, in: Med. Device Mater. Proc. Mater. Process. Med. Devices Conf. Mater. Park. OH ASM Int., 2004: pp. 253–259.

[18] R. Tolouei, J. Harrison, C. Paternoster, S. Turgeon, P. Chevallier, D. Mantovani, The use of multiple pseudo-physiological solutions to simulate the degradation behavior of pure iron as a metallic resorbable implant: A surface-characterization study, Phys. Chem. Chem. Phys. 18 (2016) 19637–19646. https://doi.org/10.1039/c6cp02451c.

[19] A. V. Chobanian, G.L. Bakris, H.R. Black, W.C. Cushman, L.A. Green, J.L. Izzo, D.W. Jones, B.J. Materson, S. Oparil, J.T. Wright, E.J. Roccella, The Seventh Report of the Joint National Committee on Prevention, Detection, Evaluation, and Treatment of High Blood Pressure: The JNC 7 Report, J. Am. Med. Assoc. 289 (2003) 2560–2572. https://doi.org/10.1001/jama.289.19.2560.

[20] A.R. Grüntzig, Å. Senning, W.E. Siegenthaler, Nonoperative Dilatation of Coronary-Artery

Stenosis, N. Engl. J. Med. 301 (1979) 61–68. https://doi.org/10.1056/NEJM197907123010201.

[21] F.J. Schoen, R.F. Padera, Endovascular Stents, Vascular Grafts, and Stent Grafts, in: B.D. Ratner, A.S. Hoffmann, F.J. Schoen, J.E. Lemons (Eds.), Biomater. Sci., 3rd ed., Elsevier, 2013: pp. 771–784. https://doi.org/10.1016/B978-0-08-087780-8.00068-1.

[22] F. Alfonso, R.A. Byrne, F. Rivero, A. Kastrati, Current Treatment of In-Stent Restenosis, J. Am. Coll. Cardiol. 63 (2014) 2659–2673. https://doi.org/10.1016/j.jacc.2014.02.545.

[23] Y. Zhu, H. Zhang, Y. Zhang, H. Wu, L. Wei, G. Zhou, Y. Zhang, L. Deng, Y. Cheng, M. Li, H.A. Santos, W. Cui, Endovascular Metal Devices for the Treatment of Cerebrovascular Diseases, Adv. Mater. (2018) 1805452. https://doi.org/10.1002/adma.201805452.

[24] P. Poncin, J. Proft, Stent Tubing: Understanding the Desired Attributes, in: Med. Device Mater. Proc. Mater. Process. Med. Devices Conf. Mater. Park. OH ASM Int., 2004: pp. 253–259.

[25] F.J. Schoen, R.N. Mitchell, Tissues, the Extracellular Matrix, and Cell-Biomaterial Interactions, in: Biomater. Sci. An Introd. to Mater. Third Ed., Third Edit, Elsevier, 2013: pp. 452–474. https://doi.org/10.1016/B978-0-08-087780-8.00039-5.

[26] J.A. Ormiston, P.W.S. Serruys, Bioabsorbable coronary stents, Circ. Cardiovasc. Interv. 2 (2009) 255–260. https://doi.org/10.1161/CIRCINTERVENTIONS.109.859173.

[27] Y.F. Zheng, X.N. Gu, F. Witte, Biodegradable metals, Mater. Sci. Eng. R Reports. 77 (2014) 1–34. https://doi.org/10.1016/j.mser.2014.01.001.

[28] Q. Chen, G.A. Thouas, Metallic implant biomaterials, Mater. Sci. Eng. R Reports. 87 (2015) 1–57. https://doi.org/10.1016/j.mser.2014.10.001.

[29] U. Sigwart, J. Puel, V. Mirkovitch, F. Joffre, L. Kappenberger, Intravascular Stents to Prevent Occlusion and Re-Stenosis after Transluminal Angioplasty, N. Engl. J. Med. 316 (1987) 701–706. https://doi.org/10.1056/NEJM198703193161201.

[30] U. Sigwart, P. Urban, S. Golf, U. Kaufmann, C. Imbert, A. Fischer, L. Kappenberger, Emergency stenting for acute occlusion after coronary balloon angioplasty., Circulation. 78 (1988) 1121–7. https://doi.org/10.1161/01.cir.78.5.1121.

[31] S.C. Wong, D.S. Baim, R.A. Schatz, P.S. Teirstein, S.B. King, R.C. Curry, R.R. Heuser, S.G. Ellis, M.W. Cleman, P. Overlie, J.W. Hirshfeld, C.M. Walker, F. Litvack, D. Fish, J.A. Brinker,

M. Buchbinder, S. Goldberg, Ya Chien Chuang, M.B. Leon, Immediate results and late outcomes after stent implantation in saphenous vein graft lesions: The multicenter U.S. Palmaz-Schatz stent experience, J. Am. Coll. Cardiol. 26 (1995) 704–712. https://doi.org/10.1016/0735-1097(95)00217-R.

[32] R. Virmani, A. Farb, Pathology of in-stent restenosis., Curr. Opin. Lipidol. 10 (1999) 499–506. https://doi.org/10.1097/00041433-199912000-00004.

[33] R. Köster, D. Vieluf, M. Kiehn, M. Sommerauer, J. Kähler, S. Baldus, T. Meinertz, C.W. Hamm, Nickel and molybdenum contact allergies in patients with coronary in-stent restenosis, Lancet. 356 (2000) 1895–1897. https://doi.org/10.1016/S0140-6736(00)03262-1.

[34] J. Iqbal, J. Gunn, P.W. Serruys, Coronary stents: Historical development, current status and future directions, Br. Med. Bull. 106 (2013) 193–211. https://doi.org/10.1093/bmb/ldt009.

[35] E. Camenzind, P.G. Steg, W. Wijns, Stent Thrombosis Late After Implantation of First-Generation Drug-Eluting Stents, Circulation. 115 (2007).

[36] E.P. McFadden, E. Stabile, E. Regar, E. Cheneau, A.T. Ong, T. Kinnaird, W.O. Suddath, N.J. Weissman, R. Torguson, K.M. Kent, A.D. Pichard, L.F. Satler, R. Waksman, P.W. Serruys, Late thrombosis in drug-eluting coronary stents after discontinuation of antiplatelet therapy, Lancet. 364 (2004) 1519–1521. https://doi.org/10.1016/S0140-6736(04)17275-9.

[37] Y. Sotomi, Y. Onuma, C. Collet, E. Tenekecioglu, R. Virmani, N.S. Kleiman, P.W. Serruys, Bioresorbable scaffold: The emerging reality and future directions, Circ. Res. 120 (2017) 1341–1352. https://doi.org/10.1161/CIRCRESAHA.117.310275.

[38] C. Indolfi, S. De Rosa, A. Colombo, Bioresorbable vascular scaffolds — basic concepts and clinical outcome, Nat. Rev. Cardiol. 13 (2016) 719–729. https://doi.org/10.1038/nrcardio.2016.151.

[39] S. Nishio, K. Kosuga, K. Igaki, M. Okada, E. Kyo, T. Tsuji, E. Takeuchi, Y. Inuzuka, S. Takeda, T. Hata, Y. Takeuchi, Y. Kawada, T. Harita, J. Seki, S. Akamatsu, S. Hasegawa, N. Bruining, S. Brugaletta, S. de Winter, T. Muramatsu, Y. Onuma, P.W. Serruys, S. Ikeguchi, Long-Term (10 Years) Clinical Outcomes of First-in-Human Biodegradable Poly-l-Lactic Acid Coronary Stents: Clinical Perspective, Circulation. 125 (2012) 2343–2352. https://doi.org/10.1161/CIRCULATIONAHA.110.000901.

[40] J.J. Wykrzykowska, R.P. Kraak, S.H. Hofma, R.J. van der Schaaf, E.K. Arkenbout, A.J. IJsselmuiden, J. Elias, I.M. van Dongen, R.Y.G. Tijssen, K.T. Koch, J. Baan, M.M. Vis, R.J. de Winter, J.J. Piek, J.G.P. Tijssen, J.P.S. Henriques, Bioresorbable Scaffolds versus Metallic Stents in Routine PCI, N. Engl. J. Med. 376 (2017) 2319–2328. https://doi.org/10.1056/NEJMoa1614954.

[41] P.W. Serruys, B. Chevalier, Y. Sotomi, A. Cequier, D. Carrié, J.J. Piek, A.J. Van Boven, M. Dominici, D. Dudek, D. McClean, S. Helqvist, M. Haude, S. Reith, M. de Sousa Almeida, G. Campo, A. Iñiguez, M. Sabaté, S. Windecker, Y. Onuma, Comparison of an everolimus-eluting bioresorbable scaffold with an everolimus-eluting metallic stent for the treatment of coronary artery stenosis (ABSORB II): a 3 year, randomised, controlled, single-blind, multicentre clinical trial, Lancet. 388 (2016) 2479–2491. https://doi.org/10.1016/S0140-6736(16)32050-5.

[42] Z.A. Ali, P.W. Serruys, T. Kimura, R. Gao, S.G. Ellis, D.J. Kereiakes, Y. Onuma, C. Simonton, Z. Zhang, G.W. Stone, 2-year outcomes with the Absorb bioresorbable scaffold for treatment of coronary artery disease: a systematic review and meta-analysis of seven randomised trials with an individual patient data substudy, Lancet. 390 (2017) 760–772. https://doi.org/10.1016/S0140-6736(17)31470-8.

[43] FDA, UPDATE on Increased Rate of Major Adverse Cardiac Events Observed in Patients Receiving Abbott Vascular's Absorb GT1 Bioresorbable Vascular Scaffold (BVS) - Letter to Health Care Providers, (2017). https://www.fda.gov/MedicalDevices/Safety/LetterstoHealthCareProviders/ucm582728.htm (accessed June 8, 2018).

[44] Y. Liu, Y. Zheng, X.-H. Chen, J.-A. Yang, H. Pan, D. Chen, L. Wang, J. Zhang, D. Zhu, S. Wu, K.W.K. Yeung, R.-C. Zeng, Y. Han, S. Guan, Fundamental Theory of Biodegradable Metals-Definition, Criteria, and Design, Adv. Funct. Mater. 1805402 (2019) 1805402. https://doi.org/10.1002/adfm.201805402.

[45] P.K. Bowen, E.R. Shearier, S. Zhao, R.J. Guillory, F. Zhao, J. Goldman, J.W. Drelich, Biodegradable Metals for Cardiovascular Stents: From Clinical Concerns to Recent Zn-Alloys, Adv. Healthc. Mater. 5 (2016) 1121–1140. https://doi.org/10.1002/adhm.201501019.

[46] J.M. Seitz, M. Durisin, J. Goldman, J.W. Drelich, Recent Advances in Biodegradable Metals for Medical Sutures: A Critical Review, Adv. Healthc. Mater. 4 (2015) 1915–1936. https://doi.org/10.1002/adhm.201500189.

[47] P. Lyon, I. Syed, A.J. Boden, K. Savage, Magnesium alloys containing rare earths, WO2010038016 (A1), 2010. https://worldwide.espacenet.com/publicationDetails/biblio?CC=WO&NR=2010038016A1&KC=A1&FT=D&ND=3&date=20100408&DB=&locale=en_EP# (accessed March 26, 2017).

[48] G. Yuan, P. Fu, W. Ding, Magnesium alloy used for degradable stent material in vivo and preparation method thereof, WO2011160534A1, 2011.

[49] B. Gerold, Implant made of a biodegradable magnesium alloy, US20150064054A1, 2015.

[50] L. Mao, L. Shen, J. Chen, X. Zhang, M. Kwak, Y. Wu, R. Fan, L. Zhang, J. Pei, G. Yuan, C. Song, J. Ge, W. Ding, A promising biodegradable magnesium alloy suitable for clinical vascular stent application, Sci. Rep. 7 (2017) 46343. https://doi.org/10.1038/srep46343.

[51] M. Haude, H. Ince, A. Abizaid, R. Toelg, P.A. Lemos, C. von Birgelen, E.H. Christiansen, W. Wijns, F.-J. Neumann, C. Kaiser, E. Eeckhout, S.T. Lim, J. Escaned, H.M. Garcia-Garcia, R. Waksman, Safety and performance of the second-generation drug-eluting absorbable metal scaffold in patients with de-novo coronary artery lesions (BIOSOLVE-II): 6 month results of a prospective, multicentre, non-randomised, first-in-man trial, Lancet. 387 (2016) 31–39. https://doi.org/10.1016/S0140-6736(15)00447-X.

[52] H.M. Garcia-Garcia, M. Haude, K. Kuku, A. Hideo-Kajita, H. Ince, A. Abizaid, R. Tölg, P.A. Lemos, C. von Birgelen, E.H. Christiansen, W. Wijns, J. Escaned, J. Dijkstra, R. Waksman, In vivo serial invasive imaging of the second-generation drug-eluting absorbable metal scaffold (Magmaris — DREAMS 2G) in de novo coronary lesions: Insights from the BIOSOLVE-II First-In-Man Trial, Int. J. Cardiol. 255 (2018) 22–28. https://doi.org/10.1016/j.ijcard.2017.12.053.

[53] M. Haude, H. Ince, A. Abizaid, R. Toelg, P.A. Lemos, C. von Birgelen, E.H. Christiansen, W. Wijns, F.-J. Neumann, C. Kaiser, E. Eeckhout, S.T. Lim, J. Escaned, Y. Onuma, H.M. Garcia-Garcia, R. Waksman, Sustained safety and performance of the second-generation drug-eluting absorbable metal scaffold in patients with de novo coronary lesions: 12-month clinical results and angiographic findings of the BIOSOLVE-II first-in-man trial., Eur. Heart J. 14 (2016) 24492–24500. https://doi.org/10.1093/eurheartj/ehw196.

[54] Biotronik inc., Magmaris product Details, (n.d.). http://www.magmaris.com/en/product-details (accessed April 1, 2020).

[55] Biotronik, Orsiro product details, (n.d.). http://www.orsiro.com/en/product-details (accessed September 12, 2016).

[56] P.K. Bowen, J. Drelich, J. Goldman, Zinc Exhibits Ideal Physiological Corrosion Behavior for Bioabsorbable Stents, Adv. Mater. 25 (2013) 2577–2582. https://doi.org/10.1002/adma.201300226.

[57] A.J. Drelich, S. Zhao, R.J. Guillory, J.W. Drelich, J. Goldman, Long-term surveillance of zinc implant in murine artery: Surprisingly steady biocorrosion rate, Acta Biomater. 58 (2017) 539–549. https://doi.org/10.1016/j.actbio.2017.05.045.

[58] G.R. Edwards, J.C. Shyne, O.D. Sherby, Strain softening in powder metallurgy zinc, Metall. Trans. 2 (1971) 2955–2958. https://doi.org/10.1007/BF02813287.

[59] E. Mostaed, M. Sikora-Jasinska, J.W. Drelich, M. Vedani, Zinc-based alloys for degradable vascular stent applications, Acta Biomater. 71 (2018) 1–23. https://doi.org/10.1016/j.actbio.2018.03.005.

[60] M. Peuster, P. Wohlsein, M. Brügmann, M. Ehlerding, K. Seidler, C. Fink, H. Brauer, A. Fischer, G. Hausdorf, A novel approach to temporary stenting: degradable cardiovascular stents produced from corrodible metal-results 6-18 months after implantation into New Zealand white rabbits., Heart. 86 (2001) 563–9. https://doi.org/10.1136/HEART.86.5.563.

[61] M. Peuster, C. Hesse, T. Schloo, C. Fink, P. Beerbaum, C. von Schnakenburg, Long-term biocompatibility of a corrodible peripheral iron stent in the porcine descending aorta, Biomaterials. 27 (2006) 4955–4962. https://doi.org/10.1016/j.biomaterials.2006.05.029.

[62] H. Hermawan, H. Alamdari, D. Mantovani, D. Dubé, Iron–manganese: new class of metallic degradable biomaterials prepared by powder metallurgy, Powder Metall. 51 (2008) 38–45. https://doi.org/10.1179/174329008X284868.

[63] M. Schinhammer, A.C. Hänzi, J.F. Löffler, P.J. Uggowitzer, Design strategy for biodegradable Fe-based alloys for medical applications, Acta Biomater. 6 (2010) 1705–1713. https://doi.org/10.1016/j.actbio.2009.07.039.

[64] H. Hermawan, D. Dubé, D. Mantovani, Degradable metallic biomaterials: design and development of Fe-Mn alloys for stents., J. Biomed. Mater. Res. A. 93 (2010) 1–11. https://doi.org/10.1002/jbm.a.32224.

[65] J. Crossgrove, W. Zheng, Manganese toxicity upon overexposure, NMR Biomed. 17 (2004) 544–553. https://doi.org/10.1002/nbm.931.

[66] B.C. De Cooman, Y. Estrin, S.K. Kim, Twinning-induced plasticity (TWIP) steels, Acta Mater. 142 (2018) 283–362. https://doi.org/10.1016/j.actamat.2017.06.046.

[67] O. Bouaziz, S. Allain, C.P. Scott, P. Cugy, D. Barbier, High manganese austenitic twinning induced plasticity steels: A review of the microstructure properties relationships, Curr. Opin. Solid State Mater. Sci. 15 (2011) 141–168. https://doi.org/10.1016/j.cossms.2011.04.002.

[68] H.G. Seiler, H. Sigel, A. Sigel, Handbook on toxicity of inorganic compounds, Marcel Dekker, New York, 1988.

[69] E. Mouzou, C. Paternoster, R. Tolouei, A. Purnama, P. Chevallier, D. Dubé, F. Prima, D. Mantovani, In vitro degradation behavior of Fe–20Mn–1.2C alloy in three different pseudo-physiological solutions, Mater. Sci. Eng. C. 61 (2016) 564–573. https://doi.org/10.1016/j.msec.2015.12.092.

[70] T. Kraus, F. Moszner, S. Fischerauer, M. Fiedler, E. Martinelli, J. Eichler, F. Witte, E. Willbold, M. Schinhammer, M. Meischel, P.J. Uggowitzer, J.F. Löffler, A. Weinberg, Biodegradable Fe-based alloys for use in osteosynthesis: outcome of an in vivo study after 52 weeks., Acta Biomater. 10 (2014) 3346–53. https://doi.org/10.1016/j.actbio.2014.04.007.

[71] P. Sotoudehbagha, S. Sheibani, M. Khakbiz, S. Ebrahimi-Barough, H. Hermawan, Novel antibacterial biodegradable Fe-Mn-Ag alloys produced by mechanical alloying, Mater. Sci. Eng. C. 88 (2018) 88–94. https://doi.org/10.1016/j.msec.2018.03.005.

[72] M. Caligari Conti, B. Mallia, E. Sinagra, P. Schembri Wismayer, J. Buhagiar, D. Vella, The effect of alloying elements on the properties of pressed and non-pressed biodegradable Fe–Mn–Ag powder metallurgy alloys, Heliyon. 5 (2019) e02522. https://doi.org/10.1016/j.heliyon.2019.e02522.

[73] T. Niendorf, F. Brenne, P. Hoyer, D. Schwarze, M. Schaper, R. Grothe, M. Wiesener, G. Grundmeier, H.J. Maier, Processing of New Materials by Additive Manufacturing: Iron-Based Alloys Containing Silver for Biomedical Applications, Metall. Mater. Trans. A. 46 (2015) 2829–2833. https://doi.org/10.1007/s11661-015-2932-2.

[74] M. Wiesener, K. Peters, A. Taube, A. Keller, K.P. Hoyer, T. Niendorf, G. Grundmeier,

Corrosion properties of bioresorbable FeMn-Ag alloys prepared by selective laser melting, Mater. Corros. 68 (2017) 1028–1036. https://doi.org/10.1002/maco.201709478.

[75] Biotronik inc., Orsiro product details, (n.d.). http://www.orsiro.com/en/product-details (accessed January 11, 2019).

[76] G.S. Berenson, S.R. Srinivasan, W. Bao, W.P. Newman, R.E. Tracy, W.A. Wattigney, Association between Multiple Cardiovascular Risk Factors and Atherosclerosis in Children and Young Adults, N. Engl. J. Med. 338 (1998) 1650–1656. https://doi.org/10.1056/NEJM199806043382302.

[77] M. Ng, T. Fleming, M. Robinson, B. Thomson, N. Graetz, C. Margono, E.C. Mullany, S. Biryukov, C. Abbafati, S.F. Abera, J.P. Abraham, N.M.E. Abu-Rmeileh, T. Achoki, F.S. Albuhairan, Z.A. Alemu, R. Alfonso, M.K. Ali, R. Ali, N.A. Guzman, W. Ammar, P. Anwari, A. Banerjee, S. Barquera, S. Basu, D.A. Bennett, Z. Bhutta, J. Blore, N. Cabral, I.C. Nonato, J.C. Chang, R. Chowdhury, K.J. Courville, M.H. Criqui, D.K. Cundiff, K.C. Dabhadkar, L. Dandona, A. Davis, A. Dayama, S.D. Dharmaratne, E.L. Ding, A.M. Durrani, A. Esteghamati, F. Farzadfar, D.F.J. Fay, V.L. Feigin, A. Flaxman, M.H. Forouzanfar, A. Goto, M.A. Green, R. Gupta, N. Hafezi-Nejad, G.J. Hankey, H.C. Harewood, R. Havmoeller, S. Hay, L. Hernandez, A. Husseini, B.T. Idrisov, N. Ikeda, F. Islami, E. Jahangir, S.K. Jassal, S.H. Jee, M. Jeffreys, J.B. Jonas, E.K. Kabagambe, S.E.A.H. Khalifa, A.P. Kengne, Y.S. Khader, Y.H. Khang, D. Kim, R.W. Kimokoti, J.M. Kinge, Y. Kokubo, S. Kosen, G. Kwan, T. Lai, M. Leinsalu, Y. Li, X. Liang, S. Liu, G. Logroscino, P.A. Lotufo, Y. Lu, J. Ma, N.K. Mainoo, G.A. Mensah, T.R. Merriman, A.H. Mokdad, J. Moschandreas, M. Naghavi, A. Naheed, D. Nand, K.M.V. Narayan, E.L. Nelson, M.L. Neuhouser, M.I. Nisar, T. Ohkubo, S.O. Oti, A. Pedroza, D. Prabhakaran, N. Roy, U. Sampson, H. Seo, S.G. Sepanlou, K. Shibuya, R. Shiri, I. Shiue, G.M. Singh, J.A. Singh, V. Skirbekk, N.J.C. Stapelberg, L. Sturua, B.L. Sykes, M. Tobias, B.X. Tran, L. Trasande, H. Toyoshima, S. Van De Vijver, T.J. Vasankari, J.L. Veerman, G. Velasquez-Melendez, V.V. Vlassov, S.E. Vollset, T. Vos, C. Wang, X. Wang, E. Weiderpass, A. Werdecker, J.L. Wright, Y.C. Yang, H. Yatsuya, J. Yoon, S.J. Yoon, Y. Zhao, M. Zhou, S. Zhu, A.D. Lopez, C.J.L. Murray, E. Gakidou, Global, regional, and national prevalence of overweight and obesity in children and adults during 1980-2013: A systematic analysis for the Global Burden of Disease Study 2013, Lancet. 384 (2014) 766–781. https://doi.org/10.1016/S0140-6736(14)60460-8.

[78] R. Köster, D. Vieluf, M. Kiehn, M. Sommerauer, J. Kähler, S. Baldus, T. Meinertz, C.W. Hamm, Nickel and molybdenum contact allergies in patients with coronary in-stent restenosis., Lancet

(London, England). 356 (2000) 1895–7. https://doi.org/10.1016/S0140-6736(00)03262-1.

[79] R.D. Alexy, D.S. Levi, Materials and manufacturing technologies available for production of a pediatric bioabsorbable stent, Biomed Res. Int. 2013 (2013). https://doi.org/10.1155/2013/137985.

[80] M. Heiden, E. Walker, L. Stanciu, Magnesium, Iron and Zinc Alloys, the Trifecta of Bioresorbable Orthopaedic and Vascular Implantation: A Review, J Biotechnol Biomater. 5 (2015). https://doi.org/10.4172/2155-952X.1000178.

[81] P.H. Adler, G.B. Olson, W.S. Owen, Strain Hardening of Hadfield Manganese Steel, Metall. Mater. Trans. A. 17 (1986) 1725–1737. https://doi.org/10.1007/BF02817271.

[82] S. Allain, J.P. Chateau, O. Bouaziz, S. Migot, N. Guelton, Correlations between the calculated stacking fault energy and the plasticity mechanisms in Fe-Mn-C alloys, Mater. Sci. Eng. A. 387–389 (2004) 158–162. https://doi.org/10.1016/j.msea.2004.01.059.

[83] V.H. Schumann, Martensitische Umwandlung in austenitischen mangan-kohlenstoff-stählen, Neue Hütte. 17 (1972) 605–609.

[84] M. Azaouzi, A. Makradi, S. Belouettar, Numerical investigations of the structural behavior of a balloon expandable stent design using finite element method, Comput. Mater. Sci. 72 (2013) 54–61. https://doi.org/10.1016/j.commatsci.2013.01.031.

[85] D. Djurovic, B. Hallstedt, J. von Appen, R. Dronskowski, Thermodynamic assessment of the Fe–Mn–C system, Calphad. 35 (2011) 479–491. https://doi.org/10.1016/j.calphad.2011.08.002.

[86] M. Farina, D.S. Avila, J.B.T. Da Rocha, M. Aschner, Metals, oxidative stress and neurodegeneration: A focus on iron, manganese and mercury, Neurochem. Int. 62 (2013) 575–594. https://doi.org/10.1016/j.neuint.2012.12.006.

[87] Y.S. Zhang, X.M. Zhu, Electrochemical polarization and passive film analysis of austenitic Fe-Mn-Al steels in aqueous solutions, Corros. Sci. 41 (1999) 1817–1833. https://doi.org/10.1016/S0010-938X(99)00017-7.

[88] M.B. Kannan, R.K.S. Raman, S. Khoddam, S. Liyanaarachchi, Corrosion behavior of twinning-induced plasticity (TWIP) steel, Mater. Corros. 64 (2013) 231–235. https://doi.org/10.1002/maco.201106356.

[89] M.G. Alvarez, Pitting Corrosion, Shreir's Corros. (2010) 772–800.

[90] E. Mouzou, C. Paternoster, R. Tolouei, P. Chevallier, C.A. Biffi, A. Tuissi, D. Mantovani, CO2-rich atmosphere strongly affects the degradation of Fe-21Mn-1C for biodegradable metallic implants, 2016. https://doi.org/10.1016/j.matlet.2016.06.017.

[91] H.P. Hack, Galvanic Corrosion, Shreir's Corros. (2010) 828–856.

[92] K. Mijnendonckx, N. Leys, J. Mahillon, S. Silver, R. Van Houdt, Antimicrobial silver: uses, toxicity and potential for resistance, BioMetals. 26 (2013) 609–621. https://doi.org/10.1007/s10534-013-9645-z.

[93] D. Herzog, V. Seyda, E. Wycisk, C. Emmelmann, Additive manufacturing of metals, Acta Mater. 117 (2016) 371–392. https://doi.org/10.1016/j.actamat.2016.07.019.

[94] M. Schinhammer, C.M. Pecnik, F. Rechberger, A.C. Hänzi, J.F. Löffler, P.J. Uggowitzer, Recrystallization behavior, microstructure evolution and mechanical properties of biodegradable Fe–Mn–C(–Pd) TWIP alloys, Acta Mater. 60 (2012) 2746–2756. https://doi.org/10.1016/j.actamat.2012.01.041.

[95] C. Di Mario, H. Griffiths, O. Goktekin, N. Peeters, J. Verbist, M. Bosiers, K. Deloose, B. Heublein, R. Rohde, V. Kasese, C. Ilsley, R. Erbel, Drug-eluting bioabsorbable magnesium stent, J. Interv. Cardiol. 17 (2004) 391–395. https://doi.org/10.1111/j.1540-8183.2004.04081.x.

[96] F. Witte, N. Hort, C. Vogt, S. Cohen, K.U. Kainer, R. Willumeit, F. Feyerabend, Degradable biomaterials based on magnesium corrosion, Curr. Opin. Solid State Mater. Sci. 12 (2008) 63–72. https://doi.org/http://dx.doi.org/10.1016/j.cossms.2009.04.001.

[97] A.M.P. Romani, Magnesium in Health and Disease, in: A. Sigel, H. Sigel, R.K.O. Sigel (Eds.), Interrelat. between Essent. Met. Ions Hum. Dis., Springer Netherlands, 2013: pp. 49–79. https://doi.org/10.1007/978-94-007-7500-8_3.

[98] J.R. Rumble, ed., Electrochemical series, in: CRC Handb. Chem. Phys., 100th ed., CRC Press/Taylor & Francis, Boca Raton, FL, 2019: pp. 5-97-5–103. http://hbcponline.com/faces/documents/05_22/05_22_0001.xhtml.

[99] M. Pourbaix, Atlas of Electrochemical Equilibria in Aqueous Solutions, National Association of Corrosion Engineers, Houston, 1974.

[100] Y. Chen, Z. Xu, C. Smith, J. Sankar, Recent advances on the development of magnesium alloys for biodegradable implants, Acta Biomater. 10 (2014) 4561–4573. https://doi.org/10.1016/j.actbio.2014.07.005.

[101] E.O. Hall, The Deformation and Ageing of Mild Steel .3. Discussion of Results, Proc. Phys. Soc. London Sect. B. 64 (1951) 747–753. https://doi.org/10.1088/0370-1301/64/9/303.

[102] P. Zartner, R. Cesnjevar, H. Singer, M. Weyand, First successful implantation of a biodegradable metal stent into the left pulmonary artery of a preterm baby, Catheter. Cardiovasc. Interv. 66 (2005) 590–594. https://doi.org/10.1002/ccd.20520.

[103] D. Schranz, P. Zartner, I. Michel-Behnke, H. Akintürk, Bioabsorbable metal stents for percutaneous treatment of critical recoarctation of the aorta in a newborn, Catheter. Cardiovasc. Interv. 67 (2006) 671–673. https://doi.org/10.1002/ccd.20756.

[104] P. Zartner, M. Buettner, H. Singer, M. Sigler, First biodegradable metal stent in a child with congenital heart disease: Evaluation of macro and histopathology, Catheter. Cardiovasc. Interv. 69 (2007) 443–446. https://doi.org/10.1002/ccd.20828.

[105] M. Maeng, L.O. Jensen, E. Falk, H.R. Andersen, L. Thuesen, Negative vascular remodelling after implantation of bioabsorbable magnesium alloy stents in porcine coronary arteries: a randomised comparison with bare-metal and sirolimus-eluting stents., Heart. 95 (2009) 241–6. https://doi.org/10.1136/hrt.2007.139261.

[106] L. Mao, L. Shen, J. Niu, J. Zhang, W. Ding, Y. Wu, R. Fan, G. Yuan, Nanophasic biodegradation enhances the durability and biocompatibility of magnesium alloys for the next-generation vascular stents, Nanoscale. 5 (2013) 9517. https://doi.org/10.1039/c3nr02912c.

[107] P.L. Carver, Metal Ions and Infectious Diseases. An Overview from the Clinic, in: A. Sigel, H. Sigel, R.K.O. Sigel (Eds.), Interrelat. between Essent. Met. Ions Hum. Dis., 1st ed., Springer Netherlands, 2013: pp. 1–28. https://doi.org/10.1007/978-94-007-7500-8_1.

[108] B. Beverskog, I. Puigdomenech, Revised pourbaix diagrams for zinc at 25-300°C, Corros. Sci. 39 (1997) 107–114. https://doi.org/10.1016/S0010-938X(97)89246-3.

[109] R.J. Guillory, M. Sikora-Jasinska, J.W. Drelich, J. Goldman, In Vitro Corrosion and in Vivo Response to Zinc Implants with Electropolished and Anodized Surfaces, ACS Appl. Mater. Interfaces. 11 (2019) 19884–19893. https://doi.org/10.1021/acsami.9b05370.

[110] Y. Su, H. Yang, J. Gao, Y. Qin, Y. Zheng, D. Zhu, Interfacial Zinc Phosphate is the Key to Controlling Biocompatibility of Metallic Zinc Implants, Adv. Sci. 1900112 (2019) 1900112. https://doi.org/10.1002/advs.201900112.

[111] H. Yang, C. Wang, C. Liu, H. Chen, Y. Wu, J. Han, Z. Jia, W. Lin, D. Zhang, W. Li, W. Yuan, H. Guo, H. Li, G. Yang, D. Kong, D. Zhu, K. Takashima, L. Ruan, J. Nie, X. Li, Y. Zheng, Evolution of the degradation mechanism of pure zinc stent in the one-year study of rabbit abdominal aorta model, Biomaterials. 145 (2017) 92–105. https://doi.org/10.1016/j.biomaterials.2017.08.022.

[112] E. Mostaed, M. Sikora-Jasinska, M.S. Ardakani, A. Mostaed, I.M. Reaney, J. Goldman, J.W. Drelich, Towards revealing key factors in mechanical instability of bioabsorbable Zn-based alloys for intended vascular stenting, Acta Biomater. (2020). https://doi.org/10.1016/j.actbio.2020.01.028.

[113] N.S. Murni, M.S. Dambatta, S.K. Yeap, G.R. a. Froemming, H. Hermawan, Cytotoxicity evaluation of biodegradable Zn–3Mg alloy toward normal human osteoblast cells, Mater. Sci. Eng. C. 49 (2015) 560–566. https://doi.org/10.1016/j.msec.2015.01.056.

[114] E. Mostaed, M. Sikora-Jasinska, A. Mostaed, S. Loffredo, A.G. Demir, B. Previtali, D. Mantovani, R. Beanland, M. Vedani, Novel Zn-based alloys for biodegradable stent applications: Design, development and in vitro degradation, J. Mech. Behav. Biomed. Mater. 60 (2016) 581–602. https://doi.org/10.1016/j.jmbbm.2016.03.018.

[115] P.K. Bowen, J.M. Seitz, R.J. Guillory, J.P. Braykovich, S. Zhao, J. Goldman, J.W. Drelich, Evaluation of wrought Zn-Al alloys (1, 3, and 5 wt % Al) through mechanical and in vivo testing for stent applications, J. Biomed. Mater. Res. - Part B Appl. Biomater. (2017). https://doi.org/10.1002/jbm.b.33850.

[116] C. Zhou, H.F. Li, Y.X. Yin, Z.Z. Shi, T. Li, X.Y. Feng, J.W. Zhang, C.X. Song, X.S. Cui, K.L. Xu, Y.W. Zhao, W.B. Hou, S.T. Lu, G. Liu, M.Q. Li, J. ying Ma, E. Toft, A.A. Volinsky, M. Wan, X. jun Yao, C. bin Wang, K. Yao, S. kun Xu, H. Lu, S.F. Chang, J.B. Ge, L.N. Wang, H.J. Zhang, Long-term in vivo study of biodegradable Zn-Cu stent: A 2-year implantation evaluation in porcine coronary artery, Acta Biomater. 97 (2019) 657–670. https://doi.org/10.1016/j.actbio.2019.08.012.

[117] S. Zhao, J.-M. Seitz, R. Eifler, H.J. Maier, R.J. Guillory, E.J. Earley, A. Drelich, J. Goldman,

J.W. Drelich, Zn-Li alloy after extrusion and drawing: Structural, mechanical characterization, and biodegradation in abdominal aorta of rat, Mater. Sci. Eng. C. (2017). https://doi.org/10.1016/j.msec.2017.02.167.

[118] H.F. Li, X.H. Xie, Y.F. Zheng, Y. Cong, F.Y. Zhou, K.J. Qiu, X. Wang, X. Wang, L. Huang, L. Tian, L. Qin, Development of biodegradable Zn-1X binary alloys with nutrient alloying elements Mg, Ca and Sr, Sci. Rep. 5 (2015). https://doi.org/http://dx.doi.org/10.1038/srep10719.

[119] M. Sikora-Jasinska, E. Mostaed, A. Mostaed, R. Beanland, D. Mantovani, M. Vedani, Fabrication, mechanical properties and in vitro degradation behavior of newly developed Zn-Ag alloys for degradable implant applications, Mater. Sci. Eng. C. 77 (2017) 1170–1181. https://doi.org/10.1016/j.msec.2017.04.023.

[120] A. Oliver, R. John, G. Ii, K.L. Flom, L.M. Morath, T.M. Kolesar, E. Mostaed, M. Sikora-jasinska, J.W. Drelich, J. Goldman, Analysis of vascular inflammation against bioresorbable Zn-Ag based alloys, (2020). https://doi.org/10.1021/acsabm.0c00740.

[121] R.C. Hider, X. Kong, Iron: Effect of overload and deficiency, in: A. Sigel, H. Sigel, R.K.O. Sigel (Eds.), Met. Ions Life Sci., 1st ed., Springer Netherlands, Dororecht, 2013: pp. 229–294. https://doi.org/10.1007/978-94-007-7500-8-8.

[122] N.S. Fagali, C.A. Grillo, S. Puntarulo, M.A. Fernández Lorenzo de Mele, Cytotoxicity of corrosion products of degradable Fe-based stents: Relevance of pH and insoluble products, Colloids Surfaces B Biointerfaces. 128 (2015) 480–488. https://doi.org/10.1016/j.colsurfb.2015.02.047.

[123] N.S. Fagali, C.A. Grillo, S. Puntarulo, M.A. Fernández Lorenzo de Mele, Is there any difference in the biological impact of soluble and insoluble degradation products of iron-containing biomaterials?, Colloids Surfaces B Biointerfaces. 160 (2017) 238–246. https://doi.org/10.1016/j.colsurfb.2017.09.032.

[124] E. Scarcello, A. Herpain, M. Tomatis, F. Turci, P.J. Jacques, D. Lison, Hydroxyl radicals and oxidative stress: the dark side of Fe corrosion, Colloids Surfaces B Biointerfaces. 185 (2020) 110542. https://doi.org/10.1016/j.colsurfb.2019.110542.

[125] E. Scarcello, I. Lobysheva, C. Bouzin, P.J. Jacques, D. Lison, C. Dessy, Endothelial dysfunction induced by hydroxyl radicals – The hidden face of biodegradable Fe-based materials for

coronary stents, Mater. Sci. Eng. C. 105 (2020) 110938. https://doi.org/10.1016/j.msec.2020.110938.

[126] P.P. Mueller, T. May, A. Perz, H. Hauser, M. Peuster, Control of smooth muscle cell proliferation by ferrous iron, Biomaterials. 27 (2006) 2193–2200. https://doi.org/10.1016/j.biomaterials.2005.10.042.

[127] J. He, F.-L. He, D.-W. Li, Y.-L. Liu, Y.-Y. Liu, Y.-J. Ye, D.-C. Yin, Advances in Fe-based biodegradable metallic materials, RSC Adv. 6 (2016) 112819–112838. https://doi.org/10.1039/C6RA20594A.

[128] C. Shuai, W. Yang, Y. Yang, H. Pan, C. He, F. Qi, D. Xie, H. Liang, Selective laser melted Fe-Mn bone scaffold: microstructure, corrosion behavior and cell response, Mater. Res. Express. (2019). https://doi.org/10.1088/2053-1591/ab62f5.

[129] N.B. Sing, A. Mostavan, E. Hamzah, D. Mantovani, H. Hermawan, Degradation behavior of biodegradable Fe35Mn alloy stents, J. Biomed. Mater. Res. - Part B Appl. Biomater. 103 (2015) 572–577. https://doi.org/10.1002/jbm.b.33242.

[130] E. Mouzou, C. Paternoster, R. Tolouei, P. Chevallier, C.A. Biffi, A. Tuissi, D. Mantovani, CO2-rich atmosphere strongly affects the degradation of Fe-21Mn-1C for biodegradable metallic implants, Mater. Lett. 181 (2016) 362–366. https://doi.org/10.1016/j.matlet.2016.06.017.

[131] L. Strause, P. Saltman, Role of Manganese in Bone Metabolism, in: C. Kies (Ed.), Nutr. Bioavailab. Manganese, American Chemical Society, 1987: pp. 46–55. https://doi.org/10.1021/bk-1987-0354.ch005.

[132] C. Scott, S. Allain, M.M. Faral, N. Guelton, The development of a new Fe-Mn-C austenitic steel for automotive applications, Rev. Métallurgie. 103 (2006) 293–302. https://doi.org/10.1051/metal:2006142.

[133] J. Martínez, S.M. Cotes, A.F. Cabrera, J. Desimoni, A. Fernández Guillermet, On the relative fraction of ε martensite in γ-Fe–Mn alloys, Mater. Sci. Eng. A. 408 (2005) 26–32. https://doi.org/10.1016/j.msea.2005.06.019.

[134] M. Dargusch, A. Dehghan-Manshadi, M. Shahbazi, J. Venezuela, X. Tran, J. Song, N. Liu, C. Xu, Q. Ye, C. Wen, Exploring the role of manganese on the microstructure, mechanical properties, biodegradability and biocompatibility of porous iron-based scaffolds, ACS Biomater.

Sci. Eng. (2019) acsbiomaterials.8b01497. https://doi.org/10.1021/acsbiomaterials.8b01497.

[135] M. Heiden, A. Kustas, K. Chaput, E. Nauman, D. Johnson, L. Stanciu, Effect of microstructure and strain on the degradation behavior of novel bioresorbable iron-manganese alloy implants., J. Biomed. Mater. Res. A. 103 (2015) 738–45. https://doi.org/10.1002/jbm.a.35220.

[136] M. Heiden, E. Walker, E. Nauman, L. Stanciu, Evolution of novel bioresorbable iron-manganese implant surfaces and their degradation behaviors in vitro., J. Biomed. Mater. Res. A. 103 (2015) 185–93. https://doi.org/10.1002/jbm.a.35155.

[137] M. Dehestani, K. Trumble, H. Wang, H. Wang, L.A. Stanciu, Effects of microstructure and heat treatment on mechanical properties and corrosion behavior of powder metallurgy derived Fe–30Mn alloy, Mater. Sci. Eng. A. 703 (2017) 214–226. https://doi.org/10.1016/j.msea.2017.07.054.

[138] A. Drynda, T. Hassel, F.W. Bach, M. Peuster, In vitro and in vivo corrosion properties of new iron-manganese alloys designed for cardiovascular applications, J. Biomed. Mater. Res. Part B Appl. Biomater. 103 (2015) 649–660. https://doi.org/10.1002/jbm.b.33234.

[139] B. Liu, Y.F. Zheng, L. Ruan, In vitro investigation of Fe30Mn6Si shape memory alloy as potential biodegradable metallic material, Mater. Lett. 65 (2011) 540–543. https://doi.org/10.1016/j.matlet.2010.10.068.

[140] X. Zhang, T. Sawaguchi, Twinning of deformation-induced ε-martensite in Fe-30Mn-6Si shape memory alloy, Acta Mater. (2017). https://doi.org/10.1016/j.actamat.2017.10.009.

[141] W.Y. Jang, Q. Gu, J. Van Humbeeck, L. Delaey, Microscopic Observation of g-Phase and e- and a'-Martensite in Fe-Mn-Si-Based Shape Memory Alloys, Mater. Charact. 34 (1995) 67–72. https://doi.org/http://dx.doi.org/10.1016/1044-5803(94)00054-O.

[142] F. Moszner, A.S. Sologubenko, M. Schinhammer, C. Lerchbacher, A.C. Hänzi, H. Leitner, P.J. Uggowitzer, J.F. Löffler, Precipitation hardening of biodegradable Fe-Mn-Pd alloys, Acta Mater. 59 (2011) 981–991. https://doi.org/10.1016/j.actamat.2010.10.025.

[143] Y.P. Feng, N. Gaztelumendi, J. Fornell, H.Y. Zhang, P. Solsona, M.D. Baró, S. Suriñach, E. Ibáñez, L. Barrios, E. Pellicer, C. Nogués, J. Sort, Mechanical properties, corrosion performance and cell viability studies on newly developed porous Fe-Mn-Si-Pd alloys, J. Alloys Compd. 724 (2017) 1046–1056. https://doi.org/10.1016/j.jallcom.2017.07.112.

[144] Y.P. Feng, A. Blanquer, J. Fornell, H. Zhang, P. Solsona, M.D. Baro, S. Surinach, E. Ibanez, E. Garcia-Lecina, X. Wei, R. Li, L. Barrios, E. Pellicer, C. Nogues, J. Sort, Novel Fe-Mn-Si-Pd alloys: insights into mechanical, magnetic, corrosion resistance and biocompatibility performances, J. Mater. Chem. B. 4 (2016) 6402–6412. https://doi.org/10.1039/C6TB01951J.

[145] L.J. Swartzendruber, The Ag−Fe (Silver-Iron) system, Bull. Alloy Phase Diagrams. 5 (1984) 560–564. https://doi.org/10.1007/BF02868316.

[146] I. Karakaya, W.T. Thompson, The Ag-Mn (Silver-Manganese) system, Bull. Alloy Phase Diagrams. 11 (1990) 480–486. https://doi.org/10.1007/BF02898263.

[147] M. Caligari Conti, D. Aquilina, C. Paternoster, D. Vella, E. Sinagra, D. Mantovani, G. Cassar, P. Schembri Wismayer, J. Buhagiar, Influence of cold rolling on in vitro cytotoxicity and electrochemical behaviour of an Fe-Mn-C biodegradable alloy in physiological solutions, Heliyon. 4 (2018) e00926. https://doi.org/10.1016/j.heliyon.2018.e00926.

[148] D. Hong, D.T. Chou, O.I. Velikokhatnyi, A. Roy, B. Lee, I. Swink, I. Issaev, H.A. Kuhn, P.N. Kumta, Binder-jetting 3D printing and alloy development of new biodegradable Fe-Mn-Ca/Mg alloys, Acta Biomater. 45 (2016) 375–386. https://doi.org/10.1016/j.actbio.2016.08.032.

[149] J. Čapek, Š. Msallamová, E. Jablonská, J. Lipov, D. Vojtěch, A novel high-strength and highly corrosive biodegradable Fe-Pd alloy: Structural, mechanical and in vitro corrosion and cytotoxicity study, Mater. Sci. Eng. C. 79 (2017) 550–562. https://doi.org/10.1016/j.msec.2017.05.100.

[150] J. Čapek, K. Stehlíková, A. Michalcová, Š. Msallamová, D. Vojtěch, Microstructure, mechanical and corrosion properties of biodegradable powder metallurgical Fe-2 wt% X (X = Pd, Ag and C) alloys, Mater. Chem. Phys. (2016). https://doi.org/10.1016/j.matchemphys.2016.06.087.

[151] T. Huang, J. Cheng, Y.F. Zheng, In vitro degradation and biocompatibility of Fe-Pd and Fe-Pt composites fabricated by spark plasma sintering, Mater. Sci. Eng. C. 35 (2014) 43–53. https://doi.org/10.1016/j.msec.2013.10.023.

[152] T. Huang, J. Cheng, D. Bian, Y. Zheng, Fe-Au and Fe-Ag composites as candidates for biodegradable stent materials, J. Biomed. Mater. Res. Part B Appl. Biomater. 104 (2016) 225–240. https://doi.org/10.1002/jbm.b.33389.

[153] M. Sikora-Jasinska, C. Paternoster, E. Mostaed, R. Tolouei, R. Casati, M. Vedani, D. Mantovani,

Synthesis, mechanical properties and corrosion behavior of powder metallurgy processed Fe/Mg2Si composites for biodegradable implant applications, Mater. Sci. Eng. C. 81 (2017) 511–521. https://doi.org/10.1016/j.msec.2017.07.049.

[154] M. Sikora-Jasinska, P. Chevallier, S. Turgeon, C. Paternoster, E. Mostaed, M. Vedani, D. Mantovani, Long-term in vitro degradation behaviour of Fe and Fe/Mg 2 Si composites for biodegradable implant applications, RSC Adv. 8 (2018) 9627–9639. https://doi.org/10.1039/C8RA00404H.

[155] M. Sikora-Jasinska, P. Chevallier, S. Turgeon, C. Paternoster, E. Mostaed, M. Vedani, D. Mantovani, Understanding the effect of the reinforcement addition on corrosion behavior of Fe/Mg2Si composites for biodegradable implant applications, Mater. Chem. Phys. 223 (2019) 771–778. https://doi.org/10.1016/j.matchemphys.2018.11.068.

[156] R.A. Hadfield, Hadfield's Manganese Steel, Science (80-.). 12 (1888) 284–286. http://www.jstor.org/stable/1762549.

[157] M. Koyama, E. Akiyama, K. Tsuzaki, Effect of hydrogen content on the embrittlement in a Fe – Mn – C twinning-induced plasticity steel, Corros. Sci. 59 (2012) 277–281. https://doi.org/10.1016/j.corsci.2011.09.022.

[158] M. Koyama, E. Akiyama, T. Sawaguchi, D. Raabe, K. Tsuzaki, Hydrogen-induced cracking at grain and twin boundaries in an Fe-Mn-C austenitic steel, Scr. Mater. 66 (2012) 459–462. https://doi.org/10.1016/j.scriptamat.2011.12.015.

[159] C. Verhaegen, S. Lepropre, M. Octave, D. Brusa, L. Bertrand, C. Beauloye, P.J. Jacques, J. Kefer, S. Horman, Bioreactivity of Stent Material : In Vitro Impact of New Twinning-Induced Plasticity Steel on Platelet Activation, J. Biomater. Nanobiotechnol. 10 (2019) 175–189. https://doi.org/10.4236/jbnb.2019.104010.

[160] M. Schinhammer, I. Gerber, A.C. Hänzi, P.J. Uggowitzer, On the cytocompatibility of biodegradable Fe-based alloys, Mater. Sci. Eng. C. 33 (2013) 782–789. https://doi.org/10.1016/j.msec.2012.11.002.

[161] J. Hufenbach, H. Wendrock, F. Kochta, U. Kühn, A. Gebert, Novel biodegradable Fe-Mn-C-S alloy with superior mechanical and corrosion properties, 2017. https://doi.org/10.1016/j.matlet.2016.10.037.

[162] J. Hufenbach, F. Kochta, H. Wendrock, A. Voß, L. Giebeler, S. Oswald, S. Pilz, U. Kühn, A. Lode, M. Gelinsky, A. Gebert, S and B microalloying of biodegradable Fe-30Mn-1C - Effects on microstructure, tensile properties, in vitro degradation and cytotoxicity, Mater. Des. 142 (2018) 22–35. https://doi.org/10.1016/j.matdes.2018.01.005.

[163] M. Paunovic, M. Schlesinger, Fundamentals of Electrochemical Deposition: Second Edition, 2005. https://doi.org/10.1002/0470009403.

[164] M. Moravej, S. Amira, F. Prima, A. Rahem, M. Fiset, D. Mantovani, Effect of electrodeposition current density on the microstructure and the degradation of electroformed iron for degradable stents, Mater. Sci. Eng. B. 176 (2011) 1812–1822. https://doi.org/10.1016/j.mseb.2011.02.031.

[165] M. Moravej, A. Purnama, M. Fiset, J. Couet, D. Mantovani, Electroformed pure iron as a new biomaterial for degradable stents: In vitro degradation and preliminary cell viability studies☆, Acta Biomater. 6 (2010) 1843–1851. https://doi.org/10.1016/j.actbio.2010.01.008.

[166] A. Mostavan, C. Paternoster, R. Tolouei, E. Ghali, D. Dubé, D. Mantovani, Effect of electrolyte composition and deposition current for Fe/Fe-P electroformed bilayers for biodegradable metallic medical applications, Mater. Sci. Eng. C. 70 (2017) 195–206. https://doi.org/10.1016/j.msec.2016.08.026.

[167] M. Moravej, Développement Et Validation Des Matériaux Métalliques Pour Stents Cardiovasculaires Biodégradables, Université Laval, 2011. http://theses.ulaval.ca/archimede/meta/27897.

[168] P.J. Kelly, R.D. Arnell, Magnetron sputtering: A review of recent developments and applications, Vacuum. 56 (2000) 159–172. https://doi.org/10.1016/S0042-207X(99)00189-X.

[169] T. Jurgeleit, E. Quandt, C. Zamponi, Magnetron sputtering a new fabrication method of iron based biodegradable implant materials, Adv. Mater. Sci. Eng. 2015 (2015). https://doi.org/10.1155/2015/294686.

[170] T. Jurgeleit, E. Quandt, C. Zamponi, Magnetron Sputtering as a Fabrication Method for a Biodegradable Fe32Mn Alloy, Materials (Basel). 10 (2017) 1196. https://doi.org/10.3390/ma10101196.

[171] M. Fernández-Barcia, S. Kurdi, A. Terzopoulou, Z.H. Barber, V. Hoffmann, C. Damm, L. Giebeler, S. Pané, M. Uhlemann, U. Wolff, K. Nielsch, A. Gebert, Comparative study of the

sustainable preparation of FeMn thin films via electrodeposition and magnetron co-sputtering, Surf. Coatings Technol. 375 (2019) 182–196. https://doi.org/10.1016/j.surfcoat.2019.07.022.

[172] T. Jurgeleit, L.K. Jessen, E. Quandt, C. Zamponi, Magnetron-Sputtered, Biodegradable FeMn Foils: The Influence of Manganese Content on Microstructure, Mechanical, Corrosion, and Magnetic Properties, Materials (Basel). 11 (2018) 482. https://doi.org/10.3390/ma11040482.

[173] Y. Li, H. Jahr, K. Lietaert, P. Pavanram, A. Yilmaz, L.I. Fockaert, M.A. Leeflang, B. Pouran, Y. Gonzalez-Garcia, H. Weinans, J.M.C. Mol, J. Zhou, A.A. Zadpoor, Additively manufactured biodegradable porous iron, Acta Biomater. 77 (2018) 380–393. https://doi.org/10.1016/j.actbio.2018.07.011.

[174] Y. Li, H. Jahr, P. Pavanram, F.S.. Bobbert, U. Puggi, X.-Y. Zhang, B. Pouran, M.A. Leeflang, H. Weinans, J. Zhou, A.A. Zadpoor, Additively manufactured functionally graded biodegradable porous iron, Acta Biomater. 96 (2019) 646–661. https://doi.org/10.1016/j.actbio.2019.07.013.

[175] J. Zhou, Y. Yang, M. Alonso Frank, R. Detsch, A.R. Boccaccini, S. Virtanen, Accelerated Degradation Behavior and Cytocompatibility of Pure Iron Treated with Sandblasting, ACS Appl. Mater. Interfaces. 8 (2016) 26482–26492. https://doi.org/10.1021/acsami.6b07068.

[176] S. Bagheri, M. Guagliano, Review of shot peening processes to obtain nanocrystalline surfaces in metal alloys, Surf. Eng. 25 (2009) 3–14. https://doi.org/10.1179/026708408X334087.

[177] H. Jazaeri, F.J. Humphreys, The transition from discontinuous to continuous recrystallization in some aluminium alloys: I - The deformed state, Acta Mater. 52 (2004) 3239–3250. https://doi.org/10.1016/j.actamat.2004.03.030.

[178] S. Bagherifard, M.F. Molla, D. Kajanek, R. Donnini, B. Hadzima, M. Guagliano, Accelerated biodegradation and improved mechanical performance of pure iron through surface grain refinement, Acta Biomater. 98 (2019) 88–102. https://doi.org/10.1016/j.actbio.2019.05.033.

[179] H. Wang, Y. Zheng, Y. Li, C. Jiang, Improvement of in vitro corrosion and cytocompatibility of biodegradable Fe surface modified by Zn ion implantation, Appl. Surf. Sci. 403 (2017) 168–176. https://doi.org/10.1016/j.apsusc.2017.01.158.

[180] T. Huang, Y. Zheng, Y. Han, Accelerating degradation rate of pure iron by zinc ion implantation, Regen. Biomater. 3 (2016) 205–215. https://doi.org/10.1093/rb/rbw020.

[181] T. Huang, Y. Cheng, Y. Zheng, In vitro studies on silver implanted pure iron by metal vapor vacuum arc technique, Colloids Surfaces B Biointerfaces. 142 (2016) 20–29. https://doi.org/10.1016/j.colsurfb.2016.01.065.

[182] H. Wang, Y. Zheng, C. Jiang, Y. Li, Y. Fu, In vitro corrosion behavior and cytocompatibility of pure Fe implanted with Ta, Surf. Coatings Technol. 320 (2017) 201–205. https://doi.org/10.1016/j.surfcoat.2017.01.051.

[183] Q. Feng, D. Zhang, C. Xin, X. Liu, W. Lin, W. Zhang, S. Chen, K. Sun, Characterization and in vivo evaluation of a bio-corrodible nitrided iron stent, J. Mater. Sci. Mater. Med. 24 (2013) 713–724. https://doi.org/10.1007/s10856-012-4823-z.

[184] W. Lin, L. Qin, H. Qi, D. Zhang, G. Zhang, R. Gao, H. Qiu, Y. Xia, P. Cao, X. Wang, W. Zheng, Long-term in vivo corrosion behavior, biocompatibility and bioresorption mechanism of a bioresorbable nitrided iron scaffold, Acta Biomater. 54 (2017) 454–468. https://doi.org/10.1016/j.actbio.2017.03.020.

[185] T. Huang, Y. Zheng, Uniform and accelerated degradation of pure iron patterned by Pt disc arrays, Sci. Rep. 6 (2016) 23627. https://doi.org/10.1038/srep23627.

[186] Y. Qi, H. Qi, Y. He, W. Lin, P. Li, L. Qin, Y. Hu, L. Chen, Q. Liu, H. Sun, Q. Liu, G. Zhang, S. Cui, J. Hu, L. Yu, D. Zhang, J. Ding, Strategy of Metal–Polymer Composite Stent To Accelerate Biodegradation of Iron-Based Biomaterials, ACS Appl. Mater. Interfaces. 10 (2018) 182–192. https://doi.org/10.1021/acsami.7b15206.

[187] M. Haude, H. Ince, S. Kische, A. Abizaid, R. Tölg, P.A. Lemos, N.M. Van Mieghem, S. Verheye, C. Von Birgelen, E.H. Christiansen, W. Wijns, H.M. Garcia-Garcia, R. Waksman, Sustained safety and clinical performance of a drug-eluting absorbable metal scaffold up to 24 months: Pooled outcomes of BIOSOLVE-II and BIOSOLVE-III, EuroIntervention. 13 (2017) 432–439. https://doi.org/10.4244/EIJ-D-17-00254.

[188] R. Piccolo, G. Giustino, R. Mehran, S. Windecker, Stable coronary artery disease: Revascularisation and invasive strategies, Lancet. 386 (2015) 702–713. https://doi.org/10.1016/S0140-6736(15)61220-X.

[189] A. Francis, Y. Yang, S. Virtanen, A.R. Boccaccini, Iron and iron-based alloys for temporary cardiovascular applications., J. Mater. Sci. Mater. Med. 26 (2015) 138. https://doi.org/10.1007/s10856-015-5473-8.

[190] J. Crossgrove, W. Zheng, Manganese toxicity upon overexposure, NMR Biomed. 17 (2004) 544–553. https://doi.org/10.1002/nbm.931.

[191] P. Sotoudeh Bagha, M. Khakbiz, S. Sheibani, H. Hermawan, Design and characterization of nano and bimodal structured biodegradable Fe-Mn-Ag alloy with accelerated corrosion rate, J. Alloys Compd. 767 (2018) 955–965. https://doi.org/10.1016/j.jallcom.2018.07.206.

[192] I. Karakaya, W.T. Thompson, The Ag-Mn (Silver-Manganese) system, Bull. Alloy Phase Diagrams. 11 (1990) 480–486. https://doi.org/10.1007/BF02898263.

[193] S. Kang, Y.S. Jung, J.H. Jun, Y.K. Lee, Effects of recrystallization annealing temperature on carbide precipitation, microstructure, and mechanical properties in Fe-18Mn-0.6C-1.5Al TWIP steel, Mater. Sci. Eng. A. 527 (2010) 745–751. https://doi.org/10.1016/j.msea.2009.08.048.

[194] H. Idrissi, K. Renard, L. Ryelandt, D. Schryvers, P.J. Jacques, On the mechanism of twin formation in Fe-Mn-C TWIP steels, Acta Mater. 58 (2010) 2464–2476. https://doi.org/10.1016/j.actamat.2009.12.032.

[195] J.B. Seol, J.E. Jung, Y.W. Jang, C.G. Park, Influence of carbon content on the microstructure, martensitic transformation and mechanical properties in austenite/-martensite dual-phase Fe-Mn-C steels, Acta Mater. 61 (2013) 558–578. https://doi.org/10.1016/j.actamat.2012.09.078.

[196] O. Grässel, L. Krüger, G. Frommeyer, L.. Meyer, High strength Fe–Mn–(Al, Si) TRIP/TWIP steels development — properties — application, Int. J. Plast. 16 (2000) 1391–1409. https://doi.org/10.1016/S0749-6419(00)00015-2.

[197] W.S. Choi, S. Sandlöbes, N. V. Malyar, C. Kirchlechner, S. Korte-Kerzel, G. Dehm, P.P. Choi, D. Raabe, On the nature of twin boundary-associated strengthening in Fe-Mn-C steel, Scr. Mater. 156 (2018) 27–31. https://doi.org/10.1016/j.scriptamat.2018.07.009.

[198] K. Renard, S. Ryelandt, P.J. Jacques, Characterisation of the Portevin-Le Châtelier effect affecting an austenitic TWIP steel based on digital image correlation, Mater. Sci. Eng. A. 527 (2010) 2969–2977. https://doi.org/10.1016/j.msea.2010.01.037.

[199] S. Allain, J.-P. Chateau, O. Bouaziz, A physical model of the twinning-induced plasticity effect in a high manganese austenitic steel, Mater. Sci. Eng. A. 387–389 (2004) 143–147. https://doi.org/10.1016/j.msea.2004.01.060.

[200] J. Nakano, P.J. Jacques, Effects of the thermodynamic parameters of the hcp phase on the stacking fault energy calculations in the Fe–Mn and Fe–Mn–C systems, Calphad. 34 (2010) 167–175. https://doi.org/10.1016/j.calphad.2010.02.001.

[201] S. Lee, J. Kim, S.J. Lee, B.C. De Cooman, Effect of Cu addition on the mechanical behavior of austenitic twinning-induced plasticity steel, Scr. Mater. 65 (2011) 1073–1076. https://doi.org/10.1016/j.scriptamat.2011.09.019.

[202] S.-J. Lee, Y.-S. Jung, S.-I. Baik, Y.-W. Kim, M. Kang, W. Woo, Y.-K. Lee, The effect of nitrogen on the stacking fault energy in Fe–15Mn–2Cr–0.6C– x N twinning-induced plasticity steels, Scr. Mater. 92 (2014) 23–26. https://doi.org/10.1016/j.scriptamat.2014.08.004.

[203] A.A. Saleh, E. V. Pereloma, A.A. Gazder, Texture evolution of cold rolled and annealed Fe-24Mn-3Al-2Si-1Ni-0.06C TWIP steel, Mater. Sci. Eng. A. 528 (2011) 4537–4549. https://doi.org/10.1016/j.msea.2011.02.055.

[204] T. Leffers, R.K. Ray, The brass-type texture and its deviation from the copper-type texture, Prog. Mater. Sci. 54 (2009) 351–396. https://doi.org/10.1016/j.pmatsci.2008.09.002.

[205] Y. Lü, B. Hutchinson, D.A. Molodov, G. Gottstein, Effect of deformation and annealing on the formation and reversion of ε-martensite in an Fe–Mn–C alloy, Acta Mater. 58 (2010) 3079–3090. https://doi.org/10.1016/j.actamat.2010.01.045.

[206] Y. Ono, T. Tsuchiyama, S. Takaki, Microstructural Change during Isothermal Aging in High Manganese Austenitic Steels, Tetsu-to-Hagane. 84 (1998) 309–314. https://doi.org/10.2355/tetsutohagane1955.84.4_309.

[207] F. Jiménez-Villacorta, J.L. Marion, T. Sepehrifar, L.H. Lewis, Tuning exchange anisotropy in nanocomposite AgMn alloys, J. Appl. Phys. 111 (2012) 07E141. https://doi.org/10.1063/1.3679048.

[208] K. Ishibashi, Y. Tsunoda, N. Kunitomi, J.W. Cable, Magnetic diffuse scattering in AgMn spin glass alloys, Solid State Commun. 56 (1985) 585–588. https://doi.org/10.1016/0038-1098(85)90961-5.

[209] E. Mouzou, Étude de la dégradation in-vitro d'alliages Fe-Mn-C pour des applications de stents cardiovasculaires, Université Laval, 2017.

[210] S. Loffredo, C. Paternoster, N. Giguère, G. Barucca, M. Vedani, D. Mantovani, The addition of silver affects the deformation mechanism of a twinning-induced plasticity steel: Potential for thinner degradable stents, Acta Biomater. 98 (2019) 103–113. https://doi.org/10.1016/j.actbio.2019.04.030.

[211] L. Bracke, K. Verbeken, L. Kestens, J. Penning, Microstructure and texture evolution during cold rolling and annealing of a high Mn TWIP steel, Acta Mater. 57 (2009) 1512–1524. https://doi.org/10.1016/j.actamat.2008.11.036.

[212] S. Vercammen, B. Blanpain, B.C. De Cooman, P. Wollants, Cold rolling behaviour of an austenitic Fe-30Mn-3Al-3Si TWIP-steel: The importance of deformation twinning, Acta Mater. 52 (2004) 2005–2012. https://doi.org/10.1016/j.actamat.2003.12.040.

[213] H. Gwon, J.-K. Kim, S. Shin, L. Cho, B. C. De Cooman, The effect of vanadium micro-alloying on the microstructure and the tensile behavior of TWIP steel, Mater. Sci. Eng. A. 696 (2017) 416–428. https://doi.org/10.1016/j.msea.2017.04.083.

[214] D. Barbier, N. Gey, S. Allain, N. Bozzolo, M. Humbert, Analysis of the tensile behavior of a TWIP steel based on the texture and microstructure evolutions, Mater. Sci. Eng. A. 500 (2009) 196–206. https://doi.org/10.1016/j.msea.2008.09.031.

[215] C. Haase, L.A. Barrales-Mora, F. Roters, D.A. Molodov, G. Gottstein, Applying the texture analysis for optimizing thermomechanical treatment of high manganese twinning-induced plasticity steel, Acta Mater. 80 (2014) 327–340. https://doi.org/10.1016/j.actamat.2014.07.068.

[216] N.K. Tewary, S.K. Ghosh, S. Bera, D. Chakrabarti, S. Chatterjee, Influence of cold rolling on microstructure, texture and mechanical properties of low carbon high Mn TWIP steel, Mater. Sci. Eng. A. 615 (2014) 405–415. https://doi.org/10.1016/j.msea.2014.07.088.

[217] Y.F. Shen, Y.D. Wang, X.P. Liu, X. Sun, R. Lin Peng, S.Y. Zhang, L. Zuo, P.K. Liaw, Deformation mechanisms of a 20Mn TWIP steel investigated by in situ neutron diffraction and TEM, Acta Mater. 61 (2013) 6093–6106. https://doi.org/10.1016/j.actamat.2013.06.051.

[218] C. Haase, T. Ingendahl, O. Güvenç, M. Bambach, W. Bleck, D.A. Molodov, L.A. Barrales-Mora, On the applicability of recovery-annealed Twinning-Induced Plasticity steels: Potential and limitations, Mater. Sci. Eng. A. 649 (2016) 74–84. https://doi.org/10.1016/j.msea.2015.09.096.

[219] D.B. Santos, A.A. Saleh, A.A. Gazder, A. Carman, D.M. Duarte, É.A.S. Ribeiro, B.M. Gonzalez, E. V. Pereloma, Effect of annealing on the microstructure and mechanical properties of cold rolled Fe-24Mn-3Al-2Si-1Ni-0.06C TWIP steel, Mater. Sci. Eng. A. 528 (2011) 3545–3555. https://doi.org/10.1016/j.msea.2011.01.052.

[220] J.K. Hwang, Correlation of strain path, texture, twinning, and mechanical properties in twinning-induced plasticity steel during wire drawing, Materials (Basel). 13 (2020). https://doi.org/10.3390/ma13102250.

[221] M. Haude, R. Erbel, P. Erne, S. Verheye, H. Degen, P. Vermeersch, N. Weissman, F. Prati, N. Bruining, R. Waksman, J. Koolen, Safety and performance of the DRug-Eluting Absorbable Metal Scaffold (DREAMS) in patients with de novo coronary lesions: 3-year results of the prospective, multicentre, first-in-man BIOSOLVE-I trial, EuroIntervention. 12 (2016) 160–166. https://www.pcronline.com/eurointervention/99th_issue/volume-12/number-2/29/safety-and-performance-of-the-drug-eluting-absorbable-metal-scaffold-dreams-in-patients-with-de-novo-coronary-lesions-3-year-results-of-the-prospective-multicentre-first-in-man-bi.

[222] S. Verheye, A. Wlodarczak, P. Montorsi, J. Bennett, J. Torzewski, M. Haude, M. Vrolix, T. Buck, A. Aminian, R.J. Van Der Schaaf, ; Amin, A. Nuruddin, ; Michael, K.Y. Lee, Safety and performance of a resorbable magnesium scaffold under real-world conditions: 12-month outcomes of the first 400 patients enrolled in the BIOSOLVE-IV registry, EuroIntervention. 15 (2019) e1383–e1386. https://doi.org/10.4244/EIJ-D-18-01058.

[223] Z. Ma, M. Gao, D. Na, Y. Li, L. Tan, K. Yang, Study on a biodegradable antibacterial Fe-Mn-C-Cu alloy as urinary implant material, Mater. Sci. Eng. C. 103 (2019) 109718. https://doi.org/10.1016/j.msec.2019.05.003.

[224] ASTM, Standard guide for laboratory immersion corrosion testing of metals, ASTM Int. G31-12a (2012) 1–10. https://doi.org/10.1520/G0031-12A.

[225] A.C. Hänzi, I. Gerber, M. Schinhammer, J.F. Löffler, P.J. Uggowitzer, On the in vitro and in vivo degradation performance and biological response of new biodegradable Mg–Y–Zn alloys☆, Acta Biomater. 6 (2010) 1824–1833. https://doi.org/10.1016/j.actbio.2009.10.008.

[226] S. Loffredo, C. Paternoster, N. Giguère, M. Vedani, D. Mantovani, Effect of Silver on Corrosion Behavior of Plastically Deformed Twinning-Induced Plasticity Steel for Biodegradable Stents, JOM. 72 (2020) 1892–1901. https://doi.org/10.1007/s11837-020-04111-

w.

[227] A. Altomare, C. Cuocci, C. Giacovazzo, A. Moliterni, R. Rizzi, QUALX: a computer program for qualitative analysis using powder diffraction data, J. Appl. Crystallogr. 41 (2008) 815–817. https://doi.org/10.1107/S0021889808016956.

[228] B.M. Al-Hasni, G. Mountjoy, E. Barney, A. Gismelseed, A complete study of amorphous iron phosphate structure, J. Non. Cryst. Solids. 380 (2013) 141–152. https://doi.org/10.1016/j.jnoncrysol.2013.08.031.

[229] S. Zhu, N. Huang, L. Xu, Y. Zhang, H. Liu, H. Sun, Y. Leng, Biocompatibility of pure iron: In vitro assessment of degradation kinetics and cytotoxicity on endothelial cells, Mater. Sci. Eng. C. 29 (2009) 1589–1592. https://doi.org/10.1016/j.msec.2008.12.019.

[230] J.K. Heuer, J.F. Stubbins, An XPS characterization of FeCO3 from CO2 corrosion, Corros. Sci. 41 (1999) 1231–1243.

[231] P. Marcus, V. Maurice, H. Strehblow, Localized corrosion (pitting): A model of passivity breakdown including the role of the oxide layer nanostructure, Corros. Sci. 50 (2008) 2698–2704. https://doi.org/10.1016/j.corsci.2008.06.047.

[232] P. Sotoudeh Bagha, M. Khakbiz, S. Sheibani, S. Ebrahimi-Barough, H. Hermawan, In vitro degradation, hemocompatibility and cytocompatibility of nanostructured absorbable Fe-Mn-Ag alloys for biomedical application, ACS Biomater. Sci. Eng. (2020). https://doi.org/10.1021/acsbiomaterials.0c00263.

[233] J. Lévesque, H. Hermawan, D. Dubé, D. Mantovani, Design of a pseudo-physiological test bench specific to the development of biodegradable metallic biomaterials, Acta Biomater. 4 (2008) 284–295. https://doi.org/10.1016/j.actbio.2007.09.012.

[234] S. Loffredo, C. Paternoster, D. Mantovani, Iron-Based Degradable Implants, Encycl. Biomed. Eng. (2019) 374–385. https://doi.org/10.1016/B978-0-12-801238-3.11023-2.

[235] M. Talha, Y. Ma, P. Kumar, Y. Lin, A. Singh, Role of protein adsorption in the bio corrosion of metallic implants – A review, Colloids Surfaces B Biointerfaces. 176 (2019) 494–506. https://doi.org/10.1016/j.colsurfb.2019.01.038.

[236] S. Höhn, S. Virtanen, A.R. Boccaccini, Protein Adsorption on Magnesium and its alloys: A

review, Appl. Surf. Sci. (2018). https://doi.org/10.1016/j.apsusc.2018.08.173.

[237] H. Hermawan, D. Dubé, D. Mantovani, Developments in metallic biodegradable stents, Acta Biomater. 6 (2010) 1693–1697. https://doi.org/10.1016/j.actbio.2009.10.006.

[238] A.G. Demir, B. Previtali, Additive manufacturing of cardiovascular CoCr stents by selective laser melting, Mater. Des. 119 (2017) 338–350. https://doi.org/10.1016/j.matdes.2017.01.091.

[239] B.S.P.K. Kandala, G. Zhang, T.M. Hopkins, X. An, S.K. Pixley, V. Shanov, In vitro and in vivo testing of zinc as a biodegradable material for stents fabricated by photo-chemical etching, Appl. Sci. 9 (2019). https://doi.org/10.3390/app9214503.

[240] J. Fiocchi, C.A. Biffi, S. Gambaro, C. Paternoster, D. Mantovani, A. Tuissi, Effect of Laser welding on the mechanical and degradation behaviour of Fe-20Mn-0.6C bioabsorbable alloy, J. Mater. Res. Technol. (2020) 124658. https://doi.org/10.1016/j.jmrt.2020.09.104.

[241] M.S. Dargusch, J. Venezuela, A. Dehghan-Manshadi, S. Johnston, N. Yang, K. Mardon, C. Lau, R. Allavena, In Vivo Evaluation of Bioabsorbable Fe-35Mn-1Ag: First Reports on In Vivo Hydrogen Gas Evolution in Fe-Based Implants, Adv. Healthc. Mater. 2000667 (2020) 1–15. https://doi.org/10.1002/adhm.202000667.